Title

Zero-Dimensional and One-Dimensional Graphene Nanomaterials: Synthesis, Application, and Nanocrystal Composites Thereof

Author

Rogers, Cameron Randolph

Publication Date

2017

Zero-Dimensional and One-Dimensional Graphene Nanomaterials: Synthesis, Application, and Nanocrystal Composites Thereof

by

Cameron Rogers

A dissertation submitted in partial satisfaction of the

requirements for the degree of

Doctor of Philosophy

in

Chemistry

in the

Graduate Division

of the

University of California, Berkeley

Committee in charge:

Professor Felix Fischer, Chair
Professor Christopher Chang
Professor K. Peter Vollhardt
Professor Alessandra Lanzara

Fall 2017

Zero-Dimensional and One-Dimensional Graphene Nanomaterials: Synthesis, Application, and Nanocrystal Composites Thereof

Abstract

Zero-Dimensional and One-Dimensional Graphene Nanomaterials: Synthesis, Application, and Nanocrystal Composites Thereof

by

Cameron Rogers

Doctor of Philosophy in Chemistry

University of California, Berkeley

Professor Felix Fischer, Chair

The bottom-up synthesis of graphene nanomaterials has recently emerged as an important approach for accessing carbon materials featuring desirable or exotic electronic properties. The ability to produce these materials with structural precision and synthetic flexibility makes bottom-up synthesis a powerful tool both for understanding materials at the nanoscale and for designing the next generation of high-performance nanomaterials. Although a handful of robust bottom-up synthetic techniques has been developed, investigation has been quite limited with regard to both the types of graphene nanomaterials produced and the applications for which those materials are considered. In this thesis, the extant tools of bottom-up synthesis are applied to the production of novel zero-dimensional and one-dimensional graphene nanomaterials. This includes the use of surface-assisted techniques for the synthesis of unique nanographenes featuring exotic electronic and magnetic properties, facilitated by development of a robust and general solution chemistry methodology to access challenging acene derivatives. This work also examines the unprecedented application of bottom-up synthesized one-dimensional graphene nanoribbons (GNRs) as composite materials with inorganic nanoparticles, and describes the exceptional performance these diverse composites achieve through the rational design of nanomaterial interfaces.

Contents

I Introduction 1

II Surface-Assisted Synthesis of Graphene Nanostructures 23

List of Figures

List of Schemes

List of Tables

Acknowledgments

The work described here has been highly collaborative, and I am thankful for that. Synthetic chemistry is inherently lonely, and I feel very fortunate that my synthetic efforts have grown into projects far broader, with diverse colleagues from whom I have learned a great deal. I am very fond of Epictetus' observation that life's great key is to associate with those people who call forth your best. In that spirit, thank you especially to my advisor Felix, as well as to the many collaborators who have forced me to grow as a scientist. To the Fischer group: always remember the Traditions, and thank you for all our fun times.

Part I

Introduction

Chapter 1

Carbon Nanomaterials as Composites with Metal Nanoparticles

Application of inorganic nanoparticles frequently requires the use of a support material, a complementary component that can interface with the active material at the nanoscale to provide stability, maximize active surface area, and dictate the particle's reactive environment. This introductory chapter will examine the role of the support material and how perception of that role has changed over time. It will further examine the design principles that are employed to create high-performance composites across varied applications, and what material properties contribute to an ideal support. Specific examples will highlight the use of graphene nanomaterials and the properties that have led to their widespread application in composites with metal nanoparticles. Special attention will be paid to a specific phenomenon, the Mott-Schottky Effect, that dictates the behavior of certain metal-semiconductor interfaces important to catalysis. Lastly, the physical and electronic properties of narrow, bottom-up synthesized graphene nanoribbons will be considered in this context, as a forerunner to their experimental examination later in this thesis.

1.1 Introduction to Support Materials

Across a wide array of energy applications, inorganic nanomaterials have proven to be powerful and versatile tools for facilitating challenging chemical transformations.[1,2] As catalysts or as active materials, metals, their oxides and their alloys carry an inherent diversity that provides for a broad set of available reactivities, and nanosizing serves to alter and amplify this reactivity by increasing surface area and introducing high-energy facets and edges. Historically, efforts to optimize these materials have primarily relied on altering structural parameters of the metal nanoparticles (MNPs) themselves, such as their size, shape, or composition, producing remarkable performance enhancements in nearly every energy-related field.[3–5]

Most frequently, inorganic nanoparticles rely on a secondary material—the support material—to achieve what is termed *dispersion*, the physical separation of the nanoparticles from each other. High dispersion serves to maximize the accessible surface area of the nanoparticle ensemble, and thereby maximize the desired reactivity occurring at the nanoparticle surface.[6] In this way, the role of the support material is also to confer stability to the resulting composite; by separating the nanoparticles and their reactive facets from one another, dispersive support materials serve to slow or prevent nanoparticle aggregation and the corresponding loss of surface area.[7] Traditionally, therefore, an ideal nanoparticle support is a chemically inert material with high surface area so as to achieve the best possible dispersion, with porosity to facilitate mass transport.[8] Many porous metal oxides, such as silica, alumina, or titania, have therefore been employed as nanoparticle supports for many decades.

Hydrogen sorption has long been a common method for measuring dispersion in composite materials with catalytic metals, in which one hydrogen atom is chemisorbed per accessible surface atom of the metal, allowing for a quantitative understanding of the active metal surface.[10] It was these hydrogen sorption measurements that would reveal an anomalous behavior, termed in 1978 the "strong metal-support interaction" (SMSI), that served to upset the traditional model of the support material.[11] For catalytic metals (e.g. Pt, Rh, Ni) supported on reducible metal oxides (most commonly TiO_2), hydrogen sorption was strongly suppressed or eliminated following activation in hydrogen, indicating a strong perturbation of the metal by the support.[8] This was in contrast with the classical model of MNPs sitting passively on the support surface; although Fermi level equilibration would of course occur at the solid-solid interface, screening by the metal makes this insufficient to explain the profound shift in behavior for particles larger than 1–2 nm.[10,12] Most notably, systems exhibiting SMSI were not simply deactivated, but were in fact found to exhibit dramatically enhanced activity for Fischer-Tropsch CO hydrogenation, with catalytic turnover rates increased by factors as large as 30 (Figure 1.1).[8,9,13] Simple explanations such as nanoparticle aggregation were quickly ruled out, prompting a substantial scientific effort towards understanding the support-metal interface in such systems.[14]

These investigations discovered a complex interfacial system most notably involving migration of reduced metal oxide onto a portion of the MNP surface, forming a sub-monolayer of, for example, TiO_x ($x < 2$).[10,15] This is accompanied by significant electron transfer from

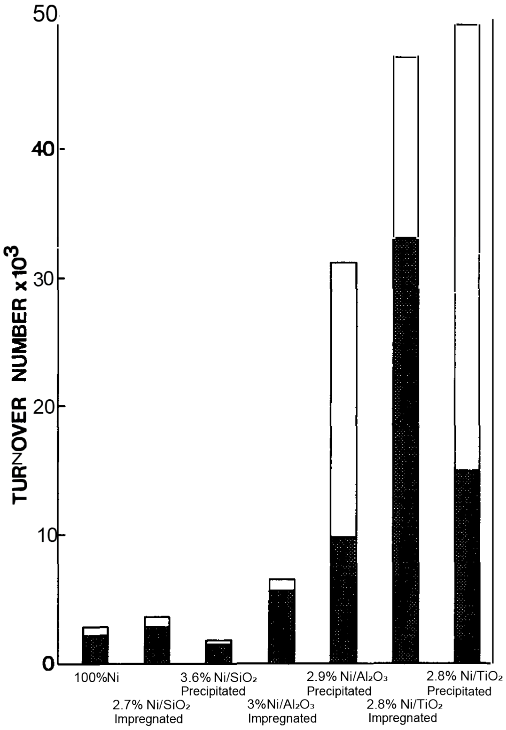

Figure 1.1: Strong metal-support interaction (SMSI) was found to increase catalytic activity for CO hydrogenation by factors as large as 30-fold in comparison to composites that cannot participate in SMSI, such as SiO_2. Solid bars correspond to CH_4 production, empty bars indicate C_2 product production. Figure reproduced from reference [9].

the reduced metal oxides to the metal surface, a large proportion of which was in intimate contact with oxide due to the aforementioned migration, leading to the observed change in behavior.[13,16] The altered catalytic behavior of the composite reflects both this electronic shift and a cooperative catalytic mechanism, most notably involving hydrogen activation by the oxide.[10] Outside of these specific revelations, full investigation of this phenomenon yielded two broad conclusions. First, these studies helped to alter the picture of support material interactions from one of passive facilitation to one of active participation.[10] As the author who in 1978 coined the term SMSI wrote in 1987,[15]

> "This information has forced us to change our picture of supported metal catalysts.... It has become clear that the traditional view of metal particles resting unperturbed on an oxide surface is not always correct."

Second, they helped to establish the idea of a support material as a tool for enhancing catalysis directly, and in so doing began to change what attributes constitute an ideal nanoparticle support.[12,17,18] Rather than simply seeking to maximize surface area, materials capable of intimately interfacing with metal nanoparticles and interacting with their surface electronically became desirable as advanced support materials for promoting nanoparticle activity.

This increased attention to the role of support materials coincided with a time of exploding interest in and availability of carbon nanomaterials, headlined by the rise of carbon nanotubes (CNTs) in the 1990s and later by graphene and its chemical derivatives.[19–21] Carbon nanomaterials can be prepared with very high surface area, and, as comparatively mechanically flexible materials, they generally interface capably with other nanomaterials.[22–25] Notably, support materials based on sp^2 carbon exhibit good thermal conductivity, aiding in nanoparticle function and stability, and offer good resistance to acidic and basic media.[23,26] Perhaps most importantly, graphene nanomaterials also provide excellent electrical conductivity, especially in comparison with most oxide supports, making them premier support materials for metal nanoparticle electrocatalysis.[23,27] Carbon nanomaterials are diverse and tunable, with a variety of 1D, 2D, and 3D structures of readily modified porosity and chemical functionality together constituting myriad tools for engineering support-metal interactions.[24,28–32] These notably include single-wall and multiwall CNTs, carbon fibers, graphitic carbon nitrides, graphene, graphene oxide (GO), reduced graphene oxide (rGO), and abundant chemically or structurally modified porous carbons.[22,33–39]

As was true of oxide support materials, the first-order goals of carbon nanomaterial supports are high dispersion and stability. Much in the way that oxide supports accomplish these goals through the anchoring of metal nanoparticles at defect and dopant sites, graphitic edges and sites of heteroatom substitution play an important role in immobilizing metal nanoparticles on graphene nanomaterials.[16,31,35,40–42] Although metals are known to interact electronically with the extended π structure of graphene and graphene nanomaterials, and for some metals this attraction can be quite strong, many carbon nanomaterial supports augment this interaction through heteroatom doping, and observe improved dispersion and stability as a result.[27,28,43,44] Some composite systems, in particular those using CNT support materials, make use of designed covalent tethers to thoroughly immobilize included MNPs, as illustrated in Figure 1.2.[36,45] More commonly, however, support materials are simply functionalized with Lewis-basic heteroatoms, such as nitrogen or oxygen, within the nanomaterial structure.[26,46]

Many graphene nanomaterial supports achieve strong anchoring interaction and high dispersion through *in-situ* synthesis of metal nanoparticles, in which nanoparticles are grown in the presence of the support material rather than being synthesized separately and later introduced to the support.[25,47,48] Because nucleation of nanoparticle growth occurs on the support material, the resulting MNPs are bound to the support, and therefore tend to exhibit enhanced stability and dispersion.[36,49] *In-situ* synthesis is generally accomplished by impregnation of the support material with a solution of a metal salt, which is then reduced to form nanoparticles by various chemical or thermal conditions. In this approach, functionalization of the graphene nanomaterial with heteroatom moieties is crucial; heteroatoms serve as sites of MNP nucleation, and as a result *in-situ*–synthesized composites with heavily oxygen- or nitrogen-functionalized support materials exhibit smaller and more uniform MNPs, with higher dispersion and better stability.[22,39,50] *In-situ* nanoparticle synthesis has consequently become a very common strategy for the fabrication of composites with a material like graphene oxide, which features a highly defective surface including abundant available oxygen functionalities.[27,37,50–52] Although composites made in this way do benefit from

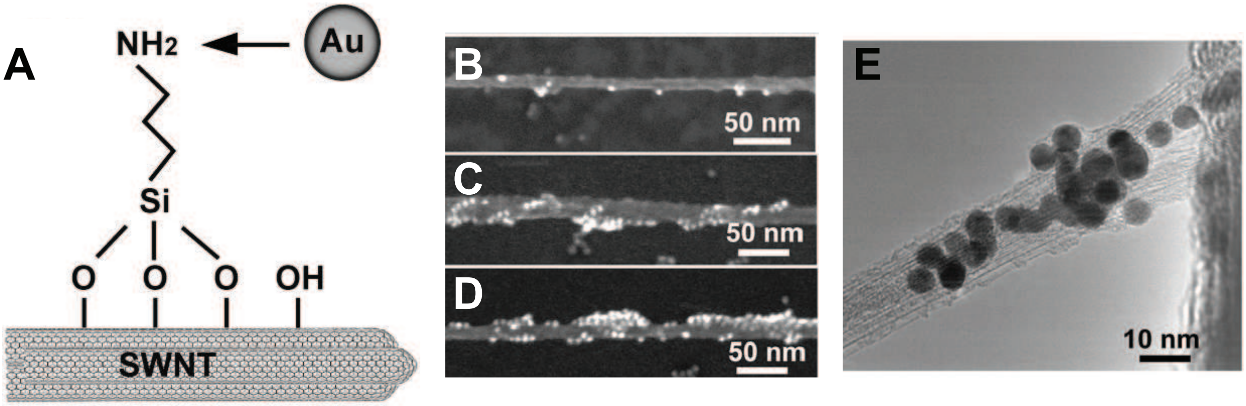

Figure 1.2: (A) Schematic representation of AuNP-SWCNT composite synthesis using a designed covalent tether. (B-D) Dark-field SEM images reveal a dependence of AuNP density when using (B) 1x (C) 5x and (D) 10x linker concentration. (E) Bright-field TEM images clearly show AuNPs anchored to a SWCNT bundle. Figures from reference [45].

robust MNP-support interaction, *in-situ* nanoparticle synthesis is less well controlled and less tunable than traditional colloidal MNP synthesis.[36] Additionally, comparison between composites prepared by this approach is challenging, since an observed difference between composites could either stem directly from support material interaction or from altered nanoparticle morphology.

Across a variety of composite material applications, the diverse benefits associated with nitrogen-containing support nanomaterials have made nitrogen the most common dopant used in carbon supports.[53] Depending on the manner of heteroatom incorporation, nitrogen doping frequently serves to lower the valence band of the carbon support material, which both alters its electronic interaction with MNPs and lends the support itself improved oxidative stability.[54] As discussed above, the Lewis basicity of nitrogen atoms also leads to increased support-metal binding directly, enhancing MNP stability and dispersion.[33,42,53,55] Improved catalytic activity for metal nanoparticles supported on nitrogen-doped graphene nanomaterials has been observed quite broadly, and is especially common for Pt nanoparticles in fuel cell applications.[28,41,46,47] Importantly, nitrogen dopants introduced to graphene nanomaterials by top-down fabrication are always present as a varied and unpredictable mixture of pyrrolic, pyridinic, graphitic and oxidized nitrogen sites, which frequently confounds precise determination of their role and the manner of their interaction with MNPs.[26]

Beyond the goals of achieving high dispersion, nanoparticle stability, and good support-MNP contact, the design considerations for support materials vary significantly between applications, and the diversity of carbon nanomaterials is crucial to meeting these disparate demands. For example, many lithium-ion battery materials rely on defect and heteroatom sites in support materials to promote full reversibility of their lithiation reactions; without active facilitation from the support material, nanoscale irreversibility of certain solid phases can cause loss of capacity and eventual loss of function.[56–59] Other nanoparticle active mate-

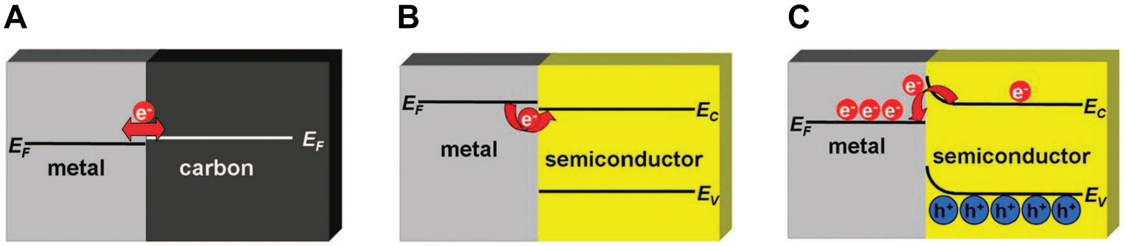

Figure 1.3: Schematic depictions of possible metal interfaces with varied support materials. (A) Ohmic contact between a metal and semimetal, e.g. graphite. (B) Ohmic contact between a metal and a semiconductor of low-lying Fermi level. (C) Rectifying contact between a semiconductor (here an n-type semiconductor) and a metal, resulting in the accumulation of electron density on the metal and a Schottky barrier at the interface. Figures reproduced from reference [53].

rials for battery or gas storage experience large volume changes during cycling, and demand a flexible support material to accomodate these expansive and contractive cycles without being pulverized.[39,49,55,60] Still other applications emphasize porosity, stability in harsh oxidative conditions, or a support material that can aid in determining the local pH at the active metal surface.[30,35,61] In each case, well-designed support materials take an active role in promoting and maintaining the function of metal nanoparticles.

1.2 Mott-Schottky Effect at Support-Catalyst Interfaces

Among the possible electronic interfaces between metals and support materials, one case merits special consideration in the context of this work. Unlike ohmic contacts formed between a metal and a semimetal (e.g. graphite, Figure 1.3A) or between a metal and a high work function semiconductor (e.g. TiO_2, Figure 1.3B), a rectifying interface forms between a semiconductor and a metal of appropriate Fermi level (Figure 1.3C). As is well known from solid-state physics, charge transfer between the materials proceeds until the equilibration of their Fermi levels at the interface, known as the Mott-Schottky effect.[13] The resulting interfacial band structure is commonly termed a Schottky barrier; importantly, as a rectifying contact the Schottky barrier only provides a significant impediment to charge transfer in one direction. For example, the Schottky barrier shown in Figure 1.3C resulting from electron transfer from the semiconductor to the metal would not impede the further flow of electrons towards the metal under an applied bias, but would significantly impede the flow of electrons away from the metal under reverse bias.

For nanoscale metals, the implications of this charge transfer for their catalytic behavior can be quite significant. Metal oxide support materials generally have band energies too low-lying to participate in this effect, but it has been demonstrated with a number of well-

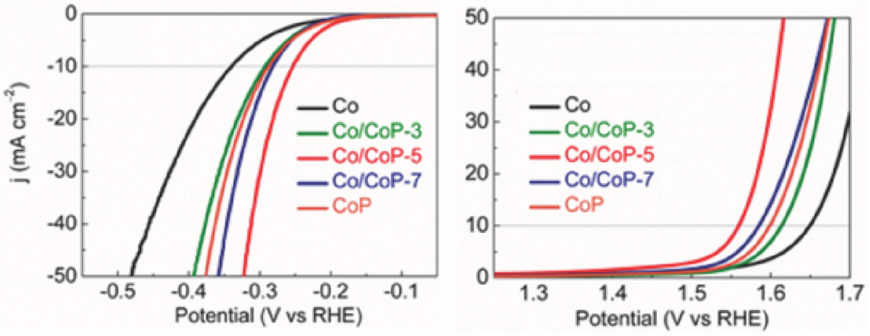

Figure 1.4: The Mott-Schottky effect can drastically alter onset potentials for electrocatalytic nanoparticles. Here, cobalt nanoparticles in contact with semiconducting cobalt phosphide exhibit shifted onset potentials for the hydrogen evolution reaction (HER, left) and oxygen evolution reaction (OER, right) reflecting varied degrees of electron tranfer from CoP to Co. Figure from reference [64].

chosen semiconducting organic and inorganic nanomaterials.[53] Because catalytic metals are frequently more “noble” (lower Fermi level) than these semiconducting supports, the Mott-Schottky effect most commonly results in a concentration of electron density at the metal surface. This additional electron density serves to activate transition states and alter reactant adsorption, thereby increasing reactive rates at the metal surface.[62,63] The Mott-Schottky effect is particularly pronounced for electrocatalytic composites, since the effect of raising the Fermi level at the catalytic MNP surface is to lower the additional applied potential required to reach the reactive energy threshold. The result is a lowered onset potential for electrocatalytic systems designed to employ the Mott-Schottky effect, achieving improved catalytic energy efficiency through well-designed nanomaterial interfaces (Figure 1.4).[64]

As discussed above, heteroatom doping generally and nitrogen doping in particular are common methods for tuning the energy levels of graphenic materials, leading to abundant examples of Mott-Schottky support systems using nitrogen-doped carbons or carbon nitrides.[30,53,65] For example, graphitic carbon nitride (g-C_3N_4) has frequently been employed as a support for palladium nanoparticles, boosting their activity for both thermal and photochemical catalysis of such varied reactivities as Suzuki reactions, formic acid dehydrogenation, and ammonia borane hydrolysis.[66–70] Other studies using lower work function metals (e.g. cobalt) observe electron transfer from the metal to the semiconducting support material, activating the metal towards oxidative chemistry (Figure 1.5).[63] Further examples make use of inorganic Schottky support materials, especially as catalysts for dye-sensitized solar cells.[62,71–74] One such system, shown in Figure 1.6, found optimum catalytic performance for the only Pt-Fe alloy with a work function positioned to facilitate Mott-Schottky electron transfer from the Ni_3S_4 support, neatly demonstrating the design and execution of metal-semiconductor heterojunctions for catalysis.[74]

Related results have been observed in a number of other metal nanoparticle composites with graphene nanomaterials, although they are frequently not referred to using the same

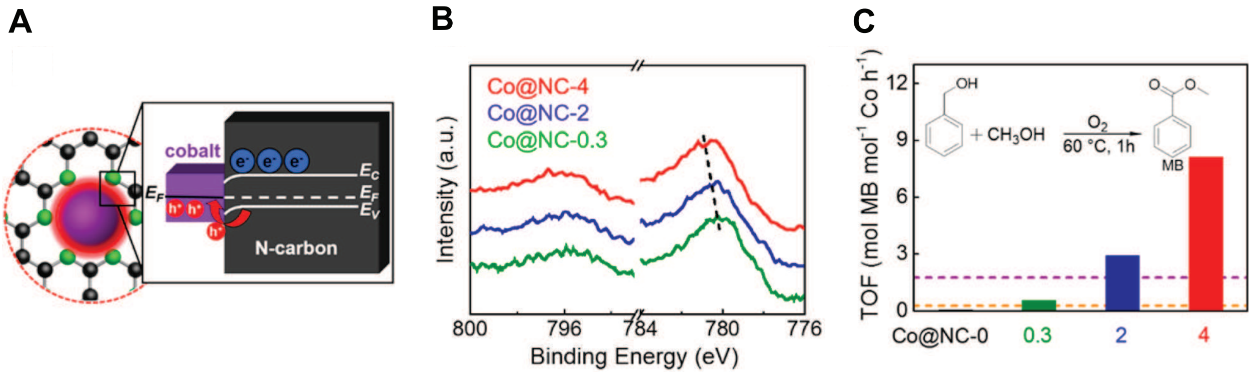

Figure 1.5: (A) Schematic illustrating hole transfer at the Mott-Schottky heterojunction between graphitic carbon nitride and cobalt, a lower work function metal. (B) X-ray photoelectron spectroscopy shows a shift in the Co 2p signal towards higher binding energies as the electron density on cobalt is depressed. (C) The composites with greater interfacial charge transfer show higher activity for aerobic esterification of benzyl alcohol at the cobalt nanoparticle surface. Figures from reference [63].

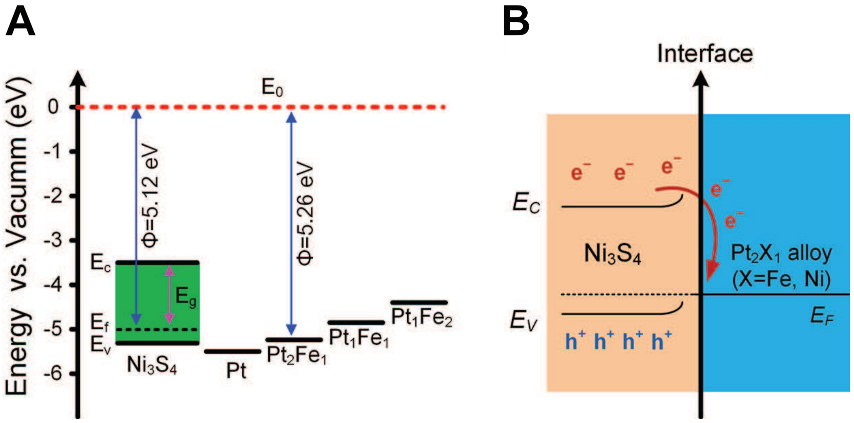

Figure 1.6: (A) Band structure of semiconducting Ni_3S_4 compared to the work functions of Pt and its alloys with Fe. Among these, only Pt_2Fe is positioned to form a Mott-Schottky heterojunction with Ni_3S_4 as shown in (B), and this composite was found to outperform the others tested. Figure from reference [74]

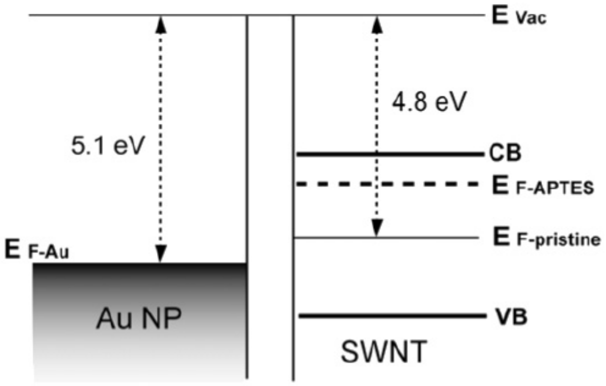

Figure 1.7: Schematic illustrating the electronic structures of a gold nanoparticle (AuNP) and a semiconducting SWCNT. The higher Fermi level ($E_{F-\mathrm{pristine}}$) of the CNT leads to electron transfer towards the AuNP until their Fermi levels equilibrate: the Mott-Schottky effect. Doping of the CNT raised its Fermi level ($E_{F-\mathrm{APTES}}$), which led to greater observed interfacial charge transfer. Figure from reference [45].

Mott-Schottky terminology. For example, interfacial charge transfer between semiconducting SWCNTs and assorted metals has been observed in a variety of contexts. Figure 1.7 shows the band structures of SWCNTs and gold nanoparticles (AuNPs), a representative high work function metal nanoparticle; in this example, electron transfer to the metal led to improved conductivity in the SWCNTs, improving their performance as transistor materials.[45] Doping the CNTs to raise the Fermi level ($E_{F-\mathrm{pristine}}$ to $E_{F-\mathrm{APTES}}$) led to an increase in the observed electron transfer as well as further increased CNT conductivity. Similar schemes have used metal nanoparticles to improve CNT conductivity for other applications, such as transparent conductive films.[48] Most notably, the same interfacial effects have led to shifted onset potentials for Pt nanoparticles used as fuel cell catalysts when supported on semiconducting CNTs rather than other carbon support materials like carbon black.[35] Although these examples are not explicitly attributed in the literature to Schottky effects, they clearly indicate that the effect has been successfully utilized in composite materials with semiconducting supports for over a decade, albeit largely to dictate the behavior of the semiconductor.

In addition to the direct catalytic effects of altered electron density at the metal surface, the dynamic at the semiconductor-metal interface generates secondary effects that can further benefit catalysis. A Schottky barrier serves to enhance the rate of charge separation at the MNP-semiconductor interface and extend the lifetime of high-energy charge carriers, an important concern in photocatalytic systems.[53] As mentioned above, the Schottky barrier also effectively prevents the movement of charge in the reverse of the intended direction during catalysis. Most notably, the formation of charged regions at the metal-support interface serves to enhance catalytic stability, as Coulombic attraction across the interface creates an additional anchoring effect that aids in the primary support material goals of dispersing and immobilizing metal nanoparticles.[62] Turning again to the shifting concept of the "ideal" metal nanoparticle support, it is reasonable to conclude that the modern ideal for a support material includes a semiconducting electronic structure with a significant bandgap and tunable energy levels to fully harness the Schottky effect across varied composites.

1.3 Graphene Nanoribbons as Support Materials

Bottom-up synthesized graphene nanoribbons (GNRs) are a recently-developed class of quasi-one dimensional graphene nanomaterial featuring narrow widths (approximately 1 nm) and high aspect ratio (See Section 2.2, page 16). Although they have not previously been studied for composite materials in any context, consideration of their properties in the context of factors outlined in this chapter suggests they could serve quite capably as support materials for metal nanoparticles. Graphene nanoribbons are semiconducting, with significant bandgaps and comparatively low work functions that make them ideal for participation in the Mott-Schottky interfacial effect described above. Importantly, their preparation through bottom-up synthesis creates significant structural and electronic tunability using the tools of synthetic organic chemistry. GNRs are flexible nanomaterials that form extended ultramicroporous networks and could therefore interact with the entire surface area of an intercalated nanoparticle; although the charged regions created by interfacial electron transfer extend only a few nanometers, a support that contacts all sides of the metal nanoparticle could alter the reactivity of its entire surface. The next chapter will therefore examine the means by which graphene nanoribbons can be prepared in a bottom-up fashion, and the importance of such an approach for controlling their properties at the nanoscale.

Chapter 2

Bottom-Up Synthesis of Graphene Nanoribbons

Although graphene's remarkable properties have prompted a broad push for its application, there exist some contexts for which the material is ill-suited. For example, many of graphene's electronic properties would be quite desirable for a transistor channel material, but the lack of a bandgap precludes graphene's application in this manner. This chapter examines a specific graphene nanomaterial, the graphene nanoribbon (GNR), that by virtue of its intrinsic bandgap is well suited for the translation of graphene's desirable properties into semiconductor applications, including both transistor applications and (as detailed in Chapter 1) MNP support material applications. After a brief introduction, the focus of this chapter will be on the bottom-up synthesis of graphene nanoribbons from small-molecule organic precursors, which is crucial to the production of narrow, high-quality GNRs as these applications demand.

2.1 Graphene Nanomaterials

The scientific fervor surrounding the isolation and application of graphene, the two- dimensional material of sp^2 carbon atoms, has been inescapable, culminating in the 2010 Nobel Prize in physics.[20] The community's enthusiasm stems from a bevy of remarkable material properties across a wide range of measures; for example, graphene is flexible and strong (e.g. Young's modulus of 1.0 TPa), with extremely high theoretical surface area (2630 m^2 g^{-1}).[75,76] It exhibits outstanding thermal conductivity (5,000 W mK^{-1}) and charge carrier mobility ($2.5x10^5$ m^2 $V^{-1}s^{-1}$) while offering 97.7% optical transparency, and further plays host to exotic electronic phenomena.[20,77–80] It is unsurprising, therefore, that a great deal of work has gone towards the application of graphene in nearly every imaginable subfield of materials science.[21,47]

However, in a number of contexts and applications for which graphene's extraordinary properties would be desirable, other material requirements make application of graphene itself inappropriate. For example, despite graphene's extremely high surface area in theory, the accessible surface area of the material is limited in practice by its strong propensity for stacking and folding, making graphene itself of limited utility in applications that require high surface area.[34] In these cases, a wide variety of related sp^2 carbon materials collectively termed graphene nanomaterials can be used to deliver the remarkable capabilities of graphene to a broader set of contexts. Returning to the example of surface area, graphene nanofibers and carbon nanotubes (CNTs) benefit from graphene's characteristically high thermal and electrical conductivities while providing surface areas suitable for nanoparticle composite applications, as described in Chapter 1.[23] Chemical modification of graphene to enhance its dispersibility yields the graphene nanomaterials graphene oxide (GO) and reduced graphene oxide (rGO), which also perform admirably in these contexts while retaining many of graphene's desirable properties.[21,81] Graphene can further be modified into three-dimensional nanostructures such as foams and aerogels, demonstrating the remarkable breadth of accessible graphene nanomaterials designed to meet a given material challenge.[82,83]

In addition to the above geometric concerns, graphene's applicability is further limited by its electronic structure. The valence and conduction bands of graphene contact each other at K points of the Brillouin zone, termed the Dirac points; while this is crucial to many of graphene's remarkable and unusual electronic properties, it means that graphene is a zero-bandgap semimetal and is therefore inappropriate for applications that require a semiconducting material, most notably transistor applications.[21,79,84,86] Consequently, a number of strategies have emerged for inducing a bandgap in graphene. Few-layer stacks of graphene exhibit a bandgap under certain conditions, but are not inherently semiconductors.[79] CNTs can be semiconducting, with properties appropriate for transistor applications, but under current methods are produced as a mixture of materials with varied bandgaps, including a fraction of metallic conductors.[87] Most promising is the lateral confinement of two-dimensional graphene to a small, finite width in one of those dimensions, producing a quasi-one dimensional material termed a graphene nanoribbon (GNR) featuring a significant bandgap.[84–86] GNRs have therefore recently become materials of great interest, and

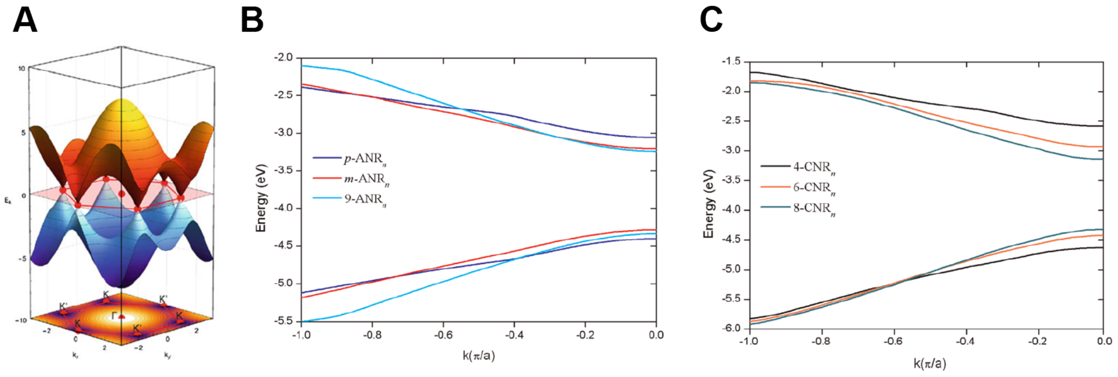

Figure 2.1: (A) The electronic structure of graphene, illustrating the contact between its valence and conduction bands that precludes its use for semiconducting applications. Figure from reference [84]. (B&C) The electronic structures of various (B) armchair and (C) chevron graphene nanoribbons feature a bandgap resulting from quantum confinement in their finite dimension. Figures from reference [85].

the remainder of this chapter will be dedicated to a discussion of their properties and their synthesis.

2.2 Introduction to Graphene Nanoribbons

GNRs are an unusual graphene nanomaterial, sharing graphene's planar topology and unbroken carbon scaffold but with a finite width in one dimension. As mentioned above, the electronic structure of a GNR is dominated by quantum confinement in this finite dimension, creating its characteristic bandgap.[88] Consequently, GNR width and edge geometry are important determinants of its properties, resulting in distinct families of GNR distinguished by their crystallographic axis and edge structure.[89] (Figure 2.2) Armchair (AGNRs) and zigzag (ZGNRs) are the simplest GNR families, featuring straight edges along crystallographic axes offset from each other by 30 degrees. Other families feature the same axes but with distinct edge structures; for example, chevron GNRs share the crystallographic axis of AGNRs, but with a serpentine edge structure that results in a different bandgap, band structure, and conductivity. Cove GNRs share the crystallographic axis of zigzag GNRs, but with protruding edges that drastically alter their elctronic structure in comparsion to the parent ZGNR. Each of these GNR types has been prepared and characterized, and their divergent properties are indicative of GNR's sensitivity to structural differences on the atomic scale.

Any application seeking to make use of GNRs, and especially any transistor application, would require a material with electronic homogeneity between nanoribbons, including a consistent bandgap.[86,90–92] The extreme sensitivity of GNR properties to width and edge structure therefore have important implications for their synthesis, since structural defects will dramatically alter the desirable electronic properties that motivated their preparation.

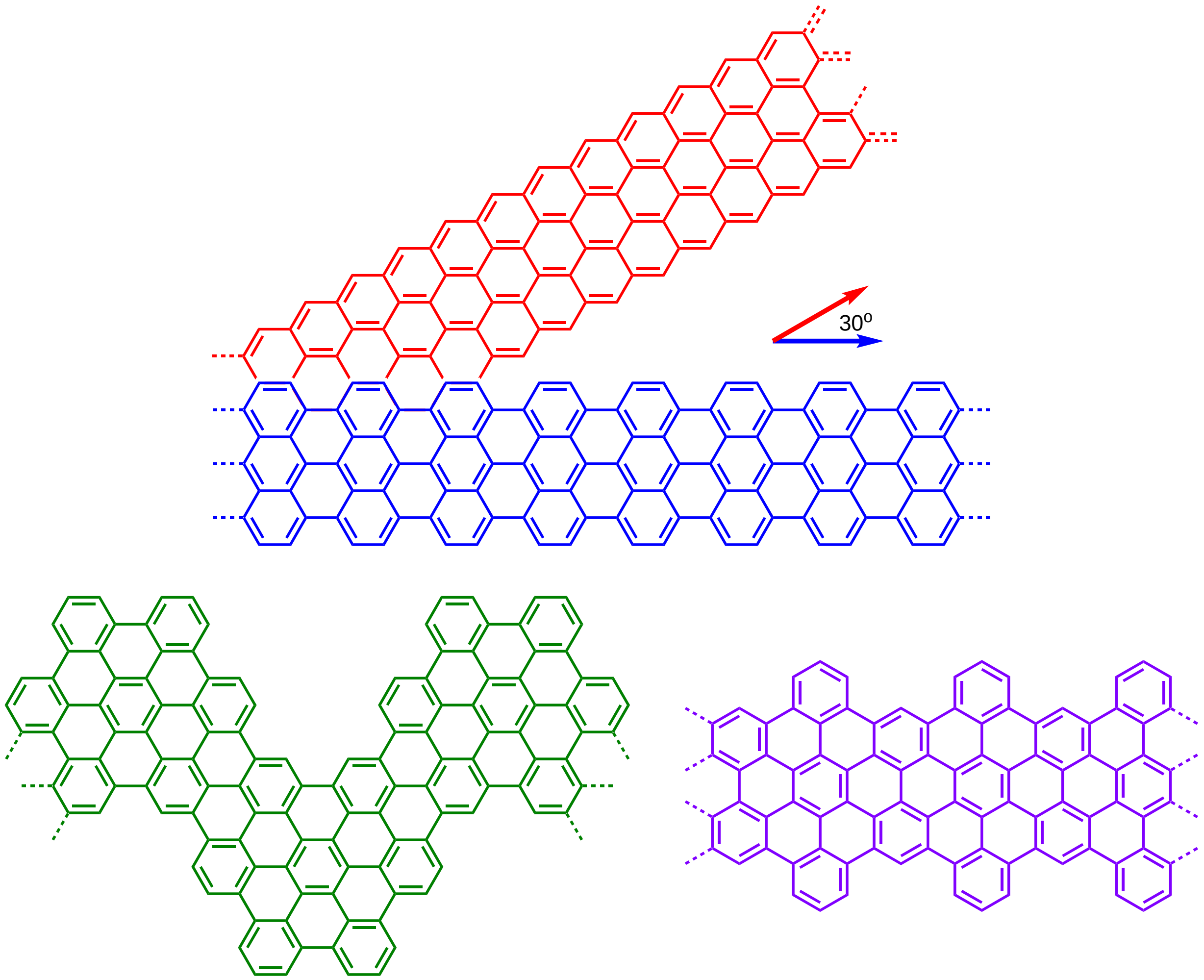

Figure 2.2: Families of GNRs are distinguished by their crysallographic axis and edge structure. Armchair (blue) and zigzag (red) are the simplest GNR families, featuring straight edges along graphene crystallographic axes offset from each other by 30 degrees. Chevron GNRs (green) share the crystallographic axis of armchair GNRs, but with a distinct serpentine edge structure. Cove GNRs (purple) share the crystallographic axis of zigzag GNRs, but with regular protrusions at the edges. In each case, the varied edge structures lead to divergent electronic properties.

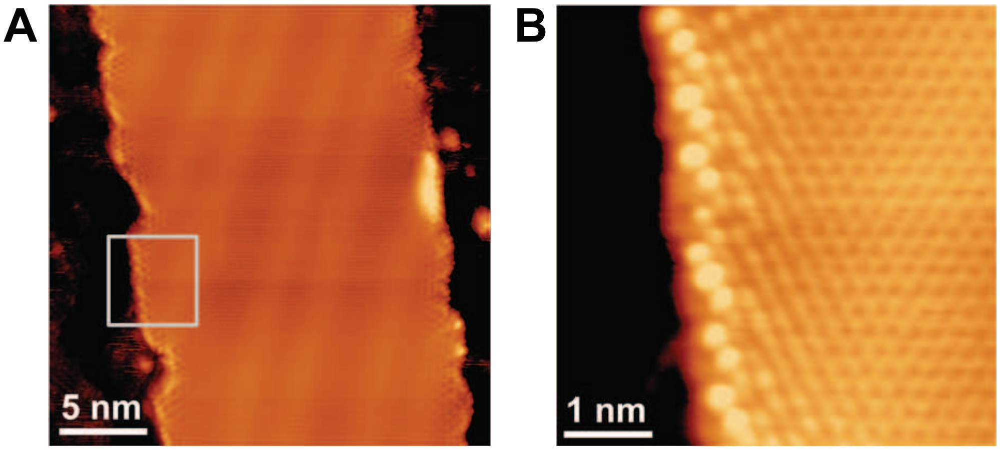

Figure 2.3: Scanning tunneling microscopy (STM) images show the nanometer-scale roughness of GNRs prepared by plasma etching of chemically unzipped nanotubes. The indicated area in (A) is shown in (B). Figure from reference [99].

In this regard, methods for GNR synthesis by top-down modification of other carbon materials fail entirely. Although an abundance of methods exist, from the sonication of graphite to the unzipping of nanotubes to the etching of graphene sheets, all rely on uncontrolled conditions that yield rough and poorly defined edges (Figure 2.3).[93–99] Additionally, many top-down fabrication techniques make use of harsh oxidizing conditions that result in chemically modified edges, further altering the electronic structure of the product.[98,100,101] Just as importantly, these methods struggle to reach relevant GNR widths. GNR bandgap displays a sharp inverse dependence on width, and is negligible (approximately 100 meV) for widths beyond 10 nm; most top-down approaches struggle to produce any sufficiently narrow GNRs.[91,100,102–104]

To access well-defined graphene nanoribbons with structural homogeneity and a usable bandgap, another synthetic approach is required. The alternative is bottom-up synthesis, in which designed small molecule precursors polymerize to form the GNR by well controlled reactivity. Since 2008, a variety of GNRs have been prepared by bottom-up synthetic techniques, yielding narrow nanoribbons of precisely controlled widths and edge geometries.[105,106] These bottom-up syntheses are executed in two divergent fashions: either by reaction of the small molecule precursors on a hot metal surface in high vacuum, or by reaction using more conventional solution-phase techniques. These two approaches will be discussed separately.

2.3 Surface-Assited Synthesis of Graphene Nanoribbons

Surface-assisted synthesis of graphene nanoribbons makes use of the enhanced reactivity associated with a noble metal surface, as well as the ability of a planar surface to template

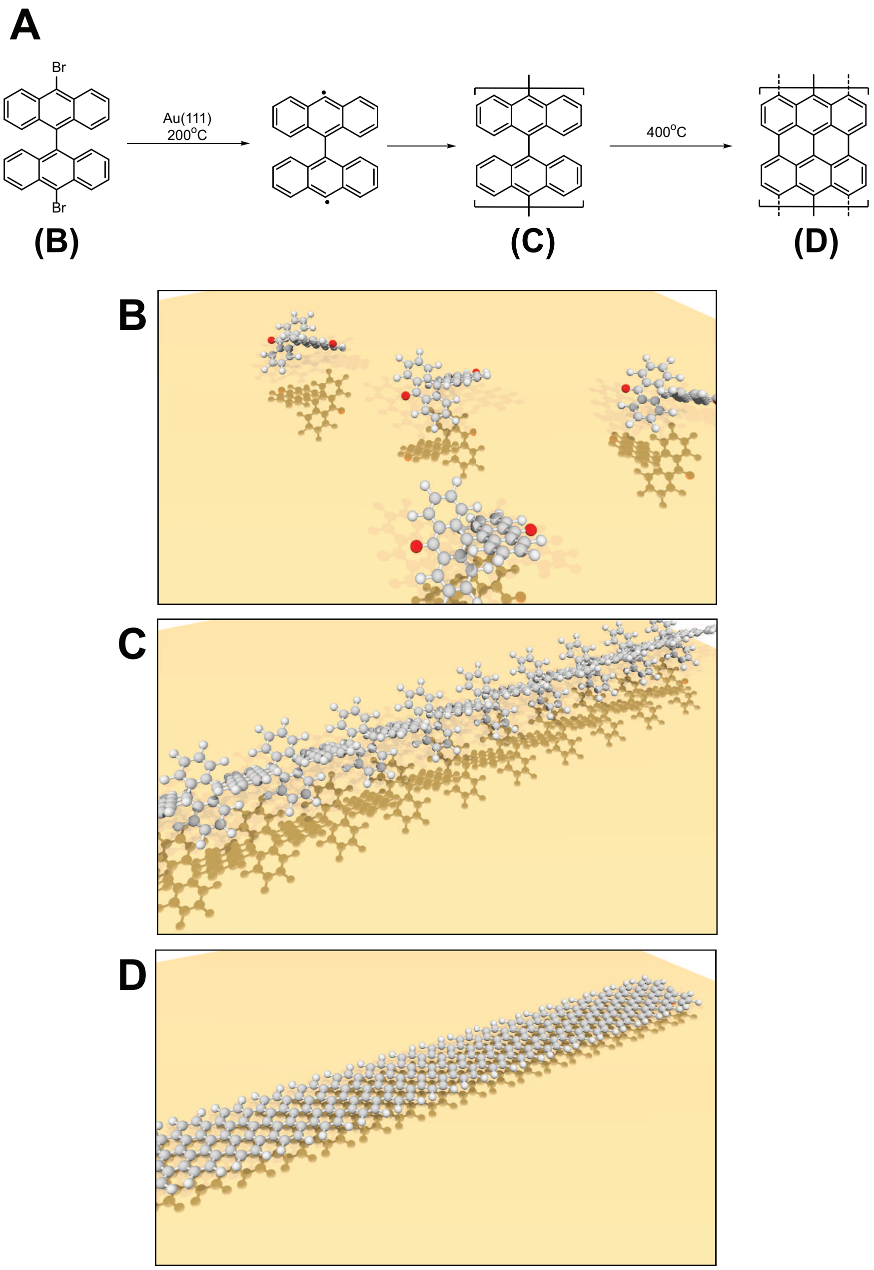

Figure 2.4: (A) Schematic depicting the surface-assisted synthesis of GNRs. (B) The process begins with the deposition of a small-molecule GNR precursor on a metal surface in ultrahigh vacuum. (C) Heating the metal surface leads to homolytic cleavage of the aryl-halogen bonds in the precursor molecules, which diffuse about the surface and polymerize via radical disproportionation. (D) Cyclodehydrogenation of the resulting polymer at elevated temperature yields the GNR.

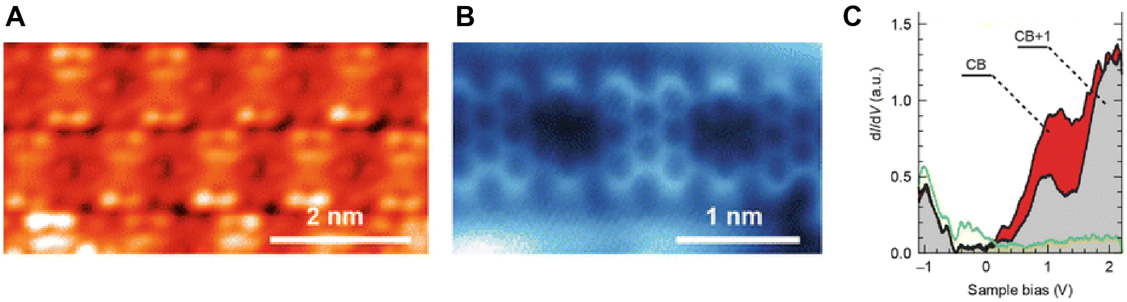

Figure 2.5: Characterization of the same GNR, a boron-doped AGNR, by three different scanning probe techniques: (A) STM, (B) nc-AFM, and (C) STS. Figure reproduced from reference [111].

polymerization in two dimensions, to thermally accomplish patterns of reactivity that would be ineffective or impossible away from the surface (Figure 2.4).[106] The reactions are carried out in ultrahigh vacuum (UHV), both to ensure cleanliness of the produced samples and to minimize undesired reactivity at elevated temperatures. To begin, small molecule organic precursors are sublimed onto the surface of a metal single crystal, most commonly Au(111) but also Ag(111), Cu(111), Au(788), and others, each providing a slightly modified reactivity.[84,106–109] Although the organic precursors are structurally diverse, they all feature at least two labile aryl-halogen bonds, designed to serve as the sites of polymerization. Due to interaction with the metal surface, relatively mild temperatures (e.g. 200 °C) accomplish homolytic cleavage of the aryl-halogen bonds, and the resulting radical species diffuse about the surface, polymerizing via radical disproportionation (Figure 2.4B). Further heating of the product poly-arylene on the metal surface results in cyclodehydrogenation, producing a planar GNR. Importantly, this irreversible cyclodehydrogenation step is extremely reliable across a variety of organic precursors, effectively yielding fully planarized products with very rare defects.[110]

The major advantage of the surface-assisted synthetic approach is its seamless integration with scanning probe microscopy techniques such as scanning tunneling microscopy (STM), scanning tunneling spectroscopy (STS), and non-contact atomic force microscopy (nc-AFM). These techniques operate within the UHV chamber used for GNR synthesis to provide both structural and electronic characterization with high resolution, and as such have become the most important tools for understanding graphene nanoribbons (Figure 2.5). STM and STS measure tunneling current between the metal surface and a fine, conducting tip positioned above the sample to gain information about the local density of electronic states (LDoS) in the intervening sample. By varying the position of the probe, the bias between the probe and the surface, and other parameters, nearly complete information can be gained about the electronic structure of the GNR on the surface (Figure 2.5A&B).[112,113] In nc-AFM, the probe is functionalized with a small molecule (generally CO) to produce an atomically fine tip, and a bond-resolved image is produced by measuring the deflection of this tip by the sample (Figure 2.5C). Together, these techniques have revealed a great deal about the relationship between structure and electronics in GNRs.[114]

Although surface-assisted synthesis is limited in the types of polymerization it can utilize, it has given rise to a great structural diversity of GNRs by facilitating challenging reactions, such as the sterically demanding coupling of two anthracene units at their central 9-positions. Armchair, zigzag, chevron, cove and other GNRs have been produced by surface-assisted synthesis using the method illustrated in Figure 2.4, and the differences in their electronic properties have been described.[106,109,113,115–117] Additionally, each of these GNR families (and especially AGNRs) has been produced with varied widths, leading to a sets of GNRs with finely tunable bandgaps.[112,118,119] Further modification of the GNR was accomplished through heteroatom incorportation, both at the ribbon's edges and at "core" positions in the backbone, with distinct implications for the nanoribbon's band positions and conductivity.[111,120–126] The wealth of examples described here illustrate the versatility of a bottom-up synthetic technique, whereby diverse graphene nanomaterials can be accessed using the modularity and flexibility inherent to organic synthesis.

2.4 Solution-Phase Synthesis of Graphene Nanoribbons

Graphene nanoribbons can also be produced in a bottom-up fashion by solution-phase techniques, in which small molecule precursors are polymerized by a variety of available reactivities and then converted to GNRs via Scholl-type oxidative chemistry catalyzed by a Lewis acid, most commonly $FeCl_3$.[105,127,128] Although GNRs produced in this way are not readily characterized with atomic resolution by scanning-probe microscopy, the solution-phase approach facilitates other characterizations and applications by producing bulk GNRs in quantities reaching the multigram scale. Solution-phase GNRs are therefore most commonly characterized by Raman spectroscopy, which is found to be quite diagnostic for these materials, as well as IR spectroscopy, atomic force microscopy (AFM), solid-state nuclear magnetic resonance spectroscopy (ssNMR), photoemission spectroscopies (e.g. XPS, UPS) and X-ray absorption spectroscopies (e.g. NEXAFS). The solution-phase approach also facilitates the isolation and purification of the precursor polymer, and its characterization by solution techniques such as gel permeation chromatography (GPC) and ^{1}H-NMR.[129] For applications that seek to employ GNRs as a bulk material (for example as a nanoparticle support material, see Chapter 1) rather than as individual ribbons, this is the preferred synthetic approach.

The oldest and most common genre of solution-phase GNR synthesis relies on metal-catalyzed cross-coupling polymerization reactions to generate the GNR precursor, followed by $FeCl_3$-catalyzed Scholl oxidation; both AGNRs and chevron GNRs have been produced by this approach (Scheme 2.1).[105,128,130,131] The use of metals in both the polymerization and oxidation steps necessitates rigorous purification of the product GNRs to ensure the absence of trace metal species, which is confirmed by XPS.[128,132] Multigram-scale quantities of chevron GNR **5** have been prepared in this way, facilitating the first measurement of

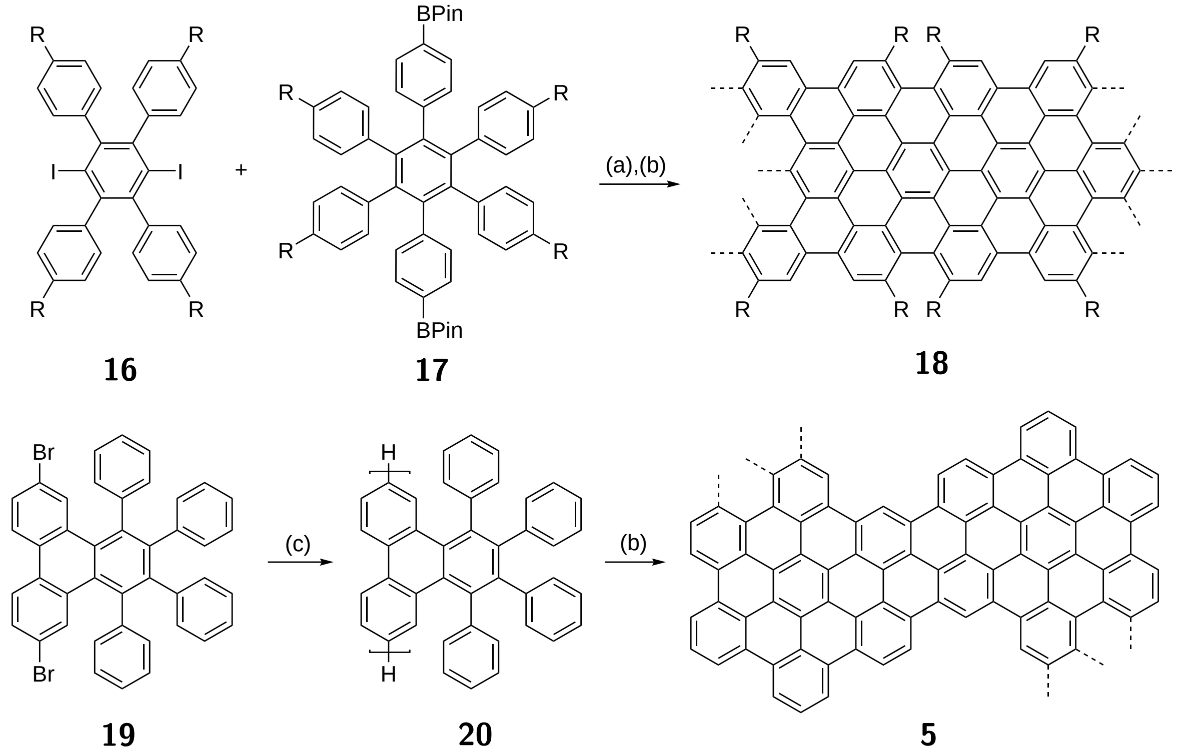

Scheme 2.1: The syntheses of armchair GNR **18** and chevron GNR **5** by solution-phase synthesis using metal-catalyzed cross-coupling polymerizations.[105,128] R=$C_{12}H_{25}$ (a) Pd-catalyzed Suzuki polymerization (b) $FeCl_3$-catalyzed Scholl oxidation (c) Ni-catalyzed Yamamoto polymerization.

their optical bandgap (1.33 eV).[128] They appear quite flexible when dropcast onto surfaces and characterized by AFM, and tend to form large, disordered aggregates as a solid or in suspension.[133] The bulk conductivity of pressed chevron GNR pellets has been measured as well; unsurprisingly, the macroscale conductivity is found to be somewhat low in comparison either to single GNRs or to other graphene nanomaterials, reflective of the disorder inherent to a pellet comprised of aggregated GNRs.[132]

Another approach for the solution-phase synthesis of GNRs proceeds via Diels-Alder polymerization of heterobifunctional monomers containing both an alkyne and a cyclopentadienone; following cheletropic extrusion of CO, Diels-Alder reaction between these functional units yields a new phenyl ring. The result is a precursor polyphenylene, which is then oxidized using Scholl conditions to yield a cove-type GNR (Scheme 2.2).[134,135] The use of this robust Diels-Alder reactivity at high temperature yields long precursor polymers, and ultimately longer GNRs on average than for the cross-coupling approaches described above.[136] As a result, these GNRs have been investigated as transistor materials using a variety of device architectures and fabrication techniques following their deposition from a suspension in organic solvent.[133,136–138] Solution-synthesized cove GNRs have also been employed as chemical

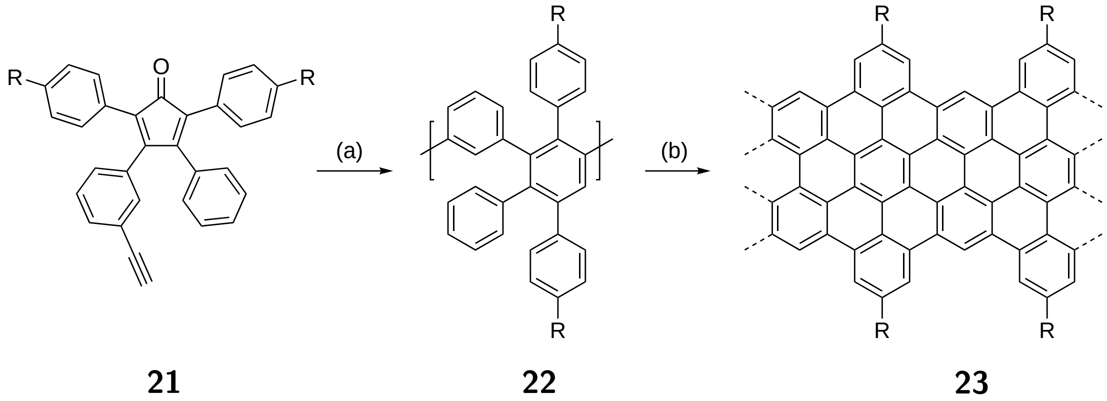

Scheme 2.2: The synthesis of alkylated cove-type GNR **23** by solution-phase synthesis.[134] R=$C_{12}H_{25}$ (a) Diels-Alder polymerization (b) $FeCl_3$-catalyzed Scholl oxidation.

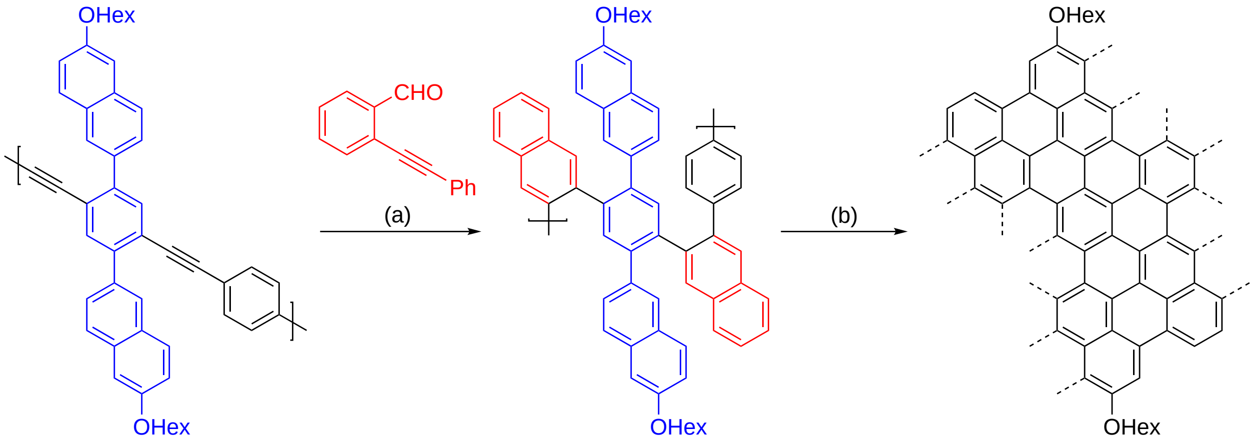

Scheme 2.3: The solution-phase synthesis of armchair-type GNRs by an laternative approach relying on Sonogashira polymerization with subsequent alkyne benzannulation and Scholl-type oxidation.[92]. (a) Benzannulation using the indicated reagent and $Cu(OTf)_2$ (b) Scholl-type oxidation using DDQ and methanesulfonic acid.

sensors, exhibiting a conductivity shift in the presence of certain adsorbates, and their charge carrier mobility has been characterized by terahertz photoconductivity spectroscopy.[134,135]

For the successful synthesis of a GNR, the precursor polymer must necessarily feature a poly-aryl backbone, since these aryl units will then fuse to form the graphenic structure of the nanoribbon. The above approaches address this either by linking pre-existing aryl units or by forming new ones during the polymerization, but a third approach is possible, in which the polymerization is carried out using alternative functionalities which can then be converted to aryl units via post-polymerization modification. The clear advantage to this approach is the added variety of usable polymerization methodologies, but the downside is that post-polymerization modifications must be extremely selective and robust to yield high-quality, homogenous product polymers. An example of this approach was recently demonstrated using Sonogashira polymerization, followed by benzannulation of the polymer's alkynes to naphthalenes, and lastly oxidation to give an AGNR; the authors claim very high conversion to the desired GNR, as demonstrated by Raman spectroscopy and ss-NMR (Scheme 2.3).[92] Alternative strategies like this one continue to be developed and refined, leading to an increasingly diverse set of nanoribbons and related materials.[139–143]

It is clear that the body of GNRs accessible through solution phase synthesis is broad and growing, with an expanding set of both polymerization techniques and oxidation strategies. A few clear challenges remain, to be addressed by future works. First, the development of solution synthetic techniques for new backbone types outside of cove, chevron and armchair GNRs is imperative, since edge structure is the primary determinant of GNR electronic structure. Second, there has been comparatively limited investigation into the modification of GNRs with heteroatoms or functional groups by solution-phase synthesis, outside of some nitrogen-containing chevron derivatives. Lastly, there has been very little exploration of bulk GNRs as a material outside the strict context of transistor applications. Much as the study of CNTs moved from initial synthetic investigation to broad materials application across myriad subfields, surely the clever consideration of GNRs will uncover diverse applications for which they are well suited.

Part II

Surface-Assisted Synthesis of Graphene Nanostructures

Chapter 3

Synthetic Techniques for the Surface-Assisted Synthesis of Electronically Exotic Nanographenes

For low-dimensional graphene nanomaterials, certain specific structural elements are known to frequently yield unusual electronic structures, such as edge-localized electronic states, topological boundary states, mid-bandgap states, or spin-polarized states. In particular, these exotic electronic structures are often associated with extended zigzag edges (See Figure 2.2, page 17), making zigzag-edged graphene nanoribbons or nanographenes materials of interest for various magnetic, electronic, optical, and spintronic applications. However, synthesis of these materials is frequently confounded by their unusual electronics, which often lead to instability and unexpected patterns of reactivity.

Surface-assisted synthesis (Section 2.3, page 18) is a well-established technique for the synthesis of planar graphene nanomaterials, in which carefully designed small molecule synthetic precursors are sublimed in ultrahigh vacuum (UHV) onto a metallic surface, where further reactivity produces the desired structure. In this work, the surface-assisted approach is applied to the synthesis of zero-dimensional and one-dimensional graphene nanomaterials with extended zigzag edges. In particular, the chapter will focus on the design and synthesis of small molecule precursors to these exotic structures, especially the antiferromagnetic nanographene peripentacene, and discuss their surface reactivity.

Scanning tunneling microscopy (STM) and non-contact atomic force microscopy (nc-AFM) in this chapter were performed by Chen Chen, Zahra Pedramrazi, Dr. Arash Omrani, Hsin-Zon Tsai, and Han Sae Jung in the group of Professor Michael Crommie. Electrochemical characterization in this chapter was performed together with Dr. Song Lin. X-ray crystallography was performed by Steven von Kugelgen.

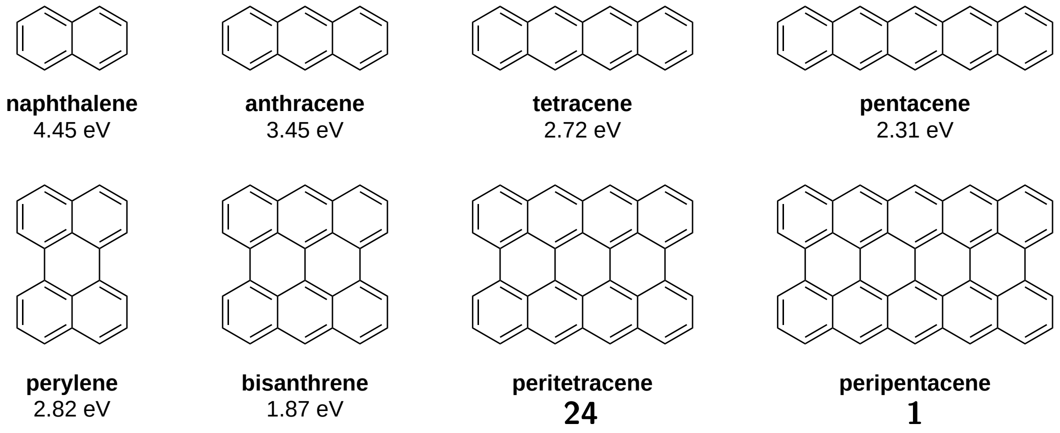

Figure 3.1: The acene (top) and periacene (bottom) families of PAHs, shown with their optical bandgaps. Although the other compounds shown here were successfully synthesized in the early decades of PAH chemistry, periacenes **24** and **1** have not previously been prepared by rational synthesis.

3.1 Introduction to Open Shell Nanographenes

The acenes and periacenes (Figure 3.1) are related families of polycyclic aromatic hydrocarbons (PAHs), featuring diverse derivatives and long synthetic histories.[144,145] Pentacene, for example, was first synthesized in 1912,[146] and noted PAH chemist Erich Clar published in the 1940s syntheses of both perylene and bisanthrene.[147] However, the larger periacenes peritetracene **24** and peripentacene **1** resisted for decades the synthetic efforts of Clar and others.[148,149] Despite their ostensible similarity to structures synthetically accessible since the early days of PAH chemistry, it became clear that **24** and **1** featured a distinct reactivity that precluded their synthesis by traditional approaches.

Insight into these compounds came from theoretical studies into the electronic structure of graphene nanomaterials featuring extended zig-zag edges.[150] Several such studies found that extended periacenes such as **1** feature an unusual antiferromagnetic ground state, with opposing spins localized to opposite zig-zag edges of the molecule.[151–154] The resulting overall radical character is termed an "open-shell" configuration, and is the predicted ground state for periacenes larger than bisanthrene. Viewed alternatively, calculations on periacenes found significant fractional occupancy of frontier natural orbitals, corresponding to polyradical character, with their HONO and LUNO localized to the zigzag edges.[155,156] This predicted exotic electronic structure shed light on the synthetic challenge associated with extended periacenes and made them compounds of interest for application in spintronic, electronic, optical, and magnetic devices.

The conclusions of these calculations can be understood intuitively by application of Clar's rule, in which the PAH resonance structure featuring the maximum possible disjoint

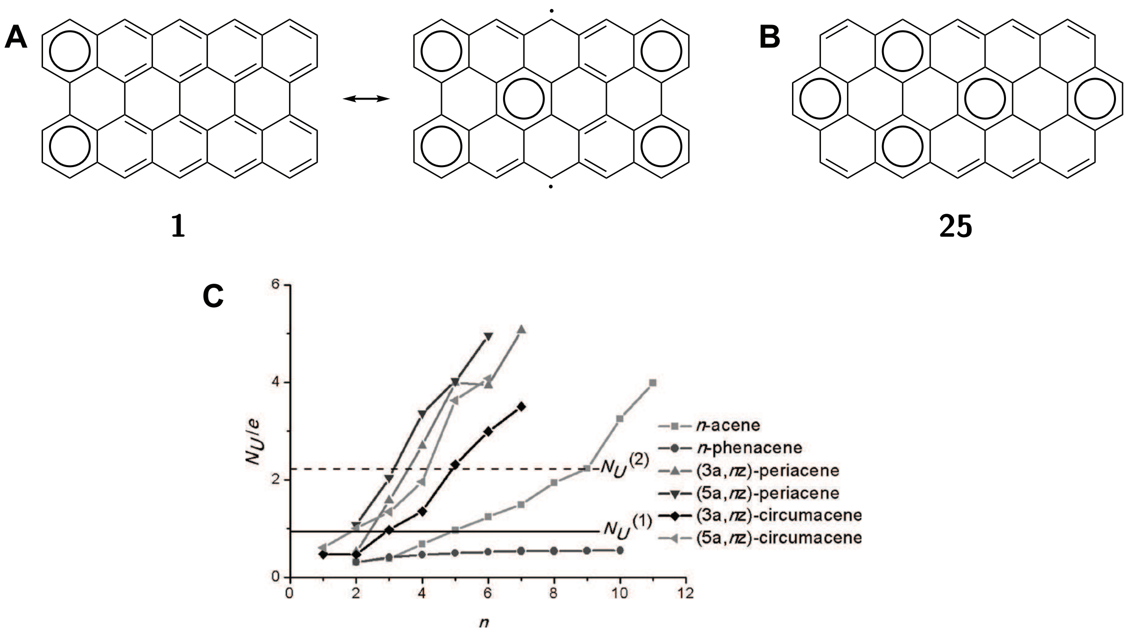

Figure 3.2: Applying Clar's rule to periacenes. (A) Resonance structures of **1** illustrate the driving force towards radical character. (B) Circumacenes such as **25** can form more sextets while remaining closed-shell. (C) Calculations predict far greater number of 'effectively unpaired electrons' (N_U) for **1** than for **25**; figure from ref. [156].

aromatic sextets is of primary importance for understanding the molecule's properties.[157] As Figure 3.2A illustrates, permitting the formation of a diradical leads to a large increase in the number of possible sextets. A related family of structures termed circumacenes, such as **25**, can form a greater number of sextets in their closed-shell state and therefore do not face the same driving force towards spin polarization, despite being larger (Figure 3.2B). This is reflected in the calculations discussed above, which predict a drastically reduced degree of diradical character for circumacenes as compared to periacenes (Figure 3.2C).[153,156] Periacenes **24** and **1** can therefore be understood as the smallest periacenes for which a sufficient number of additional sextets can be formed to offset the energetic cost of forming a spin-polarized state.

The spin polarized nature of **1** was reflected in calculations performed as part of this work. The calculations used unrestricted DFT (uB3LYP 6-31G(d)), which allows for (but does not require) the α and β spin electrons of a given orbital to be localized independently.[158,159] The resulting singly occupied molecular orbitals (SOMOs) of **1** offer a clear picture of the molecule's unusual electronic structure. While the majority of peripentacene MOs feature equivalent localization of the two spins, the HOMO and LUMO are split into strongly localized SOMOs (Figure 3.3A&B). The result is an overall spin polarization, as seen in the spin density isosurface map of **1** (Figure 3.3C).

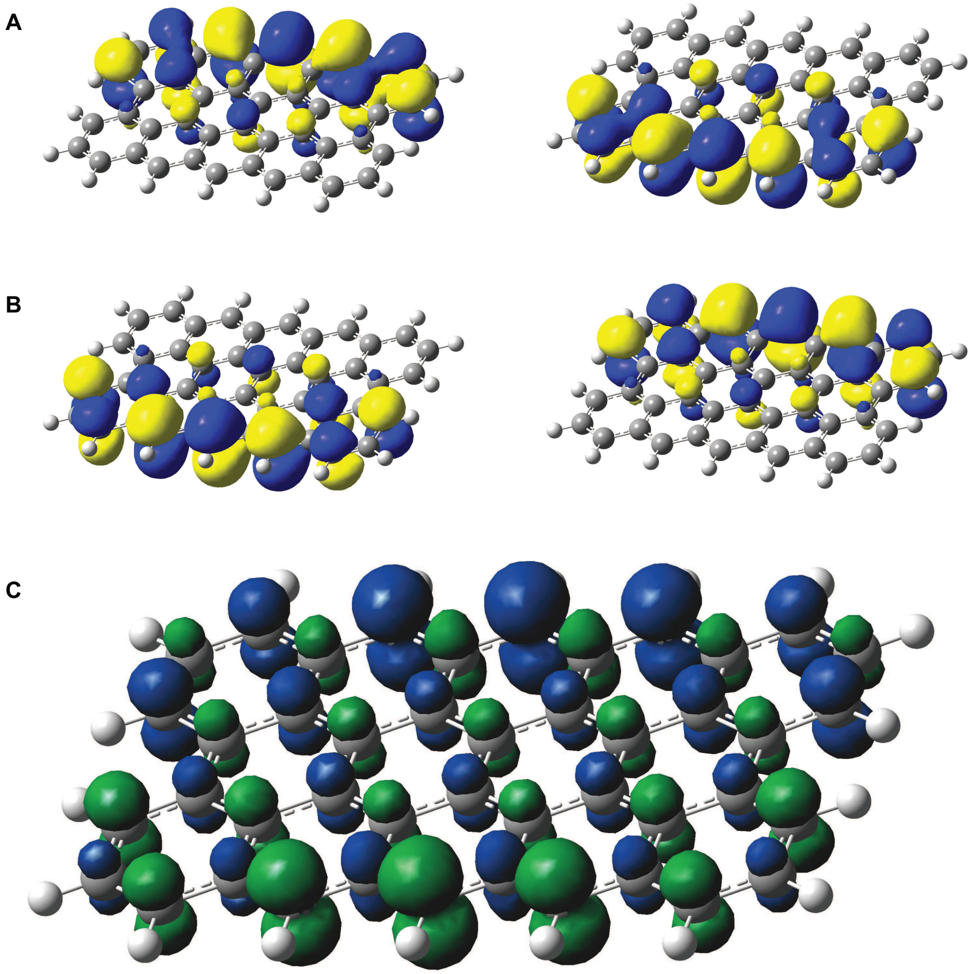

Figure 3.3: Results of unrestricted DFT calculations on **1** illustrate the molecule's spin polarization. (A) The SOMOs that comprise the calculated HOMO. (B) The SOMOs that comprise the calculated LUMO. (C) Overall spin density map for **1** calculated at the uB3LYP level shows α and β spins (blue and green) localized to opposite zig-zag edges.

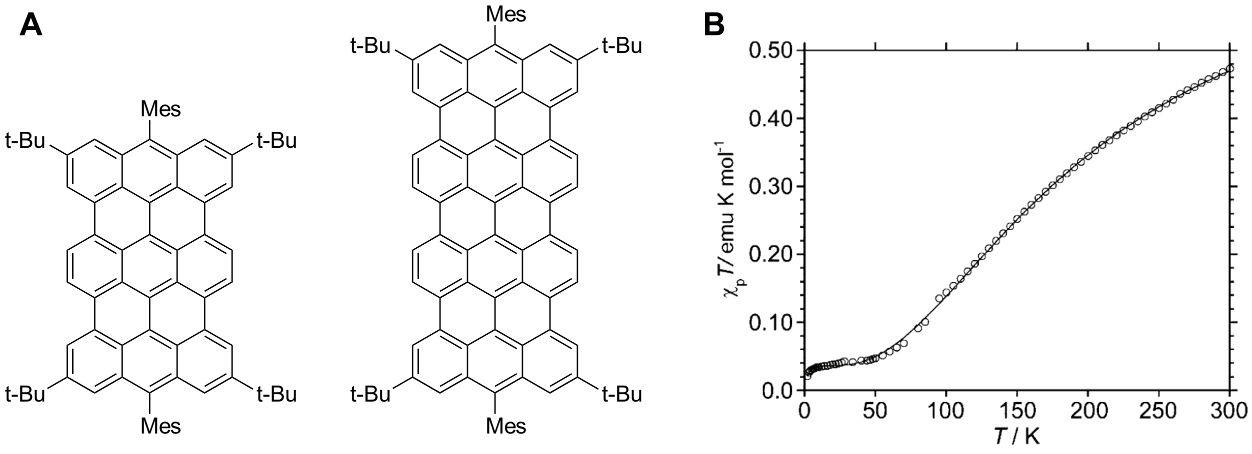

26 **28**

Figure 3.4: (A) Open-shell molecules **26** and **28** have been synthetically prepared.[160,161]. (B) $\chi T - T$ plot using SQUID data (open circles) shows magnetic susceptibility of **28** above 50 K; figure from ref. [161].

Peripentacene is not the only compound predicted to exhibit an antiferromagnetic ground state, and a variety of PAHs featuring extended zig-zag edges have been synthetically pursued. Zethrenes, extended acenes, and p-quinoidimethane derivatives have all been synthesized by solution chemistry techniques and found to have varying degrees of open-shell character.[144,145] More closely resembling **1** are the recently synthesized anthene derivatives **26** and **27**, which feature shorter zig-zag edges but longer armchair edges (Figure 3.4A).[160,161] While **26** exhibited a minimum of open shell character, quateranthene derivative **28** displayed the characteristic optical and magnetic properties of a biradical structure, including magnetic susceptibility above 50 K as measured by SQUID (Figure 3.4B).[161] While these compounds are important for experimentally establishing open-shell PAHs, periacenes like **1** are predicted to exhibit significantly greater polyradical character, and therefore remain important synthetic targets.[155]

3.2 Synthetic Approaches to Peripentacene

The antiferromagentic ground state predicted in calculations of peripentacene **1** triggered a renewed interest in the structure as a synthetic target, but these efforts were ultimately stymied by unusual reactivity, poor stability of the molecule and its intermediates, and low solubility.[145,162,163] The unusual patterns of reactivity are best exemplified by the unexpected Michael addition shown in Scheme 3.1, which ultimately derailed the approach to **1** outlined by reference [162]. Rather than add directly to the carbonyl of **29**, facilitating the con-

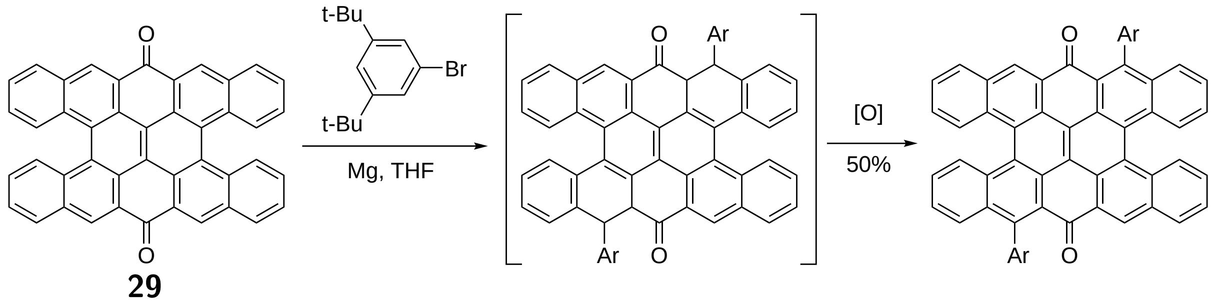

Scheme 3.1: The unexpected Michael addition demonstrated by reference [162] is an example of the unusual patterns of reactivity characteristic of acene-type structures like **29** or **1**.

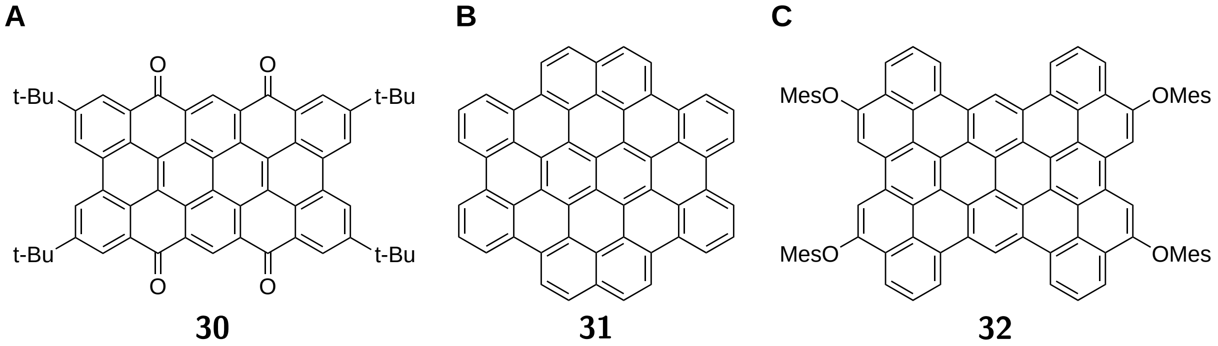

Figure 3.5: Synthesis of these PAHs was motivated by the pursuit of **1**. (A) The insoluble ketone **30** could not be convereted to **1**.[163] (B&C) These PAHs contain the 44-carbon framework of **1** but do not exhibit open-shell character.[149,164]

version of its quinoidal structure into the fully aromatized structure of **1**, the employed Grignard reagent added directly to an aryl carbon, reforming the original quinone structure following oxidation. Two additional equivalents reacted similarly, ultimately yielding a tetra-substituted derivative of the quinone **29**. Attempts at fully planarizing the structure through fusion of the outer *peri* positions were not successful.[145]

Noting that ”not many blank spots on the map of polycyclic aromatic hydrocarbons (PAHs) remain today,” the 2013 work *Toward the peri-Pentacene Framework* outlined two primary routes for the synthesis of **1**.[163] Eschewing a ”pentacene approach” like those using **29** as an intermediate, this later work opted for an alternative approach beginning from a tetra-aryl substituted pyrene. This approach allows for more facile introduction of synthetic handles and bulky solubilizing groups, and succeeded in producing the tetraketone **30** (Figure 3.5A). However, this intermediate was only soluble in strong acid, and proved resistant to any attempt at conversion to **1**.

Additionally, a number of related PAH core structures were pursued for the stated reason

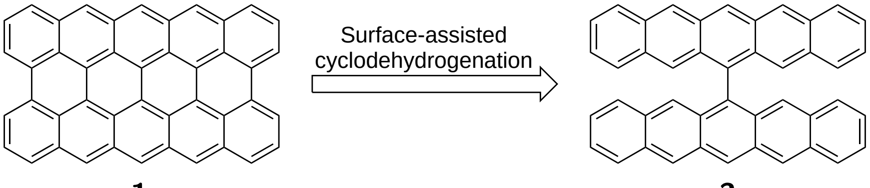

1 **3**

Scheme 3.2: To produce peripentacene **1** by surface-assisted synthesis, the ideal precursor is the unfunctionalized bispentacene **3**, itself a known synthetic target.

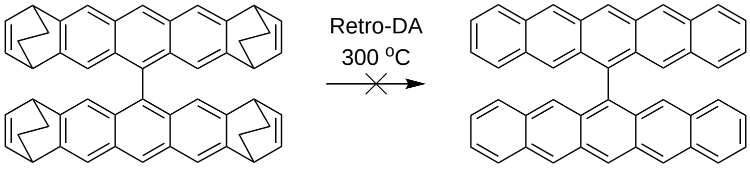

3

Scheme 3.3: Retro-Diels Alder on protected pentacene subunits successfully yielded bispentacene derivatives featuring bulky protecting substituents, but was unsuccessful in yielding **3**, which was not stable to the reaction conditions.[165]

of their similarity to **1** (Figure 3.5B&C).[149,164] However, like the circumacene shown in Figure 3.2, these related PAHs do not face the same degree of Clar frustration as the periacenes and therefore exhibit no open-shell character. The synthetic strategies developed for these molecules were not found to extend to the synthesis of **1**.

In light of these challenges, **1** seemed an ideal target for surface-assisted synthesis, which would circumvent the solubility issues of the fully planarized structure. Additionally, interaction between the metal surface and the molecule should effectively stabilize the reactive periacene without the inclusion of sterically bulky protecting groups. The unfunctionalized bispentacene **3** is the most suitable precursor to **1** for surface-assisted synthesis, which is known to excel at the peri-fusion of linked acenes like poly(anthracene) (Scheme 3.2).[106]

Unfortunately, no synthesis of unfunctionalized bispentacene was known. Although some derivatives featuring harsh conditions and bulky stabilizing groups were reported, these syntheses could not be extended to include the target molecule **3**.[165–167] For example, a strategy based around retro-Diels Alder reaction of protected pentacene subunits at 300 °C was successful for certain substituted derivatives, but did not yield **3**, which was not stable under the reaction conditions (Scheme 3.3).[165] As such, the synthesis of **3** required the development of a new synthetic strategy.

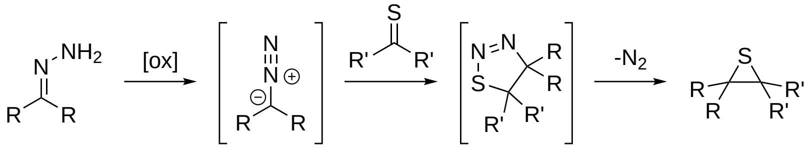

33 **34** **35**

Scheme 3.4: The general form of the diazo-thioketone coupling used in the synthesis of **3**. Because strain is introduced incrementally, the reaction functions well to create sterically crowded carbon-carbon bonds.

3.3 The Synthesis of Bispentacene

Staudinger-Type Coupling for Structural Assembly

Two key lessons regarding the synthesis of **3** emerged from several unsuccessful synthetic attempts. First, a tractable and scalable approach must avoid the twin issues of poor solubility and ready degradation associated with the fully aromatized pentacene subunits. These difficulties could be ameliorated through a strategy of late-stage aromatization, delaying the creation of the pentacene subunits until the last step of the synthesis. Second, the synthetic approach must form the central carbon-carbon bond between acene units by reaction chemistry that is robust to steric crowding (in contrast to metal-catalyzed cross-couplings, for example). A pathway relying on a Staudinger-type diazo-thioketone coupling was found to meet these twin challenges.

Diazo-thioketone coupling (Scheme 3.4) consists of the 1,3-dipolar cycloaddition of an *in-situ* generated diazo compound **33** to a thioketone to yield a thiadiazoline **34**; subsequent loss of nitrogen yields a thiirane **35** featuring a new carbon-carbon bond. Because the reaction proceeds in this stepwise fashion, strain and crowding are introduced slowly and, ultimately, irreversibly; as such, this reactivity has been used effectively for the synthesis of sterically challenging carbon scaffolds.[168–170] Additionally, this approach relies on intermediates that do not feature aromatized pentacene units, and results in a strained thiirane functional handle that can subsequently be employed for the introduction of full aromaticity.

Execution of this strategy (Scheme 3.5) began with the synthesis of 6,13-pentacenequinone **36** by tetra-Aldol condensation of phthalaldehyde with 1,4-cyclohexanedione. Reduction of **36** with sodium dithionite gave pentacen-6(13H)-one **37**;[171] however, treatment of **37** with hydrazine monohydrate under dehydrating conditions did not yield isolable amounts of hydrazone **39**. If, instead, **37** was converted into the thioketone **38** prior to the reaction with hydrazine,[172] the desired hydrazone **40** was obtained in 60% yield. Oxidation of **39** with MnO_2 gave the corresponding intermediate diazo compound, which was subjected to a 1,3-dipolar cycloaddition with **38** to give the thiirane **2** after loss of N_2.

Notably, thiirane **2** (Figure 3.6) contains the entire 44 carbon framework of bipentacene **3**, including the sterically demanding central carbon-carbon bond. It is bench stable and readily

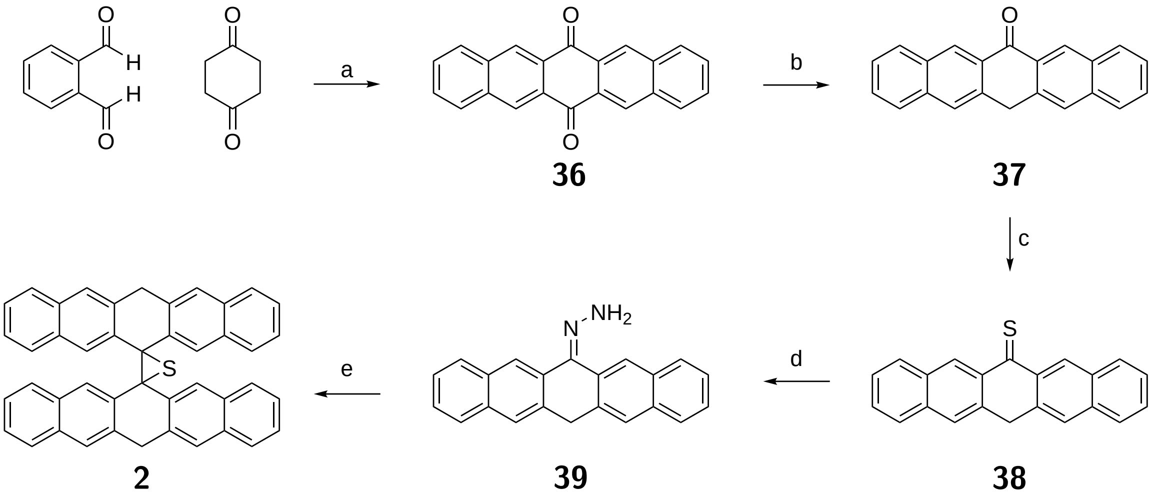

Scheme 3.5: The synthesis of thiirane **2**. (a) KOH, EtOH, 60 °C, 76%; (b) H_2SO_4, then H_2O, NaOH, Na_2SO_4, 100 °C, 87%; (c) Lawesson's reagent, toluene, 80 °C, 62%; (d) 1-propanol, hydrazine monohydrate, 120 °C, 60%; (e) $MgSO_4$, MnO_2, NaOH, MeOH, DCM, 24 °C; then **38**, DCM, 24 °C, 49%.

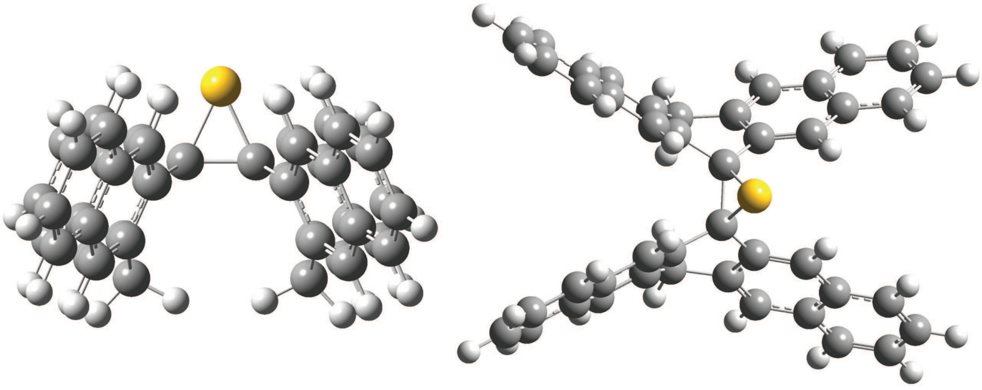

Figure 3.6: The calculated (B3LYP,6-31G) structure of thiirane **2**

soluble in a variety of organic solvents. Furthermore, the employed synthetic approach is quite scalable; **2** was produced on the multigram scale. These advantages proved crucial for the successful synthesis of **3**.

Late-Stage Aromatization to Yield Bispentacene

Following the synthesis of the intermediate thiirane **2**, only the full aromatization of the pentacene subunits (with corresponding loss of sulfur) remained for the synthesis of **3**, but no precedent for this specific reactivity was known. Comparison to published unsuccessful synthetic attempts at **3** indicated that its formation must take place under mild conditions to render the product stable and isolable. For example, a reverse Diels-Alder approach was unsuccessful in isolating **3** due to the harsh thermal deprotection conditions required. In light of this, a variety of mild chemical conditions were attempted, which are broadly summarized in Table 3.1.

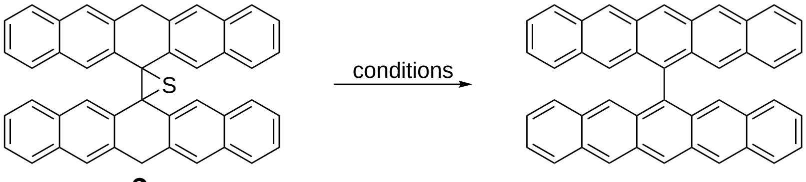

2 **3**

Approach	Example Conditions	Yield **3**	Comments
Strong Acid	H_2SO_4, 24 °C	–	SM consumed; complex mixture
Organic Acid	TsOH, 70 °C	–	No reaction, 24-70 °C
	TsOH, 90 °C	–	SM consumed; complex mixture
Alkoxide Base	NaOtBu, 70 °C	–	No reaction, even with added $Cu(OAc)_2$
Strong Base	nBuLi/THF, -78 °C	low	Formed **3** & butylated derivatives
Non-nuc. Base	DBU/THF, 24 °C	–	No reaction
	tBuLi/THF, 24 °C	–	No reaction
	LDA/THF, -78 °C	55%	Crude yield of **3** ≈90% by NMR

Table 3.1: A summary highlighting some of the various conditions attempted for the conversion of **2** to **3**

Because the desired transformation is formally a double-elimination of H_2S, a variety of acidic and basic conditions were attempted. Many attempted mildly acidic conditions led to no reaction and the recovery of starting material; predictably, harsher acidic conditions led to complex mixtures. Although some of these harsher conditions led to promising color changes, NMR and MALDI characterization of these mixtures provided little or no evidence of the desired product. In contrast, strongly basic conditions proved successful in yielding **3**, even at mild temperatures. Interestingly, nBuLi gave rise to a mixture of both **3** and butylated derivatives, as evidenced by MALDI of the reaction mixture, suggesting nBuLi

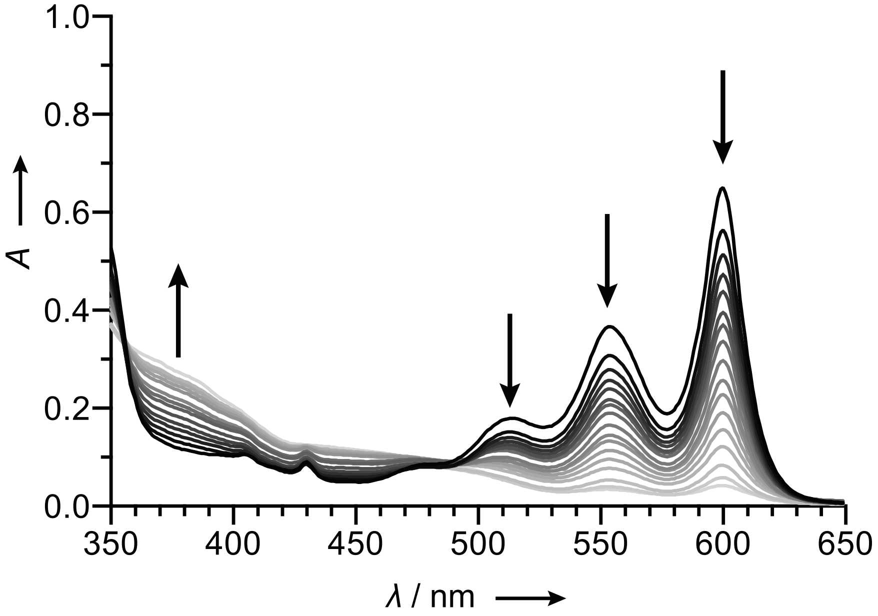

Figure 3.7: UV/Vis spectra of a dilute solution of bipentacene **3** in CH_2Cl_2. Time-dependent UV/Vis spectra of solutions of **3** exposed to air and light were recorded at 15 min intervals (04 h).

is capable of nucleophilic attack on either the product or an intermediate. Strong non-nucleophilic bases such as LDA or LiHMDS were therefore most promising; among these, LDA proved the most capable. Although the product was found to be oxygen sensitive, **3** could be isolated in moderate yield.

3.4 Solution-Phase Characterization of Bispentacene

The synthetic target **3** was isolated as a dark blue powder that, in contrast to simple pentacene, readily dissolves in a variety of organic solvents to give a strongly colored purple solution. UV/Vis spectra of **3** in CH_2Cl_2 (Figure 3.7) feature a vibrational progression characteristic of extended acenes. The longest wavelength absorption at $\lambda = 599$ nm ($\epsilon = 3.7x10^3$ L mol^{-1}cm^{-1}) reveals an optical HOMO-LUMO gap of $\Delta E_{\mathrm{UV/Vis}} = 2.07$ eV (pentacene Δ $E_{\mathrm{UV/Vis}} = 2.15$ eV).

Dilute solutions of **3** exposed to light and air undergo rapid photooxidation. Time-dependent UV/Vis spectra recorded at 15 min intervals indicate a pseudo zero-order reaction with respect to the concentration of **3** and a rate constant $k_{light} = 1.1x10^8$ mol L^{-1} s^{-1}. In the absence of light, the rate of degradation is significantly slower, at $k_{dark} = 1.2x10^9$ mol L^{-1} s^{-1}. The oxidation of **3** is therefore significantly slower than for the parent pentacene. In contrast with some acene derivatives that oxidize in a controlled fashion,[161,173] mass spectrometry of

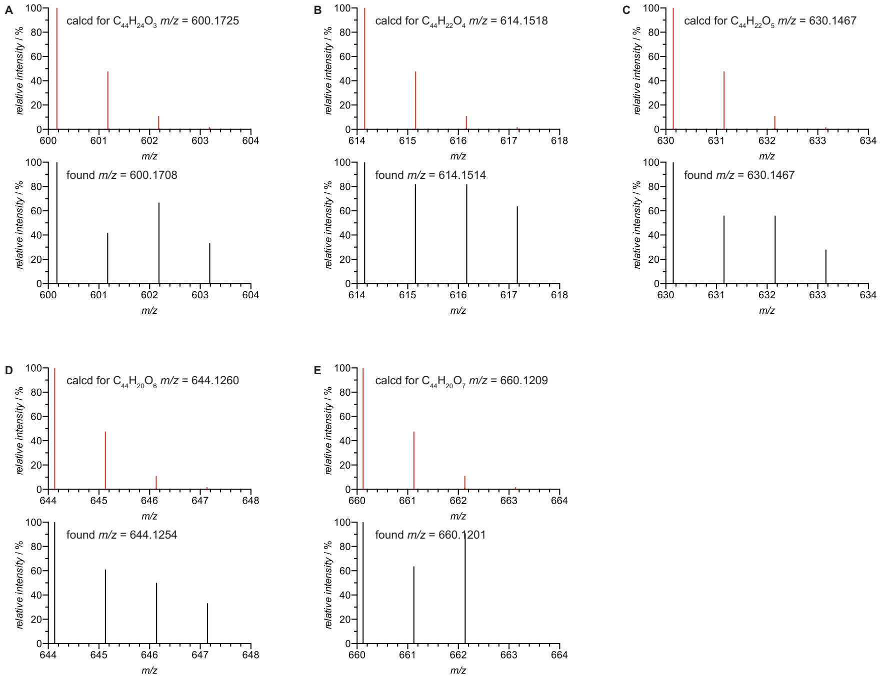

Figure 3.8: High-resolution mass spectra of a crude mixture of photooxidation products of **3** show the incorporation of three to seven O-atoms.

photooxidized samples shows the formation of a complex mixture of products resulting from the incorporation of up to seven oxygen atoms (Figure 3.8). Interestingly, **3** seemed to be stable under air indefinitely when stored as a solid at -30 °C.

These observations are consistent with the calculated cruciform structure of **3** (Figure 3.9), stemming from strong steric interaction between bound pentacene subunits. This conformation precludes the dense packing and strong interactions characteristic of pentacene crystals, leading to the observed solubility. Electronic interaction between pentacene subunits will necessarily be extremely weak in this rigidly orthogonal conformation, and as a result the optical behavior of **3** very closely resembles that of unfunctionalized pentacene. Additionally, the steric shielding of the central aromatic ring by the orthogonal arrangement of pentacene subunits obstructs the addition of dioxygen species, leading to the observed decrease in the rate of oxidation.

We further investigated the electrochemical properties of **3** by cyclic voltammetry (Figure 3.10) of degassed solutions in CH_2Cl_2 (supporting electrolyte 0.1 M Bu_4NPF_6). Figure 3.10 shows two reversible one-electron oxidation ($E^1_{Ox} = +0.73$ eV, $E^2_{Ox} = +0.94$ eV) and reduction waves ($E^1_{Red} = -1.37$ eV, $E^2_{Red} = -1.47$ eV) associated with the sequential oxidation/reduction of both pentacene subunits (reference SCE; Figure 3.10B&C). The resulting electrochemical HOMO-LUMO gap $\Delta E_{EC} = 2.10$ eV is in good agreement with the optical gap (2.07 eV) derived from UV/Vis spectroscopy. The linear dependence of the peak

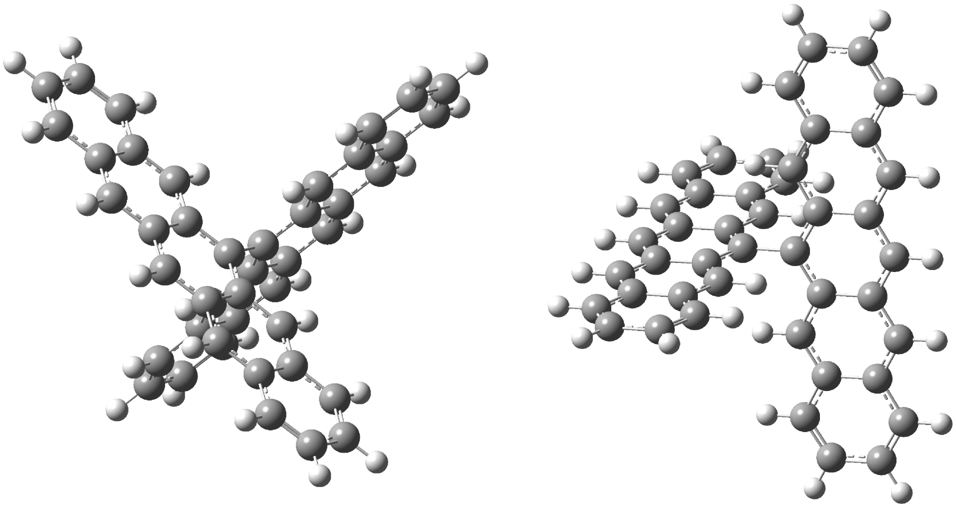

Figure 3.9: The calculated (B3LYP, 6-31G) structure of **3**, showing its sterically enforced cruciform conformation.

current on the square root of the scan rate is consistent with a freely diffusing system with facile electron transfer and limiting mass transport (Figure 3.10D-G).[174] Notably, **3** shows excellent stability toward electrochemical cycling with no decrease in the peak current over dozens of oxidation and reduction cycles over a large potential range (-2 to +1.5 V).

3.5 Surface-Assisted Synthesis and Characterization of Peripentacene

Transformation of **3** into the planarized synthetic target peripentacene **1** relied on the established practice of surface-assisted synthesis of graphene nanostructures by thermal cyclodehydrogenation on a Au(111) surface, enabling subsequent characterization by scanning probe microscopy. This began with sublimation of **3** at 260 °C in ultrahigh vacuum (UHV) onto a Au(111) surface held at 24 °C. STM imaging of the surface at 7 K reveals that the deposited **3** assembles into highly ordered islands of linearly arranged molecules on the Au surface (Figure 3.11A). The average apparent height of alternating bright spots along a line of self-assembled molecules is 2.6 ± 0.1 Å with respect to the gold substrate (Figure 3.11B). This periodicity is consistent with the preferred dihedral angle adopted between two pentacene subunits in **3** when adsorbed onto the surface (see inset in Figure 3.11A).

Annealing samples of **3** on Au(111) at 200 °C for 30 min induces thermal cyclodehydrogenation of all peri-positions to form the fully cyclized peripentacene **1**. STM images (7 K) of **1** reveal a sub-monolayer coverage of uniform discrete rectangular structures (Figure

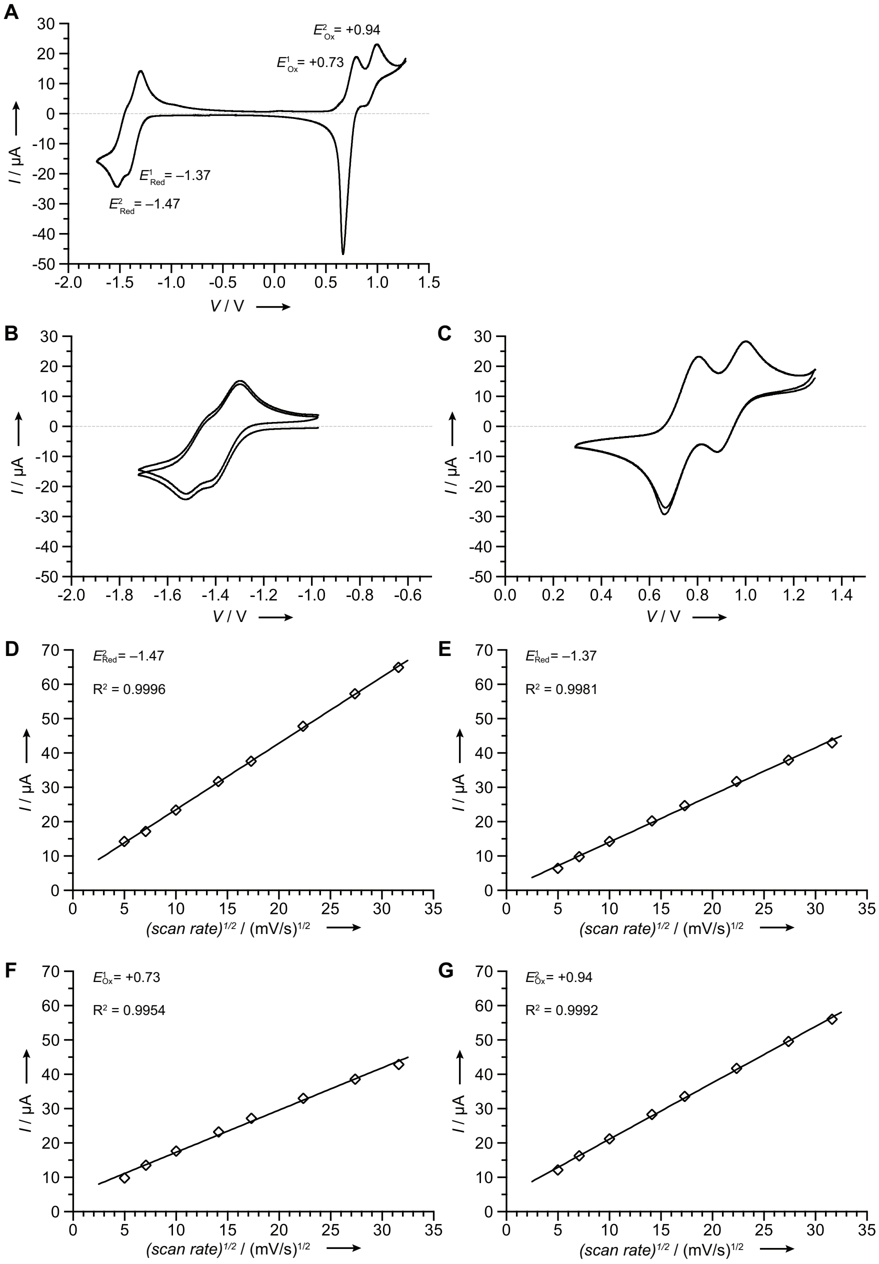

Figure 3.10: Electrochemical characterization of **3**. (A-C) Cyclic voltammograms; 0.1 M Bu_4NPF_6 in dry CH_2Cl_2 under N_2; scan rate 100 mV s^{-1}. (A) Oxidation potentials E_{Ox} and reduction potentials E_{Red} are listed vs SCE. **3** exhibits multiple reversible reduction (B) and oxidation (C) waves. (D-G) Plots of the peak current for each reduction (D: E_{2Red}; E: E_{1Red}) and oxidation (F: E_{1Ox}; G: E_{2Ox}) event as a function of the square root of scan rate $(mV/s)^{1/2}$ show a linear relationship, indicating electron transfer is facile and the rate of each redox process is diffusion limited.

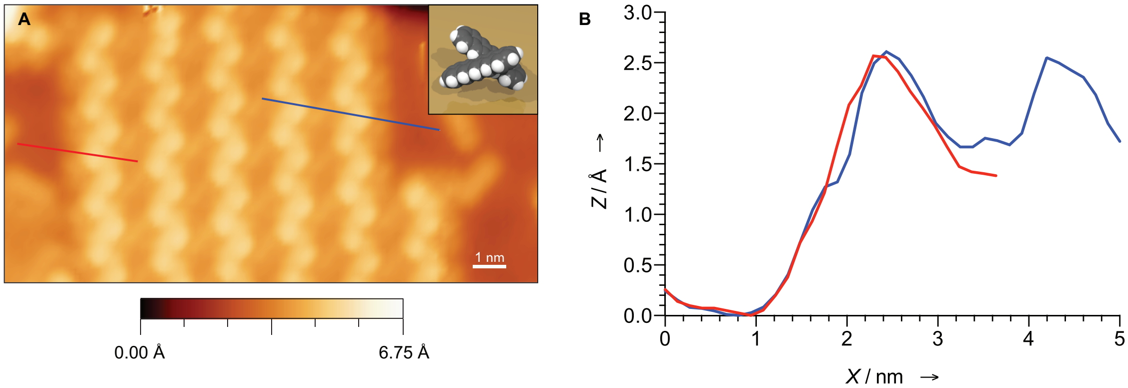

Figure 3.11: STM image of a Au(111) surface decorated with islands of 6,6-bipentacene **3**. (A) Constant-current STM image of **3** as deposited on Au(111) (I = 60 pA, V = 0.10 V, T = 7 K). Molecular models is shown in inset. (B) Height profile linescans along the lines depicted in (A).

3.12A). Large-area STM images illustrate the high yield and selectivity of the thermally induced cyclodehydrogenation reaction; fewer than 5% of the adsorbed molecules deviate from the expected rectangular geometry (Figure 3.12B). The apparent length, width, and height, 1.75 ± 0.04 nm, 1.25 ± 0.04 nm, and 0.21 ± 0.01 nm respectively, match the expected molecular dimensions of **1** (Figure 3.12C&D).

The structure of the cyclization product was unequivocally assigned through subnanometer resolved ncAFM imaging using a low-temperature qPlus-equipped commercial Omicron LT-STM/AFM at T=4.5K (Figure 3.13). The apex of the gold-coated tungsten STM tip was functionalized with a single CO molecule prior to imaging; contrast in nc-AFM images arises from the frequency shift of the qPlus resonator while scanning over the molecule at a constant height. Samples of molecule-decorated Au(111) surfaces were prepared following the deposition/annealing sequence outlined above. Unlike the diffuse STM topographic image (Figure 3.13A), which reflects frontier orbital local density of states, the ncAFM image (Figure 3.13B) reveals both the position of carbon atoms and the intramolecular bonds forming the aromatic carbon skeleton of **1**. Figure 3.13B clearly shows the two parallel-aligned zig-zag edges of **1** that are predicted to lead to exotic electronic/magnetic behavior in extended periacenes. The interaction of peripentacene with the free valences of the Au(111) surface stabilize this highly reactive molecule and prevent undesired radical side reactions that have thus far prevented the isolation of **1** from solution-based reactions.

Scanning tunneling spectroscopy (STS) performed on fully cyclized **1** on Au(111) does not reveal distinctive features within a bias range from -0.6 V to 0.5 V (Figure 3.14). The lack of clear molecular orbital signatures in this measurement could stem from from a variety of factors, such as strong hybridization of the peripentacene electronic structure with the Au surface (thus "washing out" the orbital resonances via broadening effects) or an energetic offset of the molecular orbitals due to surface-induced charge transfer (thus shifting the orbitals

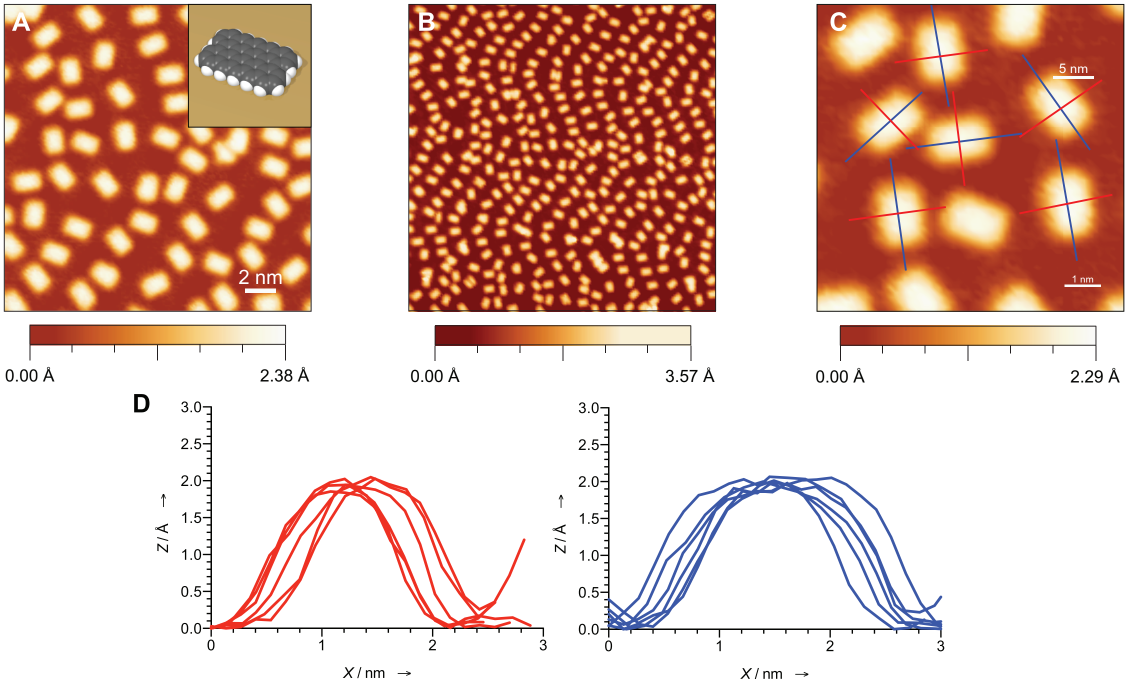

Figure 3.12: STM imaging of peripentacene **41** on Au(111). (A) Constant current STM image of **1** after annealing at 473 K for 30 min (I = 10 pA, V = 0.80 V, T = 7 K). Molecular models is shown in inset. (B) Large area STM image of a Au(111) surface decorated with **1** (I = 10 pA, V = 0.80 V, T = 7 K). (C) Constant-current STM image of **1** (I = 10 pA, V = 0.80 V, T = 7 K). (D) Height profile line scans along the lines depicted in (C).

to an energy outside of the measured spectroscopic window). Further STS characterization would therefore likely require growth of the molecule on an insulating surface, with which it could be expected to interact less strongly.

To overcome this limitation and obtain STS characterization of **1**, attempts were made to deposit **3** on a film of hexagonal boron nitride (hBN) grown on Cu(111), followed by thermal anneal to cyclodehydrogenate. These efforts were unsuccessful; although structures resembling cyclized **1** were evident, incomplete growth of the hBN film left areas of Cu exposed, and the molecules were seemingly localized to these areas (Figure 3.15A&B). Although constant-current STM images at varied applied potentials exhibited some fine structure, it could not be determined if these molecules resided on hBN or Cu(111) (Figure 3.15C&D). It is unclear if any molecules remained on the hBN film, or if the experiment could succeed on an hBN film with more complete coverage; this avenue of characterization was therefore abandoned before it could be explored fully.

However, one insight into the molecule's unusual electronic structure came from several STM images of different molecules of **1** which seemed to show lobed structures localized to one of the molecule's long edges (Figure 3.16A&B). These images bear striking resemblance

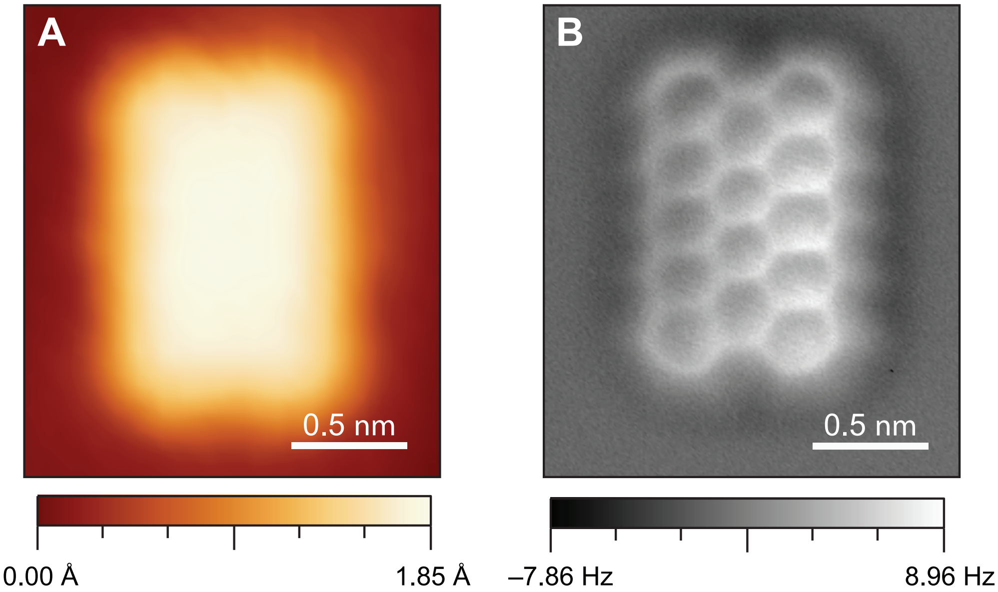

Figure 3.13: STM and nc-AFM images of a single peripentacene **1** on Au(111). (A) Constant-current STM image of **1** (I = 100 pA, V = 0.55 V, T = 7 K). (B) nc-AFM image of **1** (qPlus resonance frequency = 28.73 kHz, Q-value = $8x10^4$, oscillation amplitude = 50 pm).

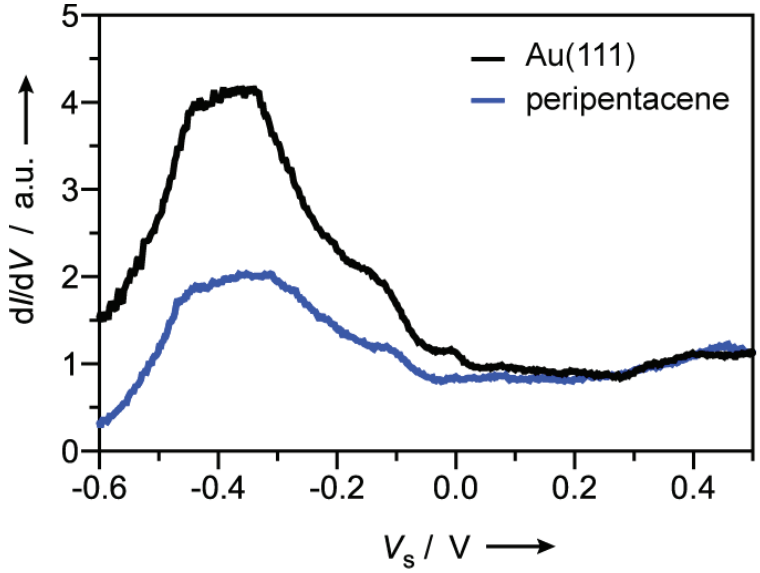

Figure 3.14: Scanning tunneling spectroscopy measurement on **1** (blue) on Au(111) surface (black) in the bias range of 0.6 V to 0.5 V (open-feed-back parameters: $V_s = 0.5$ V, $I_t = 30$ pA, modulation voltage $V_{rms} = 10$ mV).

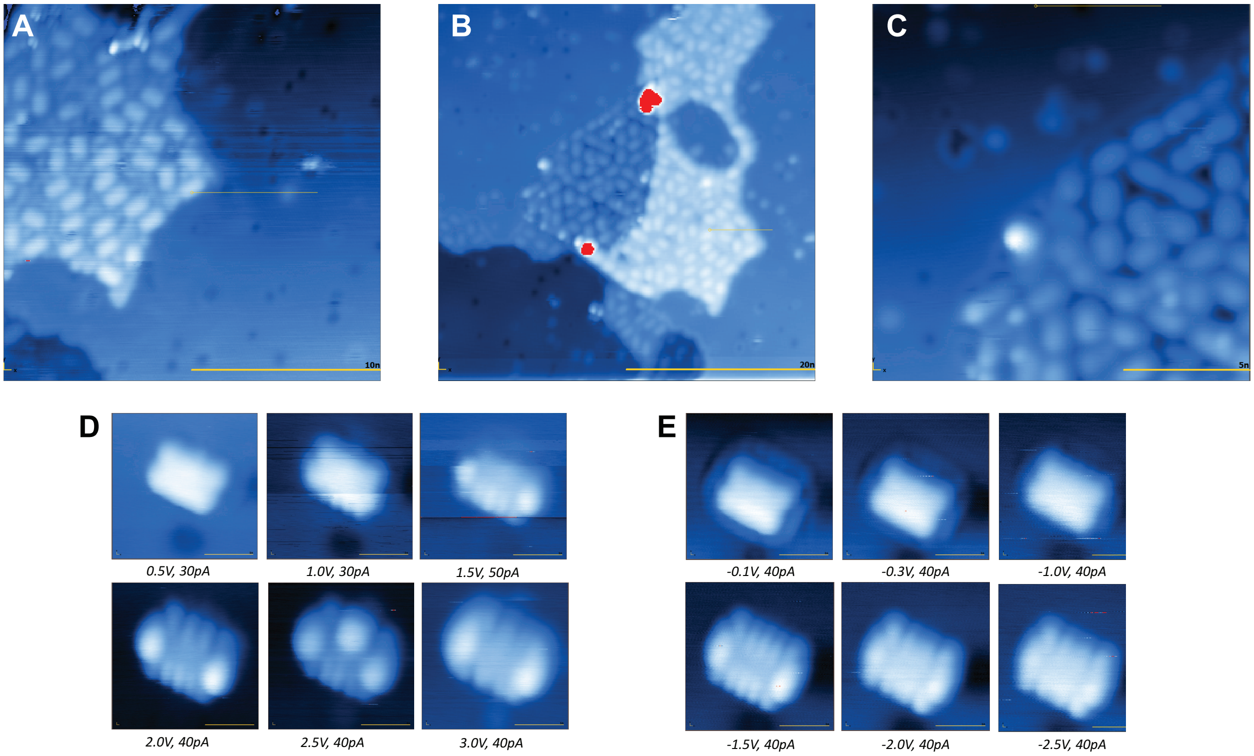

Figure 3.15: STM characterization of **1** following deposition of **3** on an incomplete hBN film grown on Cu(111) and subsequent anneal at 473 K. (A-C) STM (I = 20 pA, V = 2.0 V, T = 7 K) shows **1** localized to regions that could be exposed Cu(111). (D&E) Images taken at varied potentials exhibit some fine structure.

to the calculated frontier SOMOs of the singlet diradical peripentacene groundstate (Figures 3.3A&B; 3.16C). Although it is not appropriate to consider any STM image as reflective of a single MO, it is true that these images the reflect the frontier orbital local density of states at each point. While the SOMOs at each edge would ordinarily be degenerate, suggesting they should appear together in a scan, it is plausible that perturbation by the Au surface would break this degeneracy and cause only one to appear. It is also possible that the asymmetry in the image reflects an asymmetry in the STM tip at the time of imaging. While it is certainly true that these images do not constitute a quantitative or rigorous characterization of the exotic electronic structure of **1**, they are the first experimental evidence supporting the calculated electronic structure, and point towards a need for fuller characterization of this structure.

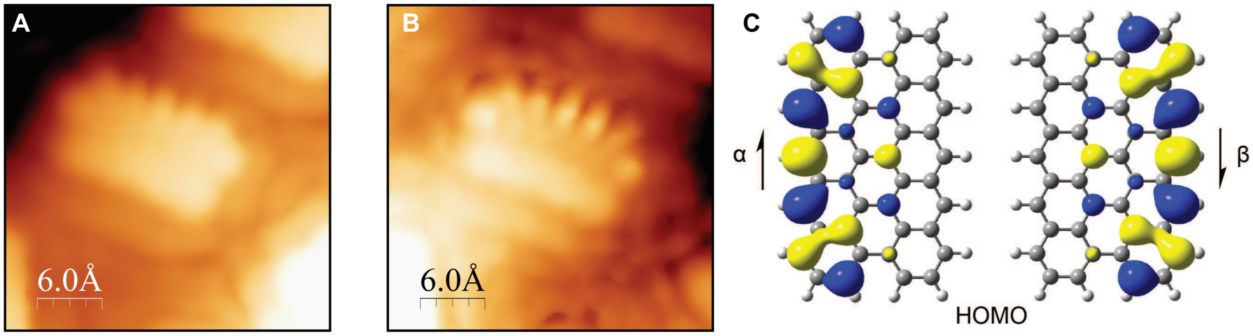

Figure 3.16: (A&B) Certain STM images of **1** exhibit a fine structure very closely matching the molecule's calculated frontier MOs. (C) The SOMOs comprising the HOMO of **1** as calculated using unrestricted DFT (uB3LYP 6-31G(d))

3.6 Dibromobispentacene for the Surface-Assisted Synthesis of 11-AGNRs

Surface-assisted synthesis is also an excellent tool for the preparation of one-dimensional graphene nanoribbons from small molecule precursors (see Section 2.3). As described above, the approach relies on the homolytic cleavage of carbon-halogen bonds to yield aryl radicals, which disproportionate to form a polymer. Applying this approach to **3**, the addition of two bromine atoms would yield **4**, ostensibly a precursor to poly(pentacene) **42** (Scheme 3.6). Surface-assisted thermal cyclodehydrogenation of this polymer would yield the 11-carbon wide armchair-edge GNR (11-AGNR) **43**, which has not been prepared previously.

The 11-AGNR **43** is an especially compelling target for investigation because of its theoretically predicted bandgap, which is lower than those of extant GNRs. This is due to the phenomenon termed *bandgap oscillation* in GNRs: narrow armchair graphene nanoribbons each belong to one of three width "families", and their bandgaps are dependent not only on width but also on the family to which they belong (Figure 3.17).[88] At 11 carbon atoms wide, **43** belongs to the $3p + 2$ family, which is predicted to have lower bandgaps than the $3p$ or $3p + 1$ families and is therefore quite attractive for transistor applications. As a result, the 11-AGNR **43** and its precursor **4** have been stated synthetic targets since the first report of bottom-up GNRs.[106]

The brominated GNR precursor **4** was prepared by addition of bromine to a solution of **3** at -78 °C. Following the addition of bromine, the solution loses its deep purple color and becomes yellow, suggesting that Br_2 has added across the central ring but not yet eliminated. As the solution is warmed to 22 °C, the blue-purple color is reformed, indicating the elimination fo HBr to reform the fully aromatized pentacene subunits. Fewer than two equivalents of bromine were used, to ensure that it was entirely consumed before the solution was warmed; use of excess bromine (or of fewer equivalents added at 22 °C) led to triply and quadruply brominated products. Mono-brominated bispentacene was therefore also formed

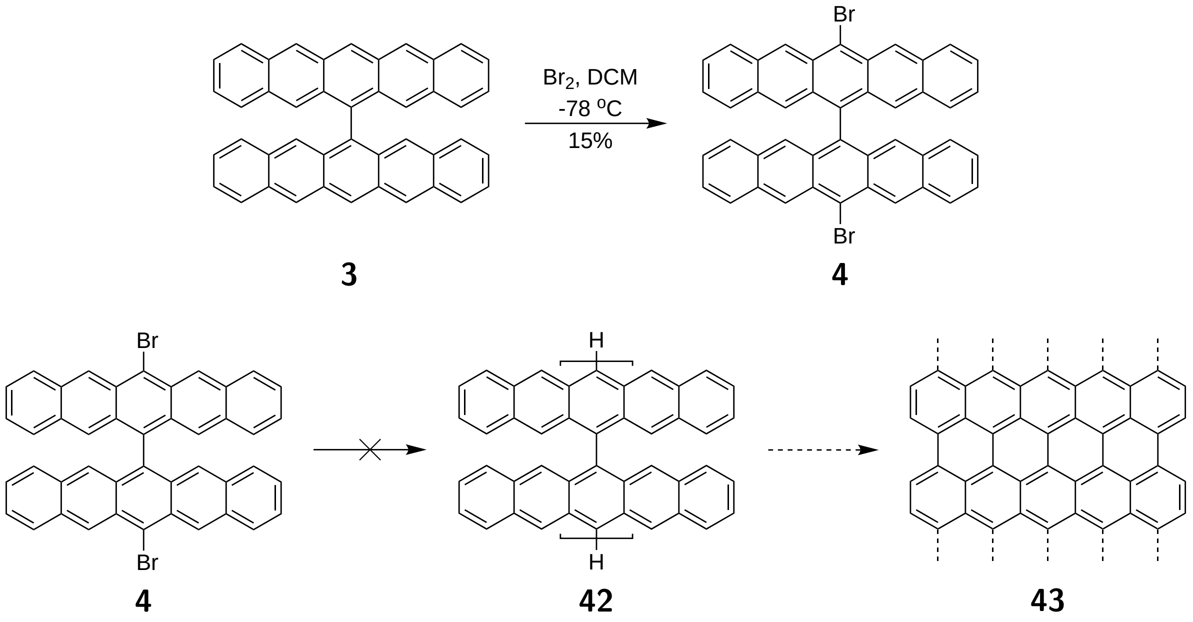

Scheme 3.6: An 11-carbon wide armchair GNR **43** could be produced by surface-assisted synthesis beginning from a brominated derivative of **3**. However, this was ultimately not successful.

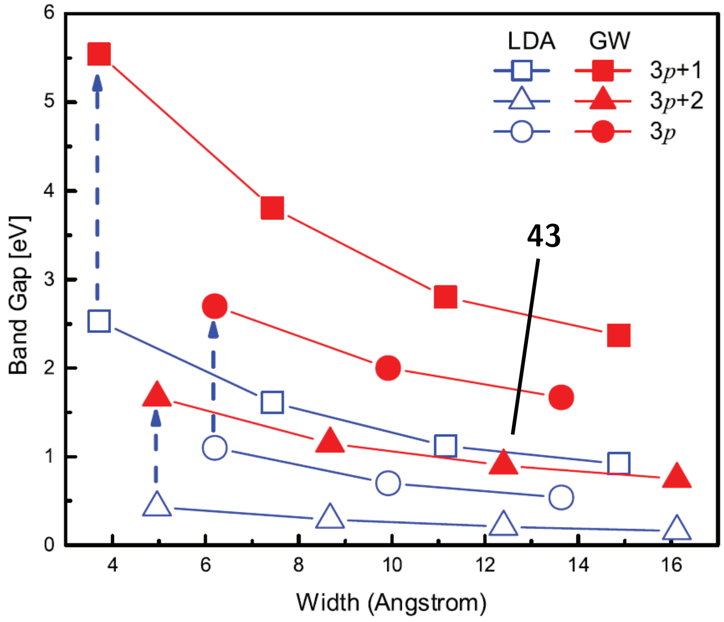

Figure 3.17: The phenomenon of bandgap oscillation categorizes GNRs into three families; **43** belongs to the the family with the lowest bandgap, $3p + 2$. Figure from reference [88].

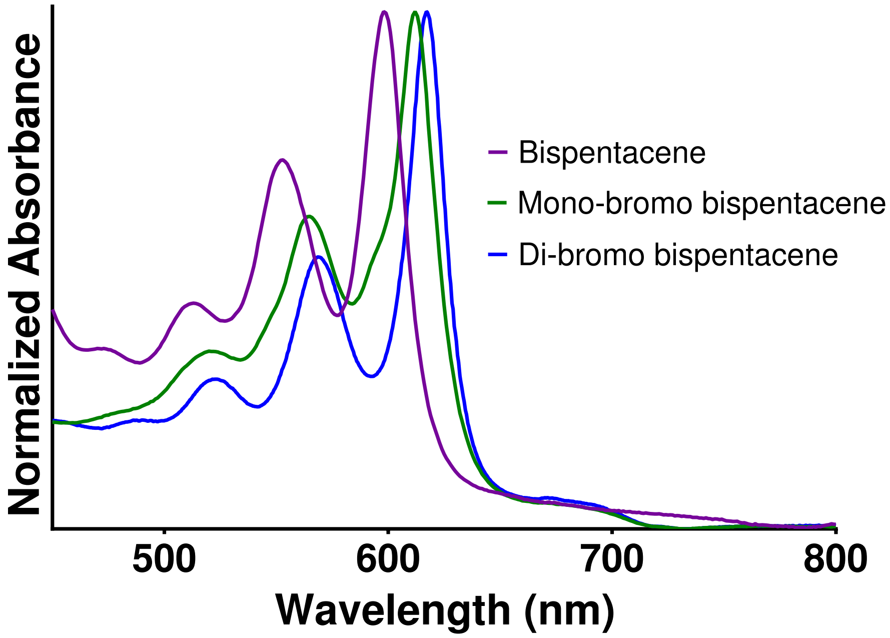

Figure 3.18: Normalized UV-Vis spectra of bispentacene **3** and its brominated derivatives in CH_2Cl_2.

by this approach, and could be isolated and characterized. Furthermore, the procedure could be modified to form **4** from the thiirane **2** in a quasi-one pot procedure by first quenching the elimination with dry MeOH, removing the solvent under reduced pressure, then adding solvent and cooling the reaction before adding Br_2. This was found to be the most effective approach for preparing sizable quantities of **4**.

Although **4** was not indefinitely stable to oxidation by air, it was found to be appreciably more stable than its unfunctionalized counterpart **3**, and could even be purified under air before transfer to a N_2 glovebox for final recrystalization. Solutions of **4** are bright blue, rather than deep purple like those of **3**, and this difference is reflected in a redshifted UV-Vis trace (Figure 3.18). Interestingly, the UV-Vis spectrum of the mono-brominated derivative shares its shape and is somewhat less redshifted, indicating a degree of electronic communication between the orthogonal pentacene subunits. Dark blue crystals of **4** suitable for X-ray analysis were grown from saturated toluene at -25 °C, and a crystal structure was obtained (Figure 3.19). Interestingly, the crystal features clear π–π and C–H–π interactions between bispentacene molecules in two dimensions (Figure 3.19; SI Figure 10.1, page 144).

Deposition of **4** on a Au(111) surface in UHV was successful, with the molecule forming ordered islands similar to those of **3**. However, attempts to polymerize the brominated molecule at 200 °C were unsuccessful; rather than forming polymers, the molecules simply cyclize to form peripentacene **1**. Although the carbon-bromine bonds appear to have been cleaved at this temperature, no structures larger than a monomer were ever detected. This

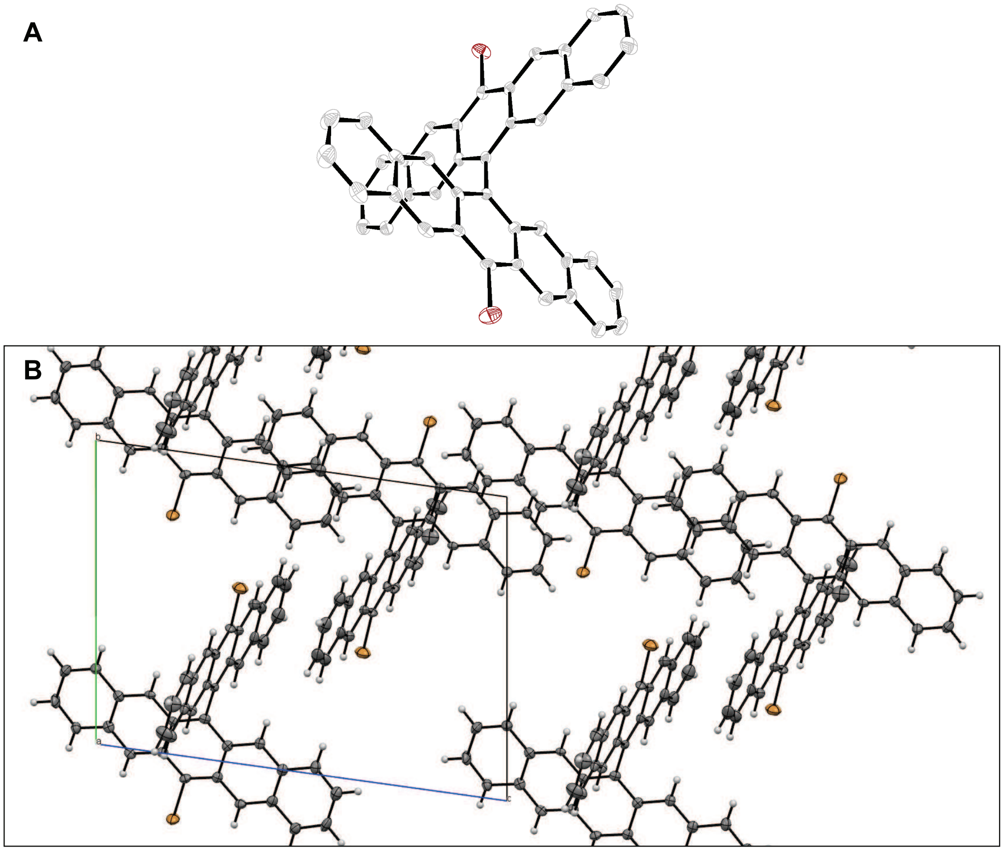

Figure 3.19: (A) X-ray crystal structure of brominated bispentacene derivative **4** illustrates its sterically enforced cruciform structure. (B) Viewing the crystal down its *a* axis, the π–π and C–H–π interactions between bispentacene molecules are evident. Toluene solvent molecules have been omitted for clarity. Additional views of the crystal are in SI Figure 10.1, page 144.

suggests that the cyclodehydrogenation of **4** on Au(111) is competitive with homolytic cleavage of the carbon-bromine bonds, yielding planar **1** interacting strongly with the Au surface, precluding polymerization. This could potentially be addressed by depositing **4** onto another surface on which carbon-halogen bonds are known to cleave at a lower temperature, such as Cu(111), so that polymerization could occur before cyclodehydrogenation. However, this experiment was never attempted.

3.7 Looking Forward: Other Zig-Zag Nanographenes

Generality is one appealing aspect of the synthetic route taken to **3**; rather than being specific to the bispentacene framework, it could readily be applied to a range of acene, periacene, and

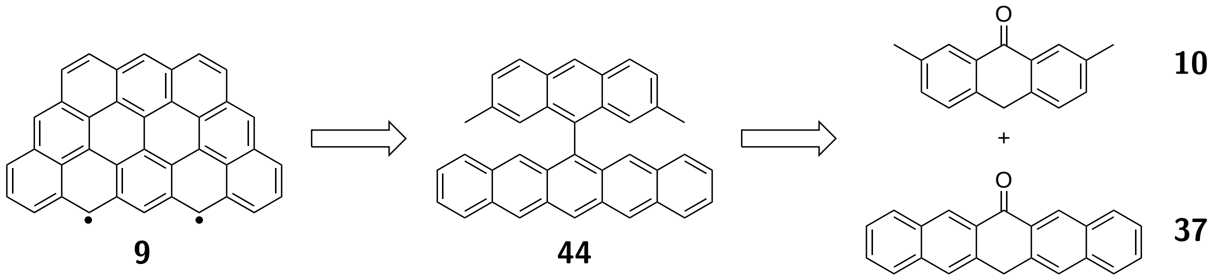

Scheme 3.7: Retrosynthesis of the non-Kekulé nanographene **9** using the synthetic approach developed for the synthesis of **3**.

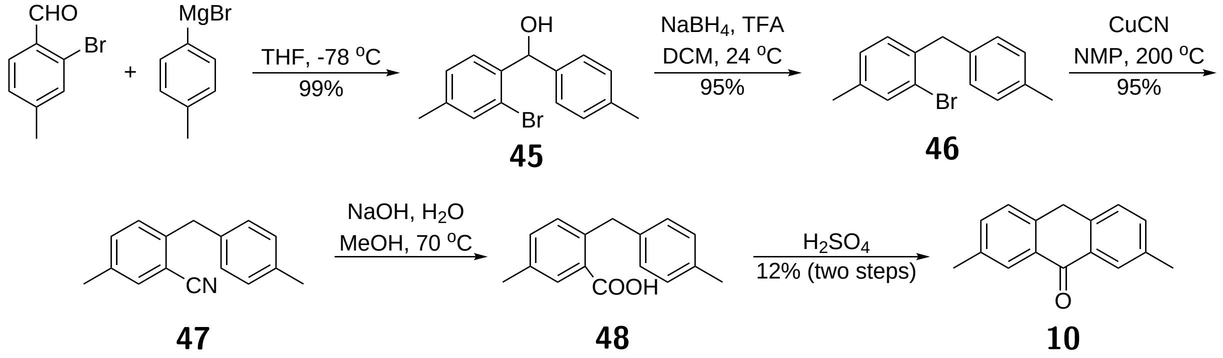

Scheme 3.8: Synthesis of the anthrone derivative **10**

related compounds. Adding to this generality, the diazo-thioketone reaction used to form the central carbon-carbon bond is a heterocoupling, providing access to asymmetric acene structures. For example, the non-Kekulé structure **9** could be prepared by surface-assisted cyclization of **44**, which could be synthesized much in the manner of bispentacene **3** by using the methylated anthrone **10** (Scheme 3.7). The anthrone **10** was successfully prepared in five steps by a modified reported procedure,[175] but conversion to either the thioketone or hydrazone was not immediately successful, and the synthesis of **9** remains incomplete (Scheme 3.8).

Additionally, the asymmetric structure **44** could be brominated to yield monomers for surface-assisted synthesis of interesting GNR structures. This approach relies on the empirical observation that asymmetric monomers featuring halogen positions at differing heights from the surface polymerize with remarkable selectivity for head-to-head and tail-to-tail polymerization. For example, the monomers **49** and **50** would be expected to selectively yield the GNRs shown in Scheme 3.9. The unusual heterostructures of these GNRs would certainly be reflected in their electronic structures, offering insight into GNR physics and possibly applicable materials.

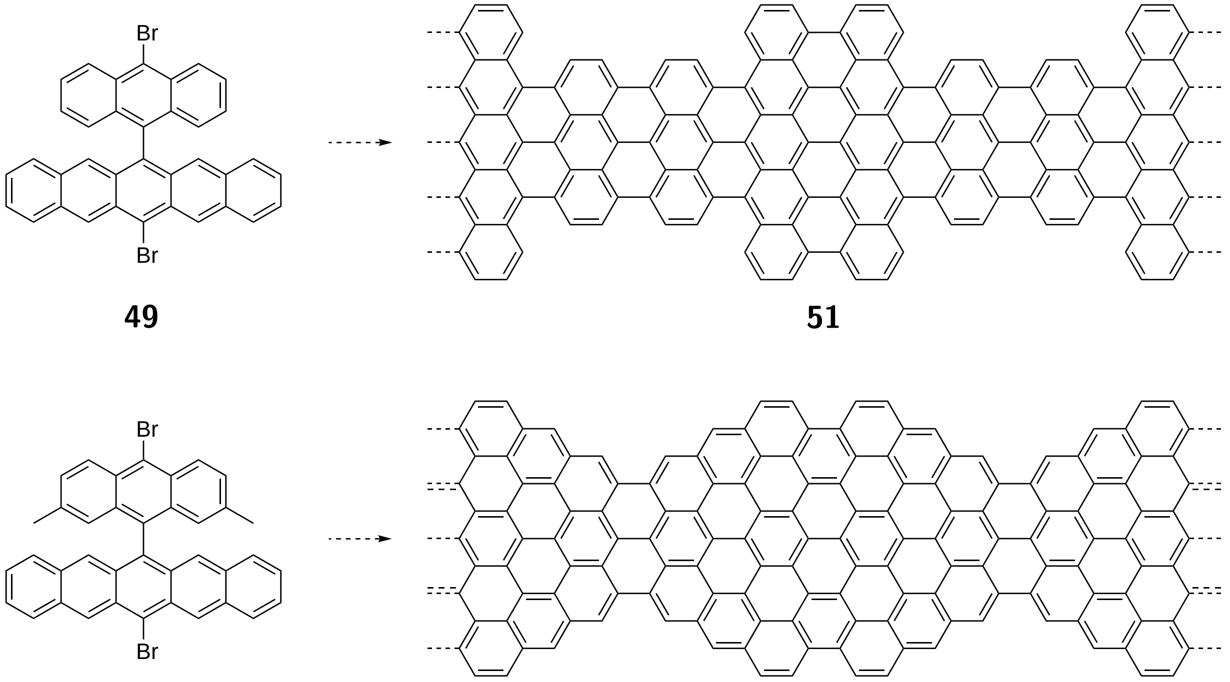

49 **51**

50 **52**

Scheme 3.9: Two examples of unusual GNR structures that could be accessed via the synthetic chemistry developed for the synthesis of **3**. The approach makes use of the selectivity exibited by surface-assisted polymerizations.

The synthetic techniques developed for the synthesis of **3** could also be applied to the synthesis of monomers for the surface-assited synthesis of fully zig-zag graphene nanoribbons (ZGNRs), which are of particular interest because edge-localized electronic states render the nanoribbons metallic.[150,176] Because of the unusual geometry of ZGNRs, any monomer to access them by surface-assisted polymerization would necessarily include methyl groups designed to ultimately cyclodehydrogenate and form part of the ZGNR edge, a technique that has been experimentally demonstrated for surface-assisted GNR synthesis. Scheme 3.10 illustrates one possible ZGNR monomer, the bis-tetracene derivative **53** bearing four methyl groups to yield ZGNR **54**. The placement of these methyl groups is strategic; because the molecule does not have a plane of symmetry through its central acene-acene bond (as **4** or **49** do, for example), rotation around that bond would yield a kinked structure rather than a smooth-edged ZGNR. The methyl groups are therefore positioned to sterically prevent cyclization in this conformation, enforcing the preferred orientation.

The synthetic precursor to ZGNR **54**, the tetracenone derivative **11**, was synthesized beginning with a Horner-Wadsworth-Emmons olefination to yield the α,β-insaturated ester **56**. Hydrogenation of **56** proved quite challenging, with all Pd-based approaches affording

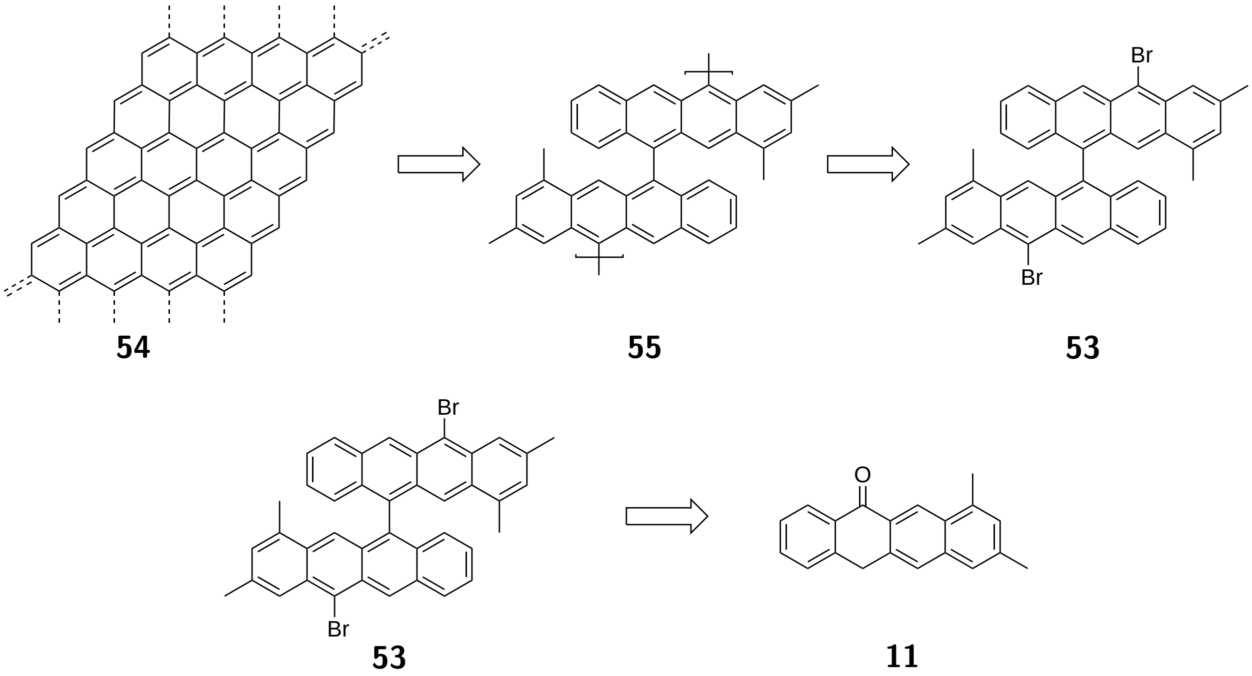

Scheme 3.10: Retrosynthesis of ZGNR **54** relying on surface-assisted polymerization and methyl cyclodehydrogenation. The monomer **53** could be accessed using the synthetic chemistry developed for the synthesis of **3**.

either no reaction or debrominated starting material, but rhodium on alumina was found to perform the hydrogenation to **57** in good yield. Saponification and Friedel-Crafts acylation yielded the tetralone **58**, and the target's second methyl group was then introduced by Grignard addition to the resulting ketone. Elimination and DDQ oxidation afforded the naphthalene derivative **59**, which was converted to the boronic acid **60** by lithiation and quenching with $B(OMe)_3$. Suzuki reaction of **60** with the benzyl bromide **61**[177] under fairly harsh conditions successfully produced the nitrile **62**, which was hydrolyzed to the carboxylic acid **63**. Friedel-Crafts acylation with polyphosphoric acid yielded **11** as detected in the crude mixture. However, **11** was never fully isolated, and its dimerization was never attempted; the synthesis remains incomplete, and efforts were promptly discontinued when zig-zag GNRs were accessed by an unrelated surface-synthesis approach.[178]

3.8 Conclusion

This chapter has demonstrated the successful development of a robust and versatile synthetic technique for the synthesis of challenging bis-acene molecules. This new method was applied for the synthesis of bispentacene **3** and its brominated derivative **4**, each a noted syn-

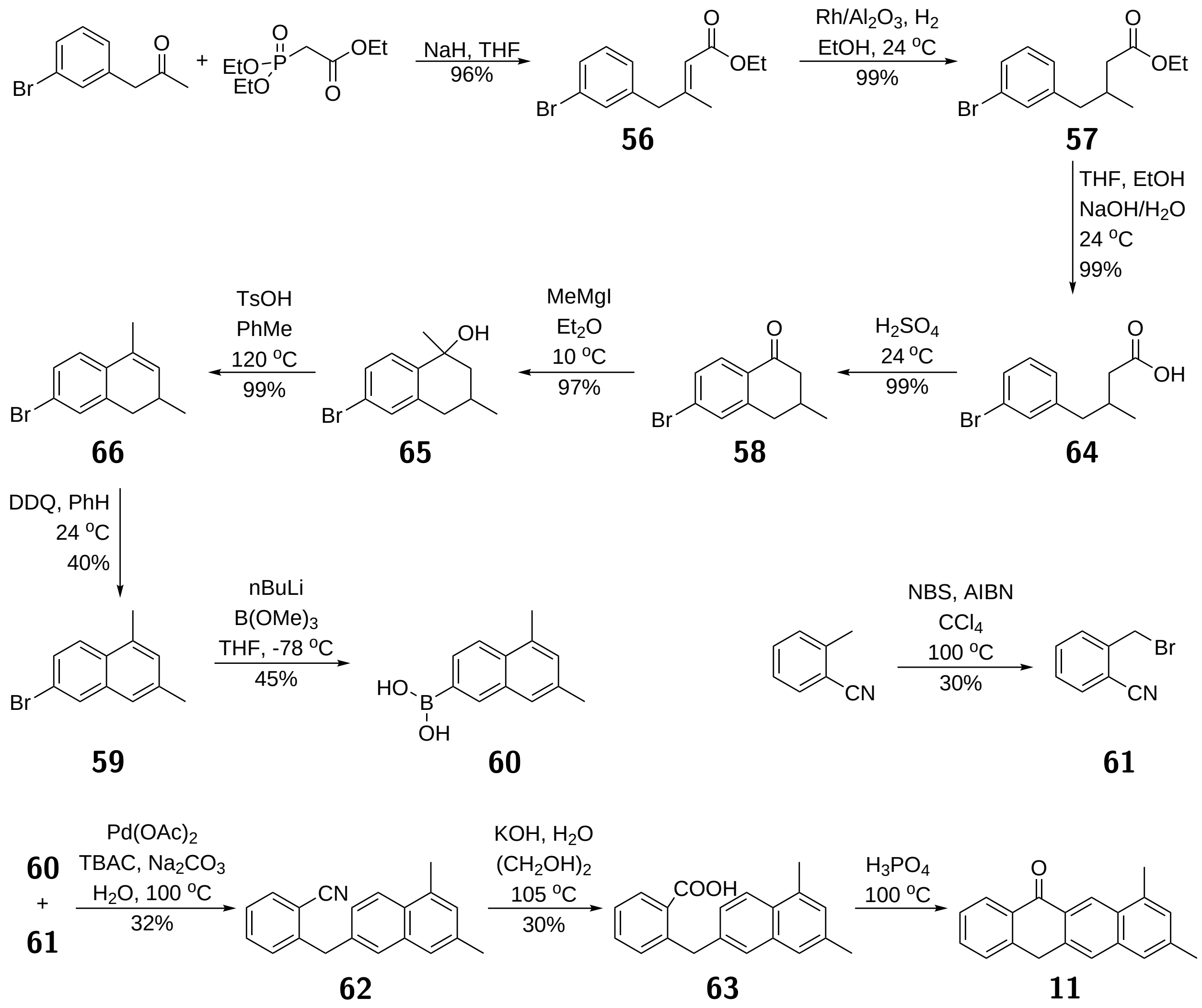

Scheme 3.11: Synthesis of ZGNR intermediate **11**.

thetic target, and afforded access to the extended zigzag nanographene peripentacene **1** by surface-assisted synthesis. As detailed above, this approach is synthetically quite versatile, potentially serving as a route to a host of assymetric and zigzag-edged graphene nanostructures predicted to exhibit exotic electronic structures. Using the techniques described in this chapter, many materials that have long been the subjects of theoretical investigation are now more accessible for experimental investigation and eventual application.

Part III

Graphene Nanoribbon Composite Materials with Inorganic Nanoparticles

Chapter 4

Solution-Phase Synthesis of Graphene Nanoribbons

Because graphene nanoribbons are a comparatively new class of nanomaterial, much remains unknown or uncertain about their properties as a bulk solid. This is especially true with regard to understanding their interactions with other nanomaterials, which is the primary focus of Part III of this thesis.

To begin, however, a broad array of GNRs must be prepared by solution-phase synthesis, so that their properties and composites can be compared. This brief chapter will introduce the various types of GNRs accessible by solution-phase synthetic techniques, and detail efforts to prepare them and their derivatives so that subsequent chapters can easily refer to structures from this library.

Some of the synthesis and characterization described in this chapter were performed either by or together with other members of the research group: Dr. Tomas Marangoni, Dr. Ryan Cloke, Dr. Wade Perkins, Rebecca Durr, Gregory Veber, and Dharati Joshi. Any structures not prepared by the author will be noted as such below.

4.1 Chevron-Type GNRs

Chevron-type graphene nanoribbons share the crystallographic axis of armchair-type GNRs, but with a serpentine backbone structure that has seen them evocatively described as "graphene nanowiggles" (Scheme 4.1).[179] First prepared by surface-assisted synthesis in 2010, and subsequently in solution in 2014, their solution-phase synthesis relies on Yamamoto polymerization of substituted triphenylenes.[106,128,129] This section describes the gram-scale solution-phase synthesis of chevron GNRs, the synthesis of several derivatives incorporating heteroatoms, and the chracterization of these GNRs prior to the introduction of any inorganic nanomaterials.

Unsubstituted Chevron GNRs

Solution-phase synthesis of all chevron-type GNRs proceeds through the brominated cyclopentadienone **67**, prepared by bromination of phenanthrenequinone and subsequent Knoevenagel condensation (Scheme 4.1).[129] Edge functionalization is then accessible by Diels-Alder reaction with various alkynes, or with diphenylacetylene to yield the unsubstituted monomer **19**. Finally, Yamamoto polymerization and Scholl oxidation yield the unsubstituted chevron-type GNR **5**. The work described in subsequent chapters relied heavily on the scalability of this synthesis, which was ultimately able to produce **5** on the gram scale. Raman spectroscopy is the primary mode of characterization for solution-phase synthesized GNRs, and samples of **5** prepared for this work exhibited the characteristic signals known to correspond to chevron-type GNRs (SI Figure 10.3, page 145).[128]

The behavior of solution-synthesized **5** was further characterized by atomic force microscopy (AFM) and scanning transmission electron microscopy (STEM) (Figures 4.1 and 4.2). These techniques all revealed a strong tendency of **5** to form disordered aggregates with typical dimensions on the order of hundreds of nanometers, routinely reaching micron size. AFM samples were prepared by sonicating **5** in THF and dropcasting onto mica. Although the predominant structures observed by AFM are large aggregates (Figure 4.1A&B), AFM of seemingly bare areas revealed smaller structures resembling fibers comprised of few GNRs, and even structures with height profiles suggesting that they were single isolated GNRs (Figure 4.1C-F).[106] These finer structures are not visible by electron microscopy, which finds only the larger, amorphous aggregates (Figure 4.2). Notably, these aggregates seem stable to the electron beam, even at accelerating voltages on 30 keV.

Nitrogen-Doped Chevron Derivatives

Nitrogen doping is known to exert a major influence on the interfacial interactions between carbon support materials and inorganic nanomaterials, often with important implications for relevant applications (See Chapter 1). To test the role of heteroatoms in dictating the behavior of chevron-type GNRs, especially with regard to their nanoparticle composites, a series of nitrogen-doped chevron derivatives were prepared (Scheme 4.2).[123,126] Termed

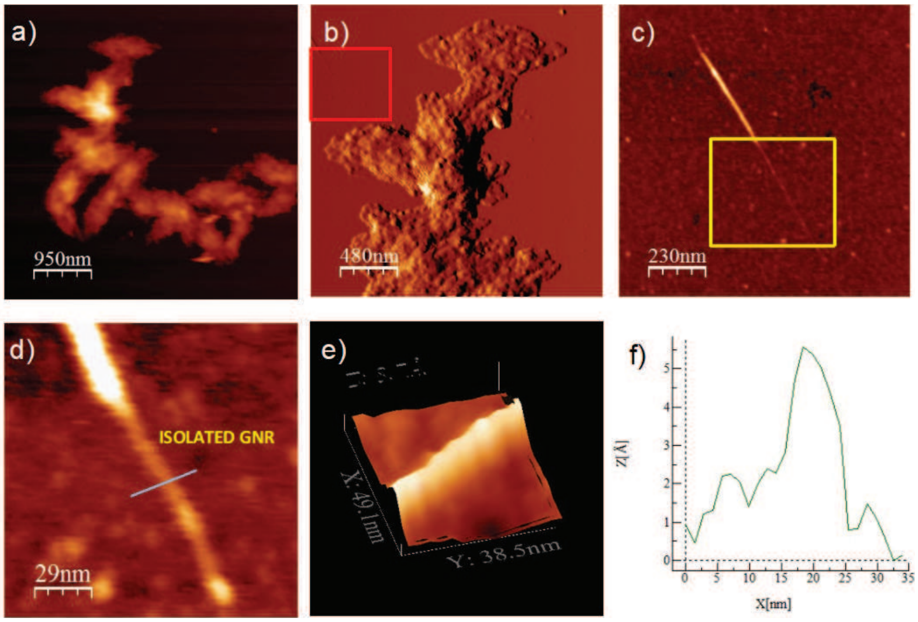

Figure 4.1: AFM characterization of GNR **5** on mica; all images from topography channel. (A&B) Large aggregates are the predominant structure formed by **5**. (C) An image taken in the red indicated area from (b) shows a smaller, fibrous structure. (D) An image taken in the yellow indicated area from (c) shows a small, flat structure. (E) 3D projection of AFM of the flat structure shown in (d). (F) Line scan of along the blue line in (d) indicates a height of approximately 3 Å, in line with the expected hight of a single GNR.

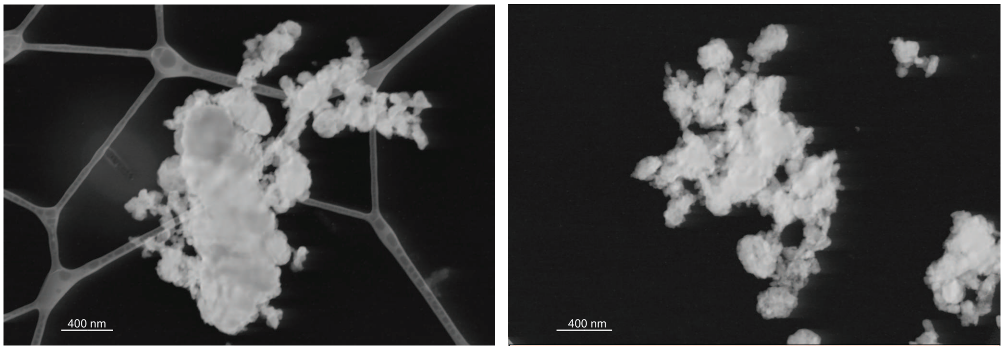

Figure 4.2: STEM images of **5** illustrate the GNR's proclivity for forming large disordered aggregates.

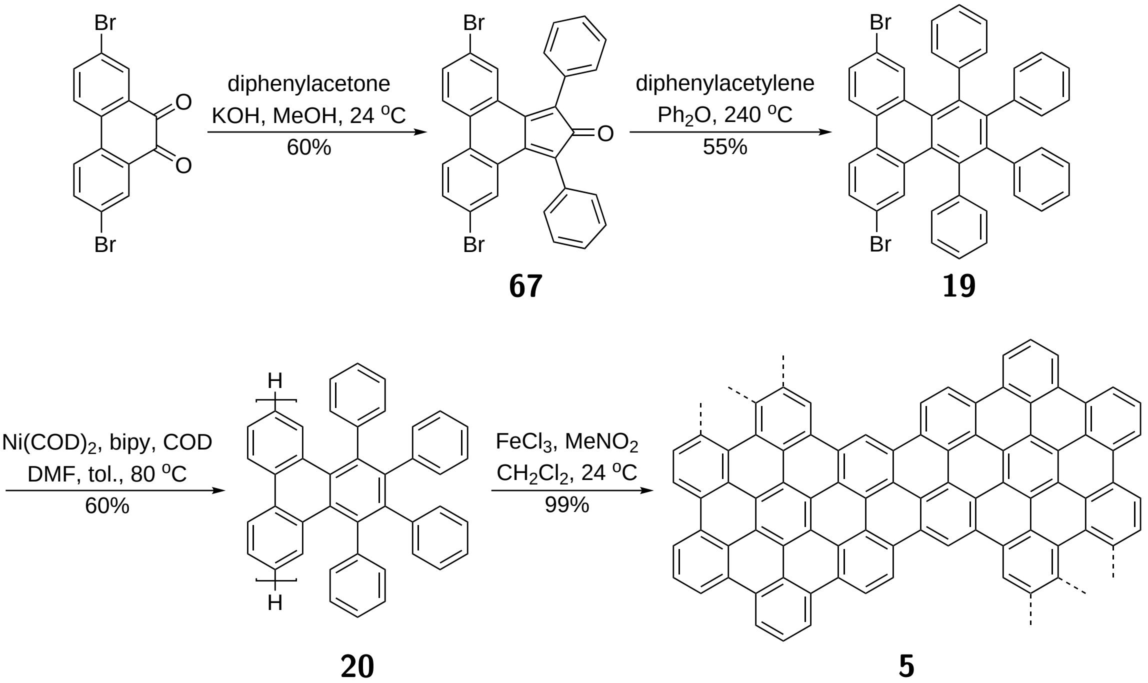

Scheme 4.1: The robust, scalable synthesis of chevron GNR **5**

the 1N-, 2N-, and 4N-chevron GNRs (**68**, **69**, and **6** respectively), each produces a Raman spectrum similar to that of **5** (SI Figure 10.3, page 145). X-ray photoelectron spectroscopy (XPS) of each GNR powder reflects the incorporation of nitrogen atoms, as well as the removal of nickel and iron impurities from the final two synthetic steps (SI Figure 10.4, page 146).

As might be expected for a polymeric material featuring abundant pyridinic nitrogen atoms, **6** exhibited dispersibility in aqueous acid much greater than that of its unfunctionalized counterpart **5**, and greater than its dispersibility in organic solvents like THF. This enhanced dispersibility created an opportunity for UV-Vis characterization of sonicated dilute suspensions of **6** (Figure 4.3). Ordinarily, high scattering by aggregated GNRs precludes meaningful UV-Vis characterization of GNRs (Figure 4.3A), but suspensions of **6** in 1 M HCl repeatably exhibit a distinct absorbance in the UV ($\lambda_{max} = 337$ nm) (Figure 4.3B&C). The significance of this transition is unknown.

As with unfunctionalized chevron GNR **5**, 4N-chevon GNR **6** was characterized by AFM after dropcasting onto mica. Samples dropcast from 1 M HCl mostly consisted of large aggregates, perhaps because more GNR remained in suspension following the mild centrifugation prior to dropcasting, but samples dropcast from THF featured abundant smaller structures (Figure 4.4). Many of the structure appear flat, with apparent heights indicative of single GNRs (SI Figure 10.5, page 147). The structures include a mixture of lengths, with many exhibiting apparent lengths of greater than 100 nm. These images highlight the flexibility

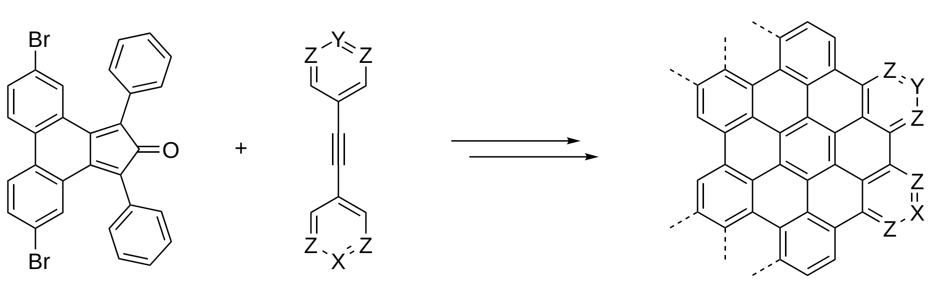

67

68 X = N; Y = Z = C
69 X = Y = N; Z = C
6 X = Y = C; Z = N

Scheme 4.2: Three derivatives of chevron GNR **5** featuring nitrogen heteroatom substitutions were synthesized by Diels-Alder reaction between **67** and various diphenylacetylene derivatives as shown, with subsequent Yamamoto polymerization and Scholl oxidation.

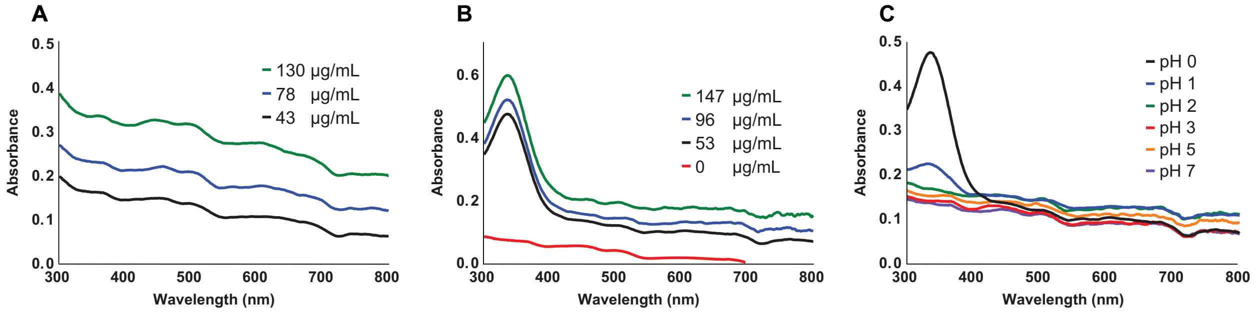

Figure 4.3: UV-Vis characterization of sonicated suspensions of **6** in (A) THF, (B) 1 M HCl, and (C) aqueous HCl of varied pH. Acidic media enhance the dispersion of **6** and exhbit a distinct absorbance in the UV ($\lambda_{max} = 337$ nm).

of individual GNRs, especially in comparison to carbon nanotubes (CNTs), the rigidity of which is enforced by their tubular structure.

Other Chevron Derivatives

In addition to the GNRs prepared as part of this work, projects examining GNR composite materials (Chapters 5-9) made frequent use of heteroatom-substituted chevron-type GNRs synthesized by other members of the research group (Scheme 4.3). By preparing a range of alkynes for Diels-Alder reaction of **67**, a broad library of chevron-type GNRs can be produced.

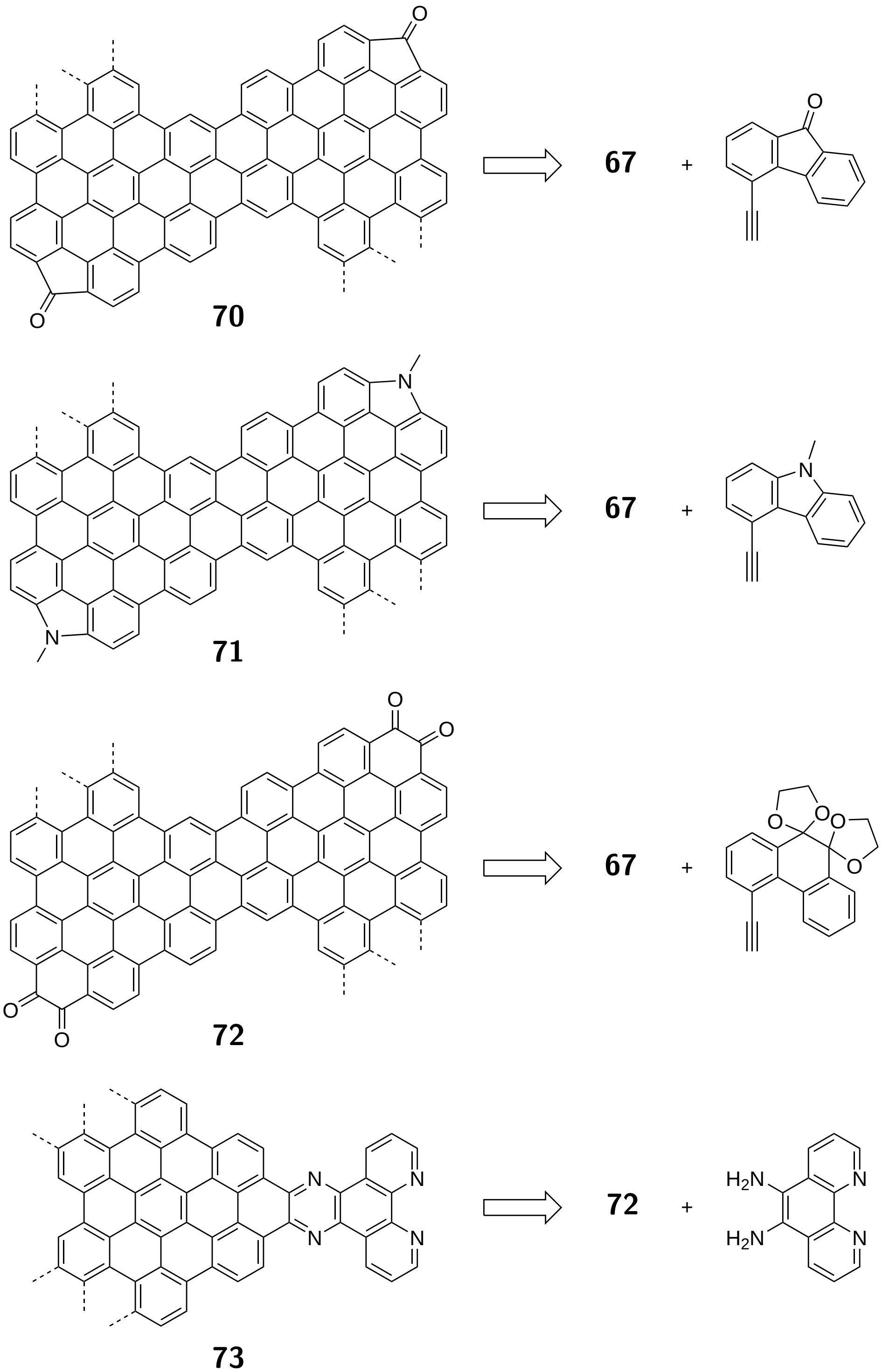

Scheme 4.3: A number of chevron-type GNRs were synthesized by other members of the research group and employed by the author in the preparation of GNR composites with inorganic nanoparticles.

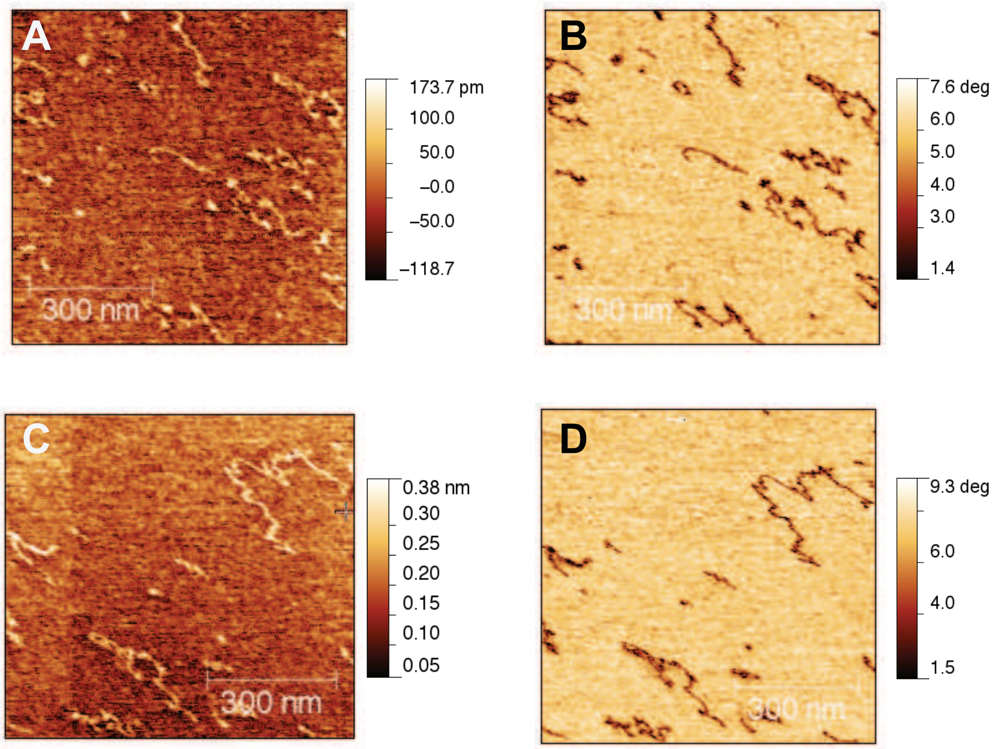

Figure 4.4: AFM characterization of GNR **6** dropcast from dilute suspensions in THF onto mica. (A) and (C) are topography images, (B) and (D) are their corresponding phase images.

4.2 Cove-Type GNRs

Cove-type GNRs are the second of two major classes of GNR accessible through solution synthesis. Cove GNRs share the crystallographic axis of zigzag GNRs, but do not exhibit the exotic electronic structure of smooth-edged zigzag GNRs because their periphery is punctuated by alternating phenyl protrusions and recessed "coves" (Scheme 4.4). The unfunctionalized cove GNR **8** is prepared by high temperature Diels-Alder polymerization of the alkyne-functionalized cyclopentadienone **74**; cheletropic extrusion of CO from the Diels-Alder adduct yields the polyphenylene backbone of the precursor polymer **75**, with subsequent Scholl oxidation to the GNR.

Although GNRs prepared using this type of reactivity were known, the cove GNR **8** had not been reported; this unfunctionalized GNR was determined to be an important synthetic target for the study of GNR interactions with inorganic nanomaterials to avoid the potentially confounding presence of alkyl side chains (Scheme 4.4). Synthesis of **8** began with a Sonogashira reaction between phenylacetylene and 1-bromo-3-iodobenzene; subsequent oxidation gives the benzil derivative **76**, which undergoes Knoevenagel condensation

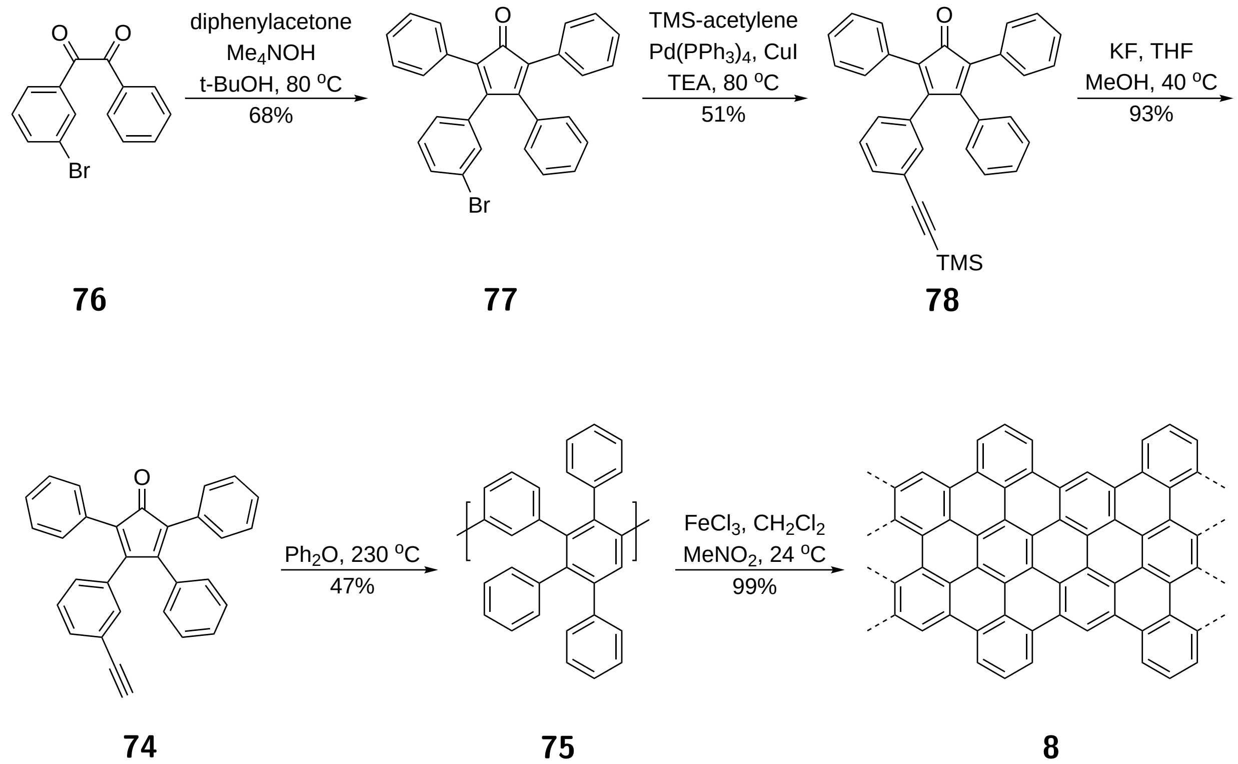

Scheme 4.4: Synthesis of cove-type GNR **8**

with diphenylacetone to yield cyclopentadienone **77**. The alkyne used in polymerization is installed by Sonogashira reaction with trimethylsilylacetylene to yield **78**, which is deprotected with KF to give **74**.

Polymerization of **74** at 230 °C gave the polyphenylene **75**. The polymer was characterized by 1H- NMR and by MALDI, which featured a characteristic pattern of signals separated by the mass of **75**'s repeat unit (SI Figure 10.2, page 145). Scholl oxidation of **75** with $FeCl_3$ gave the GNR **8**. Raman spectroscopy confirmed the formation of the GNR by the appearance of diagnostic D and G signals, as expected for a graphene nanoribbon, and XPS indicated the successful removal of trace Fe (SI Figure 10.4, page 146).

Functionalized cove GNRs were prepared by a modified synthesis introducing two bromine atoms to edge positions of the monomer, which served as functional handles for late-stage modification to a diverse set of monomers. To begin, the brominated diphenylacetone derivative **79** was synthesized by carbonylative coupling using $Fe(CO)_5$ (Scheme 4.5).[180] Knoevenagel condensation using **79** gives the brominated cyclopentadienone **80**, importantly featuring an iodine for selectivity against the brominated positions. Sonogashira reaction with triisopropylsilylacetylene yields **81**, which features a more robust TIPS group to tolerate a broad set of possible reactivities for later functionalization at the brominated positions.

The cove GNR derivative **7**, featuring two methyl esters per repeat unit, was synthesized

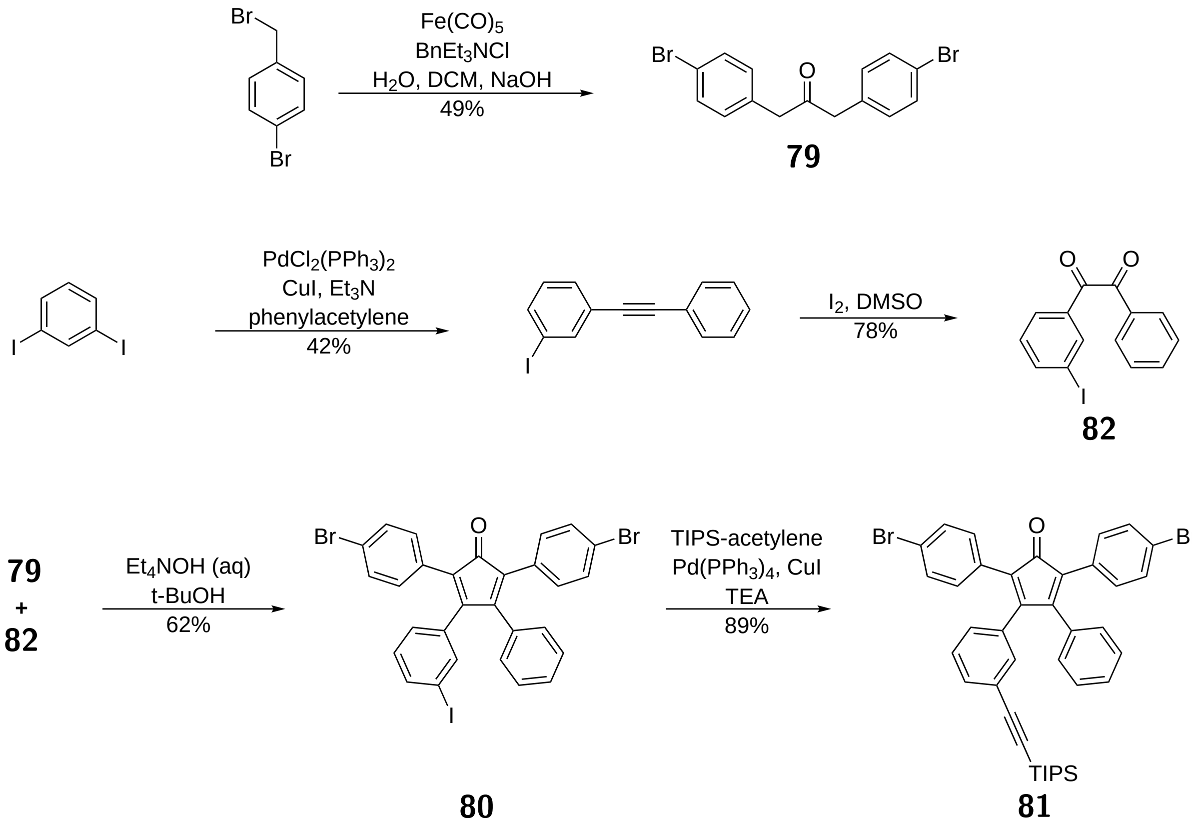

Scheme 4.5: The synthesis of **81**, a precursor to a variety of edge-functionalized cove-type GNRs.

by functionalization of **81** (Scheme 4.6). Using a recently-published procedure, methyl esters were installed by double Pd-catalyzed carbonylative coupling with CO and MeOH to yield **83**. Mild silyl deprotection with AgF was necessary to procure **84**, as **83** was found to be quite sensitive to more common deprotection conditions. Finally, polymerization and Scholl oxidation yielded the GNR **7**; ^{1}H NMR of the polymer and IR spectroscopy of the GNR confirmed the continued presence of the methyl esters through both steps (Figure 4.5).

Additional cove GNR derivatives were prepared by other members of the research group using **80**, and later studied for this work as nanoparticle composite materials (Scheme 4.7). These included the boronic acid cove derivative **13**, prepared via Miyaura borylation of **80**, and aldehyde-functionalized cove derivative **14**, accessed via Suzuki coupling using the borylated monomer **86**.

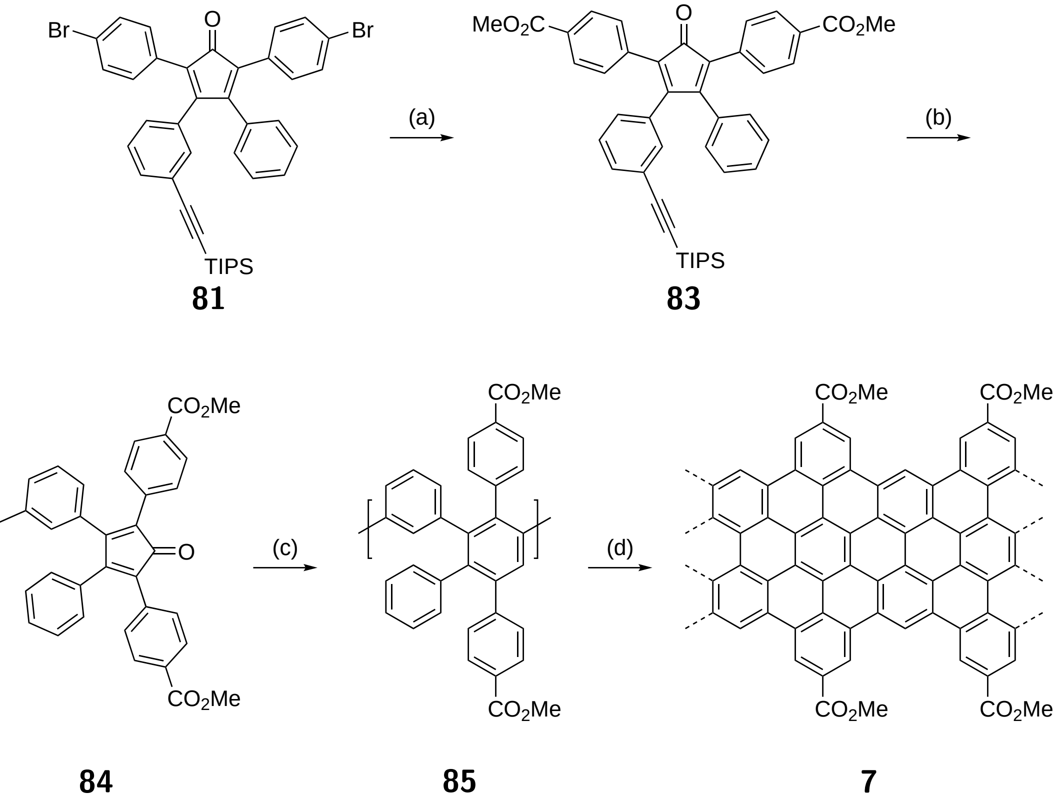

Scheme 4.6: The synthesis of **7**, a cove GNR functionalized with methyl esters at its edge. Conditions: (a) Pd(OAc), Xantphos, MeOH, CO, Et$_3$N, 24 °C, 12 h, 34%; (b) AgF, DMF, 24 °C, 12 h, 60%; (c) Ph$_2$O, 240 °C; (d) FeCl$_3$, CHCl$_2$, MeNO$_2$, 24 °C, 99%

4.3 Bay-Type GNRs

Because GNR electronic band structure is determined largely by its backbone type (i.e. their edge geometry, e.g. chevron or cove), accessing a wider array of backbone types will allow for a broader investigation of GNR electronic interactions with other nanomaterials. To complement the established backbone structures described above, a new class of GNR was devised and termed "Bay GNRs" (Scheme 4.8). The bay GNR **89** shares the crystallographic axis of armchair and chevron GNRs, but with a distinct edge geometry that resembles a condensed chevron structure. GNR **89** is synthesized, as with chevron GNRs, by Yamamoto polymerization and subsequent Scholl oxidation of a bis-aryl halide monomer such as **15**. Synthesis of **15** begins with carbonylative dimerization of 1-bromo-2-(bromomethyl)benzene using Fe(CO)$_5$ to give **90**,[181] and subsequent Knoevenagel condensation with phenanthrenequinone yields the brominated cyclopentadienone derivative **91**. Diels-Alder reaction with norbornadiene (followed by retro Diels-Alder reaction to lose cyclopentadiene) yields the desired monomer **15**. Polymerization studies of this monomer are currently ongoing, as initial at-

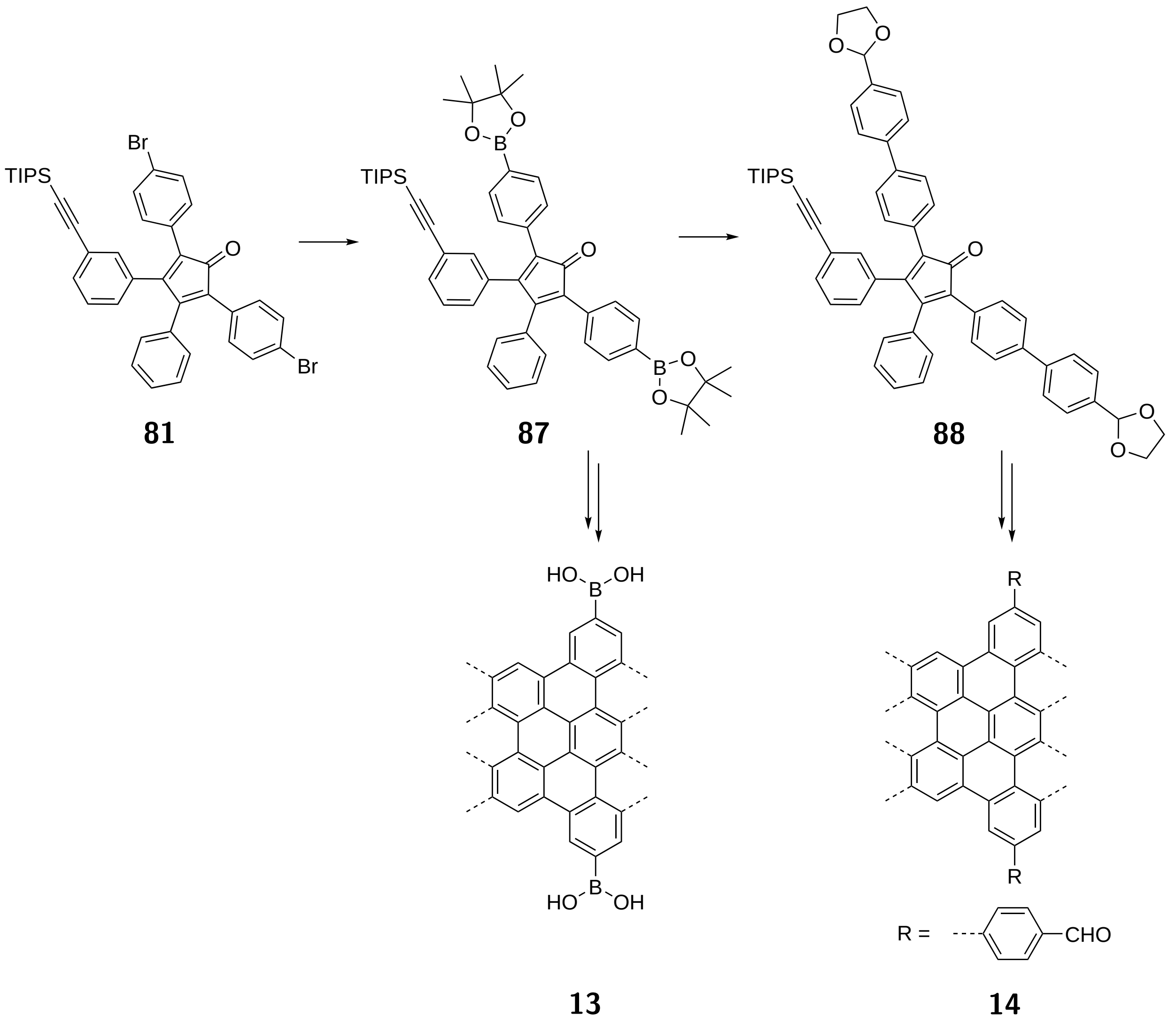

Scheme 4.7: The versatile intermediate **81** affords access to a wide variety of functionalized cove-type GNRs. These GNRs **13** and **14** were synthesized by other members of the research group and employed by the author in the preparation of GNR composites with inorganic nanoparticles.

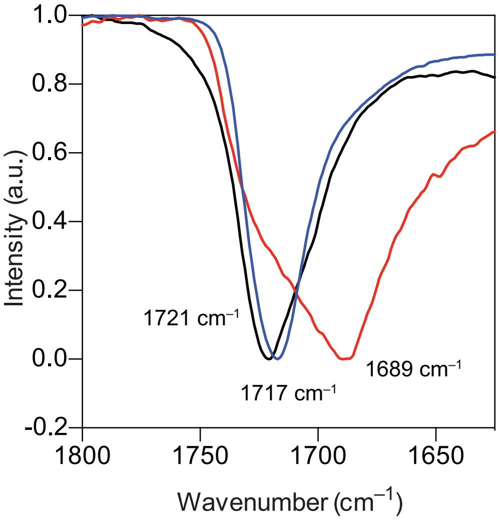

Figure 4.5: IR spectroscopy of GNR **7**. The carbonyl CO stretch of the **7** (black) following the Scholl reaction matches that of the ester-functionalized polymer **85** (blue), indicating that the esters remain intact. A partially saponified sample of **85** (red) shows a significant shift of the CO stretching frequency, which is absent in the IR spectrum of **7**, indicating that the methyl esters in **7** have not been saponified under the reaction conditions.

tempts yielded only oligomers, and more forcing Yamamoto conditions may be required to yield long polymers and GNRs.

4.4 Conclusion

This prefatory chapter described the synthesis of a variety of GNRs by solution-phase techniques; these GNRs primarily belong to either the chevron or cove backbone-type classes. Subsequent chapters will employ these GNRs as composites with inorganic nanomaterials, and investigate the ways in which their structural differences influence these interfacial interactions and ultimately dictate performance in a variety of applications.

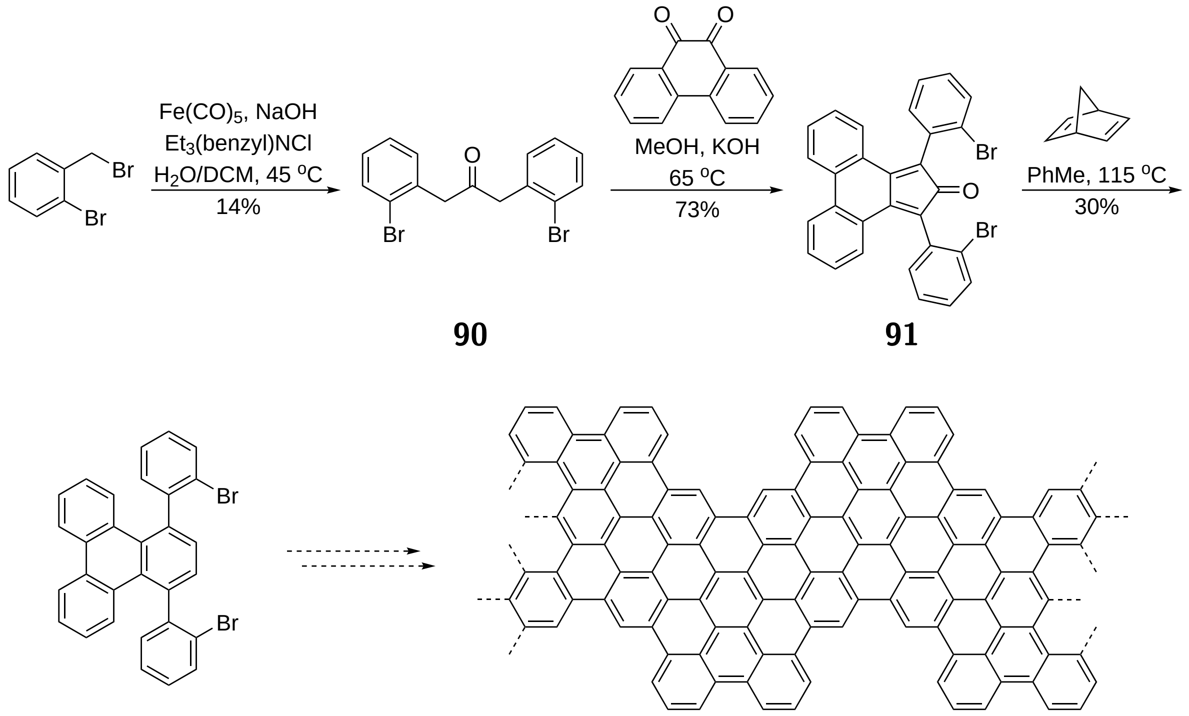

90

91

15

89

Scheme 4.8: The synthesis of **15**, a monomer designed to yield GNR **89** of an unreported backbone type termed "Bay GNR".

Chapter 5

AuNP-GNR Composites for CO_2 Reduction Electrocatalysis

As is detailed in Chapter 1, inorganic nanomaterials frequently rely on inert carbon support materials to impart nanoparticle stability and device integrity. Through their interactions with the active inorganic nanomaterials, these ostensibly passive carbon supports can also profoundly alter performance, and their design has emerged as a key parameter through which nanomaterial devices can be tuned, optimized, and understood. However, regulating the complex material environment accounting for the stability, selectivity, and activity of catalytic metal nanoparticle interfaces represents a continuing challenge to heterogeneous catalyst design. This chapter will discuss composites prepared from colloidal gold nanoparticles (AuNPs) and bottom-up synthesized graphene nanoribbons, the first application of a synthetically derived graphene nanomaterial as a nanoparticle support. When prepared with a well-chosen GNR, these composite materials are demonstrated to be excellent electrocatalysts for the reduction of CO_2, featuring increased AuNP electrochemically active surface area (ECSA), greatly reduced CO_2 reduction overpotential (catalytic onset > -0.2 V versus reversible hydrogen electrode (RHE)), increased the Faradaic efficiency (>90%), vastly improved stability (catalytic performance sustained through more than 24 h), and markedly increased total catalytic output (>100-fold improvement over traditional amorphous carbon AuNP supports). Most notably, the electrocatalytic performance is shown to be highly dependent upon the specific GNR employed, shedding light on the nature of GNR interaction with inorganic nanomaterials and establishing the structurally and electronically tunable GNRs as a means to unrivaled control over the catalytic environment in heterogenous composite systems.

Dr. Teresa Williams at the Molecular Foundry performed some of the electron microscopy described in this chapter.

		Faradaic Efficiency (%)			
Electrode	Potential (V) vs NHE	CO	$CHOO^-$	H_2	Reduced C pdts
Au	-1.14	87.1	0.7	10.2	0.0
Cu	-1.44	1.3	9.4	20.5	72.3
Pb	-1.63	0.0	97.4	5.0	0.0
Pt	-1.07	0.0	0.1	95.7	0.0

Table 5.1: Performance of certain metal foils for the electrocatalytic reduction of CO_2 in 0.1 M aqueous $KHCO_3$ saturated with CO_2. For each electrode, the reducing potential was increased until total current density reached 5.0 mA cm^{-2}. Product ratios were determined by gas chromatography; Faradaic efficiencies may not total 100%. For the Cu electrode, reduction products are mainly CH_4, C_2H_4, and EtOH. Table recreated using data from reference [182].

5.1 Gold Nanoparticles for CO_2 Reduction Electrocatalysis

Metal surfaces have been studied for decades as capable electrocatalysts for the reduction of CO_2 in aqueous media (Table 5.1).[182,183] Among these, gold surfaces are interesting test materials because of their high selectivity for reduction of CO_2 to CO at moderate potentials; this is in contrast to other metals that produce mostly formate (Pb, Sn, etc.), those that participate almost exclusively in hydrogen evolution (Ni, Fe, Pt, etc.), or those that produce a complex set of further reduced products (Cu, see Chapter 6).[182] This selectivity considerably simplifies the investigation of substrate interaction effects, making Au electrocatalysis an ideal system for the first investigation of composite materials featuring synthetically tunable support materials.

Importantly, the values listed in Table 5.1 reflect the performance of metal foils, but these are ultimately of limited utility due to their inherently low surface area. Gold nanoparticles (AuNPs) are a more desirable catalyst system because they maintain the aqueous compatability and good selectivity of Au foils while offering larger surface area, and higher reactivity.[184,185] AuNPs have been prepared by a variety of synthetic methods, with excellent control over their size and monodispersity.[186,187] However, moving to the more reactive AuNPs introduces a range of challenges, chiefly pertaining to selectivity and stability.

As CO_2 reduction electrocatalysis at the surface of AuNPs follows a proton-coupled mechanism, it necessarily faces competing proton reduction, limiting the Faradaic efficiency for CO production (FE_{CO}). As Figure 5.1 illustrates, the barriers to CO_2 reduction and hydrogen evolution vary significantly between diverse metal facets or nano-sized clusters, complicating the issue of selectivity for small, reactive AuNPs. As a result, the selectivity of AuNPs for CO_2 reduction is dependent upon their size and the manner of their production;[183,188,189] nanoparticles of roughly 8 nm diameter were found to exhibit the highest FE_{CO} among supported colloidal AuNPs.[187,190] This observed variance in reactivity between

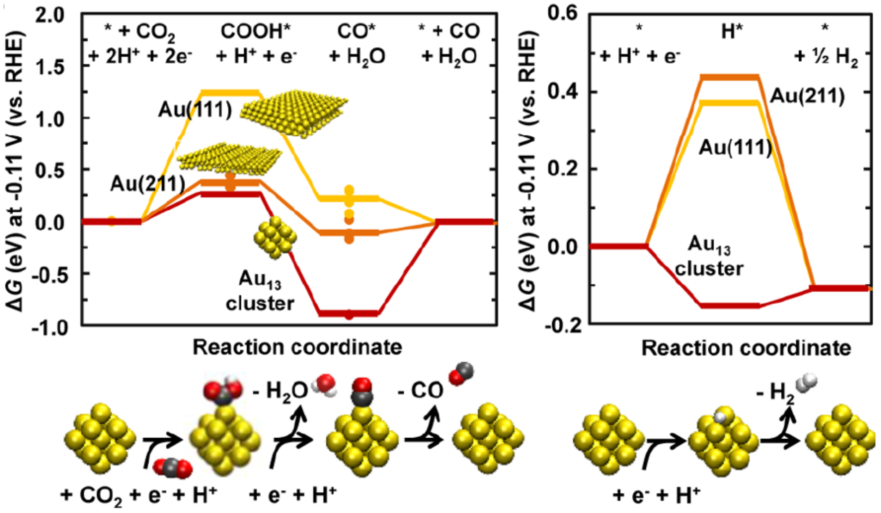

Figure 5.1: Free energy diagrams for the two competing electrocatalytic reduction reactions on Au surfaces at -0.11 V vs RHE. Horizontal lines are calculated data, while dots are experimental data. Figure from reference [187].

AuNP faces, sizes, and preparations stem from the fact that CO_2 reduction on metal surfaces follows an inner-sphere mechanism like that depicted in Figure 5.1; electron transfer to an unbound CO_2 molecule occurs only at very strongly reducing potentials, and therefore all CO_2 reduction follows a proton-coupled electron transfer to surface-bound CO_2 species.[191] As a result, the reaction is sensitive to the structural and electronic environment at the metal surface.[184,191]

Reactive AuNPs face the further challenge of stability amid harsh electrocatalytic working conditions.[7,185,192] Within minutes of polarization, AuNP samples exhibit significant decline in total current and especially in FE_{CO}, ocrrelated with a loss of electrochemically active surface area (ECSA). Recent investigation found that the primary mechanism by which this deactivation occurs is the diffusion of AuNPs leading to the collision and fusion of many nanoparticles to form large aggregates with comparatively low ECSA and selectivity.[7] (Figure 5.2) To counteract this, colloidal nanoparticles are generally dispersed in a porous carbon support material like carbon black (C_{black}), immobilizing the AuNPs to some degree and slowing their rate of deactivation.[185,187] However, C_{black} supported AuNPs still exhibit deactivation and loss of selectivity on the hours timescale, creating a demand for a support material that more effectively immobilizes AuNPs while still permitting mass transport to and from the NP surface.

As discussed in Chapter 1, support materials can exert influence beyond merely immobilizing nanoparticles by serving to modulate the structural and electronic environment at the NP surface, and some examples have demonstrated this effect in gold nanoparticles. AuNPs grown on carbon nanotubes (CNTs) have long been known to alter the CNT elec-

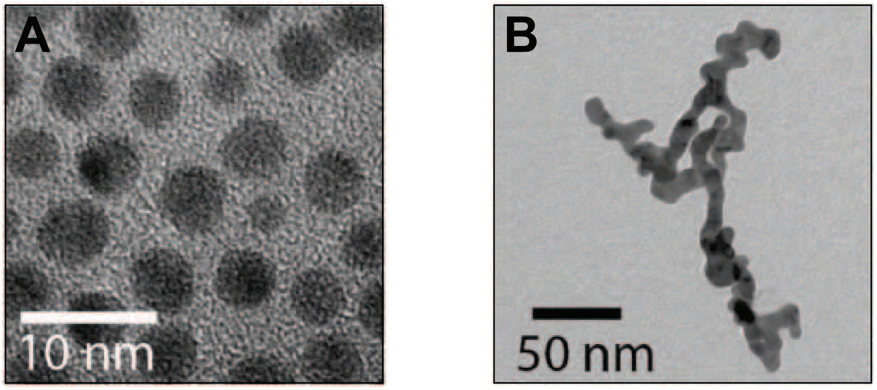

Figure 5.2: TEM images of AuNPs (A) as-synthesized and (B) following 100 min of CO_2 reduction at -1.2 V vs RHE in 0.1 M $NaHCO_3$ show the growth of large dendritic aggregates. Images from reference [7].

tronic structure through electron transfer to the AuNPs, introducing p-type dopants to the CNTs and consequently increasing the nanotube conductance.[48,193] This effect has further been applied to enhance electron transfer from other species to the CNTs themselves, as well as to alter the transistor behavior of functionalized CNTs.[45,194] AuNPs have also been utilized with nitrogen- and oxygen-doped graphene nanostructure support materials, which enhance NP-support interaction and serve to anchor *in-situ* prepared AuNPs.[30,185,195] Furthermore, a recent report have found that CO_2 reduction catalysis at the AuNP surface is quite sensitive to molecular functionalization, demonstrating that catalyst activity is readily modified through electronic interaction at the AuNP interface.[196] These precedents suggested that properly functionalized GNRs could similarly influence behavior at the nanointerface, prompting systematic investigation into GNR-AuNP substrate effects and their significance for AuNP catalysis.

5.2 Preparation of AuNP Composites and Electrodes

Graphene nanoribons used for the preparation of GNR-AuNP composites were synthesized as described in Chapter 4. Small oleylamine-capped AuNPs were prepared by the reduction of chloroauric acid, using a method derived from reported procedures.[186,192,196] High resolution TEM and high-angle annular dark field scanning transmission electron microscopy (HAADF-STEM) of the AuNPs shows a narrow size distribution centered around the an average NP diameter of 8 nm (Figure 5.3A&B). GNR-AuNP composite materials were prepared by sonicating a dispersion of equal mass of AuNPs and the respective GNRs **5** or **8** in hexane. The high affinity of AuNPs for the GNR support is immediately evident as the red AuNP solution loses its characteristic color upon sonication with GNRs, becoming a dark suspension. HAADF-STEM of the isolated black powder, rinsed with hexane and drop cast

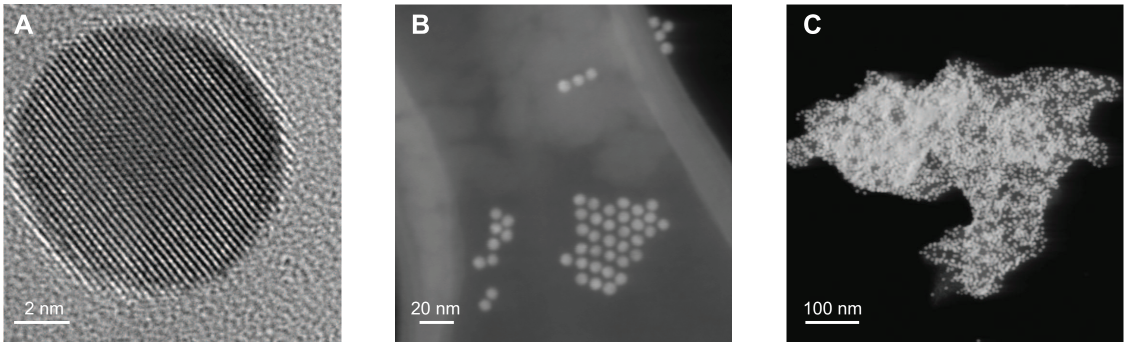

Figure 5.3: Characterization of AuNPs by (A) High-resolution TEM and (B) HAADF-STEM indicate a narrow width distribution centered around 8 nm. (C) HAADF-STEM of a composite of AuNPs and **8** show uptake of the AuNPs into the GNR matrix.

onto TEM grids, shows the uptake of the AuNPs into large nanoribbon aggregates (Figure 5.3C). GNR-AuNP composites commonly range in size from 0.2 to 1.0 μm, and aggregates appear comparable to those observed without AuNPs (see Figure 4.2, page 56). The high apparent density of AuNPs and the lateral overlap observed in transmission mode images suggest the AuNPs are embedded within the three dimensional GNR network, rather than perched on its surface.

While necessary for nanoparticle synthesis, oleylamine capping ligands act as an impediment to electrocatalysis by blocking the AuNP surface. Furthermore, they serve to insulate the AuNPs from the GNRs, introducing resistance and precluding any meaningful interaction between the nanomaterials. Although unsupported nanoparticles will form shapeless aggregates if their ligands are stripped away, incorporation into the GNR matrix serves to stabilize AuNPs following the removal of oleylamine capping ligands, accomplished by annealing the composites in air at 185 °C for 10 h.[187] IR spectra of samples prior to and immediately after annealing confirm that the oleylamine ligands have been removed, leaving pristine AuNPs behind (Figure 5.4A).[196] Raman spectra of annealed GNR-AuNP composites show no shift or broadening of the diagnostic D, G, and RBLM modes (Figure 5.4B), indicating that the integral structure of the GNRs remains unaltered. Powder X-ray diffraction (PXRD) of the black GNR-AuNP composite powder shows the characteristic broadened signals of small AuNPs (Figure 5.4C).[186,192]

Simple linear sweep voltammetry (LSV) experiments could provide initial insight into GNR-AuNP composites and their electrocatalytic capabilities, so electrodes were fabricated from a variety of GNR-AuNP composites. Electrodes were made using conductive carbon paper, a porous sheet of woven carbon microfibers that is the typical substrate for composite material electrodes.[187] Composites were prepared as described above, by sonicating a dispersion of AuNPs and the relevant GNR (1:1 by mass) in hexane, then dropcast onto a 1 cm^2 area of carbon paper, followed by annealing in air at 185 °C for 10 h. The characteristic PXRD pattern of AuNPs in these annealed electrodes matches that of the composite bulk

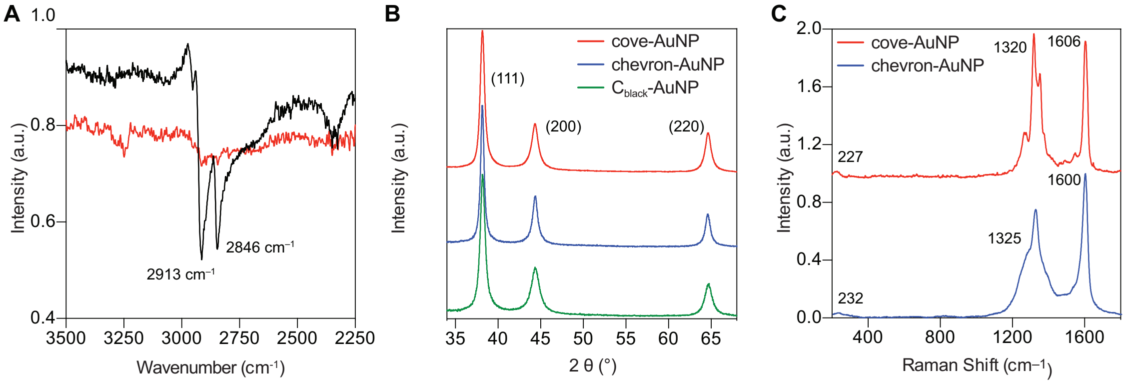

Figure 5.4: Characterization of AuNP composites with unfunctionalized GNRs **5** and **8** following an anneal in air at 185 °C for 10 h to remove oleylamine ligands. (A) IR spectroscopy shows the disappearance of the signals attributed to oleylamine following the anneal (B) Raman spectroscopy indicates the GNRs are not impacted. (C) PXRD of the composites show the characteristic signals of small AuNPs. A composite with the amorphous carbon support carbon black was included for comparison.

powders characterized above.

Additionally, other electrodes were prepared in the same manner but using carbon black (C_{black}) in place of GNRs, to act as a performance benchmark. Carbon black, an amorphous, porous carbon material formed by combustion of various organic precursors, is very commonly used as an ”innocent” conductive support in electrocatalysis applications, and therefore was the logical point of comparison for GNR composite materials.[187] AuNP composites with single-walled carbon nanotubes (SWCNTs) were examined as a second point of reference, since they resemble GNRs as one-dimensional graphene nanomaterials, but the comparatively poor performance of the SWCNT composites made them an unsuitable standard (SI Figure 10.6, page 148). Nanoparticle composites with CNTs are known to be capable catalysts under certain conditions, such as when NPs are grown directly on CNTs or otherwise tethered to them. However, while both GNRs and C_{black} formed comparatively stable composites with the free colloidal NPs employed here, the CNTs seemed incapable of similar strong interaction with the NPs, likely as a result of their relatively rigid structure.

5.3 Initial Characterization of GNR-AuNP Composite Electrocatalysis

Initial CV experiments of the AuNP composite electrodes in 0.5 M aqueous KHCO3 saturated with CO2 (pH 7.3) revealed a strong synergistic effect between nanoparticles and GNRs. A composite electrode prepared using chevron GNR **5** and AuNPs delivered much greater current than corresponding electrodes made from either AuNPs alone or **5** alone

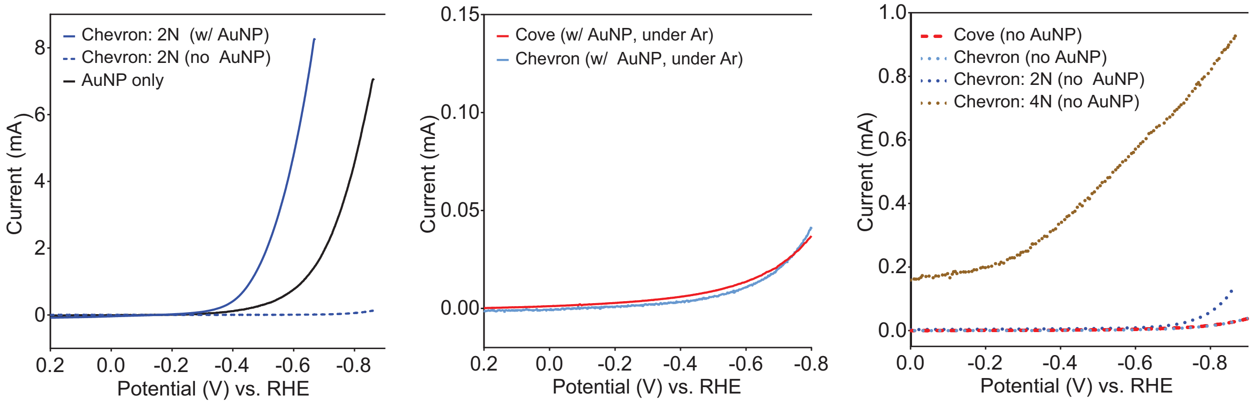

Figure 5.5: Linear sweep voltammetry of GNR-AuNP composites reveals a synergistic enhancement in CO_2 reduction electrocatalysis. (A) LSV in 0.5 M aqueous $KHCO_3$ saturated with CO_2 (pH 7.3) shows far greater current for a composite of AuNPs with chevron-type GNR **69** than for either the GNR or the AuNPs individually. (B) LSV of AuNP-GNR composite electrodes taken in the absence of CO_2, under an atmosphere of Ar, exhibit much lower current than that shown in (A), suggesting that the additional current drove CO_2 reduction electrocatalysis. (C) LSV in 0.5 M aqueous $KHCO_3$ of GNR-only electrodes prepared without AuNPs generally exhibited little current in the relevant potential range. However, some GNRs, like nitrogen-doped chevron GNR **6**, exhibit significant current and are therefore unsuited for further investigation.

(Figure 5.5A). The current enhancement observed in GNR-AuNP composite electrodes disappears in the absence of CO_2 (Figure 5.5B), suggesting the excess current drives CO_2 reduction. Importantly, CV of most GNRs (such as **5** or **8**) without any added AuNPs exhibited minimal current across the entire examined potential window (Figure 5.5C), indicating that the GNRs themselves are not electrochemically active. However, some GNRs, like the 4N-chevron GNR **6**, did provide significant current when tested without AuNPs. The persistence of this current when tested under N_2 indicates that the GNR was catalyzing hydrogen evolution, and was therefore an unsuitable candidate for further testing, since this behavior will lower the CO_2 reduction selectivity of the composite.

The synergistic CO_2 reduction current enhancement exhibited by AuNP composites with **5** spurred investigation into a wide range of GNR composites by linear sweep voltammetry (LSV) in 0.5 M aqueous $KHCO_3$ saturated with CO_2, which furnished four primary conclusions (Figure 5.6A).

1. Composites featuring many GNR types exhibit dramatically different performance from the baseline composite made with C_{black}, generally (but not exclusively) featuring a lower catalytic onset potential and higher currents for each potential.

2. GNR backbone type (i.e. cove vs. chevron vs. armchair) exerts significant influence

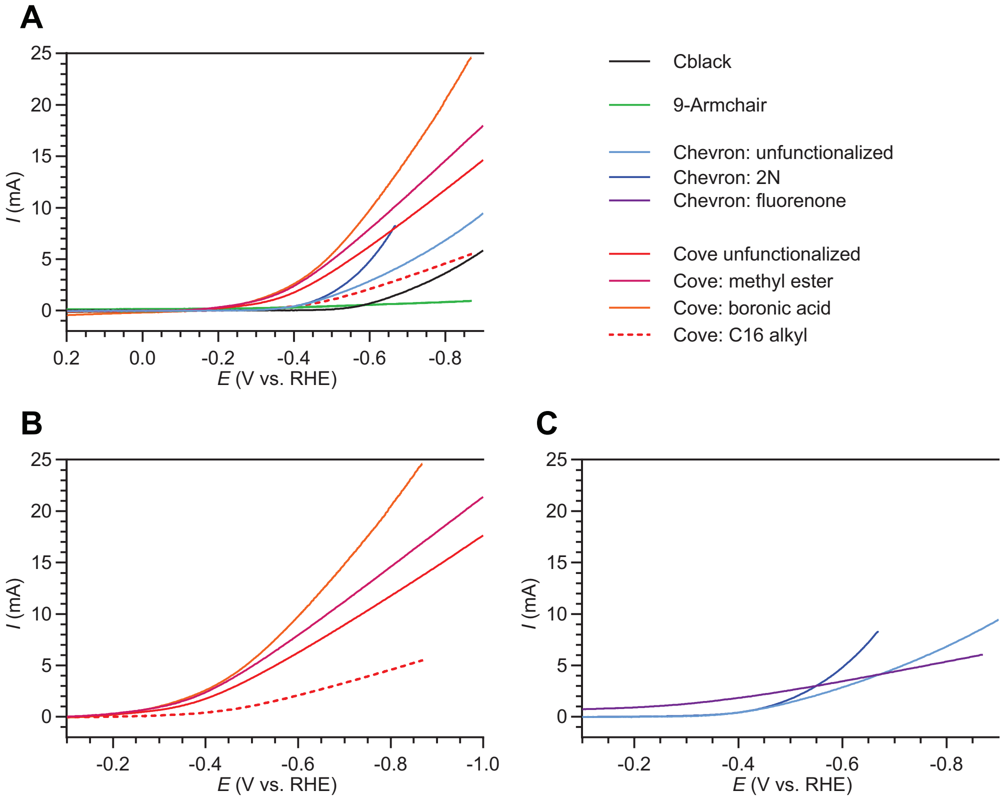

Figure 5.6: Linear sweep voltammetry of GNR-AuNP composites in 0.5 M aqueous KHCO$_3$ saturated with CO$_2$ (pH 7.3). (A) The behavior of GNR-AuNP composites differs dramatically from that of the reference composite prepared with C$_{black}$. Composites appear to organize into families depending upon their GNR backbone type, such as (B) cove or (C) chevron. Current within those families is influenced significantly by the inclusion of heteroatom functional groups.

on the behavior of the AuNP composite. For example, composites made with the same GNR backbone type (e.g. **8**, **7** and **13**) generally exhibit clustered catalytic onset potentials. The composite made with the armchair GNR **18** effectively shut down all reactivity of the AuNPs in the relevant potential window.

3. Heteroatom functionalization of GNRs also plays a significant role in the LSV behavior of their AuNP composites. Within GNR families, the inclusion of polar functional groups led to large changes in post-onset catalytic current (Figure 5.6B&C). With some exceptions, like the unexpected LSV behavior of the fluorenone GNR **70** composite, these polar groups increased the slope of the I-V curve past catalytic turn-on, yielding higher currents.

4. As might be expected, the inclusion of insulating alkyl chains like the C16 chains of

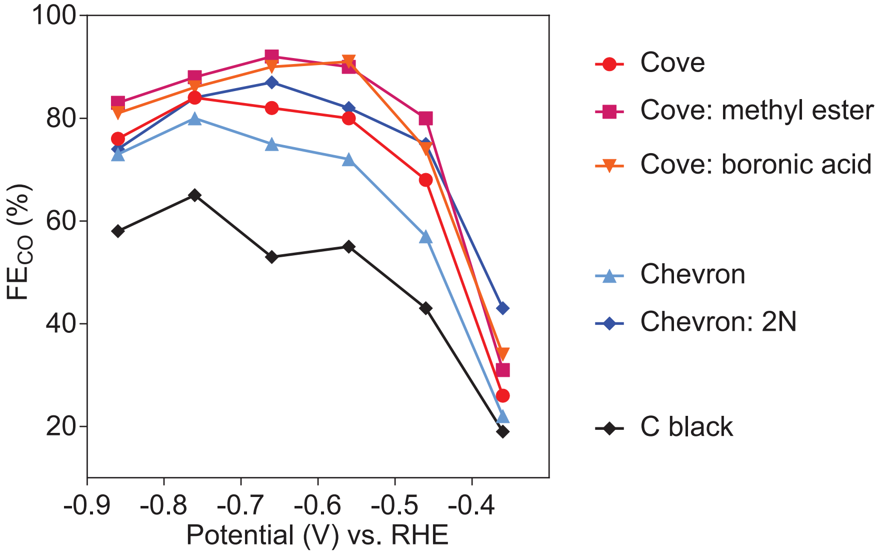

Figure 5.7: Faradaic efficiency for CO_2 reduction by various GNR-AuNP composites, tested for one hour in 0.5 M aqueous $KHCO_3$ saturated with CO_2 at 100 mV intervals over a potential range from -0.87 to -0.37 V. Composites made with C_{black} are included as a performance standard.

92 dramatically cut the catalytic current for its AuNP composite relative to that of the composite prepared with **8**.

In addition to establishing these general trends in GNR composite behavior, LSV experiments identified the five GNRs that were most appropriate for further investigation: the chevron GNR **5** and its 2N-derivative **69**, as well as cove GNR **8** and its edge-functionalized derivatives **7** and **93**. Composites using these GNRs were tested further by one hour controlled-potential electrolysis experiments to establish their Faradaic efficiency for CO_2 reduction (FE_{CO}) (Figure 5.7). Composites were tested in 0.5 M aqueous $KHCO_3$ saturated with CO_2 at 100 mV intervals over a potential range from -0.87 to -0.37 V (all potentials versus reversible hydrogen electrode (RHE)), such that each data point in Figure 5.7 represents a distinct electrode tested for one hour. This experiment established that GNR composites do not merely pass higher current than the C_{black} reference electrode, but do so at a much higher efficiency for CO_2 reduction, with functionalized cove derivatives in particular reaching FE_{CO} values greater than 90%.

The divergent behaviors of composites featuring 2N-chevron GNR **69** and 4N-chevron GNR **6** serve as a particularly compelling case for the utility of examining substrate effects through the bottom-up synthesis of support materials. Recall that electrodes with **6** produced hydrogen too readily for use as a support material; in contrast, composites prepared wtih **69** exhibit Faradaic efficiencies for CO_2 reduction as high as 87%. Any top-down synthetic method to access comparable nitrogen-doped graphene nanomaterials would unavoidably contain sites resembling **69** and sites resembling **6**, with no ability to disentangle the competing effects provided by the two doping motifs.

For reasons of clarity and expediency, a full materials and electrochemical characterization was carried out only for three GNR composites, chosen to best highlight the differences between composites and understand the breadth of AuNP-GNR interactions. These were the chevron GNR **5**, the cove GNR **8**, and the methyl ester-functionalized cove GNR **7**. The composites of these three GNRs, as well as the composites of reference material C_{black}, will be the focus of the remainder of this chapter.

5.4 Materials Characterization of GNR-AuNP Composites

Annealed AuNP composites with GNRs **5**, **8**, and **7** were examined by a variety of material characterization techniques to more fully understand the environment of the AuNPs and their interaction with the GNR matrix. STEM and TEM images of annealed samples show that composite aggregates remain intact and are comparable in size and morphology to those observed prior to annealing (Figure 5.8). Although the NPs have been stripped of their stabilizing ligand shell, only minimal coalescence of the nanoparticles during the annealing process is observed by STEM, indicating an efficient stabilization of uncapped AuNPs through dispersion interaction with the GNR matrix.

Traditionally, NP support materials emphasize high surface area as a crucial factor to dynamic mass transport to and from the catalytically active surface.[197–199] However, surface area measurements derived from N_2 adsorption at 77 K (BET model, Table 5.2) showed that both **8**-AuNP (5.9 m^2 g^{-1}) and **5**-AuNP (19.8 m^2 g^{-1}) composites present quite low surface areas, and lower than that of the reference composite prepared from C_{black}-AuNP (26.8 mm^2 g^{-1}). This behavior is not unexpected in aggregates of a graphitic material, for which strong dispersion interactions between graphene planes lead to stacking and low BET surface area.[200] Furthermore, it has been shown that N_2 adsorption at 77 K does not appreciably capture ultramicroporosity (pore size < 0.7 nm) due to restricted diffusion of N_2 into micropores at low temperature.[201–205] CO_2 absorption at 298 K is not restricted by micropore diffusion and provides a better approximation for the transport of small gas molecules through the GNR matrix.[206,207] AuNP composites of **5** and **8** show more than twice the CO_2 uptake measured for the C_{black}-AuNP reference (Figure 5.9), reversing the trend in BET surface area observed for N_2 adsorption. These results suggest a significant microporosity for the GNR aggregates in comparison to the C_{black} composite, and is an indication that GNRs, despite their inherently low surface area, can facilitate mass transport within NP composite aggregates.

We determined the electrochemically active surface area (ECSA) of AuNP composites using lead underpotential deposition experiments (Pb-UPD) (Figure 5.10 and Table 5.2).[196,208–210] All samples display two characteristic signals in the Pb-UPD voltammograms,

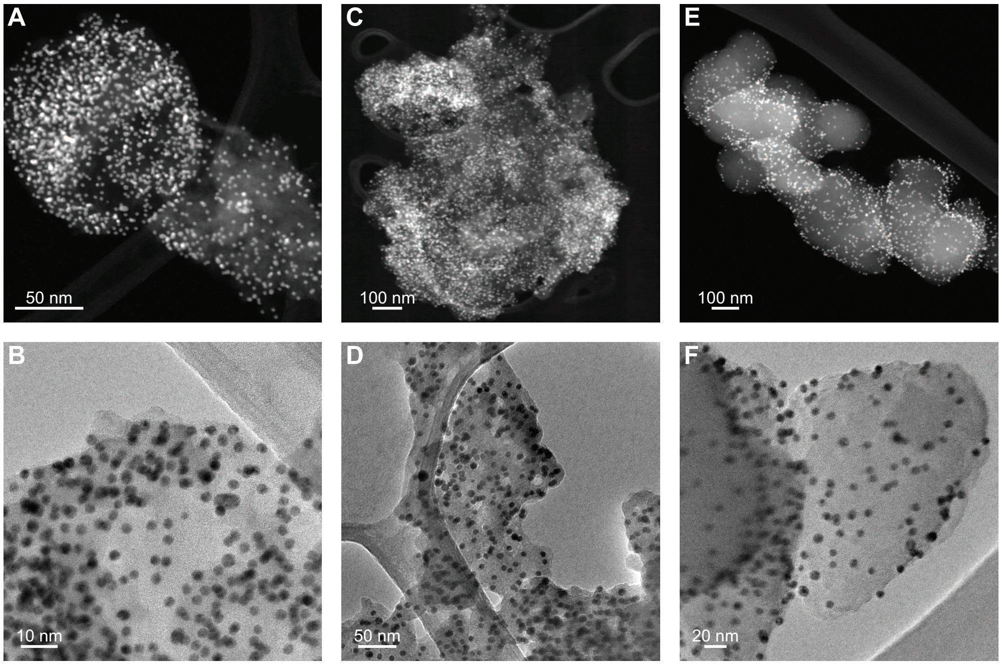

Figure 5.8: Electron microscopy of AuNP-GNR composites. (A) HAADF-STEM and (B) TEM images of **5**-AuNP composite after annealing. (C) HAADF-STEM and (D) TEM images of **8**-AuNP composite after annealing. (E) HAADF-STEM and (F) TEM images of **7**-AuNP composite after annealing.

Composite	BET surface area (m^2g^{-1})	ECSA cm^2/mg AuNP
5-AuNP	19.8	2.87
8-AuNP	5.9	4.60
7-AuNP	12.6	4.4
C_{black}-AuNP	26.8	1.70

Table 5.2: BET surface area (as measured by N_2 adsorption at 77 K) and electrochemically active AuNP surface area (as measured by lead underpotential deposition) for each GNR-AuNP composite.

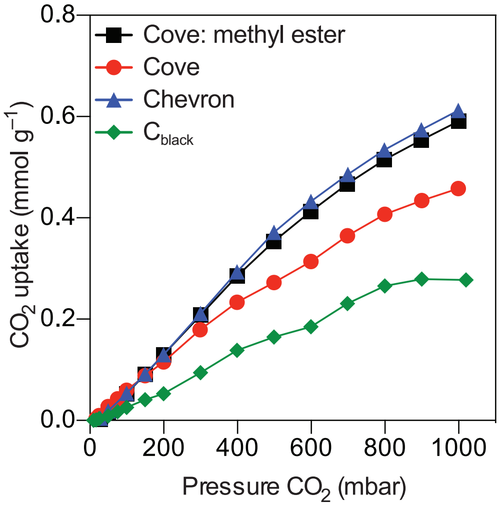

Figure 5.9: 298 K CO_2 adsorption experiment for GNR- and C_{black}-AuNP composites. Despite having lower BET surface areas, GNR composites uptake more CO_2 than the comparable C_{black} composite, reflecting their greater microporosity.

corresponding to lead deposition on the Au(111) and Au(110) faces, respectively. Integration of the peaks in comparison to a Au foil standard provides a quantitative measure of the accessible surface area of the AuNPs. Electrodes fabricated from GNR-AuNP composites have greater ECSA values (2.87 and 4.60 cm^2/mg AuNP for **5**- and **8**-AuNP composites, respectively) than the corresponding C_{black}-AuNP reference (1.70 cm^2/mg AuNP) at the same nanoparticle loading. ECSA is a direct quantitative measure for the ability of a support material to disperse and immobilize nanoparticles without obstructing the transport of reactants and products to and from the nanoparticle surface.[35,37,211,212] The significantly higher ECSA measured for GNR-AuNP composites indicates that GNRs, and in particular GNR **8**, facilitate the dispersion of AuNPs and do not obstruct access to the catalytically active metal surface.

Across these modes of characterization, AuNP composites prepared from the ester-modified **7** strongly resembled those of **8**. In addition to their identical appearance by STEM and TEM (Figure 5.8E&F), **7**-AuNP composites displayed a similar low surface area (12.6 m^2 g^{-1}) and CO_2 uptake behavior at 298 K (Figure 5.9 and Table 5.2). The ECSA of **7**-AuNP as measured by Pb-UPD (4.4 cm^2/mg AuNP) was very similar to that of the parent **8**-AuNP composite (Figure 5.10). These results are consistent with **7** forming very structurally similar AuNP composites to those of **8**, suggesting that any observed differences in their electrochemical behavior can be attributed directly to the presence of methyl esters in the catalytic environment, rather than to any major structural difference between the composites.

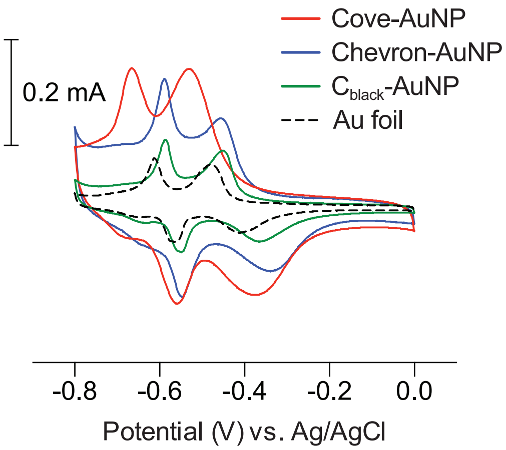

Figure 5.10: Lead underpotential deposition experiments to determine the AuNP electrochemically active surface area (ECSA) of AuNP composite electrodes. Pb-UPD experiments for **5**-AuNP composite electrodes (blue), **8**-AuNP composite electrodes (red), and **7**-AuNP composite electrodes (black) indicate much higher ECSA for the GNR composites than for C_{black}-AuNP composite electrodes (green). The active surface area was determined by comparison to a reference Au foil electrode (black).

5.5 Electrochemical Performance and Discussion

As revealed preliminarily by linear sweep voltammetry, GNRs exert a strong influence over the electrocatalytic behavior of intercalated AuNPs. This was explored more fully for the three selected GNR composites (those with GNRs **5**, **8** and **7**), beginning with cyclic voltammetry (CV) experiments reaching to more strongly reducing potentials than those explored initially by LSV (Figure 5.11A). As Figure 5.11A and Table5.3 together make clear, the suite of GNRs exert two separate effects on AuNP CO_2 reduction electrocatalysis: one dictating onset potentials and another influencing post-onset rates, which merit separate discussion.

When compared to the C_{black}-AuNP reference, GNR composites exhibit a catalytic onset (defined here as the potential at which current density exceeds 0.5 mA cm^{-2}) at significantly positively shifted potentials (−0.14 V vs RHE for both **8** and **7** composites, −0.36 V for **5**-AuNP, and −0.54 V for C_{black}-AuNP, Table 5.3), indicating that interaction with the GNR support significantly lowers the required overpotential for CO_2 reduction on AuNPs. This shift in catalytic onset is consistent with the formation of a Mott-Schottky heterojunction at the GNR-AuNP interface.[53,65,213–215] As discussed in Chapter 1, lower work function materials promote charge migration across the semiconductor-NP interface toward the high work function AuNPs, increasing electron density at the metal surface and shifting the catalytic onset.[13,35,45,48,193,194,216–219] The observed dependence upon GNR edge type is significant because backbone structure is the primary determinant of electronic band structure and position in GNRs. Theory and experiment indicate that, while functional groups or heteroatoms substituted at edge positions exert minimal influence on overall GNR band

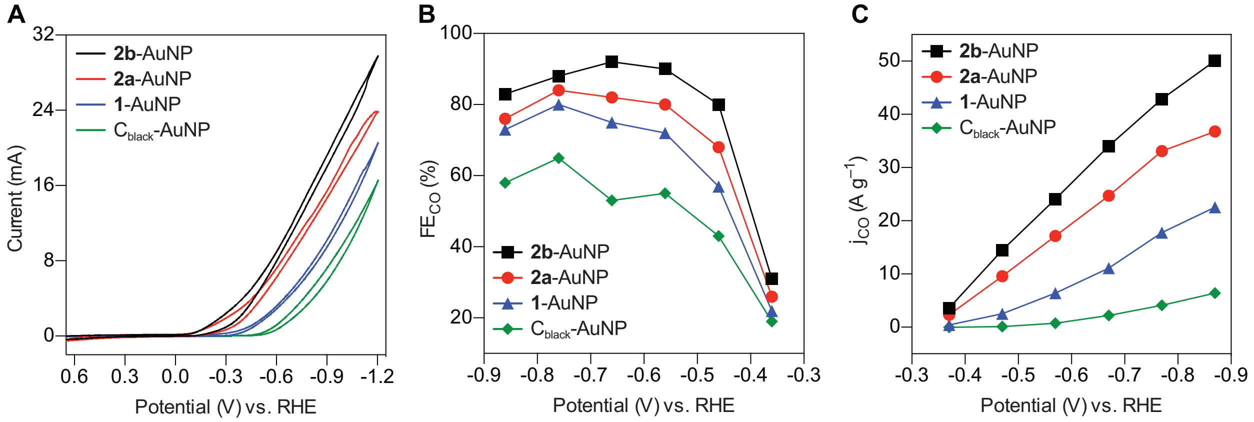

Figure 5.11: (A) Cyclic voltammograms of **5**-AuNP (blue), **8**-AuNP (red), and **7**-AuNP (black) composite materials in 0.5 M aqueous $KHCO_3$ saturated with CO_2 (pH 7.3). The performance of Cblack-AuNP (green) serves as a standard reference. (B) Faradaic efficiencies for CO production (FE_{CO}) by **5**-AuNP (blue triangles), **8**-AuNP (red circles), **7**-AuNP (black squares), and C_{black}-AuNP (green diamonds) composite electrodes. Electrolysis performed for 1 h at potentials from -0.37 to -0.87 V vs RHE in 0.5 M aqueous $KHCO_3$ saturated with CO_2 (pH 7.3). (F) Partial current for CO production (j_{CO}) by **5**-AuNP (blue triangles), **8**-AuNP (red circles), **7**-AuNP (black squares), and C_{black}-AuNP (green diamonds) composite electrodes. Electrolysis performed for 1 h at regular potentials from -0.37 to -0.87 V vs RHE in 0.5 M aqueous $KHCO_3$ saturated with CO_2 (pH 7.3).

structure, cove- and chevron-type GNRs exhibit differing valence and conduction band positions. Furthermore, the semiconducting GNRs employed here, and particularly cove-type GNRs, feature appreciably lower work functions than other carbon supports like graphene or C_{black}, promoting charge migration at the interface consistent with the positively shifted onset potentials observed (Table 5.3).[30,44,115,128,218,220–223]

One hour controlled-potential electrolysis experiments over a potential range from -0.87 to -0.37 V underline the synergy between AuNPs and GNRs; both Faradaic efficiency (FE_{CO}, Figure 5.11B) and partial current (j_{CO}, Figure 5.11C) for CO_2 reduction to CO by GNR-AuNP composites dramatically exceed those of C_{black}-AuNP across a broad potential window. Selectivity in particular was starkly improved for GNR composites, with increased j_{CO} leading to FE_{CO} values exceeding 80% for composites with **8** and exceeding 90% for composites with **7**, despite their AuNPs being identical to those producing 53% FE_{CO} as C_{black} composites at the same potential. The performance of the unfunctionalized cove and chevron composites is consistent with their larger ECSA and positively-shifted CO_2 reduction onset potential; notably, their ECSA-normalized activities (mA cm^{-2}, Table 5.3) at potentials distant from their catalytic onset are quite similar, suggesting their AuNPs behave similarly to each other in this regime. This is not true of AuNP composites with GNR **7**, which exhibit significantly higher FE_{CO} and j_{CO} at all potentials despite exhibiting

Electrode	AuNP ECSA[a] (cm^2 mg^{-1})	onset potential[b] (V vs RHE)	CO_2 reduction activity[c] j_{CO} (A g^{-1})	ECSA-normalized CO_2 reduction activity[c] j_{CO} (mA cm^{-2})
C_{black}-AuNP	1.70	-0.54	6.4	3.76
5-AuNP	2.87	-0.36	22.6	7.87
8-AuNP	4.60	-0.14	36.8	8.00
7-AuNP	4.4	-0.14	50.1	11.4

Table 5.3: Activities and onset potentials for select GNR-AuNP composites. [a]Measured by lead underpotential deposition. [b]Potential at which total CV activity exceeded 0.5 mA cm^{-2}, measured in 0.5 M aqueous $KHCO_3$ saturated with CO_2 (pH 7.3). [c]Partial current for CO production over 1 h at -0.87 V vs RHE, measured in 0.5 M aqueous $KHCO_3$ saturated with CO_2 (pH 7.3).

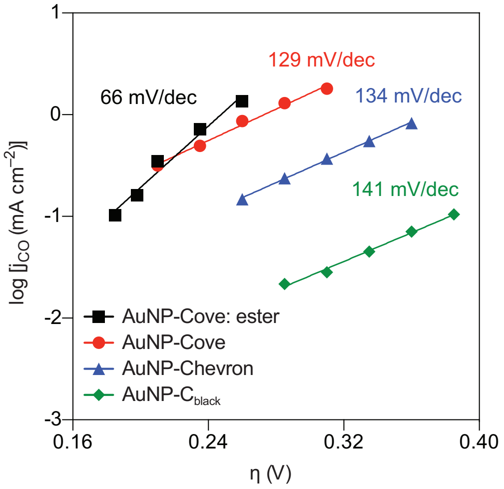

Figure 5.12: Tafel study of CO_2 reduction by GNR- and C_{black}-AuNP composite materials. A Tafel analysis shows the CO_2 reduction behavior of AuNP composites with **5** (blue triangles) and **8** (red circles). Tafel slopes are comparable to that of the C_{black} (green diamonds) composite, indicating no shift in the mechanism of CO_2 reduction for those materials. For the **7**-AuNP composite (black squares), however, the Tafel slope is markedly different, indicating that the catalytic environment created by the support material changed the mechanism of CO_2 reduction at the AuNP surface.

both ECSA and onset potential nearly identical to those of the **8**-AuNP composite. In the case of this ester-functionalized composite, clearly an additional activity-boosting effect is at work.

To better understand the source of the marked increase in performance exhibited by **7**-AuNP composites, the kinetics of CO_2 reduction for each composite were studied using Tafel analysis. Figure 5.12 shows that the functionalization of cove GNRs with methyl car-

Electrode	Total Charge (C)	Vol. CO (mL)	FE$_{CO}$ (%)	Vol. H_2 (mL)	FE$_{H_2}$
5-AuNP	4.6	0.33	57.3	0.29	49.2
8-AuNP	13.4	1.16	68.1	0.58	34.1
7-AuNP	15.6	1.54	78.2	0.50	25.2
C_{black}-AuNP	0.66	0.04	42.9	0.05	60.7

Table 5.4: Results of 1 h controlled potential electrolysis experiments at −0.47 V make it clear that GNRs do not supress H_2 production, but rather achieve high FE$_{CO}$ by disproportionately accelerating CO_2 reduction. NB: The TCD channel of the GC has a high detection limit for H_2 and the internal standard C_2H_4, leading to some uncertainty in the quantification of H_2. As a result, the Faradaic efficiency for H_2 and the overall Faradaic efficiency have an error of up to 10%. However, the CO quantification by GC (FID) is accurate, and therefore so are the corresponding Faradaic efficiencies.

boxylates alters the mechanistic pathway for CO_2 reduction at the Au nanoparticle surface. A Tafel slope of 141 mV/decade for C_{black}-AuNP is consistent with the expected value for a rate-limiting single-electron transfer to adsorbed CO_2 to generate the radical anion.[189,224,225] This observation and proposed mechanism conform with previous studies of aqueous CO_2 reduction by AuNPs.[189,196] Composites made from both GNRs **5** and **8**, although delivering greater overall current, exhibit similar Tafel slopes to that of the C_{black} composite, indicating that the mechanism for CO_2 reduction is unchanged for these materials. In contrast, the Tafel slope for the composite made with GNR **7** is only 66 mV/decade, suggesting a change in the rate-limiting step, and thus a significant change in the overall electrocatalytic mechanism. The Tafel slope observed for the ester-functionalized GNR-AuNP composite is consistent with a pre-equilibrating one electron transfer followed by a rate-limiting chemical step.[188,224,225] These data suggest that an interaction between the reactant and the introduced methyl carboxylates stabilizes the transition state of the erstwhile rate-limiting electron-transfer step, thereby changing the mechanism and leading to the increased activity observed for this composite. This experiment serves as primary evidence that nanoparticle electrocatalysis is responsive to the immediate catalytic environment created by the support material, and supports the assertion that the chemical tunability of a bottom-up synthesized support material can greatly improve catalytic performance.

In evaluating the interaction between GNRs and catalytic AuNPs, the origin of the observed improved selectivity (FE$_{CO}$) merits closer investigation. As Table 5.4 makes clear, GNR-AuNP composites do not suppress hydrogen evolution; rather, all three GNR composites catalyzed hydrogen evolution at a higher rate than the C_{black} composite, producing as much as twelve times the total hydrogen over 1 h at the tested potential (-0.47 V). The improved FE$_{CO}$, therefore, reflects interaction with GNRs disproportionately accelerating CO_2 reduction by AuNPs. This is especially true of the **7** composite, which produced nearly 40 times more CO than the C_{black} reference composite, and more than 30% more than the unfunctionalized **8** composite, leading to the increased FE$_{CO}$.

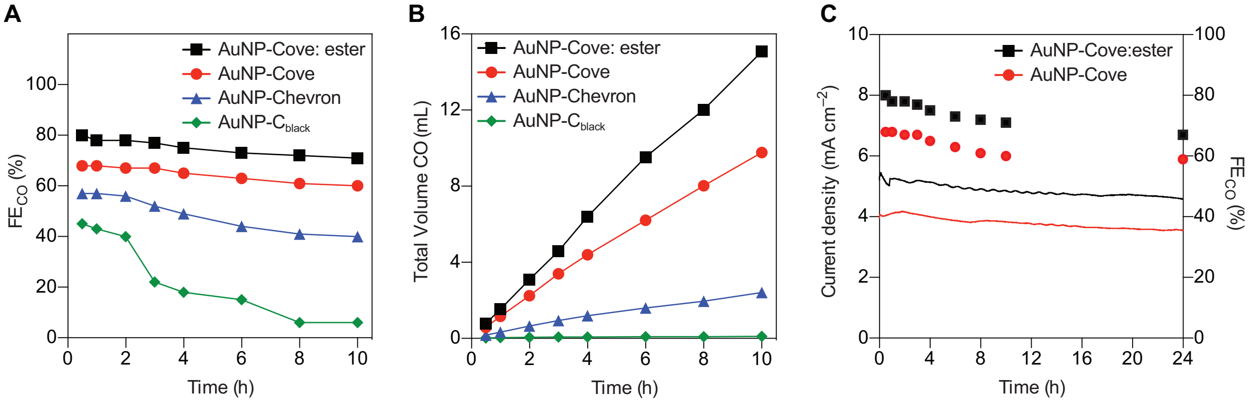

Figure 5.13: (A) Faradaic efficiencies for CO production (FE$_{C}O$) by **5**-AuNP (blue triangles), **8**-AuNP (red circles), **7**-AuNP (black squares), and C$_{black}$-AuNP (green diamonds) composite electrodes. Electrolysis performed at −0.47 V vs RHE in 0.5 M aqueous KHCO$_3$ saturated with CO$_2$ (pH 7.3). (B) Total volume (at STP) of CO produced by **5**-AuNP (blue triangles), **8**-AuNP (red circles), **7**-AuNP (black squares), and C$_{black}$-AuNP (green diamonds) composite electrodes. Electrolysis performed at −0.47 V vs RHE in 0.5 M aqueous KHCO$_3$ saturated with CO$_2$ (pH 7.3). (C) Total current density for **8**-AuNP (red line) and **7**-AuNP (black line) over 24 h. Faradaic efficiency for CO production with **8**-AuNP (red circles) and **7**-AuNP (black squares) over 24 h. Both current density and Faradaic efficiency show little change between 10 and 24 h of fixed potential electrolysis at -0.47 V vs RHE.

Stability of the composite during catalysis is key to a successful support material. Fixed potential bulk electrolysis experiments were therefore undertaken to evaluate the ability of GNRs to stabilize AuNPs over extended reaction times (Figure 5.13, full tabular results in Supporting Information Tables 10.1–10.4, page 149). AuNPs supported by C$_{black}$ degrade rapidly, delivering only 22% FE$_{CO}$ after 3 h. Electrodes instead fabricated from GNR-AuNP composites maintain superior performance for more than 10 h of continuous electrolysis. At -0.47 V, **8**-GNR composites retained 88% of their original FE$_{CO}$ after 10 h of catalysis, and produced more than 33 mL CO/mg of AuNP, compared with only 0.4 mL CO/mg AuNP for the C$_{black}$ composite electrodes prepared from the same AuNPs (Figure 5.13A&B). Longer controlled-potential experiments indicated that the **8**-AuNP composite in particular achieves a plateau of stability; with over 24 h of uninterrupted catalysis at -0.47 V, the composite delivered 87% of its original FE$_{CO}$, nearly unchanged from the 10 h experiment (Figure 5.13C). The improved performance of **7**-AuNP composites is retained throughout long-term experiments, exhibiting similar overall stability performance to its parent **8**-AuNP composite. Across a 10 h experiment at -0.47 V, **7**-AuNP electrodes deliver an overall FE$_{CO}$ of 71%, retaining 91% of the FE$_{CO}$ performance (78%) exhibited in the first hour at that potential. A 24 h experiment at the same potential delivered an overall FE$_{CO}$ of 67% (86% of the FE$_{CO}$ recorded for the first hour), with the composites characteristic increased activity remaining nearly constant for the duration. Over the course of 10 h, the ester-functionalized

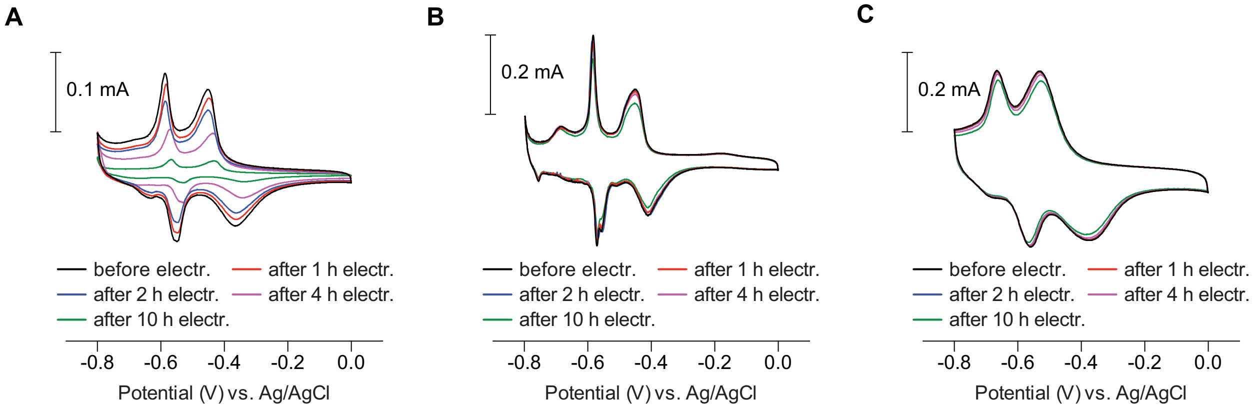

Figure 5.14: Cyclic voltammograms for lead underpotential deposition experiments on AuNP composite electrodes following extended controlled-potential electrolysis at -0.47 V vs RHE, to measure the change in AuNP ECSA. Cyclic voltammetry was performed in 0.1 M aqueous KOH containing 1 mM $Pb(OAc)_2$ and purged with Ar. (A) C_{black}-AuNP composite electrodes exhibit a significant decline in ECSA following fixed potential electrolysis experiments. (B) **5**-AuNP composites and (C) **8**-AuNP composites retain almost all of their ECSA following fixed potential electrolysis experiments.

composite produced more than 50 mL of CO/mg AuNP, representing a 137-fold increase in total catalytic output over the same nanoparticles embedded in a C_{black} matrix. The overall efficiency performance of the **7**-AuNP composite after 10 h of electrocatalysis is comparable to the first hour of composite **8**, and exceeds the initial performance of any other material tested.

To interrogate the origin of nanoparticle stabilization in GNR-AuNP composites, Pb-UPD experiments at selected time points during bulk electrolysis were used reveal any change in the ECSA of the catalytic AuNPs. During electrolysis using C_{black}-AuNP composites (-0.47 V), a significant reduction in active Au surface area can be observed within hours, that correlating with the loss of catalytic activity (Figure 5.14A). After 4 h of catalysis, only 48% of the original Au surface area remains, and only 15% is retained after 10 h. TEM images of C_{black}-AuNP composites recorded following 3 h of bulk electrolysis suggest that a plausible mechanism of deactivation relies on the coalescence of AuNPs to form larger aggregates with significantly reduced active surface area (Figure 5.15).[7] In contrast, **5**-AuNP (Figure 5.14B) and **8**-AuNP (Figure 5.14C) composites effectively prevent NP coalescence and the associated reduction in ECSA. **8**-AuNP composites in particular lose only 4% of their active Au surface area over 4 h of catalysis, and merely 10% over 10 h. This suggests that the effective immobilization of the NPs through strong dispersion interactions with the matrix of narrow, flexible GNRs effectively precludes NP mobility and prevents coalescence into larger structures. This strong interaction would be enhanced by the charge-transferring Mott-Schottky interactions discussed above, consistent with the improved stability observed for cove-type GNRs **8** and **7** in comparison to the chevron-type GNR **5**.

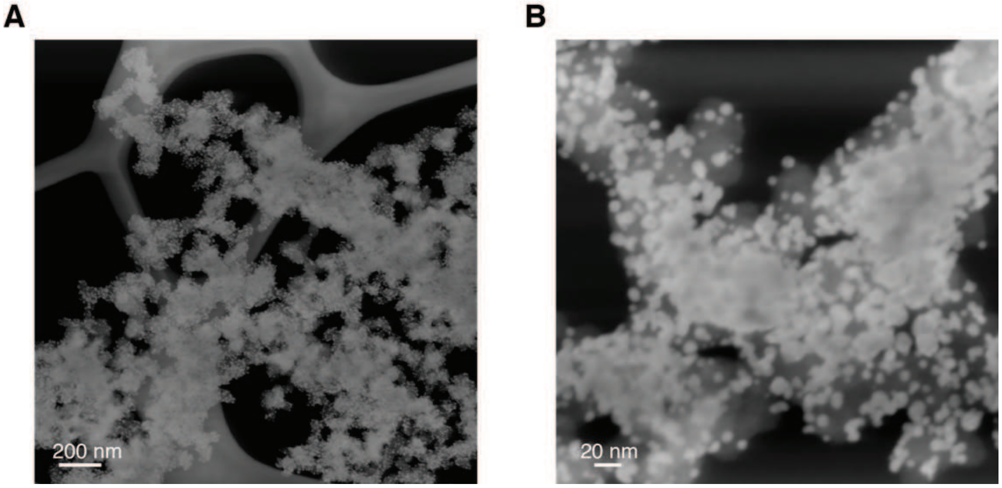

Figure 5.15: (A) HAADF-STEM image of C_{black}-AuNP composites after annealing but before electrocatalysis show a narrow size distribution centered around an average NP diameter of 8 nm. (B) HAADF-STEM image of C_{black}-AuNP composites after 3 h of bulk electrocatalysts in 0.5 M aqueous $KHCO_3$ saturated with CO_2 (pH 7.3) show large AuNP aggregates with significant broadening of the AuNP size distribution as a result of nanoparticle sintering.

5.6 Conclusion

Through the greatly enhanced CO_2 reduction performance of electrocatalytic AuNPs, this chapter has demonstrated that narrow, bottom-up synthesized GNRs excel as functional catalyst support materials. The catalytic environment created by the GNR-NP interaction led to reduced onset potential and high activity, with excellent nanoparticle dispersion reflected in a greatly increased ECSA. Electrocatalytic stability was markedly improved for GNR composites, yielding consistent catalytic performance and stable ECSA over periods as long as 24 h. Furthermore, the bottom-up synthetic approach to these materials imparts an unrivaled ability to precisely tune the catalytic environment, demonstrated by the marked increase in performance and change in mechanism following the synthetic functionalization of a GNR support. These results establish for the first time the utility of precise, synthetically derived support nanomaterials for both studying and optimizing processes occurring at nanomaterial interfaces, a theme that will be extended to a diverse set of systems in the subsequent chapters.

Chapter 6

GNR-CuNP Composites for CO Reduction Electrocatalysis

Having demonstrated the successful application of GNRs as support materials in CO_2 reduction electrocatalysis (Chapter 5), the next step was the extension of this work to the study of copper nanoparticles (CuNPs). Compared to AuNP electrocatalysts, CuNPs are clearly a more challenging system, featuring a host of possible reduction products, increased hydrogen evolution activity, and metal surfaces that readily oxidize in air. However, CuNP electrocatalysis ultimately offers greater potential towards application, since it can further reduce CO and thereby directly yield higher-value products. CO reduction by Cu surfaces is a comparatively underexplored field, but recent results have rekindled interest in the reaction and demonstrated its sensitivity to surface modification, making it an appealing system for investigation with GNR composites.

In this chapter, GNR composites with various CuNPs are prepared and examined for their CO reduction ability. Although attractive preliminary results prompted aggressive investigation of this system, inconsistency and irreproducibility have thus far precluded the formation of any firm conclusions. Additionally, the removal of insulating ligands has proven to be a significant impediment to the formation of GNR-CuNP composites with sufficient electronic contact between the two species. This research is ongoing, with continued investigation focusing both on the synthesis of ligand-free CuNPs *in situ* with GNRs and on systems with ligands expected to be more labile.

Electrochemical studies described in this chapter were performed by Yifan Li in the group of Professor Peidong Yang. CuNP nanocubes (Section 6.6) were provided by the Yang group; other nanoparticles were synthesized by the author.

6.1 Introduction to CO Reduction

Although CO reduction electrocatalysis by copper electrodes has been reported for decades, the field has received far less attention than has been paid to CO_2 reduction catalysis, and has largely been pursued as a means by which to indirectly study CO_2 reduction systems.[226–229] This is primarily because of large challenges facing CO reduction electrocatalysis; most notably, the reaction required very high overpotentials and was out-competed by rapid proton reduction. If these issues could be overcome, however, CO reduction electrocatalysis represents an interesting technology for two primary reasons. Firstly, because CO is accessible as a common product of CO_2 reduction by a host of catalytic methods, CO reduction electrocatalysis represents an appealing complementary technology for further reduction to value-added products in an energy-efficient fashion, potentially surpassing the overall energy-intensive Fischer-Tropsch process. Additionally, CO reduction under well-chosen conditions displays high selectivity for C_2 reduction products over less desirable one-carbon products, stemming from a mechanism in which the rate-determining electrochemical reduction is coupled to C-C bond formation.[229,230]

A major breakthrough towards viability for CO reduction electrocatalysis came in 2014, when Kanan and coworkers reported capable CO reduction performance from a Cu film prepared by reduction of Cu_2O (oxide-derived Cu, OD-Cu).[231] The resulting boundary-rich nanocrystalline material catalyzed CO reduction at greatly reduced overpotentials, leading to greatly reduced hydrogen evolution and good selectivity for value added products, and prompting renewed investigation into CO reduction on Cu as a viable technology.[5,230,232,233] Although suppressing hydrogen evolution, boosting CO reduction activity, and controlling product distribution are all continuing challenges, this work has established CO reduction as a topic of interest in its own right. Additionally, recent studies have demonstrated that CO reduction at Cu surfaces is sensitive to interface modification and substrate effects, introducing an alternative approach for enhancing CO reduction performance and suggesting that interaction with a well-chosen support material could serve to positively influence CO reduction by CuNPs.[234]

6.2 Preliminary CO Reduction Results: C4 Products

GNRs used in this chapter were synthesized as described in Chapter 4. A batch of small CuNPs was prepared by a reported procedure involving the reduction of $Cu(acac)_2$ in the presence of oleylamine and oleic acid.[235] These CuNPs were a black powder and blue-green in suspension, and readily formed GNR composites by sonication with GNRs (1:1 mass ratio with either chevron-type GNR **5** or cove-type GNR **8**) in hexane or chloroform. As with the electrodes prepared in Chapter 5, the sonicated composite was dropcast onto conductive carbon paper and annealed in air at 185 °C for 10 h, and reference composites were made in the same fashion using carbon black. Electrocatalysis was performed in 0.1 M aqueous KOH (pH 13) saturated with CO by bubbling 20 min; gaseous products were quantified by

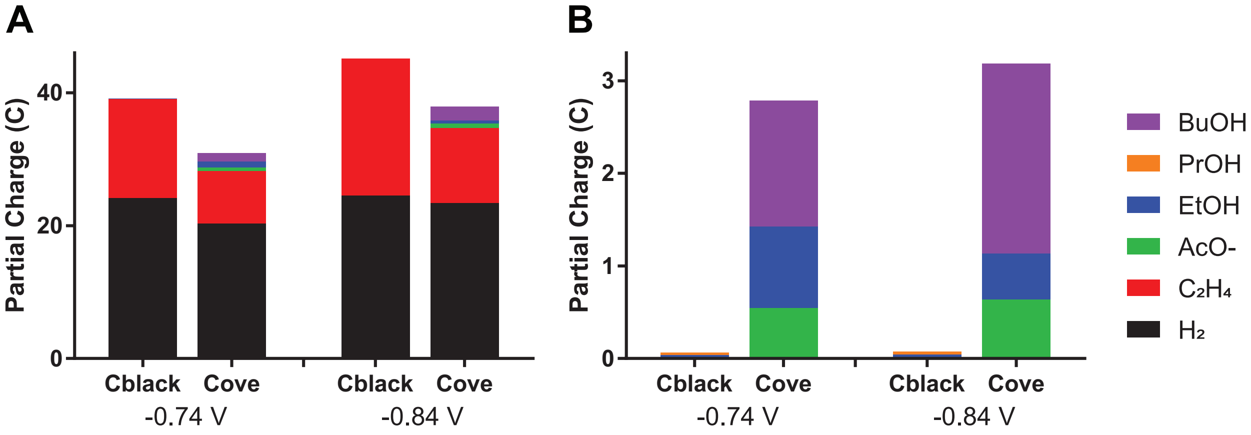

Figure 6.1: Comparison of composite materials prepared using identical CuNPs and either C_{black} or GNR **8** support material. Partial charge for (A) every observed product and (B) all liquid products for 1 h fixed potential electrolysis experiments performed in 0.1 M aqueous KOH saturated with CO (pH 13).

GC and liquid products by ^{1}H NMR.

The electrochemical performance of these initial CuNP-GNR composites was striking. When compared to the C_{black} reference composites, which produced predominantly H_2 and C_2H_4 at the tested potentials, the GNR composites yielded comparable hydrogen evolution and reduced ethylene production but drastically increased liquid product formation (Figure 6.1). As with all reported Cu electrocatalysts for CO reduction, observed liquid products for the reference C_{black} composite were acetate, EtOH, and *n*PrOH, but each was produced with <0.1% FE, indicating that the CuNPs used are inherently poor CO reduction catalysts. In contrast, GNR composites using the same CuNPs exhibit comparatively rapid production of acetate and ethanol, together with remarkably robust production of the unprecedented four-carbon CO reduction product 1-butanol (Figure 6.2). This is accompanied by the total shutdown of propanol production for the GNR composites, indicating that interaction with the GNR initiates a significant shift in accessible CO reduction pathways at the CuNP surface. The observed substrate-dependent shift in product formation is a striking demonstration of the power interfacial interactions can exert on nanoparticle catalysis (Figure 6.3).

However, experiments performed with these materials were always characterized by significant variability between electrodes. The difficulty in assigning any clear trends between potentials or between materials was exacerbated by sizable inconsistencies even for nominally identical electrodes tested under the same conditions. Figure 6.4 illustrates this by plotting divergent results for three identically prepared **8**-CuNP electrodes tested at identical potentials; one electrode produced no liquid products at all, while two others produced liquid products in very different ratios. Notable amidst the variability, no GNR composite (using either **8** or **5**) ever produced observable propanol, and every GNR composite to produce liquid products included significant butanol. Speculatively, this inconsistency may

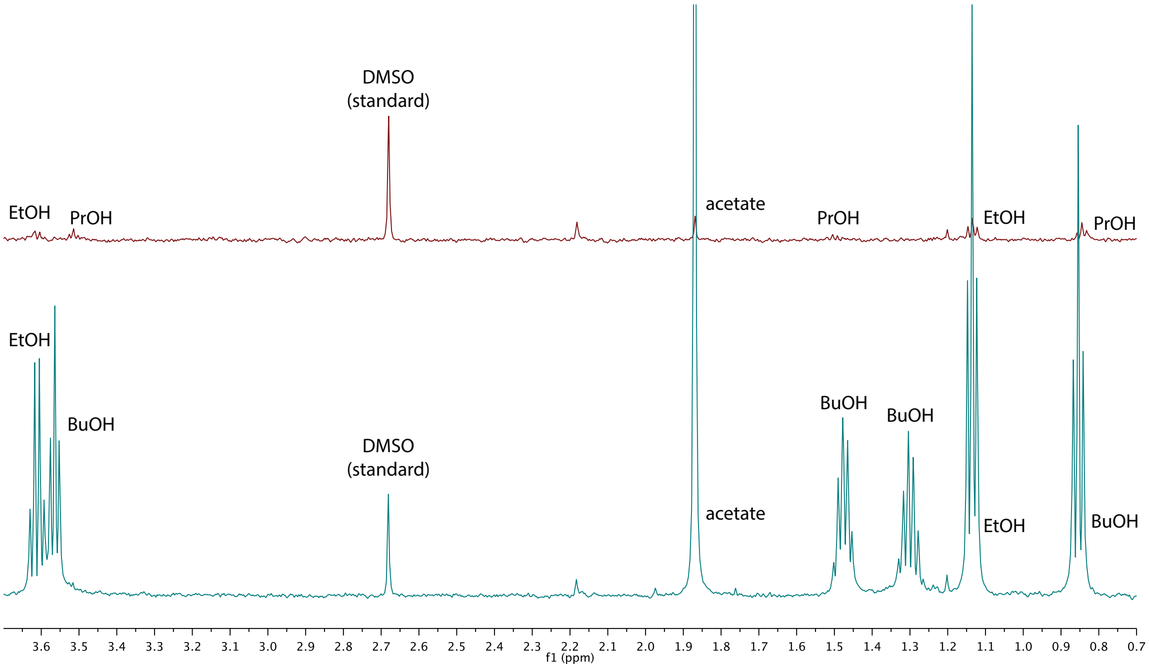

Figure 6.2: ^{1}H-NMR characterization of liquid products of 1 h CuNP composite CO reduction electrocatalysis at -0.74 V vs RHE; experiments performed in 0.1 M aqueous KOH saturated with CO (pH 13). The DMSO concentration in each sample is 0.028 μmol mL^{-1}.

stem from the long thermal treatment in air of an oxidation-prone material. Although the CuNP surface is certainly oxidized upon exposure to air, and re-reduced under reductive electrocatalysis conditions, extensive oxidation during the annealing step may lead to structural inconsistencies upon re-reduction. Alternatively, inconsistencies may have been present within the batch of CuNPs itself, especially as the CuNPs began to degrade over extended periods of storage in air.

Unfortunately, attempts to reproduce these results with a second set of identically prepared CuNPs were never successful; butanol production was only observed using CuNPs from the original batch. As detailed below, the synthetic method to produce those CuNPs exhibited significant run-to-run inconsistency, with especially divergent behaviors observed for varied temperatures and reagents. This set off an effort to synthesize CuNPs by a variety of methods, including the original method, as a broad attempt to characterize CuNP-GNR interactions, understand their influence on CO reduction electrocatalysis, and reproduce the remarkable results described above.

6.3 Synthesis of CuNPs by Reduction of Cu(acac)$_2$

A great deal of variability was observed between synthetic attempts using the Cu(acac)$_2$-reduction CuNP procedure described above (Figure 6.5). Some attempts, rather than yield-

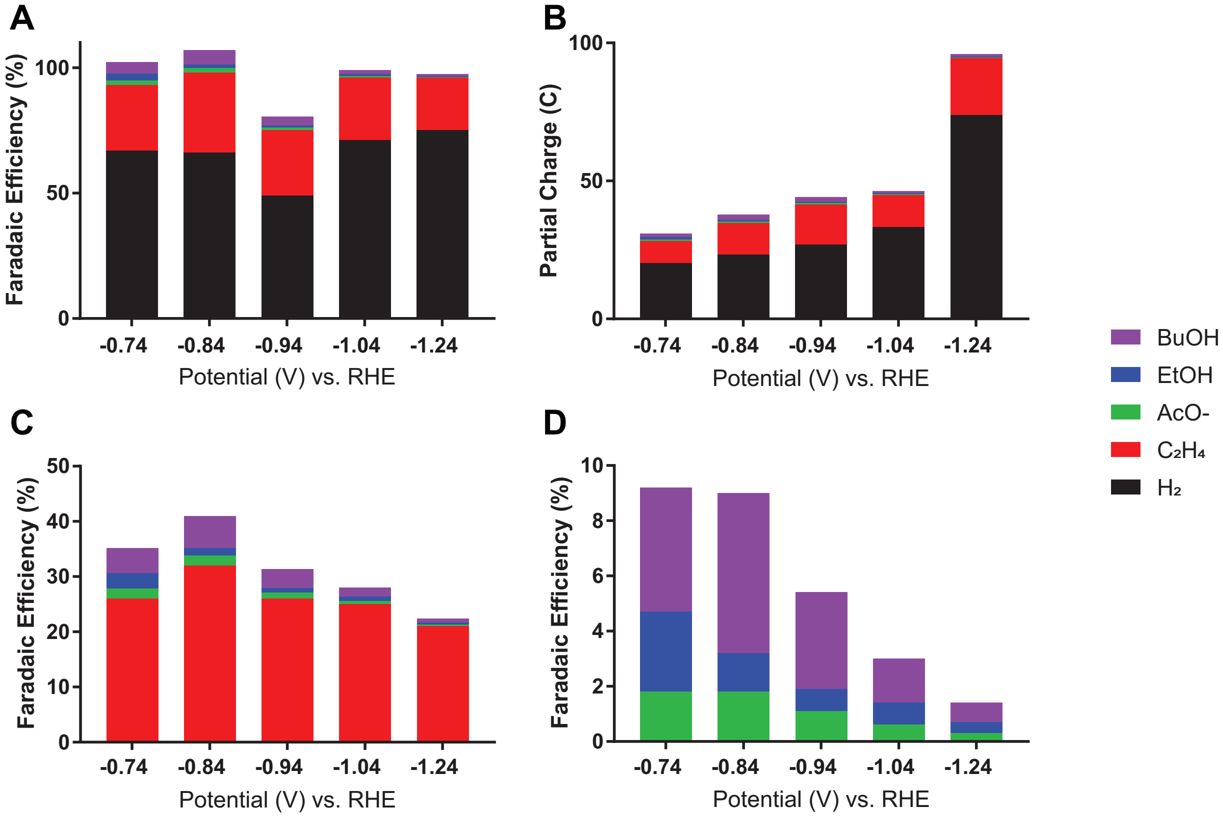

Figure 6.3: Electrocatalytic CO reduction performance of **8**-CuNP composites for 1 h fixed potential electrolysis experiments at varied potentials (-0.74 to -1.24 V vs RHE); experiments performed in 0.1 M aqueous KOH saturated with CO (pH 13). (A) Faradaic efficiency for all products. (B) Partial charge for all products. (C) Faradaic efficiency for all CO reduction products. (D) Faradaic efficiency for all liquid products.

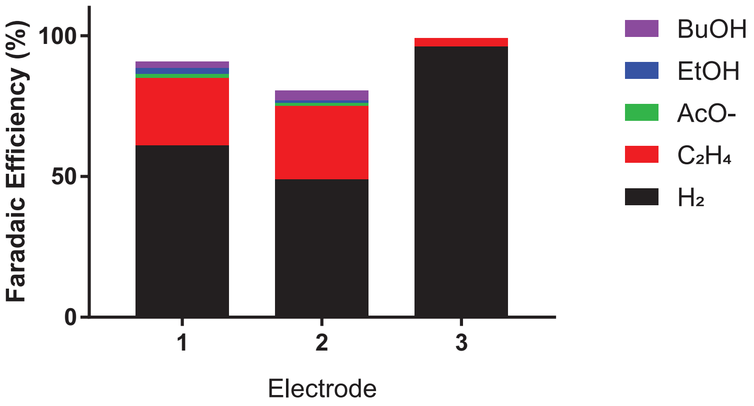

Figure 6.4: Comparison of Faradaic efficiencies for three nominally identical **8**-CuNP electrodes in 1 h fixed potential electrolysis experiments at -0.94 V vs RHE; experiments performed in 0.1 M aqueous KOH saturated with CO (pH 13).

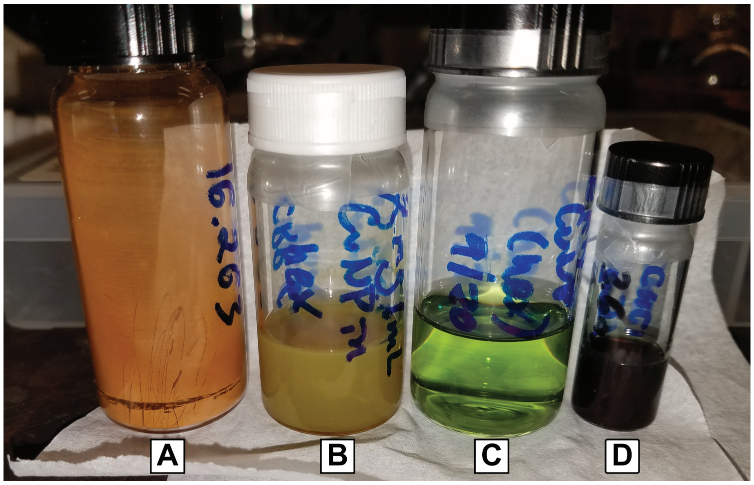

Figure 6.5: Visual demonstration of the diverse products afforded by varied CuNP synthetic procedures. (A) Powder of poorly dispersible large Cu_2O NPs. (B) Mixed production of both Cu and Cu_2O NPs, shown as a dispersion in hexane. (C) CuNPs as a solution in hexane. (D) A concentrated solution of the same CuNPs in hexanes appears blue.

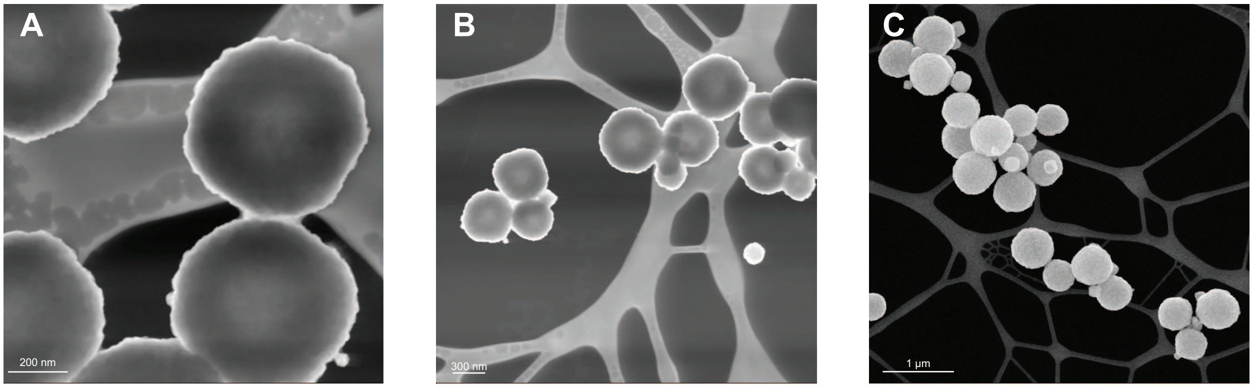

Figure 6.6: (A&B) STEM and (C) SEM images of Cu_2O nanoparticles synthesized by the reduction of $Cu(acac)_2$.

ing a dark material that disperses into a blue-green solution, instead furnished an orange material with very poor dispersibility. SEM of this material found large round structures, with diameters reaching hundreds of nanometers (Figure 6.6, and PXRD confirmed the material was pure Cu_2O (Figure 6.7). It should be noted that this behavior persisted through many attempts featuring very rigorous exclusion of O_2, including those run entirely in a N_2 glovebox. Reassuringly, precedent exists for very similar CuNP synthesis reactions forming Cu_2O NPs under air-free conditions, with precise control of time and temperature evidently crucial for production of the desired CuNPs.[236]

Other synthetic attempts using this procedure yielded CuNPs matching those prepared

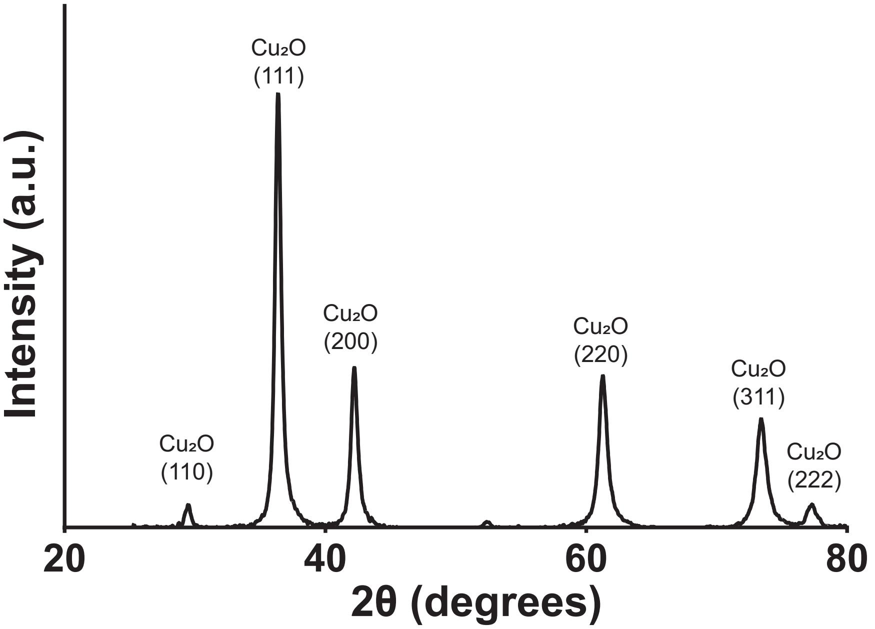

Figure 6.7: PXRD of the poorly dispersible orange powder confirms the material is Cu_2O, rather than the intended Cu nanoparticles

originally. Production of the desired CuNPs (rather than Cu_2O) was found to be dependent upon the use of specific reagent formulations (e.g. 90% technical grade 1,2-hexadecanediol rather than 98%) as described in the Supporting Information (Section 10.3, page 139). Additionally, the desired reactivity was aided by drying the n-octyl ether via filtration through activated alumina in a N_2 glovebox, although the reported procedure makes no mention of any drying. Lastly, prolonging the intermediate temperature step at 105 °C was also observed to drive the reaction towards the desired pathway. Many synthetic attempts were partially successful, yielding a mixture of both Cu_2O- and Cu-nanoparticles, but those employing all the above methods yielded nanoparticle products visibly lacking any orange Cu_2O. These NPs were black as a powder and blue in suspension, appearing identical to the original batch; STEM images of the CuNPs and their GNR composites show small, round CuNPs with mild size variability (Figure 6.8).

However, the CO reduction reactivity of composites made with these NPs did not resemble that of the original batch. Rather, GNR composites with these CuNPs performed in a manner indistinguishable from C_{black} composites, producing significant H_2 and C_2H_4 with minimal liquid products, and no observed butanol. That is to say, these composites behave in the manner expected of CuNPs for CO reduction, but not in line with previous observations for ostensibly identical GNR-CuNP composites. As such, the origin of the previously observed behavior remains unknown, and experiments into recreating that performance are continuing.

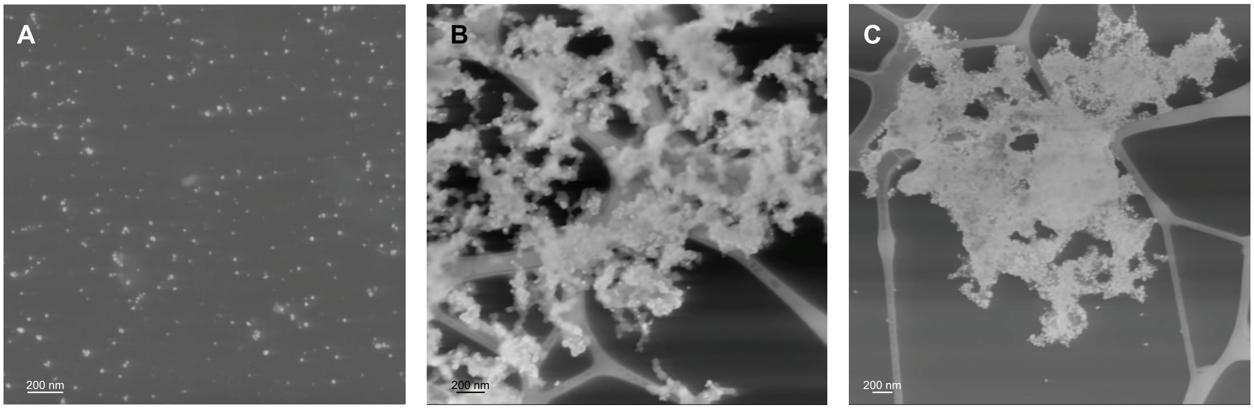

Figure 6.8: STEM images of CuNPs synthesized by the reduction of $Cu(acac)_2$. (A) Unsupported CuNPs. (B) CuNP composite with C_{black}. (C) CuNP composite with GNR **8**.

6.4 Synthesis of CuNPs by Reduction of Cu(OAc)

In addition to the original synthetic method, alternative methods of CuNP synthesis were pursued with the goal of creating and studying a diverse set of GNR-CuNP composites. These included a widely used and comparatively robust reported method relying on the reduction of Cu(OAc) in the presence of tetradecylphosphinic acid, which reliably yielded small and monodisperse CuNPs. (Figure 6.9A) These CuNPs formed stable green solutions in a variety of organic solvents and readily form composites when sonicated with GNR powder (Figure 6.9B&C).

However, these GNR-CuNP composites are very poor catalysts for both CO and CO_2 reduction, exhibiting near-unity Faradaic efficiencies for hydrogen evolution in either case. This behavior is unsurprising because the CuNPs in these composites retain their insulating capping ligands, obstructing the metal surface and precluding catalysis. Unsupported CuNPs are known to lose ligand density under electrocatalysis conditions, leading to appreciable CO_2 reduction activity, and this was observed for electrodes prepared with extra CuNPs such that some remained outside the composite (Figure 6.9D).[237,238] However, GNR-supported CuNPs evidently do not to lose ligands under electrocatalysis conditions, and thus do not participate in CO or CO_2 reduction.

It was therefore apparent that these GNR-CuNP composites could only become competent catalysts following removal of their insulating ligands prior to electrocatalysis. The most common option for NP ligand removal is thermal annealing, either in air, in another gas, under vacuum. Initial attempts at annealing in air found the ligands to be quite robust; 10 h annealing at either 200 or 250 °C was ineffective for ligand removal, as evidenced by the unsupported CuNPs remaining unagglomerated (Figure 6.10A&B). Catalysis with these composites matches that described above for ligand-capped CuNPs. In contrast, even much shorter annealing times at 300 °C under air entirely destroyed both supported and unsupported CuNPs (Figure 6.10C). Interestingly, the composites were observed to behave

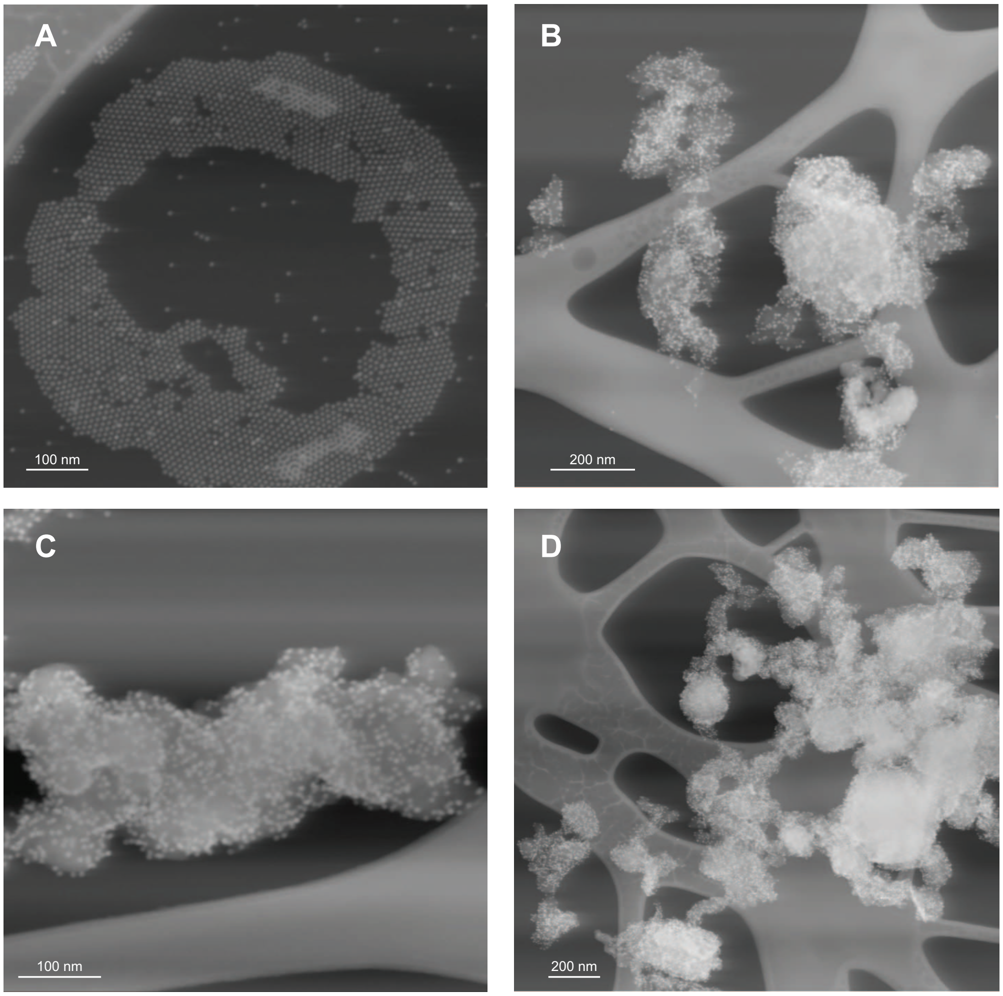

Figure 6.9: STEM images of CuNPs synthesized by the reduction of CuOAc (A) as free NPs and (B–D) as composites with GNR **8**.

differently when annealed under vacuum; a 4 h anneal at 250 °C in vacuum repeatably produced mild agglomeration of CuNPs, suggesting that these conditions could be tuned to remove ligands cleanly. This approach is currently being further refined, and its impact on catalysis is yet to be determined.

Several chemical methods for removing the CuNP ligand sphere were also attempted. These ligand-exchange procedures aim to replace large, organic, insulating nanoparticle ligands with a stabilizing layer of smaller, inorganic species like SCN^- or $BF_4{}^-$.[239–241] Such procedures are very well precedented for a variety of semiconducting metal chalcogenide nanocrystals and are known to succeed for some metal nanoparticles like AuNPs or iron-platinum NPs.[242,243] However, this literature is comparatively thin with regard to ligand-exchange for CuNPs, and preliminary experiments using the phosphonate-capped CuNPs described above were not successful. Treatment of CuNP solutions in hexane under mild

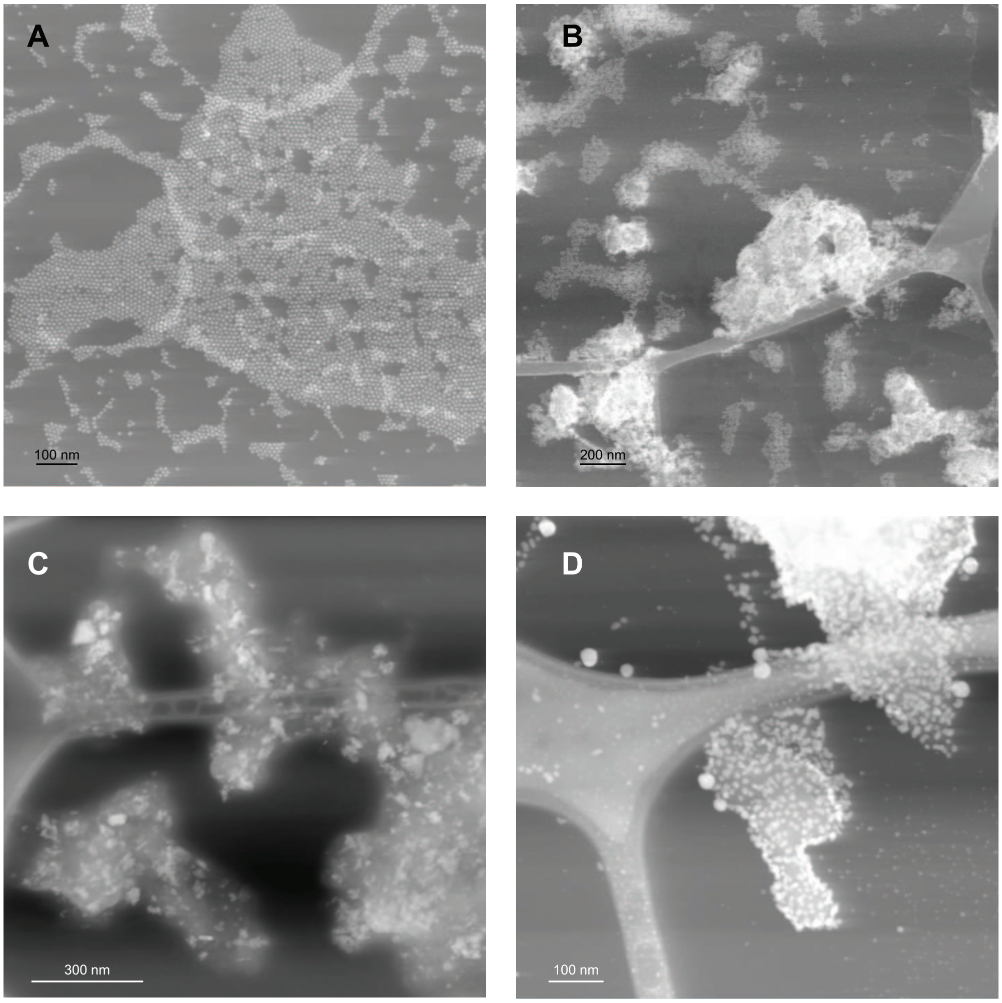

Figure 6.10: STEM images of CuNPs annealed (A) for 10 h at 185 °C in air or (B) for 10 h at 250 °C in air show no signs of ligand removal, as unsupported CuNPs appear unchanged following the anneal. (C) CuNPs annealed for 10 at 300 °C in air appear destroyed. (D) CuNPs annealed for 10 at 250 °C under vacuum exhibit mild agglomeration.

conditions, such as Meerwein's reagent ($Et_3O \cdot BF_4$), $Et_2O \cdot BF_3$, or $Me_3O \cdot BF_4$ in acetonitrile or DMF, gave no reaction; the nanoparticles remained oleophilic, rather than migrating to the polar phase as ligand-exchanged NPs would. In contrast, harsher, more acidic reagents like $NOBF_4$ or NH_4SCN seemed to etch the CuNPs, yielding solutions of salts rather than isolable NPs. As a result, this approach was promptly abandoned in favor of thermal treatments or alternative syntheses.

6.5 Synthesis of CuNPs by Reduction of $CuCl_2$

In light of the challenges posed by insulating capping ligands in GNR-CuNP composites, CuNPs were also prepared by an alternative synthetic method that omits them entirely, forming solvent-stabilized CuNPs by the reduction of $CuCl_2$ with Li metal via biphenyl electron transfer catalyst.[244,245] To prevent aggregation, the resulting CuNPs are dispersed onto a support material before they are dried, creating a composite material. This approach successfully yielded small, monodisperse CuNPs with diameters of roughly 8 nm as a composite with GNR **5** (Figure 6.11A&B). However, the yield of CuNPs was low, seemingly due to incomplete consumption of the Li metal, and many CuNPs remained outside the GNR composite (dispersing instead onto the STEM substrate when dropcast for imaging). To address this, and afford better synthetic control overall, a new procedure was devised employing the slow addition of pre-synthesized lithium naphthalenide to a suspension of $CuCl_2$ and GNR **5** in THF. However, this approach yielded bizarre, misshapen composites lacking obvious distinct CuNPs (Figure 6.11C). If instead the lithium naphthalenide solution is added to a suspension of $CuCl_2$ without GNRs, a black suspension of copious black CuNPs is formed (Figure 6.11D); subsequent addition of **5** after full consumption of the lithium naphthalenide yields the desired GNR-CuNP composite (Figure 6.11E&F). This approach dramatically improved the yield of CuNPs, refinement of this approach is ongoing, and the catalytic capabilities of these composites will be tested.

6.6 Conclusion and Future work

Although recreation of the remarkable CO reduction results observed originally has thus far been unsuccessful, this chapter has described a number of ongoing efforts that promise to shed additional light on GNR-CuNP interactions and their impact for CO and CO_2 reduction electrocatalysis. These include recent work using copper nanocubes (CuNC) synthesized by collaborators, which are synthesized with oleylamine capping ligands much like the original CuNPs that formed capable CO reduction composites with GNRs.[236] Successful removal of the capping ligands from these CuNCs has been confirmed, and an investigation of their CO reduction capabilities is underway. Overall, CuNP composites with GNRs continue to be very interesting materials, and clever methods will be required to unlock the potential that these preliminary results have demonstrated.

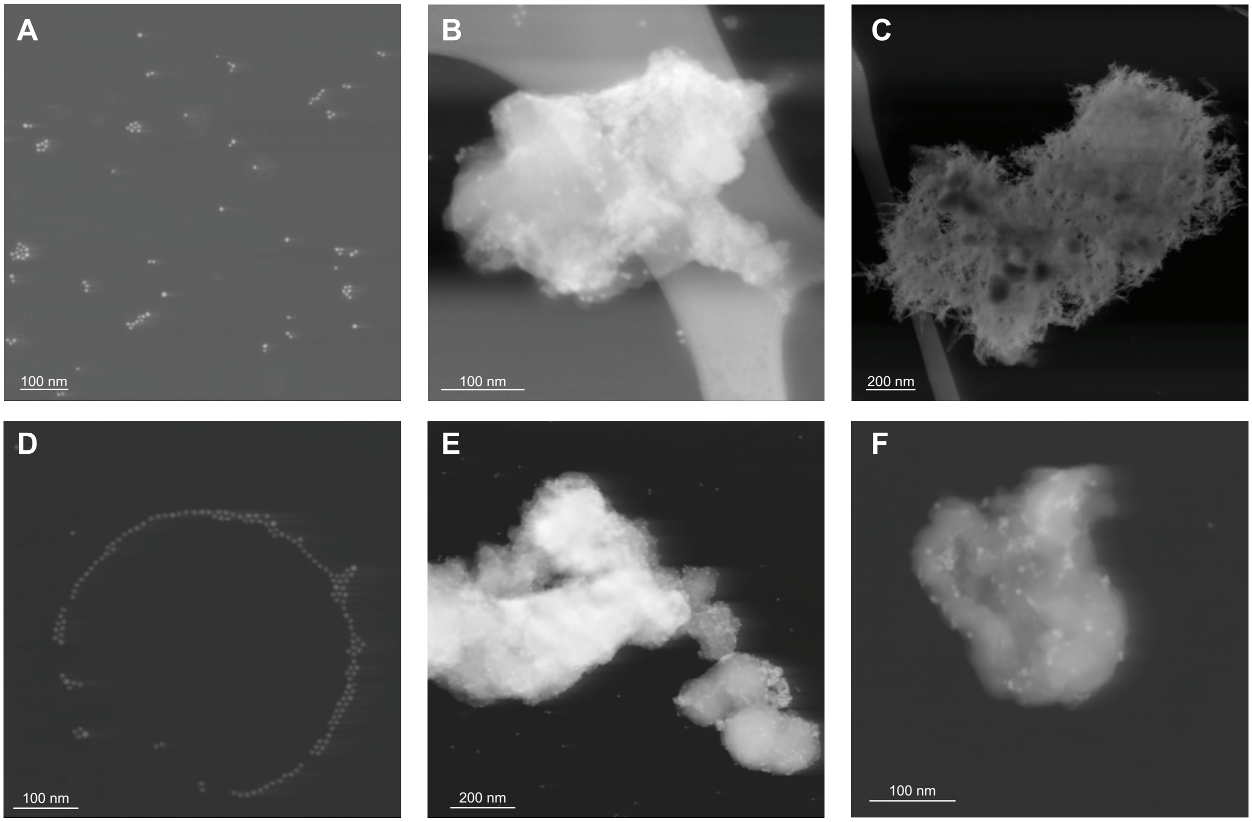

Figure 6.11: STEM images of CuNPs synthesized without insulating ligands by the reduction of $CuCl_2$, and their composites with GNR **5**. (A&B) CuNPs prepared with lithium metal as reducing agent and 4,4'-di-tert-butylbiphenyl as electron transfer catalyst. (C) Failed composite prepared by addition of lithium naphthalenide to a mixture of GNR with copper precursor. (D-F) CuNPs prepared with lithium naphthalenide as reducing agent.

Chapter 7

GNR-SnO_2 Composites for Lithium Ion Battery Anode Materials

Following the successful application of GNR composites to electrocatalysis, lithium-ion batteries (LIBs) stood out as another application that frequently employs carbon support materials as composites with inorganic nanoparticles. Additionally, the structural and electronic properties of existing top-down support materials have been demonstrated to strongly influence battery performance, making LIBs an appealing system for study using a bottom-up synthesized graphene nanomaterial featuring structural precision and tunability. GNRs are ostensibly well-suited materials for battery applications, featuring high mechanical strength and flexibility, excellent thermal and electrical conductivity, and a demonstrated ability to immobilize inorganic nanoparticles while facilitating mass transport. However, the challenges faced by LIB support materials are starkly different from those relevant to electrocatalysis, and include accommodating large volume expansion, facilitating reaction reversibility, the mass transport of charged species, and withstanding highly reactive conditions. It was therefore desirable to develop and test a proof-of-principle LIB system for gauging the suitability of GNRs for battery applications.

To that end, this chapter reports a composite of SnO_2 nanoparticles grown *in situ* on a support of bottom-up synthesized narrow graphene nanoribbons, and details investigation of the composite as an anode material for LIBs. Performance of the material was characterized by galvanostatic cycling, which revealed a high first charge capacity of 1233 mAh g^{-1}, indicating excellent transport of Li through the GNR matrix. The composite material displayed coulombic efficiency as high as 98% after 20 cycles, with stable capacity exceeding 900 mAh g^{-1} together with good rate capability. In addition, when the composite material was cycled in a more limited potential range to isolate its performance during the demanding, volume-expansive lithium alloying, the composite exhibited excellent stability together with high capacity, coulombic efficiency, and rate capability. These results conclusively demonstrate that GNRs, the first bottom-up synthesized graphene nanomaterial thus employed, are highly capable LIB support materials, and merit further investigation as a tool for the interrogation of substrate effects and a means towards rational design of battery composite materials.

Device fabrication and performance measurements described in this chapter were carried out by Dr. Abhinav Gaikwad in the group of Professor Ana Arias.

7.1 Introduction

Metal and metal oxide nanoparticles have long been investigated as potential light weight, high capacity anodes for lithium ion batteries (LIBs).[246–251] Much like the inorganic nanomaterials discussed in previous chapters, they frequently require a complementary conductive support material to retain structural integrity and device cohesion, as well as to stabilize the reactive nanoparticles amid harsh working conditions.[95,249,252–260] Additionally, a large body of work has established that structural and electronic interactions at the support-nanoparticle interface frequently exert a powerful influence on LIB behavior.[56,57,60,246,261] Across battery types and materials, understanding these interfacial interactions and ultimately harnessing their effects through rational design will be crucial to achieving optimized performance.

These existing works have necessarily relied on top-down graphene nanomaterial supports, prepared using harsh chemical treatment or pyrolysis to dictate structure and incorporate dopants, with minimal control over defect concentration or morphology.[39,56,57,60,95,246] Such an approach precludes a detailed investigation into the role of structure, edges, heteroatoms, or functional groups, and inhibits the rational design of improved support materials. LIBs therefore represented an excellent new domain for the continued study of GNR-nanoparticle interaction and the use of GNRs as support materials. In addition to their high mechanical flexibility and strength with excellent thermal and electrical conductivity, GNRs can effectively immobilize inorganic nanoparticles while also acting as a permeable membrane, facilitating diffusion to the nanoparticle surface (Chapter 5). However, the challenges faced by LIB support materials are quite distinct from those associated with electrocatalysis, and the network of narrow GNRs is quite structurally dissimilar to extant LIB support nanomaterials. It was therefore necessary to develop and characterize a proof-of-principle GNR LIB system, to better understand the suitability of narrow graphene nanoribbons for this distinct application.

SnO_2 batteries have been the subject of longstanding interest because of their high theoretical Li^+ storage capacity (1480 mAh g^{-1}) stemming from threefold reactivity involving lithium intercalation, tin reduction, and ultimately lithium alloying into the reduced tin phase. Additionally, low cost, material abundance, and low charge/discharge potential vs. Li^+/Li make SnO_2 nanoparticles an attractive battery material.[252,262–265] However, the electrochemical reactions at the anode are beset by challenging phase transitions that require stabilization of various Sn nanoparticle species by a capable support material; in the process of alloying lithium (overall reaction $SnO_2 + 8.4\ Li \rightarrow 2Li_2O + Li_{4.4}Sn$) the material undergoes volume expansion of as much as 360%. The mechanical forces associated with this volume change frequently lead to pulverization of the SnO_2 anode, disrupt the stability of the solid electrolyte interphase (SEI) layer, erode faradaic efficiency (FE), and eventually lead to loss of electrical contact and device function.[260,262–268] As such, SnO_2 batteries have been the subject of intensive research into graphene support materials, which conclude that structural defectsedges, pores, heteroatoms, and functional groupsplay an important role in battery performance. These defect sites not only play a key role in storing lithium directly, but also in immobilizing Sn nanoparticles, controlling nanoparticle growth, facilitating mass transport, enhancing reaction reversibility, and contributing to the mechanical flexibility of composite anodes.[39,56–60,95,261,269] These attributes made SnO_2 LIBs the ideal system to demonstrate the viability of a new class of graphene nanomaterial for battery applications.

7.2 Composite Synthesis and Characterization

Chevron-type GNR **5** was synthesized as descirbed in Chapter 4; no other GNRs were used in this project, and so all instances of GNR in this chapter refer to samples of **5**. SnO_2 nanoparticles were then prepared *in situ* by hydrolysis of $SnCl_2$ in the presence of a surfactant-supported aqueous suspension of GNRs, followed by annealing in air. Powder X-ray diffraction (PXRD) of the composite (Figure 7.1A) confirms the formation of nanocrystalline SnO_2, with a small average crystal size of 4 nm by Scherrer analysis. Raman spectroscopy of the GNR-SnO_2 nanocomposite (Figure 7.1B) reveals the characteristic D and G peaks of narrow GNRs, together with the higher order 2D, D+D, and 2D peaks, indicating preservation of GNR structural integrity during nanoparticle synthesis. X-ray photoelectron spectroscopy (XPS) of the electrode (Figure 7.1C; SI Figure 10.7, page 151) shows the elemental composition of the GNR-SnO2 nanocomposite used in cell production, including prominent peaks corresponding to SnO_2, graphitic carbon, and the absence of Ni and Fe impurities from the GNR synthesis. Thermogravimetric analysis (TGA, Figure 7.1D) reveals that the composite nanomaterial is comprised of approximately 69% SnO2 by mass, consistent with the expected stoichiometry based on the synthesis and suggesting complete incorporation of the GNRs.

Figures 7.2A and 7.2B show SEM micrographs for the GNR-SnO_2 nanocomposite at different magnification, highlighting the rough microstructure of the GNR composite, with SnO_2 nanoparticles dispersed throughout the larger composite structure. TEM of the composite (Figure 7.2C) indicates discrete and well dispersed SnO_2 nanoparticles with an average size of 45 nm, enclosed within a network of nanoribbons. Following synthesis, the GNR-SnO_2 composite was wet ball milled in isopropanol, mixed with carbon black (8 wt%) and PVDF binder (10 wt%), and printed on a nickel current collector foil to give an electrode with total thickness of 15 m. SEM of the electrode surface (Figure 7.2D) illustrates its smooth morphology, a product of the ball milling process prior to printing. Electrodes prepared without this milling step appear rougher by SEM (Figure 7.2E&F), and exhibited inferior battery performance (SI Figure 10.8, page 152).

7.3 Battery Performance

To gain an initial understanding of lithium storage by the GNR-SnO_2 nanocomposite, we performed cyclic voltammetry (CV) for three cycles between 0.005 and 3.0 V vs. Li^+/Li (Figure 7.3A, 0.1 mV s^{-1}). When SnO_2 is discharged in the presence of a lithium source, its reduction is known to proceed by a two-step process:

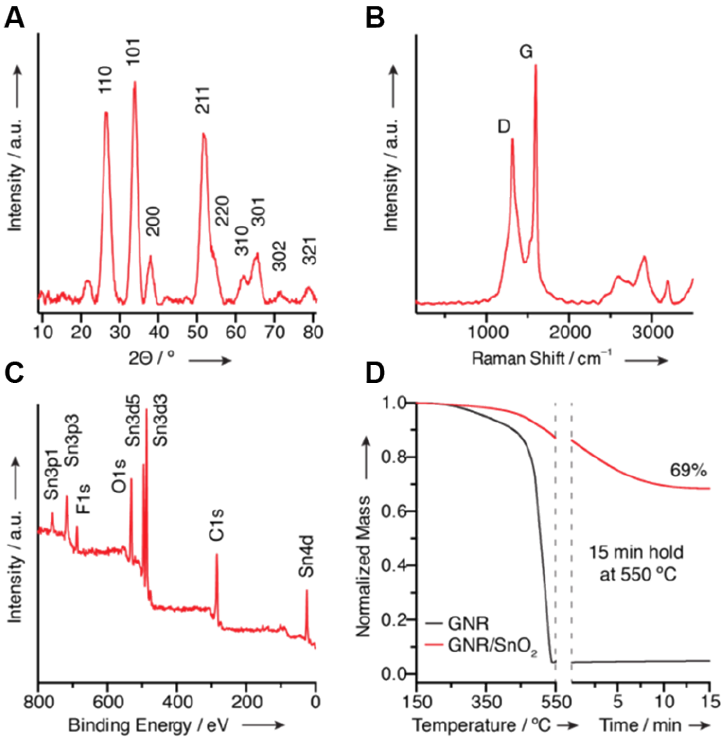

Figure 7.1: (A) XRD spectrum of the GNR-SnO_2 nanocomposite. (B) Raman spectrum of the GNR-SnO_2 composite. (C) XPS spectrum of the printed GNR-SnO_2 nanocomposite electrode. (d) TGA of GNR-SnO_2 composite (red) and GNRs (black) in air (20 °C min^{-1} ramp to 550 °C followed by 15 min hold at 550 °C).

$$SnO_2 + 4Li^+ + 4e^- \rightarrow Sn + 2Li_2O \tag{7.1}$$

$$Sn + 4.4Li^+ + 4.4e^- \rightarrow Li_{4.4}Sn \tag{7.2}$$

While reaction 7.1 is irreversible for bulk SnO_2, the process is reversible if nanocrystals of SnO_2 are used as the starting material. In the case of our GNR composite, the first cycle in the cathodic direction exhibits a slow rise in cathodic current up to 1.0 V, corresponding to Eq. 1 as well as the formation of a solid electrolyte interphase (SEI) layer. In the second cycle, the broad peak due to formation of the SEI layer is not observed, indicating the formation of a stable SEI layer during the first cycle. This indicates that the network of GNRs capably supports a stable SEI through multiple cycles, a crucial determination in demonstrating its suitability for battery applications.

Below 1.0 V in the CV of the GNR-SnO_2 nanocomposite, we observe current corresponding to Equation 7.2, the alloying of Sn with Li^+ to form $Li_{4.4}Sn$. The peak at 0.10 V can therefore be ascribed to the formation of $Li_{4.4}Sn$. Notably, the formation of Li_2O continues until the electrode reaches $\sim$0.0 V vs. Li^+/Li, and Sn formed during this process alloys with

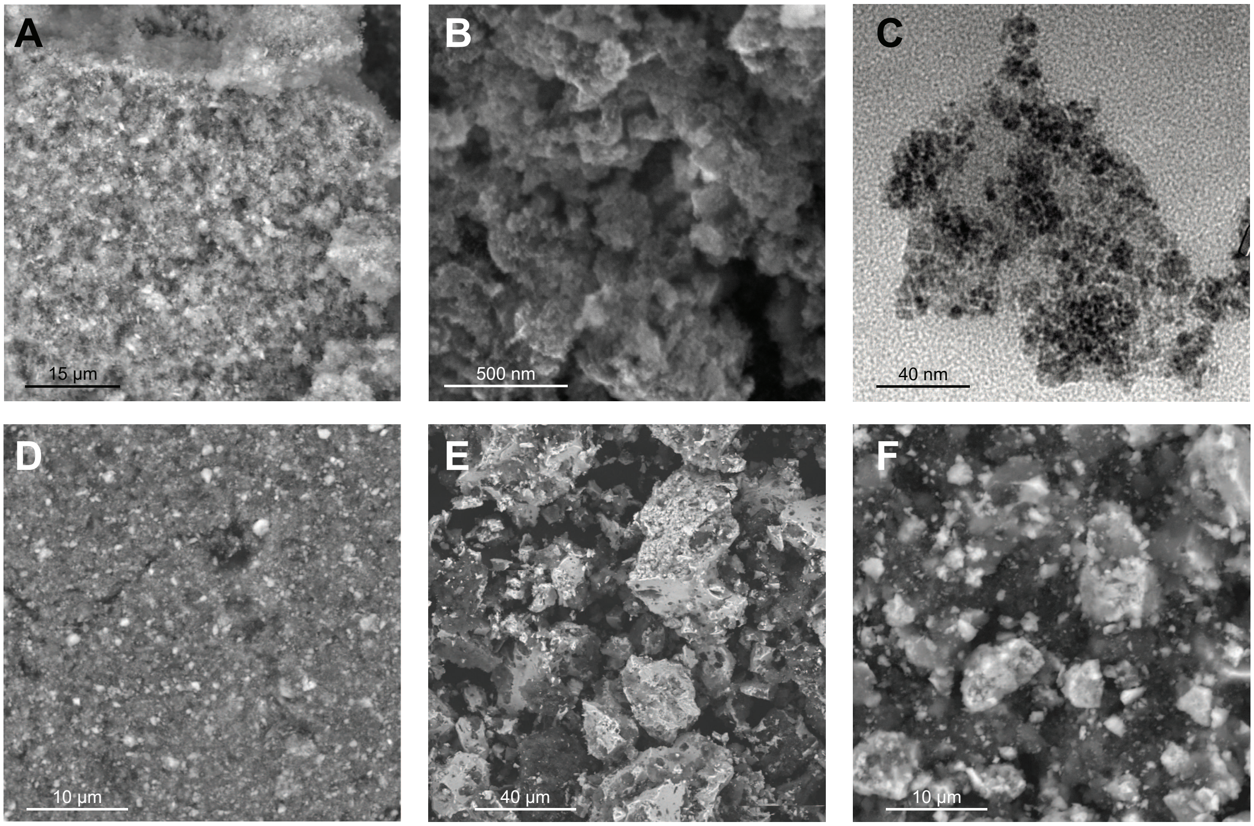

Figure 7.2: (A&B) SEM images of a GNR-SnO_2 nanocomposite. (C) TEM image of the GNR-SnO_2 nanocomposite. (D) SEM image of the printed electrode prepared from GNR-SnO_2 nanocomposite following ball milling. (E) SEM image of the rough, as-synthesized GNR-SnO_2 composite. (F) SEM image of a printed electrode prepared using as-synthesized GNR-SnO_2 nanocomposite without ball milling.

Li as soon as it is formed.[268,270] In the anodic direction, the peaks at 0.57 and 1.24 V are assigned to the delithiation of Li_xSn, and the oxidation of Sn to SnO_2, respectively. The peak at 1.24 V and the appreciable current between 1.5 and 3.0 V indicate reversible capacity due to reaction 7.1. In later cycles, the new peaks at 1.24 and 0.87 V are can be ascribed to the conversion of SnO_2 to Sn, and alloying of Sn, respectively. The potential corresponding to the formation of $Li_{4.4}Sn$ alloy, dealloying of $Li_{4.4}Sn$ to Sn and the conversion of Sn to SnO_2 remain constant. The third cycle overlaps with the previous second cycle, demonstrating excellent reversibility of the GNR-SnO_2 nanocomposite.

To better understand the full lithium storage capabilities of the GNR-SnO_2 nanocomposite, we undertook galvanostatic charge/discharge cycling experiments between 0.005 and 3.0 V vs. Li^+/Li (Figure 7.3B&C, 100 mA g^{-1}). The first cycle discharge and charge capacities of the GNR-SnO_2 electrode are 2029 and 1233 mAh g^{-1}, respectively, with a corresponding coulombic efficiency (CE) of 60.8%. The loss in capacity during the first cycle is attributed

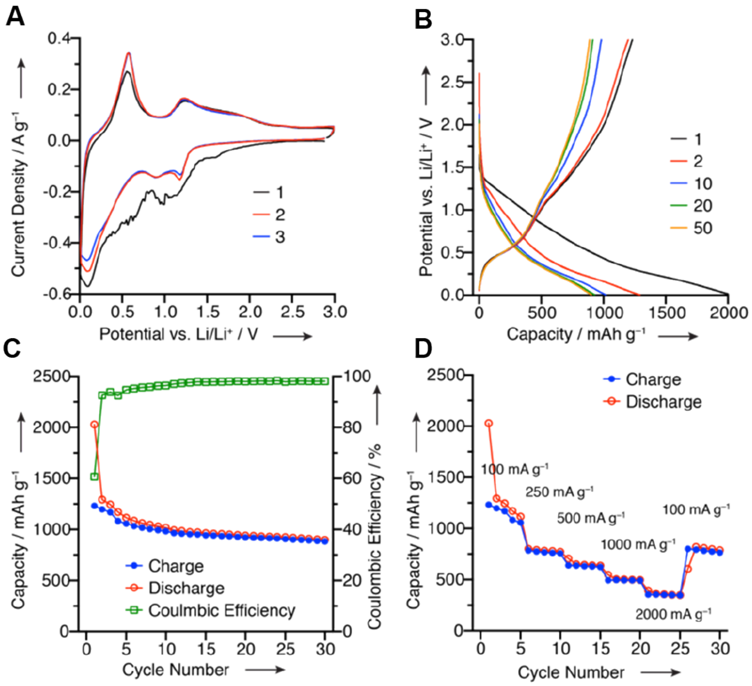

Figure 7.3: (A) Three cyclic voltammetry curve of GNR-SnO_2 nanocomposite between 3.0 to 0.005 V vs. Li^+/Li at 0.1 mV s^{-1}. (B) Galvanostatic charge/discharge curves and (C) charge/discharge capacity of GNR-SnO_2 nanocomposite cycled between 3.0 and 0.005 V vs. Li^+/Li at 100 mAh g^{-1} for 30 cycles. (D) Capacity retention of the electrode cycled between 3.0 and 0.005 V vs. Li^+/Li at 100, 250, 500, 1000, and 2000 mA g^{-1}.

to the consumption of lithium ions during formation of the SEI layer; the columbic efficiency increases to 97% within 10 cycles, and exceeds 98% after 20 cycles. The high first cycle charge capacity of 1233 mAh g^{-1} indicates that both reaction 7.1 and 7.2 are contributing to Li storage, as the capacity exceeds the theoretical limit of either reaction individually. The synergistic effect between nano-sized SnO_2 particles and narrow GNRs with high edge-to-surface ratio facilitates the conversion of Sn to SnO_2, prevents aggregation of NPs during cycling, and allows both reaction 7.1 and 7.2 to take part in reversible Li ion storage. The capacity of the electrode stabilizes to 961 mAh g^{-1} after 10 cycles and the capacity at the end of 30 cycle is 900 mAh g^{-1}. Additionally, the composite exhibits excellent rate capability of 1170, 767, 663, 502 and 360 mAh g1 at 100, 250, 500, 1000 and 2000 mA g^{-1}, respectively (Figure 7.3D). Figure 7.3B shows that the charging curves up to 1.0 vs. Li^+/Li overlap, demonstrating excellent reversibility of the alloying/dealloying process. The loss in capacity during initial cycles is due to the incomplete conversion of Sn to SnO_2.

While taking advantage of the Li^+ storing reactions of both equation 7.1 and 7.2 maximizes reversible storage capacity, it requires a wide voltage range (3.0 to 0.005 V vs Li^+/Li). A full cell making use of both reactions together with a typical high voltage transition metal oxide-based cathode would have to be discharged below 1 V, well below the input battery

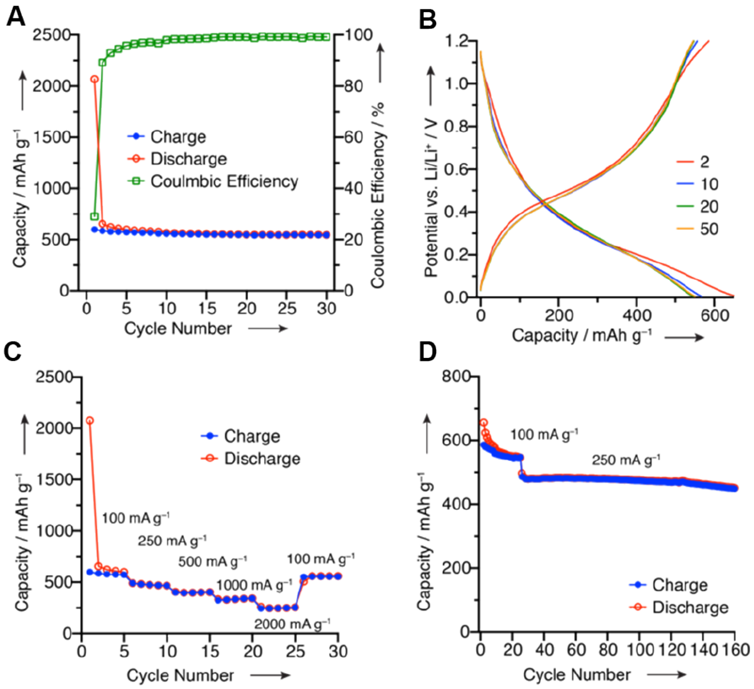

Figure 7.4: (A) Galvanostatic charge/discharge curves and (B) charge/discharge capacity of GNR-SnO_2 nanocomposite cycled between 1.2 and 0.005 V vs. Li^+/Li at 100 mA g^{-1} for 30 cycles, respectively. (C) Capacity retention of the electrode cycled between 1.2 and 0.005 V vs. Li^+/Li at 100, 250, 500, 1000 and 2000 mA g^{-1}. (D) Charge/discharge capacity of GNR-SnO_2 nanocomposite cycled between 1.2 and 0.005 V at 100 mA g^{-1} and 250 mA g^{-1}.

voltage of most consumer electronic devices. We therefore chose to focus on a cell using only reaction 7.2, the alloying and dealloying of Sn with Li; since this process takes place between 0.0 and 1.2 V vs Li^+/Li, a full cell making use of this reaction only would operate at a much more desirable voltage. Furthermore, testing exclusively reaction 7.2 isolates the capability of the GNR matrix to support volume expansive processes, an important concern for battery materials which has not been examined in GNRs. We find the GNR-SnO_2 nanocomposite displays exceptional stability behavior when cycled in the relevant potential range. Figures 7.4A&B show the galvanostatic charge/discharge curves and capacities of the GNR-SnO_2 nanocomposite cycled between 0.005 and 1.2 V vs. Li^+/Li for 30 cycles. The first cycle charge capacity of the electrode is 601 mAh g^{-1}, and more than 90% of this capacity is retained after 30 cycles. The columbic efficiency of the electrode was above 98% after 15 cycles. Consecutive charge/discharge curves overlap (Figure 7.4B), indicating a highly reversible process. The composite shows excellent rate capability of 600, 492, 400, 324 and 245 mAh g^{-1} at 100, 250, 500, 1000 and 2000 mA g^{-1}, respectively (Figure 7.4C). Figure 7.4D shows the galvanostatic charge/discharge capacity of the electrode cycled at 100 mA g^{-1} for 25 cycles and then at 250 mA g^{-1} for 125 cycles. The capacity at the start of cycling at 250 mA g^{-1} is 497 mAh g^{-1}, and at the end of 125 cycles the capacity is 458 mAh g^{-1}, demonstrating excellent capacity retention when the electrode is operated between 0.0 and 1.2 V. These results indicate that the flexible network of narrow GNRs capably accommodates volume-expansive processes, further evidencing their suitability as battery support materials.

7.4 Conclusion

This work has demonstrated that narrow, bottom-up synthesized GNRs are capable support materials for nanoparticle LIBs, successfully stabilizing SnO_2 nanomaterials amid large volume fluctuations while facilitating charge and mass transport through the device. Featuring synthetic tunability and structural precision unmatched by other graphitic materials, GNRs therefore merit continued investigation as advanced support materials for battery applications. In demonstrating this new class of graphene nanomaterial support, we hope to introduce synthetic organic chemistry as a tool for precise and detailed investigation of carefully designed support materials, so subsequent investigations can more fully understand their role in dictating the performance of composite LIBs.

Chapter 8

GNR-Mg Nanocomposites for Hydrogen Storage

Whereas the above GNR composite projects emphasized facilitating mass transport to the surface of intercalated nanoparticles, some nanocomposites utilize support materials to shield unstable nanoparticles from ambient conditions while relying on selective permeability of reactant species. For example, Mg nanocrystals (MgNPs) are a promising material for hydrogen storage because they reversibly form MgH_2, but are themselves very susceptible to oxidation. Recent reports have demonstrated that graphene nanomaterial composites can effectively shield MgNPs from oxidation while selectively allowing diffusion of H_2 under hyding conditions, suggesting that an ultramicroporous GNR network could assume a similar role. The bottom-up synthesis of GNRs would additionally facilitate a close examination of the role that heteroatom dopants play in activating the Mg surface for hydriding and dehydriding.

This chapter reports on the design and the performance evaluation of composite high-capacity hydrogen storage materials comprised of nanodisperse Mg crystals embedded in a bottom-up synthesized graphene nanoribbon (GNR) matrix. All GNR-Mg nanocomposites investigated exhibit an exceptionally high hydrogen capacity (7.1-7.3 wt% of H_2 based on the total composite), the highest of any reported Mg composite. Furthermore, the composites display a selective permeability for H_2 while protecting the encapsulated metallic Mg from ambient oxidation on the months timescale, even when using a minimum of GNR (2% GNR by mass; 98% Mg). Using bottom-up GNR synthesis to introduce precise heteroatom functionalization revealed that the hydrogen sorption and desorption kinetics of embedded Mg nanocrystals can be tuned through interfacial effects with specific heteroatom moities. These results, combined with theoretical treatment of the GNR-Mg interface, shed light on the specific interactions that activate the Mg surface, empowering subsequent rational resign of additional GNR support materials.

Hydrogen storage measurements described in this chapter were performed by Dr. Eun Seon Cho and Edmond Zaia in the group of Dr. Jeff Urban at the Molecular Foundry. XANES characterization of the Mg composites was performed by Yi-Sheng Liu, Dr. Yi-De

Chuang, and Dr. Jinghua Guo at the Advanced Light Source. All magnesium composites were prepared either by Dr. Cho or by the author. Theoretical work described in this chapter was done by Dr. Liwen (Sabrina) Wan in the group of Dr. David Prendergast at the Molecular Foundry.

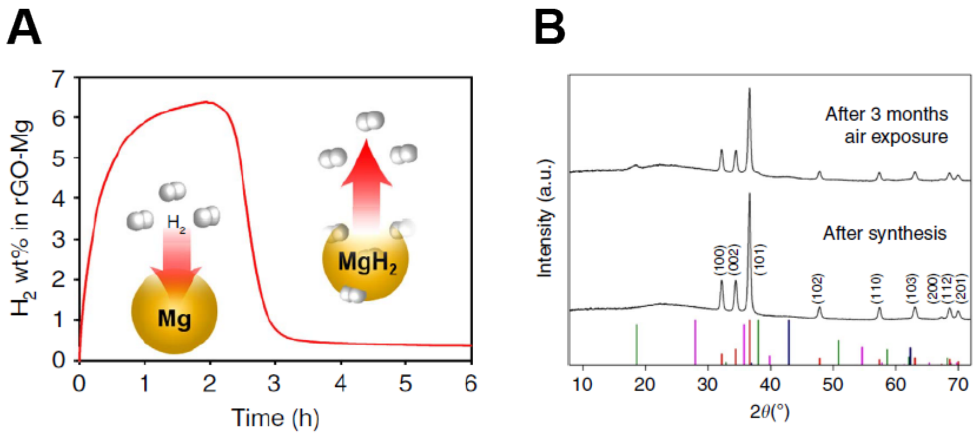

Figure 8.1: Performance of a reported Mg composite prepared with reduced graphene oxide (rGO). (A) Reversible hydrogen storage reaching 6.5 wt% of the total composite. (B) PXRD in air indicating effective stabilization of Mg^0 by rGO, with only minor oxidation evident after three months in air. Figures reproduced from reference [51]

8.1 Introduction to Magnesium Hydrogen Storage

Hydrogen is an attractive and environmentally benign mode of energy storage. It possesses unparalleled energy density among chemical fuels, is readily produced via electrocatalytic water splitting, and combusts to yield water without greenhouse gas emission.[271–273] The major impediment to implementation of a hydrogen economy is a safe, durable, and compact hydrogen storage system with high gravimetric and volumetric capacity, especially for mobile applications such as fuel cell electric vehicles.[274]

Metal hydrides have been suggested as candidates for solid-state hydrogen storage,[275,276] and magnesium hydride (MgH_2) in particular has attracted a great deal of attention as a promising hydrogen storage material due to its high gravimetric capacity (7.6 wt%), reversibility, and low cost.[274,277,278] However, use of MgH_2 for hydrogen storage is limited both by sluggish hydriding/dehydriding kinetics and especially by the oxidative instability of magnesium. Recent work from Urban and coworkers has demonstrated that composite materials, and in particular composites using graphene nanomaterials like reduced graphene oxide (rGO), can effectively prevent Mg oxidation over long timescales while still selectively allowing hydrogen permeation under hydriding conditions.[51,279] These systems emphasize minimizing "dead" mass, the total weight of materials that do not directly contribute to hydrogen storage, and thereby achieved hydrogen storage capacity as high as 6.5 wt% of H_2 based on the total composite mass. Significant oxidation is not observed until after a few months, and the system exhibits good cyclability, establishing graphene nanomaterial encapsulation as a viable strategy for protecting functional MgNPs.

As an atomically thin graphene nanomaterial, GNRs are well suited to encapsulate the active nanocrystals while minimizing dead mass, and the flexible, ultramicroporous network of GNRs (see Section 5.4, page 76) could serve to protect the Mg surface from oxidation while allowing for selective permeation of H_2. In contrast with the top-down fabrication of materials like rGO, synthesis of GNRs allows for the creation of an array of support materials for which the structure, concentration, and placement of edges and heteroatoms can be known and controlled precisely. Given the well-established and important role of defect sites both to mass transport within the material and to hydrogen sorption/desorption kinetics, GNRs therefore constitute an ideal support material for fuller investigation and better understanding of these processes.

8.2 Synthesis and Characterization of GNR-Mg Composites

GNRs used in this work were prepared as described in Chapter 4. Mg nanocomposites with chevron-type GNR **5** were synthesized via Rieke-like reaction using Cp_2Mg and lithium naphthalenide, by a procedure analagous those reported using other materials.[51,280] As determined by synthetic mass balance, the composite contains less than 2 wt% of GNR and up to 98% of Mg metal, so as to minimize the dead mass that does not directly participate in hydrogen storage. X-ray diffraction (XRD) confirmed the crystalline Mg^0 structure of **5**-Mg, with no indication of any oxidized species and average crystalline domains of 14.8 nm by Scherrer analysis (Figure 8.2A). Remarkably, the GNR-Mg composite was stable over 6 months in air without any indication of Mg oxidation by XRD, despite the exceedingly low mass fraction of support material. This enhanced oxidative stability of GNR composites exceeds that of Mg composites with any other support material, including those reported with rGO (Figure 8.1).[51]

TEM images suggest that the **5**-Mg composite is not comprised of discrete MgNPs, but rather a continuous structure of conjoined 15 nm nanocrystallites (Figure 8.2B&C). Selected area electron diffraction (SAED, inset to Figure 8.2B) confirmed the crystalline Mg metal structure within these continuous structures, and TEM elemental mapping indicated that both Mg and C are uniformly distributed throughout the observed features, supporting a homogeneous structure for the composite (Figure 8.2D-F). The continuous structure adopted by **5**-Mg is unsurprising for *in-situ* nanoparticle growth using a support material without abundant heteroatoms that can aid in nucleating nanoparticle growth.

Hydrogen absorption and desorption properties for the chevron GNR **5**-MgNP composite was tested using a Sieverts PCT-Pro instrument at, respectively, 200 °C, 15 bar H_2 and 250 °C, 0 bar H_2 (Figure 8.3A&B). Additional absorption/desorption results at varied temperatures are shown in Supporting Information Figure 10.9, page 153. The GNR-Mg nanocomposite readily absorbed hydrogen and exhibited an exceptionally high gravimetric capacity of 7.10%, the best value ever reported for Mg-based hydride materials when calculated based on the total material amount.[51] The formation of MgH_2 upon absorption was confirmed by XRD of the hydrided composite; importantly, XRD following dehydriding

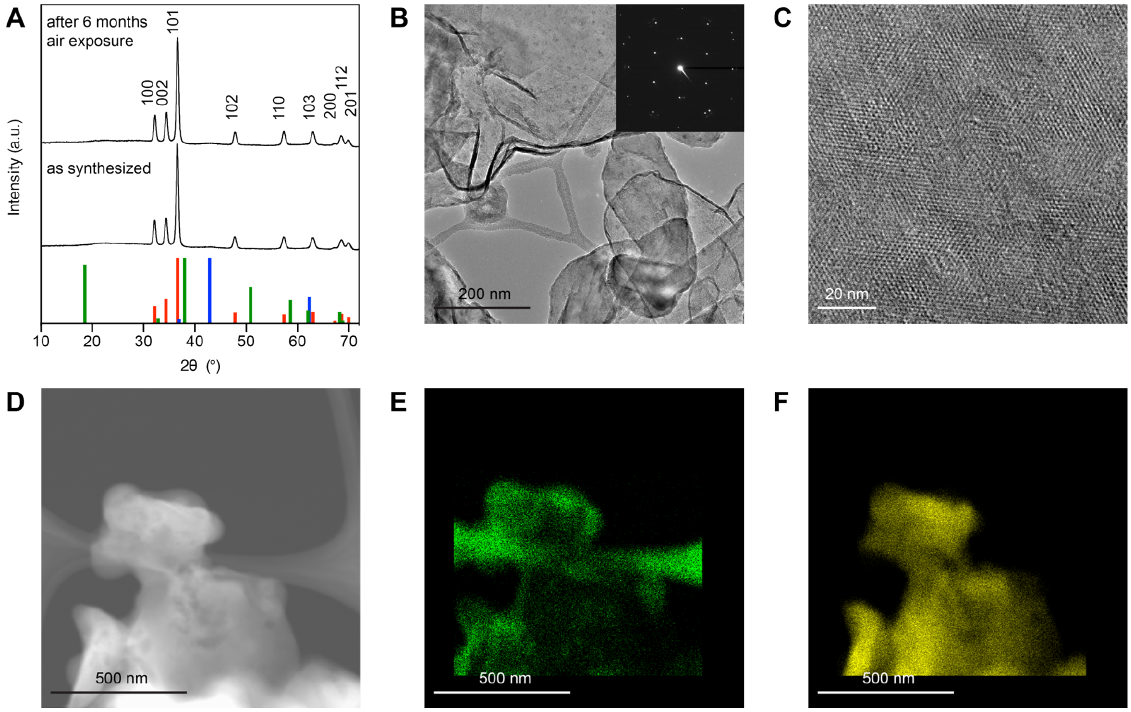

Figure 8.2: Materials characterization of Mg nanocomposites with GNR **5**. (A) XRD pattern of GNR-Mg with as-synthesized and after 6 months air-exposed. At bottom: predicted XRD patterns of Mg (red), $Mg(OH)_2$ (green) and MgO (blue). (B–D) TEM images of the GNR-Mg composite. Inset to B shows SAED pattern consistent with Mg (100). (E&F) Qualitative TEM elemental mapping of (E) carbon and (F) magnesium in the dark-field TEM image shown in (D).

closely matched that of the as-synthesized material, confirming the reformation of Mg^0 upon hydrogen desorption without major structural change in the composite (Figure 8.3C).

The reversible hydriding of **5**-Mg was examined in greater detail via X-ray absorption near-edge structure spectroscopy (XANES) measurement of three GNR-Mg samples: one as-synthesized composite, another following hydriding, and a third dehydrided Mg composite following 5 hydriding/dehydriding cycles. Also, the bare chevron GNR **5** was examined without Mg by C K-edge measurement. Figure 8.4A, B and C show the XANES spectra at the C K-edge, Mg K-edge, and Mg L-edge, respectively. At the C K-edge, the intensities of two signals at 288.4 and 290.3 eV are significantly increased for the GNR-Mg samples in comparison to the neat GNR **5**, independent of the hydriding status of the composites, indicating significant electronic interaction between GNRs and Mg crystals in the composite. At both Mg K- and L-edge scans, zero-valent Mg metal state in the composite was identified by its characteristic shoulder at 1303 eV and unique peak at 49.8 eV. These peaks are shifted to the higher energies upon hydriding, consistent with positively charged Mg, and completely restored to the original zero-valent state following dehydriding. These results

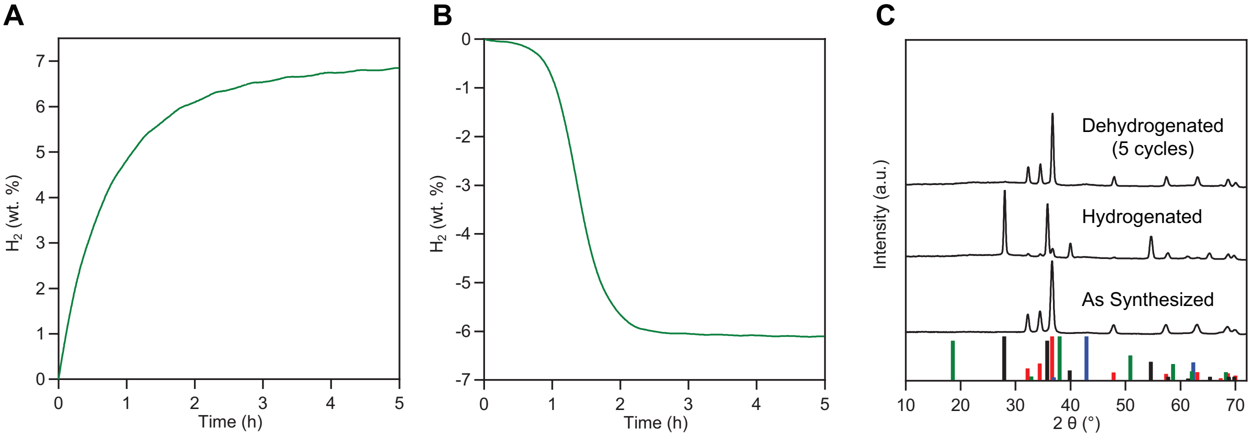

Figure 8.3: (A) Hydrogen absorption of the GNR **5**-Mg composite at 200 °C and 15 bar H_2. (B) Hydrogen desorption of the GNR **5**-Mg composite at 300 °C and 0 bar. Note that total capacities referenced in the text are for hydrogen storage cycles performed at higher temperatures, see SI Figure 10.9, page 153. (C) XRD spectra of the GNR **5**-Mg composite as synthesized, after hydrogenation, and following 5 hydogenation-dehydrogenation cycles. At bottom: predicted XRD pattern of Mg (red), MgH_2 (black) $Mg(OH)_2$ (green) and MgO (blue).

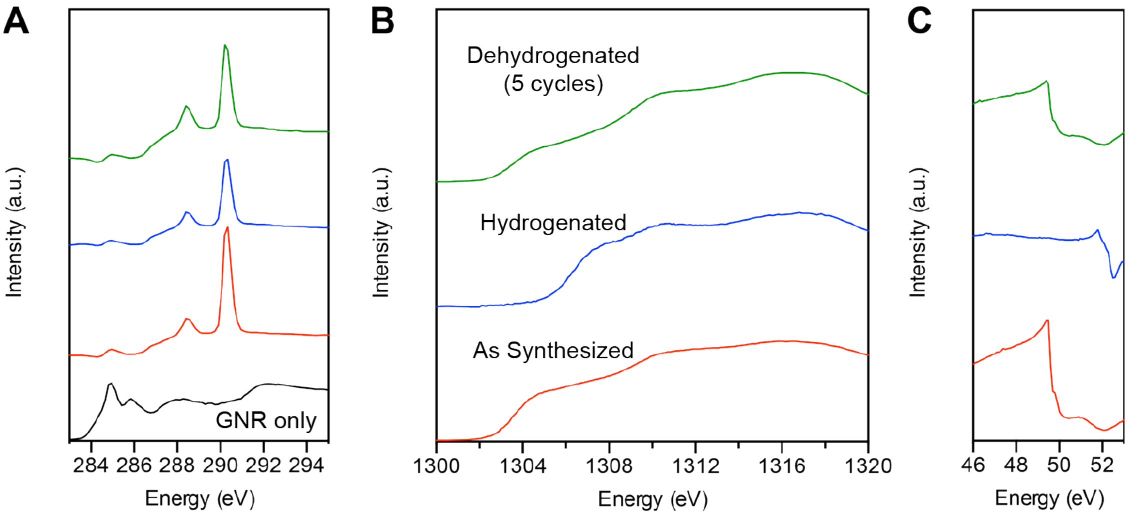

Figure 8.4: X-Ray absorption near edge structure (XANES) spectroscopy characterization of the GNR **5**-Mg composite as synthesized (red), after hydrogenation (blue), and following five hydrogenation/dehydrogenation cycles (green) at the (A) carbon K-edge, (B) magnesium K-edge, and (C) magnesium L-edge. Carbon K-edge spectrum of the bare GNR **5** (no Mg) is shown in black.

Composite	Average size (nm)
5-Mg	14.8
69-Mg	14.7
6-Mg	15.4
70-Mg	14.3

Table 8.1: Average size of Mg nanocrystalline domains in each GNR-Mg composite by Scherrer analysis of XRD spectra.

reinforce conclusions drawn from the XRD patterns shown in Figure 8.3C, supporting a fully reversible reaction between Mg and MgH_2 in the GNR composite.

8.3 Heteroatom-Doped GNRs for Improved H-Storage Kinetics

Having established the ability of chevron-type GNRs to effectively stabilize Mg nanocrystals in ambient conditions and facilitate reversible hydrogen storage at record capacity, the remaining challenge was one of Mg hydriding and dehydriding kinetics. Although Mg hydriding and dehydriding are generally moderately sluggish, overall kinetics for the **5**-Mg system were somewhat slower than for some reported systems, attributable primarily to the larger average Mg nanocrystal size observed for the GNR composite. The synthetic tunability of bottom-up GNRs offers a facile handle to address this issue through the selective heteroatom incorporation at the GNR edges. Heteroatom-doping of support materials is known to play a role in accelerating hydrogen dissociation and sorption kinetics, and the precise structural functionalization of GNRs can facilitate unprecedented insight into the specific doping patterns that best activate Mg.[281,282] This insight could then be applied to the rational design of tailored GNR-Mg composites for further kinetic improvement.

To that end, Mg-GNR composites were prepared using three heteroatom-doped chevron-type GNRs: the lightly nitrogen functionalized GNR **69**, the more extensively nitrogen doped GNR **94**, and the fluorenone-bearing chevron GNR derivative **70** (Figure 4.2, page 58 and Figure 4.3, 59). TEM imaging and XRD analysis find no significant structural differences between these heteroatom-functionalized GNR-Mg composites and the parent composite prepared with GNR **5** (Table 8.1). The composites did, however, exhibit significantly altered hydrogen storage kinetics, featuring accelerated hydriding and particularly dehydriding in comparison to the unfunctionalized **5**-Mg composite (Figure 8.5). In particular, the composites featuring **6** and **70** showed the largest kinetic improvement, a mildly surprising result given that GNR **70** features half as many heteroatoms per repeat unit as **69** does, and a quarter as many as **6**, suggesting that oxygen atom functionalization more strongly activates Mg than does nitrogen. Interestingly, the **69**-Mg composite behaves much more similarly to the unfunctionalized **5**-Mg composite than to the more heavily nitrogen-doped **6**-Mg compos-

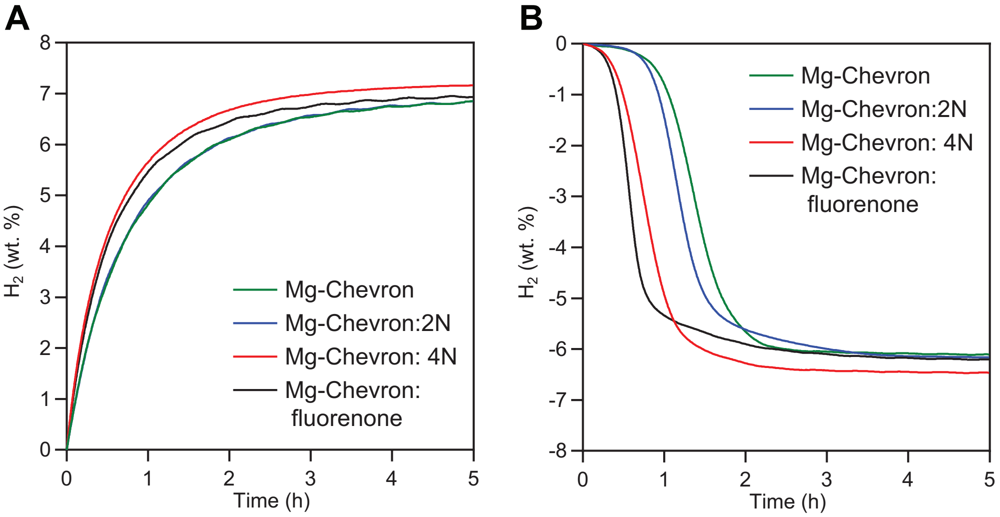

Figure 8.5: (A) Hydrogen absorption behavior of each composite at 200 °C and 15 bar H_2. (B) Hydrogen desorption behavior of each composite at 300 °C and 0 bar. Note that total capacities referenced in the text are for hydrogen storage cycles performed at higher temperatures, see SI Figure 10.9, page 153.

ite, indicating that Mg activation is not merely a function of doping amount, but reflective of interaction between the Mg surface and specific heteroatom moieties. Exploration of fine structural differences like these and their markedly differing impact on nanomaterial interfacial interactions is only possible because of the structural precision inherent to bottom-up synthesized GNRs, unrivaled among graphene nanomaterials.

The kinetics of hydrogen adsorption and desorption are illustrated more clearly by Figure 8.6, showing hydriding and dehydriding rates and their dependence upon both temperature and the processes' degree of completion. These plots reflect the increased rates for **6**-Mg and **70**-Mg composites, especially early in the hydriding and dehydriding processes. Although the complicated relationship between rate and weight percent H_2 in the composite complicates Arrhenius analysis, Arrhenius plots could be prepared for the hydrogen sorption process by choosing a fractional hydriding completion and analyzing the temperature dependence of rate at that point for each composite. The resulting Arrhenius plots analyzing each composite at 60% hydriding completeness are shown as Figure 8.7, together with the corresponding activation energies (E_a). As expected, the accelerated rates illustrated in Figure 8.5 are reflected in lower E_a values for composites prepared with **6** and **70**. As Figure 8.6 shows, the kinetics of dehydriding are less simple; speculatively, a local minimum early in the dehydriding process is perhaps indicative of comparatively rapid dehydriding at the Mg surface followed by a regime of rate-liming diffusion through the MgH_2 nanoparticles. The more complex relationship between rate, temperature, and ΔH_2 wt.% precluded meaningful Arrhenius analysis for hydrogen desorption in these materials.

A theoretical examination of the GNR-Mg interface was undertaken to better understand

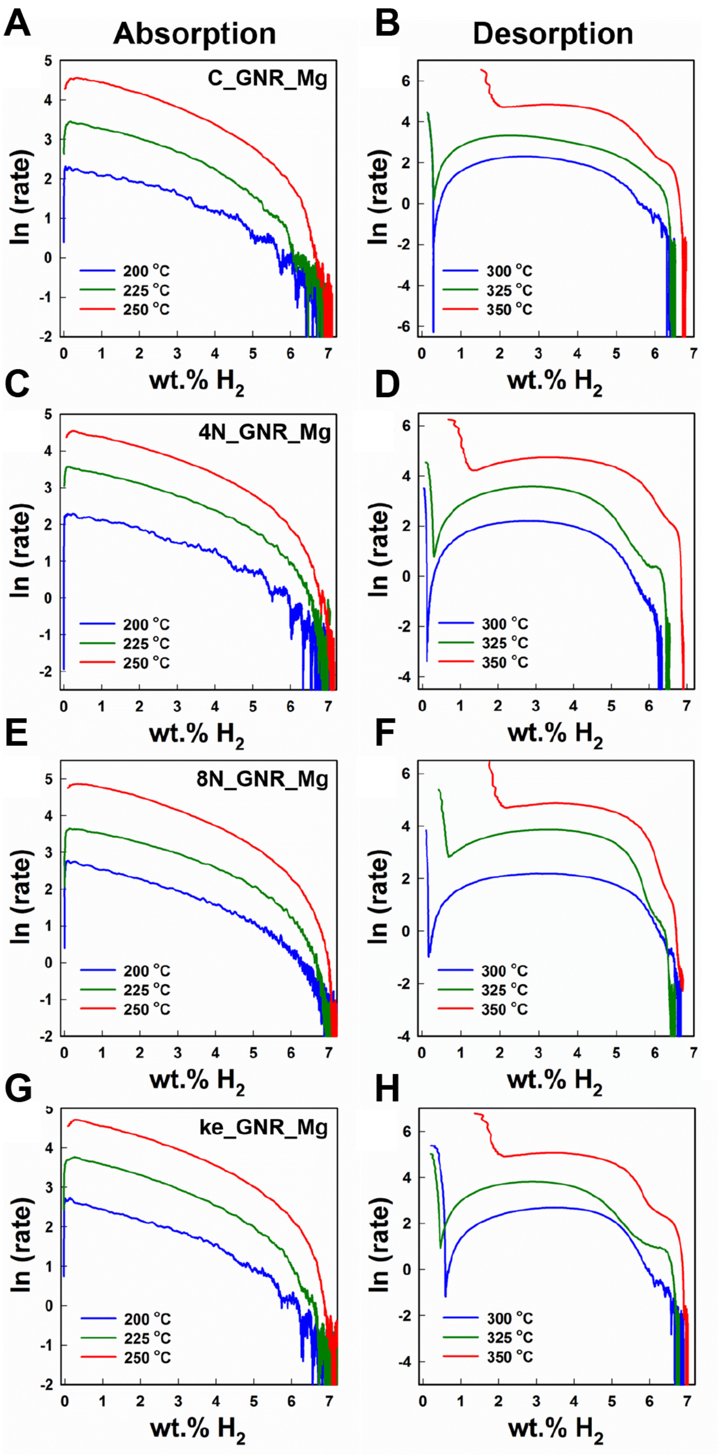

Figure 8.6: Kinetic analysis of hydrogen absorption (left) and desorption (right) for (A&B) **5**-Mg composite; (C&D) **69**-Mg composite; (E&F) **6**-Mg composite; (G&H) **70**-Mg composite.

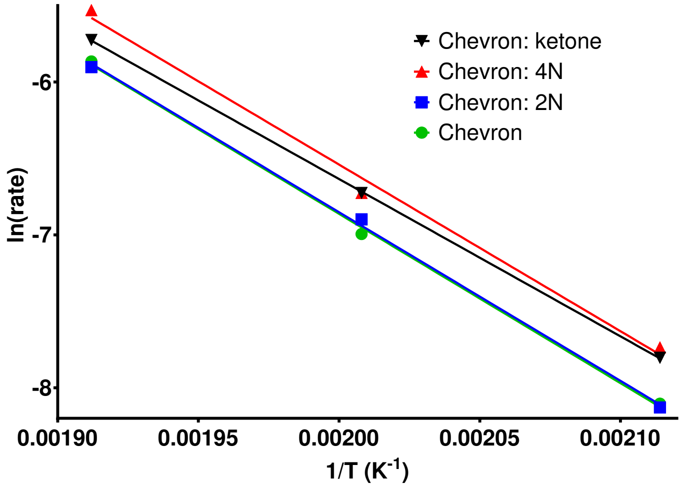

Composite	Arrhenius Slope (K)	Activation Energy (kJ mol^{-1})
5-Mg	-11071	92.0
69-Mg	-11033	91.7
6-Mg	-10899	90.6
70-Mg	-10290	85.6

Figure 8.7: Arrhenius plots for hydrogenation of each GNR-Mg composite at a fixed hydriding percentage. Although kinetic analysis of the composite hydriding behavior is complex, an approximate insight can be gained by simple Arrhenius analysis at a given point in the hydriding process.

the specific mechanism by which heteroatom doping in GNRs activates Mg to hydrogen sorption and desorption. The calculations revealed a strong interaction between certain heteroatom sites and specific surface atoms, which are drawn out of the Mg lattice to create specific activated sites for H_2 dissociation (Figure 8.8). In addition to clarifying the role of heteroatom-doped GNRs in activating Mg, these calculations predict the diminished activation observed for **69** in comparison to **6**, which clearly exhibits much greater Mg-atom displacement from the surface at the phenanthroline-like doping sites not present in **69**. The results further show an unexpected but electrostatically reasonable interaction between the Mg surface and the carbonyl carbon atoms of GNR **70**, which appears to be the source of that compound's enhanced kinetics even at low doping levels.

These results inspired the synthesis of additional GNR-Mg composites designed to make use of the interactions described above. Most notably, a Mg composite was prepared using the quinone-functionalized chevron-type GNR **72** (Figure 4.3, page 59), designed to further accelerate hydrogen storage kinetics through the strong carbonyl-Mg interactions uncovered by theory and experiment. Additionally, a composite was prepared using the cove-type GNR **8**. In light of the results described in Chapter 5, in which electronic interaction of Au with the GNR backbone was an important determinant of performance, the **8**-Mg composite will

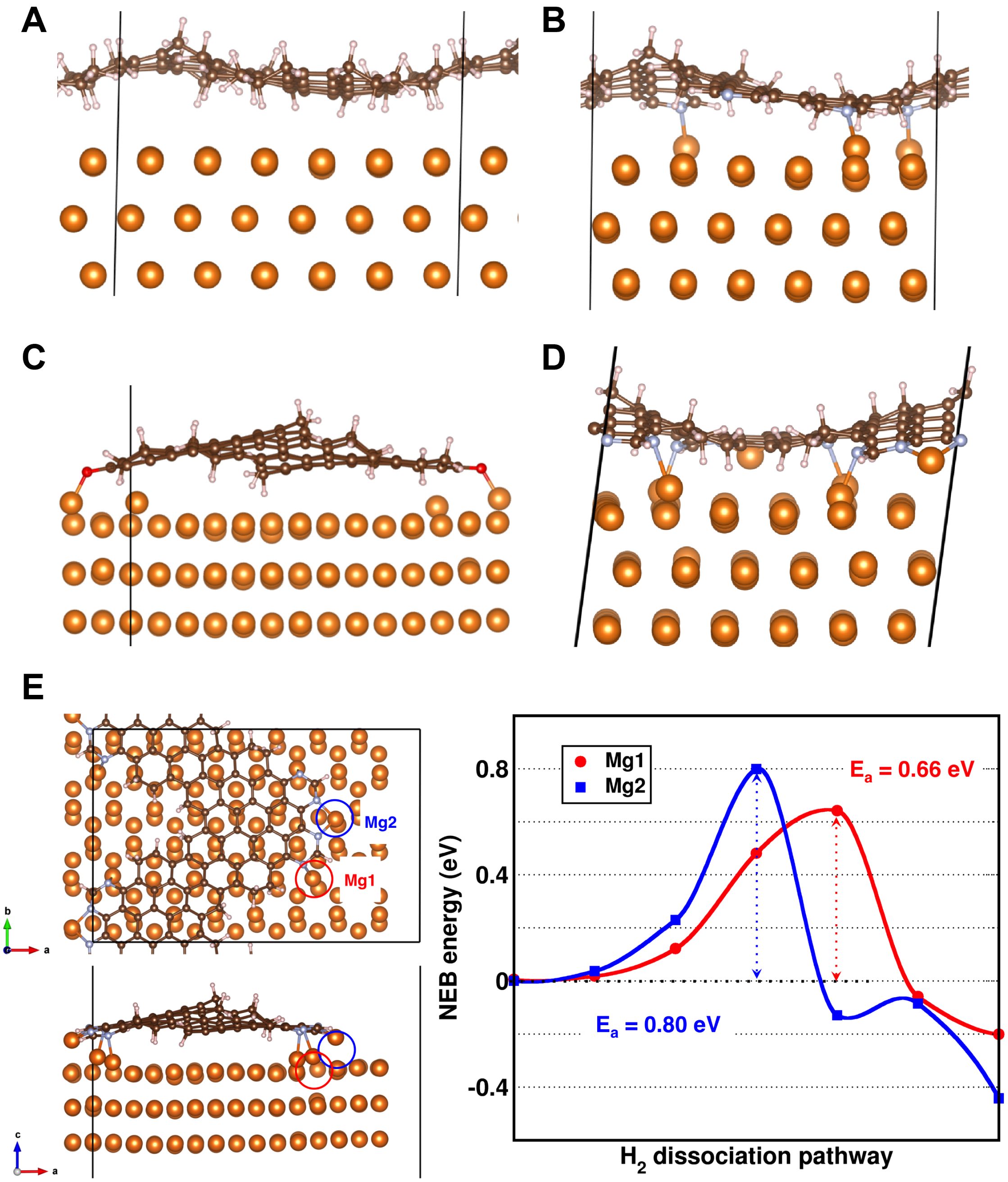

Figure 8.8: Visual representations of the calculated GNR-magnesium interface for (A) **5**-Mg, (B) **69**-Mg, (C) **70**-Mg, and (D) **6**-Mg. (E) Calculated energy diagram for H_2 dissociation at two distinct sites in the calculated **6**-Mg composite (indicated at left with red and blue circles) illustrates the significant impact that GNR-Mg interaction can have for hydrogen activation kinetics. Images shown were prepared by Dr. Liwen Wan.

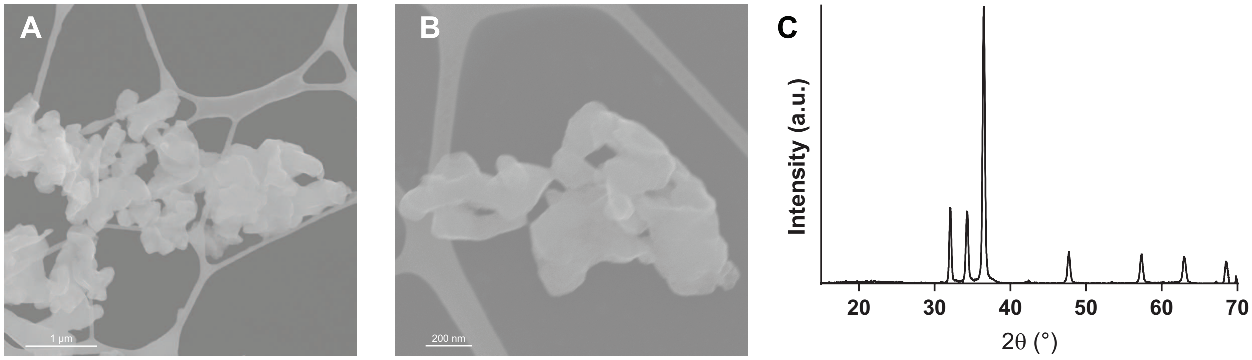

Figure 8.9: Additional GNR-Mg composites. (A) SEM image of Mg composite with cove-type GNR **8**. (B) SEM image of Mg composite with quinone-functionalized chevron-type GNR **72**. (C) PXRD of the GNR **8**-Mg composite.

indicate the degree to which analogous processes are important to the interaction between GNRs and a metal with a much lower work function. XRD and STEM imaging of these composites indicate no significant structural difference between them and the composites described above; characterization of their hydrogen storage performance is ongoing (Figure 8.9).

8.4 Conclusions and Future Work

This chapter has demonstrated that encapsulation within a network of narrow graphene nanoribbons imparts Mg nanocrystals with both an unprecedented degree of ambient stability (greater than 6 months without observed oxidation) and record-high hydrogen storage capacity (7.1-7.3 wt.% of H_2 by total composite mass). Furthermore, the synthetic tunability of bottom-up synthesized GNRs enabled an activation of hydrogen sorption kinetics at the magnesium interface, and the structural precision with which functionalized GNRs could be prepared led to an unrivaled degree of information about the role of specific heteroatom moieties. The observed kinetic results were consistent with calculations of the magnesium-GNR interface, and indicate a type of GNR-metal interfacial interaction distinct from those observed previously. These combined results empowered multiple rounds of rational design, again demonstrating the utility and versatility of bottom-up support nanomaterials. Future work will test the hydrogen storage capabilities of these latest-generation GNR-Mg nanocomposites, and will also look to extend this work to even more advanced hydrogen storage materials, such as magnesium borohydrides.

Chapter 9

GNR-Supported Ligand-Free Aluminum Nanoparticle Composites

In comparison with the widely studied inorganic nanomaterials discussed in the above chapters, aluminum nanoparticles (AlNPs) and their composites have seen less investigation of either their synthesis or their application. Aluminum microparticles and nanoparticles have historically been explored as propellants for applications like solid rocket boosters, which make use of aluminum's high energy density and high burn rate.[283] Al nanomaterials are also of interest as hydrogen storage materials, since aluminum hydride (AlH_3, also termed alane) offers a higher gravimetric capacity (10.1 wt.%) than magnesium hydride and readily desorbs hydrogen at comparatively low temperature.[283–285] However, formation of alane directly from aluminum metal is quite challenging, requiring extraordinarily high temperature and H_2 pressure.[284] In order for aluminum nanomaterials to become viable as hydrogen storage systems, an energy-efficient approach for directly generating alane must be developed. In this brief chapter, a ligand-free synthesis of GNR-AlNP composites is demonstrated, in the hope that these unusual materials might be investigated through alternative hydrogen storage methodologies.

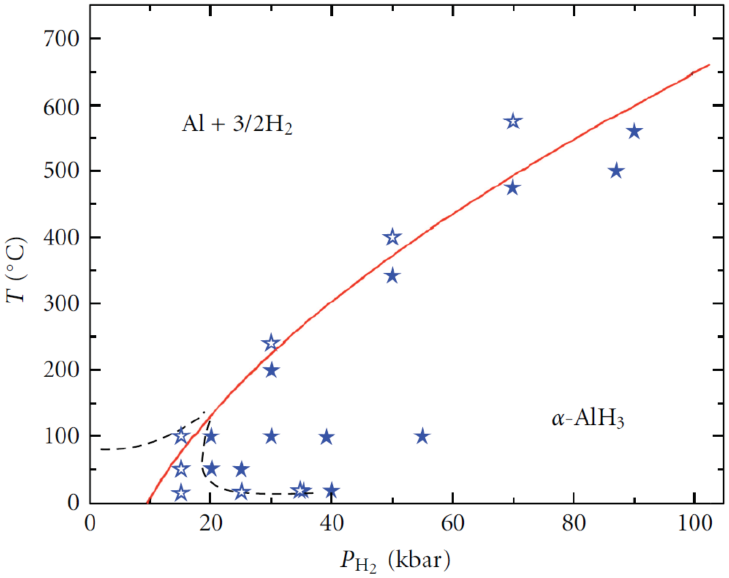

Figure 9.1: The phase diagram for Al and AlH_3 illustrates the inaccessibility of alane under mild hydrogenation conditions. Each marker represents an experimental result; solid stars indicate successful formation of AlH_3, while open stars indicate no reaction. Figure reproduced from reference [294].

9.1 Aluminum Nanoparticle Synthesis and Application

By far the most common wet-chemical synthetic approach to AlNPs is by titanium-catalyzed thermal decomposition of amine-adducts of AlH_3 with various capping or passivating agents, such as oleic acid, other carboxylic and perfluorocarboxylic acids, epoxides, dicarboxylates, or a thin layer of a transition metal.[286–293] Nanocrystals in these materials are occasionally as small as 30 nm, but are more frequently as large as 80–200 nm, and tend to aggregate with each other. Like magnesium nanoparticles, aluminum nanoparticles oxidize readily under ambient conditions, and fine aluminum nanoparticles can be pyrophoric, even when coated with certain capping agents.[286,288] A surface layer of aluminum oxide is generally evident for any AlNPs using organic capping ligands.[289]

Formation of aluminum hydride directly from aluminum is very challenging, requiring extremely high pressures of H_2 (>7kbar at 24 °C).[294] The transformation is not thermodynamically prohibitive; the free energy of formation ($\Delta G° = 46.5$ kJ mol^{-1}) is positive due to high entropic cost, but constitutes only 13% of the fuel energy contained in the fully formed hydride.[284] However, as Figure 9.1 makes clear, the low stability of the metastable alane precludes its direct synthesis under mild conditions.[294] One approach to circumvent challenging hydrogen sorption is electrochemical hydrogenation, making use of mild electrolytic potentials to drive hydrogen into a host material.[283,285] Efforts to generate electrochemically

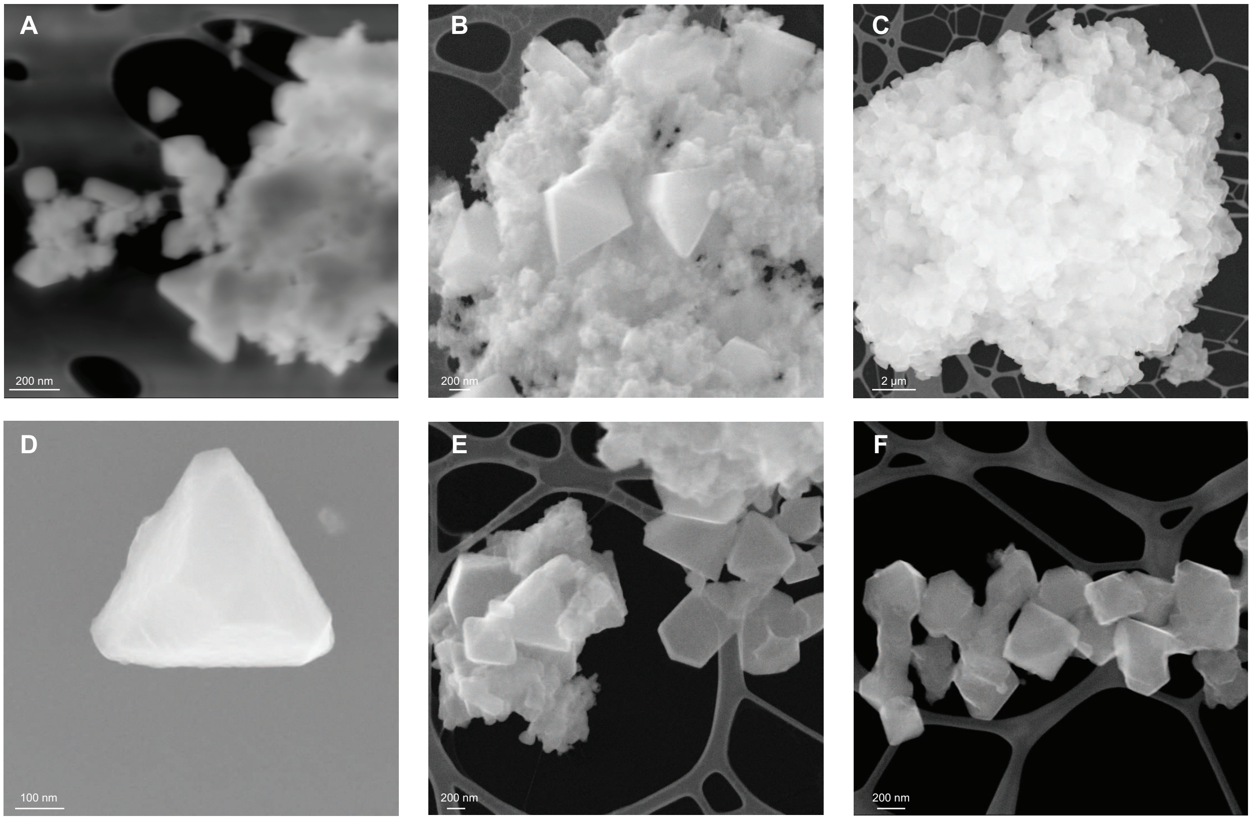

Figure 9.2: SEM and STEM images of aluminum nanoparticles. (A) STEM image of AlNPs capped with hexadecanoic acid (no GNR). (B) SEM image of AlNPs prepared with both hexadecanoic acid and GNR **5**. (C) SEM image of micron-sized Al particles formed when neither hexadecanoic acid or GNRs are used. (D-F) SEM images of AlNPs prepared as a composite with GNR **5** and without any capping ligand.

hydride aluminum date to the 1960s, when $NaAlH_4$ was used to electrochemically generate AlH_3 at an aluminum anode, and recent efforts have made significant progress in efficiently generating alane from Al foils in this manner.[284,295,296] It is for this electrochemical hydriding application that GNR-AlNP composites stood out as interesting materials. By using nanoscale aluminum and encapsulating the AlNPs within a conductive support material without oxide or capping ligands obscuring the Al surface, perhaps hydrogen can be introduced to the Al metal electrochemically using simple, low-energy chemical sources, thereby efficiently generating alane for reversible hydrogen storage.

9.2 Synthesis of GNR-AlNP Composites

To begin, AlNPs were synthesized by slight modification of a reported procedure through $Ti(OiPr)_4$-catalyzed decomposition of $AlH_3 \cdot N(Me)_2Et$ in Et_2O with hexadecanoic acid as

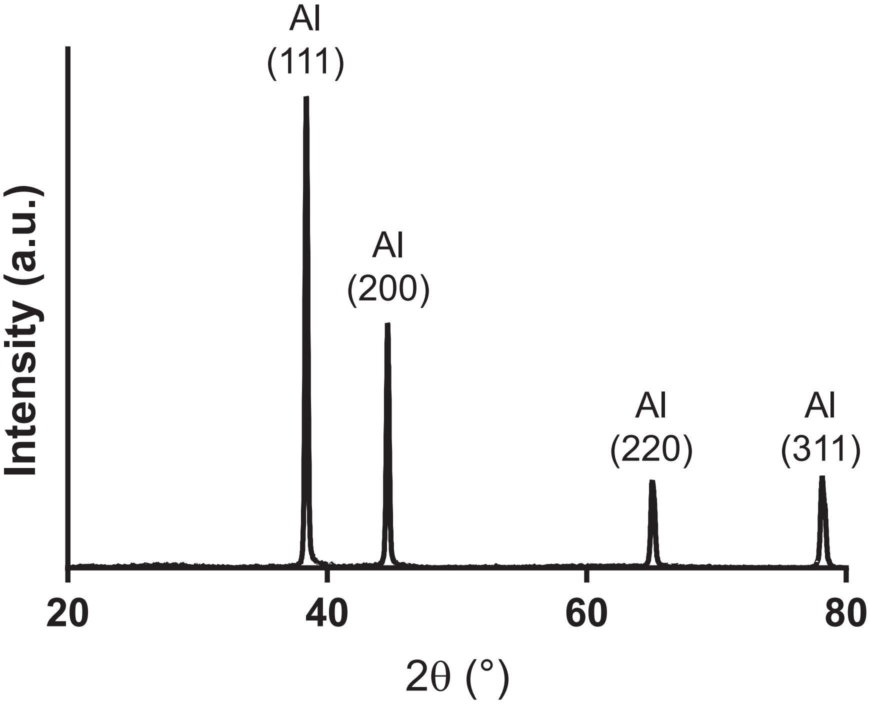

Figure 9.3: PXRD of the GNR **5**-AlNP composite. Scherrer analysis gives an average size of 70 nm.

capping ligand.[289,290] As is typical of AlNPs synthesized in this way, these nanoparticles were fairly large, frequently exhibited rough geometric forms (e.g. tetrahedra), and tended to aggregate with each other (Figure 9.2A). Then, another synthesis was performed identically, but with chevron-type GNR **5** included in the reaction mixture; these NPs appeared similar, seemingly featuring somewhat larger and more clearly defined geometric NPs (Figure 9.2B). For reference, the synthesis was also tested without the inclusion of any capping ligand (or GNRs), and as might be expected this produced shapeless particles several microns in size (Figure 9.2C). However, AlNP synthesis similarly carried out in the absence of any capping ligand but with GNR **5** included (1:8 mass ratio with $AlH_3 \cdot N(Me)_2Et$), forms defined, geometric AlNPs closely resembling those commonly synthesized with ligands. This suggests that interaction between the growing AlNPs and GNR **5** serves to template and control nanoparticle growth much in the way that ligands otherwise would, thereby yielding well-defined AlNPs without the typical insulating ligand layer. PXRD of the GNR-AlNP composites clearly illustrates the NPs are pure aluminum, and Scherrer analysis gives an average nanocrystalline domain size of 70 nm (Figure 9.3).

Several subsequent experiments began to explore and tune various means of synthetic control over these GNR-AlNP composites. AlNP synthesis, and in particular the size of the NPs produced, is known to be sensitive to solvent, so one batch was prepared with toluene in place of Et_2O (Figure 9.4A).[289] Although GNR-AlNP composites produced in toluene appeared to be larger and somewhat less well-formed, further experiments should examine other solvents frequently used for AlNP synthesis, such as THF or dioxane. Experiments using very low loadings of GNR **5** (50:1 $AlH_3 \cdot N(Me)_2Et$:GNR by mass) were not successful; these composites closely resembled the large particles formed without any GNR present (Figure 9.4B). When the concentration of $Ti(OiPr)_4$ catalyst is increased by a factor of 3–5, the impact on the resulting GNR-AlNP composite is surprisingly dramatic (Figure 9.4C&D). The AlNPs in that case seem increasingly well-defined, with a higher percentage adopting clear geometric forms, but also seem to aggregate more strongly, forming microns-wide superstructures of many AlNPs. It is unclear whether these AlNPs are fused to each other or simply aggregated.

In conclusion, the first GNR-AlNP composites were prepared, and the GNRs were found to perform quite capably at controlling AlNP growth even in the absence of any capping ligand. These encapsulated AlNP composites, lacking insulating ligands to obstruct their surface, could be interesting materials for reversible hydrogen storage, such as by the electrochemical generation of alane nanoparticles. Future synthetic efforts should focus on reducing AlNP domain size below 70 nm, perhaps through manipulation of solvent or temperature, to increase NP surface area and perhaps aid in hydriding the material.

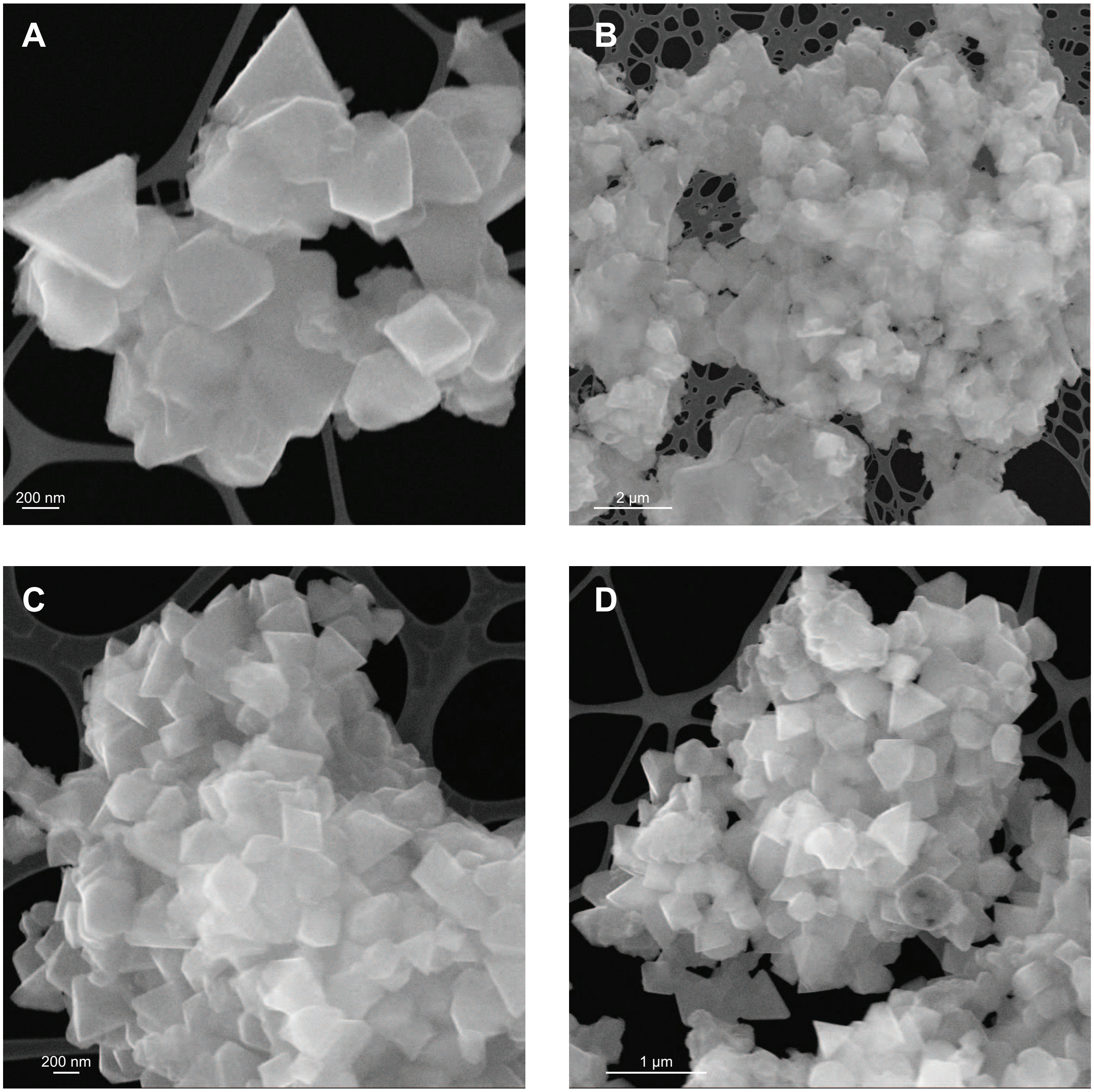

Figure 9.4: SEM and STEM images of GNR-AlNP composites. (A) SEM image of AlNPs synthesized in toluene. (B) SEM image of micron-sized Al particles formed when very little GNR **5** is used. (C&D) SEM images of large AlNP composite aggregrates formed when an increased concentration of $Ti(OiPr)_4$ catalyst is used.

Part IV

Supplementary Information

Chapter 10

Synthetic Methods

10.1 Materials and General Methods

Unless otherwise stated, all manipulations of air and/or moisture sensitive compounds were carried out in oven-dried glassware, under an atmosphere of Nitrogen. All solvents and reagents were purchased from Alfa Aesar, Spectrum Chemicals, Acros Organics, TCI America, and Sigma-Aldrich and were used as received unless otherwise noted. Organic solvents were dried by passing through a column of alumina and were degassed by vigorous bubbling of N_2 through the solvent for 20 min. Flash column chromatography was performed on SiliCycle silica gel (particle size 40-63 μm). Thin layer chromatography was carried out using SiliCycle silica gel 60 Å F-254 precoated plates (0.25 mm thick) and visualized by UV absorption. All ^{1}H and ^{13}C NMR spectra were recorded on a Bruker AV-600, AV-500, DRX-500, AVB-400, AVQ-400, or AV-300 spectrometer and are referenced to residual solvent peaks ($CDCl_3$ ^{1}H NMR = 7.26 ppm, ^{13}C NMR = 77.16 ppm; CD_2Cl_2 ^{1}H NMR = 5.32 ppm, ^{13}C NMR = 53.84 ppm). ESI mass spectrometry was performed on a Finnigan LTQFT (Thermo) spectrometer in positive ionization mode. Gel permeation chromatography (GPC) was carried out on a LC/MS Agilent 1260 Infinity set up with a guard and two Agilent Polypore 300 x 7.5 mm columns at 35 °C. All GPC analyses were performed on a 0.2 mg/mL solution of polymer in chloroform. An injection volume of 25 μL and a flow rate of 1 mL/min were used. Calibration was based on narrow polydispersity polystyrene standards ranging from Mw = 100 to 4,068,981. UV-Vis spectroscopic measurements were conducted in a Varian Cary 50 spectrophotometer (Agilent, USA). X-ray crystallography of **4** was performed on APEX II QUAZAR, using a Microfocus Sealed Source (Incoatec IS; Mo K radiation), Kappa Geometry with DX (BrukerAXS build) goniostat, a Bruker APEX II detector, QUAZAR multilayer mirrors as the radiation monochromator, and Oxford Cryostream 700. Crystallographic data were solved with SHELXT, refined with SHELXL-2014, visualized with ORTEP-32, and finalized with WinGX. X-ray absorption fine structure spectroscopy (NEXAFS) was performed on Beamline 8.0.1.3, 6.3.1, and 4.0.3 at the Advanced Light Source (ALS). The energy resolution was set to 0.1 eV, and the experimental chamber had a base pressure of $1x10^{-8}$ torr. A reference sample was measured for energy calibration before and after all NEXAFS experiments. Compounds **37**[171], **38**[172], **10**[175], **61**[177], **19**[129], **68**[123], **69**[123], **6**[126], **79**[180], and **90**[181] were synthesized by reported procedures.

10.2 Organic Synthetic Procedures

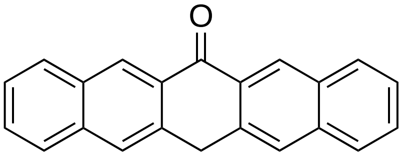

37

Pentacen-6(13H)-one (**37**): A 500 mL Erlenmeyer flask was charged with pentacene-6,13-dione (7.0 g, 22.7 mmol) in conc. H_2SO_4 (150 mL). The solution was transferred into H_2O (500 mL) in a 2 L Erlenmeyer. The yellow precipitate was collected by filtration and washed thoroughly with hot H_2O. A 2 L two-neck flask was charged under N_2 with the yellow precipitate in H_2O (500 mL), 30% aqueous NaOH solution (100 mL), and sodium dithionite (40.0 g, 0.230 mol). The reaction mixture was heated to 110 °C for 90 min. The mixture was filtered hot and washed with a solution of H_2O (250 mL), 30% aqueous NaOH solution (50 mL), and sodium dithionite (20.0 g, 0.115 mol). The residue was further washed with hot H_2O until the filtrate was neutral. The product was recrystallized from pyridine to yield **37** (3.07 g, 10.43 mmol, 46%) as a colorless solid. ^{1}H NMR (500 MHz, CD_2Cl_2, 22 °C): δ = 8.92 (s, 2H), 8.09 (d, J = 8.3 Hz, 2H), 8.00 (s, 2H), 7.92 (d, J = 8.7 Hz, 2H), 7.63 (t, J = 7.3 Hz, 2H), 7.55 (t, J = 7.4 Hz, 2H), 4.72 (s, 2H) ppm; ^{13}C NMR (151 MHz, $CDCl_3$, 25 °C): = 185.5, 135.8, 135.8, 132.1, 130.5, 130.1, 129.5, 128.8, 127.3, 126.9, 126.3, 77.2, 32.7 ppm; HRMS (ESI) m/z: calcd for $C_{22}H_{14}$ $[M]^+$ 294.1045, found 294.1043.

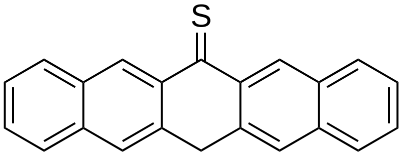

38

Pentacen-6(13H)-thione (**38**): A 500 mL two-neck flask was charged under N_2 with **37** (2.54 g, 8.63 mmol) in dry degassed toluene (200 mL). Lawessons reagent (2.45 g, 6.06 mmol) was added and the reaction mixture was heated to 80 °C for 2 h and then cooled to 24 °C. The reaction mixture was diluted with 4:1 hexane:CH_2Cl_2 (600 mL), filtered through a plug of SiO_2, and washed with 4:1 hexane:CH_2Cl_2 (700 mL) until the filtrate was colorless. The combined organic layers were concentrated on a rotary evaporator. The dark residue was triturated with hexane to yield **38** (1.66 g, 5.35 mmol, 62%) as a green-brown solid. ^{1}H NMR (400 MHz, CD_2Cl_2, 22 °C): δ = 9.11 (s, 2H; CH), 8.07 (d, ^3J(H,H) = 8.3 Hz, 2H; CH), 7.92 (s, 2H; CH), 7.88 (d, ^3J(H,H) = 8.3 Hz, 2H; CH), 7.62 (t, ^3J = 7.5 Hz, 2H; CH), 7.51

(t, ^3J = 7.5 Hz, 2H; CH), 4.56 (s, 2H; CH_2) ppm; ^{13}C NMR (126 MHz, CD_2Cl_2, 25 C): δ = 223.7, 139.5, 135.6, 132.6, 131.8, 131.0, 130.5, 129.0, 127.4, 126.6, 126.2, 100.2, 35.0 ppm; HRMS (ESI) *m/z*: calcd for $C_{22}H_{15}S$ $[M+H]^+$ 311.0894, found 311.0890.

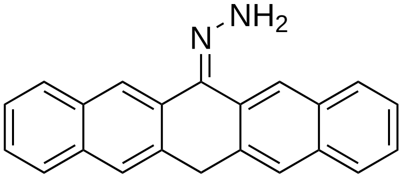

39

Pentacen-6(13H)-ylidenehydrazone (**39**): A 500 mL two-neck flask was charged under N_2 with **38** (3.84 g, 12.4 mmol) in 1-propanol (120 mL). Hydrazine monohydrate (120 mL, 2.47 mol) was added and the reaction mixture was heated to 120 °C for 3 h. The reaction mixture was cooled to 0 °C and the precipitate was isolated by filtration to yield **39** (2.58 g, 8.37 mmol, 68%) as a colorless solid. ^{1}H NMR (500 MHz, CD_2Cl_2, 22 °C): δ = 8.57 (s, 1H), 8.24 (s, 1H), 7.95-7.87 (m, 3H), 7.85 (d, ^3J(H,H) = 8.0 Hz, 1H), 7.82-7.77 (m, 2H), 7.54 (d, ^3J(H,H) = 6.8 Hz, 1H), 7.50 (d, ^3J(H,H) = 6.8 Hz, 1H), 7.46-7.41 (m, 2H), 6.22 (s, 2H), 4.30 (s, 2H) ppm; ^{13}C NMR (126 MHz, $CDCl_3$, 25 °C): δ = 164.7, 136.0, 133.8, 133.6, 133.3, 132.7, 131.6, 128.9 (2C), 128.9, 128.2, 127.9, 127.4, 127.2, 127.1, 127.0, 126.6, 126.1, 125.5 (2C), 124.7, 77.2, 36.4 ppm; HRMS (ESI) *m/z*: calcd for $C_{22}H_{17}N_2$ $[M+H]^+$ 309.1386, found 309.1385.

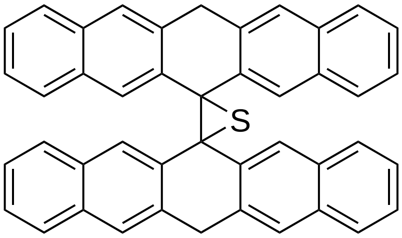

2

13H,13"H-dispiro[pentacene-6,2'-thiirane-3',6"-pentacene] (**2**): An oven-dried 1000 mL two-neck flask was charged under N_2 with **39** (2.58 g, 8.37 mmol) in dry CH_2Cl_2 (500 mL). $MgSO_4$ (63.0 g, 0.523 mol) and MnO_2 (16.2 g, 0.186 mol) were added, followed by saturated NaOH in dry MeOH (5 mL). The reaction mixture was stirred at 24 °C for 1 h, then filtered under N_2 into a 2 L two-neck flask charged with **38** (1.10 g, 3.54 mmol) in dry CH_2Cl_2 (200 mL) under N_2. The reaction mixture was stirred at 24 °C for 12 h and concentrated under dynamic vacuum. Column chromatography (SiO_2 ; 4:1 hexanes:CH_2Cl_2) yielded **2** (1.30 g, 2.21 mmol, 63%) as a pale solid. ^{1}H NMR (600 MHz, CD_2Cl_2, 22 °C): δ = 8.41 (s, 4H; CH), 7.83 (d, ^3J(H,H) = 7.6 Hz, 4H; CH), 7.59 (d, ^3J(H,H) = 7.2 Hz, 4H; CH), 7.53 (s, 4H; CH), 7.34-7.29 (m, 8H; CH), 4.41 (d, ^2J(H,H) = 16.4 Hz, 2H; CHH), 4.14 (d, ^2J(H,H) = 16.3 Hz, 2H; CH*H*) ppm; ^{13}C NMR (151 MHz, CD_2Cl_2, 25 °C): δ = 136.3, 133.3, 132.7, 131.9, 129.4, 128.2, 127.0, 126.5, 125.9, 125.1, 67.3, 37.5 ppm; HRMS (ESI) *m/z*: calcd for $C_{44}H_{28}S$ $[M]^+$ 588.1912, found 588.1902.

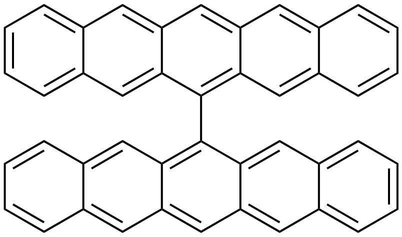

3

6,6-bipentacene (**3**): A 25 mL two-neck flask was charged under N_2 with **2** (50 mg, 0.085 mmol) in dry degassed tetrahydrofuran (12 mL). The solution was cooled to -78 °C and lithium diisopropylamine (2.0 M solution in tetrahydrofuran, 0.43 mL, 0.86 mmol) was added slowly. The reaction mixture was stirred at -78 °C for 30 min, then warmed to 24 °C and stirred for 3 h, followed by the addition of degassed methanol (2 mL). The reaction mixture was concentrated under dynamic vacuum and the residue was purified by recrystallization (benzene) to give **3** (26 mg, 0.47 mmol, 55%) as a blue solid. ^{1}H NMR (600 MHz, C_6D_6, 22 °C): $\delta = 9.21$ (s, 2H), 8.70 (s, 4H), 8.15 (s, 4H), 7.75 (d, ^3J(H,H) = 9.1 Hz, 4H), 6.96 (d, ^3J(H,H) = 7.3 Hz, 4H), 6.72-6.69 (m, 4H), 6.67-6.63 (m, 4H) ppm; ^{13}C NMR (151 MHz, CD_2Cl_2, 25 °C): $\delta = 134.1$, 132.3, 131.9, 131.0, 130.8, 128.9, 128.4, 128.4, 127.4, 125.8, 125.8, 125.5 ppm; HRMS (ESI) *m/z*: calcd for $C_{44}H_{27}$ $[M+H]^+$ 555.2107, found 555.2117.

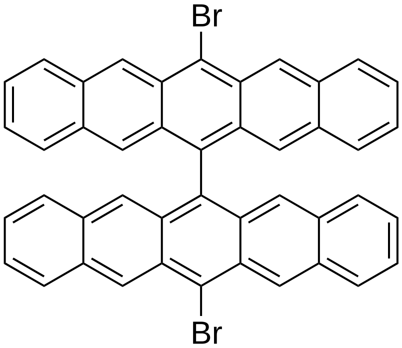

4

13,13'-dibromo-6,6'-bipentacene (**4**): A 50 mL two-neck flask was charged under N_2 with **2** (100 mg, 0.17 mmol) in dry degassed tetrahydrofuran (25 mL). The solution was cooled to -78 °C and lithium diisopropylamine (2.0 M solution in tetrahydrofuran, 1.70 mL, 3.4 mmol) was added slowly. The reaction mixture was stirred at -78 °C for 60 min, then warmed to 24 °C and stirred for 2 h, followed by the addition of degassed methanol (1 mL). The reaction mixture was concentrated under dynamic vacuum and the residue was redissolved in dry, degassed CH_2Cl_2 (40 mL). The reaction mixture was cooled to -78 °C and Br_2 (54 mg, 0.34 mmol, 18 μL) was added as a solution in degassed CH_2Cl_2. The reaction mixture was stirred 30 min at -78 °C, then warmed to 24 °C and stirred for 1 h. The reaction mixture was then concentrated under dynamic vacuum. Column chromatography (SiO_2; 1:9 CH_2Cl_2/hexanes) yielded **4** (13 mg, 18 μmol, 11% (two steps)). ^{1}H NMR (500 MHz, CD_2Cl_2, 22 °C): $\delta = 9.44$ (s, 4H), 8.08 (d, J(H,H) = 8.8 Hz, 4H), 7.75 (s, 4H), 7.33 (dd, J(H,H) = 8.6, 6.5 Hz, 4H), 7.28 (d, J(H,H) = 8.8 Hz, 4H), 7.10 (dd, J(H,H) = 8.7, 6.4 Hz, 4H) ppm. Dark crystals of

4 suitable for X-ray analysis were obtained from saturated toluene at -25 °C; **4** crystallizes in the triclinic space group $P\bar{1}$.

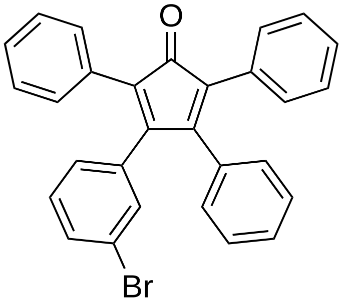

77

3-(3-Bromophenyl)-2,4,5-triphenylcyclopenta-2,4-dien-1-one (**77**): A 100 mL three neck round bottom flask with reflux condenser was charged under N_2 with 1,3-diphenylpropan-2-one (113 mg, 0.54 mmol), and 1-(3-bromophenyl)-2-pheylethane-1,2-dione (**76**) (150 mg, 0.52 mmol) in tBuOH (15 mL). The reaction mixture was heated to 80 °C and an aqueous solution of $N(CH_3)_4OH$ (20%, 0.15 mL, 0.21 mmol) was added. The reaction mixture was stirred at 80 °C for 1 h. The reaction mixture was cooled to 24 °C and quenched with 1M HCl (10 mL). The solution was cooled to 0 °C and the purple solid was filtered and washed with cold MeOH to yield compoundcovecpd (162 mg, 0.35 mmol, 68%). ^{1}H NMR (600 MHz, CD_2Cl_2, 22 °C): δ = 7.40-7.38 (m, 1H), 7.30-7.21 (m, 13H), 7.09-7.06 (m, 2H), 6.96-6.94 (m, 2H), 6.90-6.88 (m, 1H) ppm; ^{13}C NMR (101 MHz, $CDCl_3$, 22 °C) δ = 200.5, 155.0, 153.3, 135.9, 133.4, 132.6, 131.9, 131.3, 131.0, 130.7, 130.2, 129.7, 129.2, 128.7, 128.6, 128.5, 128.3, 128.1, 126.7, 126.0, 122.4 ppm; HRMS (EI$^+$) *m/z*: calcd for $C_{14}H_9I$ $[M]^+$ 303.9749, found 303.9751.

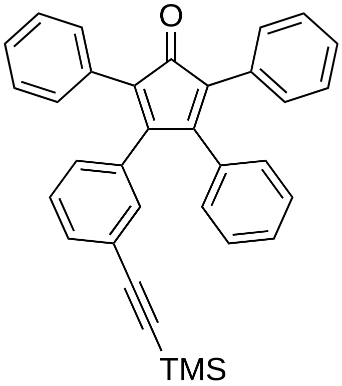

78

2,3,5-Triphenyl-4-(3-((trimethylsilyl)ethynyl)phenyl)cyclopenta-2,4-dien-1-one (**78**): A 50 mL Schlenk flask was charged under N_2 with **77** (162 mg, 0.35 mmol), $Pd(PPh_3)_4$ (70.4 mg, 0.061 mmol), and CuI (6.7 mg, 0.035 mmol) in Et_3N (20 mL). The reaction mixture was degassed and ethynyltrimethylsilane (0.16 mL, 1.09 mmol) was added dropwise. The reaction mixture was stirred at 80 °C for 18 h. The solvent was removed on a rotary evaporator, the residue dissolved in CH_2Cl_2, washed with saturated aqueous NH_4Cl solution, saturated aqueous NaCl solution, dried over $MgSO_4$, and concentrated on a rotary evaporator. Column chromatography (SiO_2; 7:13 CH_2Cl_2/hexanes) yielded **78** (86.8 mg, 0.18 mmol, 51%) as a purple solid. ^{1}H NMR (400 MHz, CD_2Cl_2, 22 °C): δ = 7.35-7.32 (m, 1H), 7.29-7.12 (m, 14H), 7.06-7.04 (m, 1H), 6.95-6.93 (m, 2H), 6.91-6.88 (m, 1H), 0.19 (s, 9H) ppm; ^{13}C NMR (101 MHz, CD_2Cl_2, 22 °C) δ = 200.7, 155.1, 154.2, 134.2, 133.4, 132.5, 132.4, 131.4, 131.1, 130.7, 130.6, 129.9, 129.7, 129.1, 128.7, 128.6, 128.6, 128.5, 128.2, 128.1, 126.3, 125.8, 123.6, 104.6, 95.4, 0.02 ppm; HRMS (EI$^+$) *m/z*: calcd for $C_{34}H_{28}OSi$ $[M]^+$ 480.1909, found 480.1912.

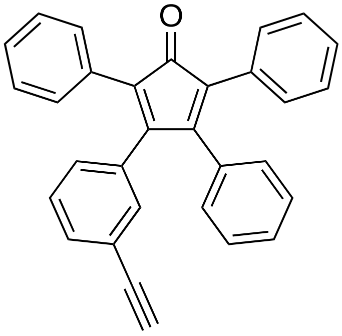

74

3-(3-Ethynylphenyl)-2,4,5-triphenylcyclopenta-2,4-dien-1-one (**74**): A 100 mL Schlenk flask was charged under N_2 with **78** (247 mg, 0.51 mmol), and KF (305 mg, 5.25 mmol) in THF/MeOH (1:1, 50 mL). The reaction mixture was stirred at 40 °C for 4 h. The solvent was removed on a rotary evaporator. Column chromatography (SiO_2; 2:3 CH_2Cl_2/hexane) yielded **74** (194 mg, 0.48 mmol, 93%) as a purple solid. ^{1}H NMR (600 MHz, CD_2cl_2, 22 °C): δ = 7.39-7.36 (m, 1H), 7.30-7.15 (m, 14H), 7.08-7.06 (m, 1H), 6.96-6.92 (m, 3H), 3.05 (s, 1H) ppm; ^{13}C NMR (125 MHz, CD_2Cl_2, 22 °C) δ = 200.6, 155.0, 153.9, 134.2, 133.4, 133.1, 132.6, 131.3, 131.1, 130.7, 130.3, 129.8, 129.2, 128.7, 128.6, 128.5, 128.3, 128.1, 126.5, 125.9, 122.5, 83.3, 78.3 ppm; HRMS (EI$^+$) *m/z*: calcd for $C_{31}H_{20}O$ $[M]^+$ 408.1514, found 408.1510.

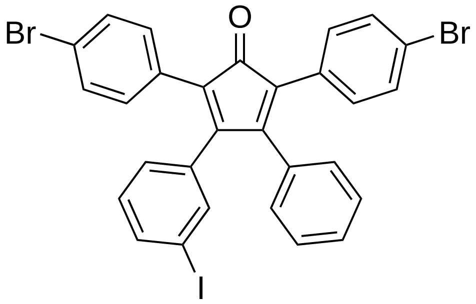

80

2,5-Bis(4-bromophenyl)-3-(3-iodophenyl)-4-phenylcyclopenta-2,4-dien-1-one (**80**): A 500 mL three neck round bottom flask with reflux condenser was charged under N_2 with 1,3-bis(4-bromophenyl)propan-2-one (4.23 g, 11.5 mmol), and 1-(3-iodophenyl)-2-pheylethane-1,2-dione **82** (3.86 g, 11.5 mmol) in tBuOH (340 mL). The reaction mixture was heated to 80 °C and an aqueous solution of $N(CH_3)_4OH$ (20%, 3.4 mL, 4.59 mmol) was added. The reaction mixture was stirred at 80 °C for 1 h. The reaction mixture was cooled to 24 °C and quenched with 1M HCl (65 mL) and extracted with CH_2Cl_2. The combined organic phases were washed with H_2O, dried over $MgSO_4$ and concentrated on a rotary evaporator. Column chromatography (SiO_2; 3:7 CH_2Cl_2/hexane) yielded **80** (6.32 g, 9.46 mmol, 82%) as a purple solid. ^1H NMR (400 MHz, CD_2Cl_2, 22 °C): δ = 7.64-7.61 (m, 1H), 7.44-7.37 (m, 4H), 7.36-7.34 (m, 1H), 7.26-7.22 (m, 3H), 7.14-7.09 (m, 4H), 6.98-6.91 (m, 4H) ppm; ^{13}C NMR (101 MHz, CD_2Cl_2, 22 °C) δ = 199.7, 155.6, 153.7, 138.4, 138.3, 135.4, 132.9, 132.2 (2C), 131.9, 131.8, 130.4, 130.2, 129.8, 129.7, 129.6, 129.0, 128.9, 125.5, 125.0, 122.7, 122.5, 94.1 ppm; HRMS (EI^+) *m/z*: calcd for $C_{29}H_{17}Br_2IO$ $[M]^+$ 669.8650, found 669.8652.

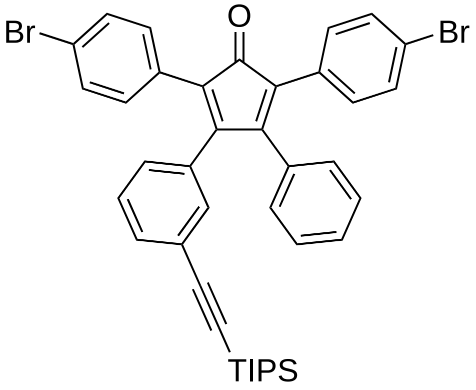

95

2,5-Bis(4-bromophenyl)-3-phenyl-4-(3-((triisopropylsilyl)ethynyl)phenyl)cyclopenta-2,4-dien-1-one (**81**): A 100 mL Schlenk flask was charged under N_2 with **80** (0.57 g, 0.85 mmol), $Pd(PPh_3)_4$ (98.1 mg, 0.085 mmol), and CuI (16.2 mg, 0.085mmol) in Et_3N (50 mL). The reaction mixture was degassed and ethynyltriisopropylsilane (0.25 mL, 1.07 mmol) was added dropwise. The reaction mixture was stirred at 30 °C for 12 h. The solvent was removed on a rotary evaporator, the residue dissolved in CH_2Cl_2, washed with saturated aqueous NH_4Cl solution, saturated aqueous NaCl solution, dried over $MgSO_4$, and concentrated on a rotary evaporator. Column chromatography (SiO_2; 1:2 CH_2Cl_2/hexane) yielded **81** (0.52 g, 0.71 mmol, 84%) as a purple solid. ^1H NMR (300 MHz, CD_2Cl_2, 22 °C): δ = 7.42-7.32 (m, 5H), 7.29-7.20 (m, 3H), 7.17-7.10 (m, 5H), 6.95-6.89 (m, 4H), 1.06 (s, 21H) ppm; ^{13}C NMR (101 MHz, CD_2Cl_2, 22 °C) δ = 199.8, 155.7, 154.5, 133.5, 133.2, 133.1, 132.4, 132.2, 131.9, 131.8, 130.2, 130.1, 129.7, 129.6, 129.5, 128.8, 128.7, 125.4, 125.0, 123.9, 122.6, 122.4, 106.7, 92.2, 18.9, 11.8 ppm; HRMS (EI^+) *m/z*: calcd for $C_{40}H_{38}Br_2OSi$ $[M]^+$ 722.1038, found 722.1046.

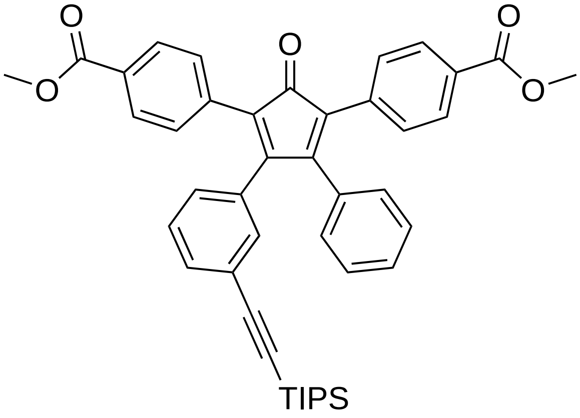

83

4,4'-(2-Oxo-4-phenyl-5-(3-((triisopropylsilyl)ethynyl)phenyl)cyclopenta-3,5-diene-1,3-diyl) dibenzoate (**83**): A 10 mL two-neck flask was charged under N_2 with **81** (0.32 g, 0.44 mmol), $Pd(OAc)_2$ (4.00 mg, 0.018 mmol), 4,5-bis(diphenylphosphino)-9,9-dimethylxanthene (20 mg, 0.035 mmol), MeOH (0.36 mL, 8.86 mmol) and Et_3N (2 mL). The reaction mixture was saturated with CO for 10 min, and stirred under 1 bar CO at 24 °C for 16 h. The reaction mixture was diluted with AcOEt and filtered through Celite. The solvent was removed on a rotary evaporator. Column chromatography (SiO_2; 3/17 AcOEt/hexane) yielded **83** as a dark red solid (102 mg, 0.15 mmol, 34%). ^1H NMR (600 MHz, CD_2Cl_2, 22 °C): $\delta = 7.90$ (dd, J = 16.6, 8.0 Hz, 4H), 7.36 (d, J = 7.7 Hz, 1H), 7.32-7.29 (m, 5H), 7.23 (t, $J = 7.6$ Hz, 2H), 7.14 (t, $J = 7.8$ Hz, 1H), 7.96-7.92 (m, 3H), 7.90 (d, $J = 7.8$ Hz, 1H), 3.87 (s, 6H), 1.06-1.02 (m, 21H) ppm; ^{13}C NMR (151 MHz, CD_2Cl_2, 22 °C) $\delta = 199.3$, 155.5 (2C), 136.1 (2C), 135.7, 135.6, 133.5, 133.0, 132.8, 132.4, 130.5 (2C), 130.5 (2C), 129.8, 129.6 (2C), 129.6, 129.5 (2C), 129.5 (2C), 128.7 (2C), 128.6, 125.9, 125.4, 123.9, 106.5 (2C), 95.6, 92.1, 52.4 (2C), 18.8 (6C), 11.7 (3C) ppm; MALDI MS *m/z* calcd for $C_{44}H_{45}O_6Si$ $[M+OH]^+$ 697.30, found 697.24.

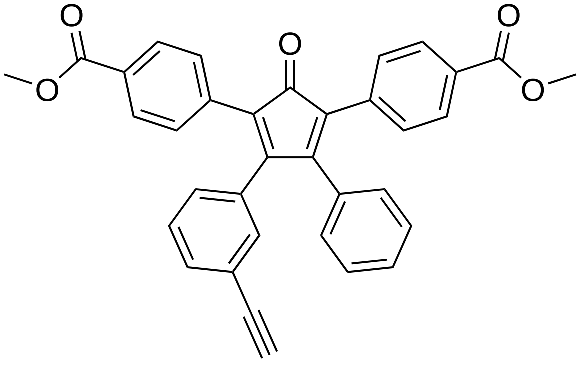

84

4,4'-(4-(3-Ethynylphenyl)-2-oxo-5-phenylcyclopenta-3,5-diene-1,3-diyl)dibenzoate (**84**): A 10 mL two-neck flask was charged under N_2 with **83** (260 mg, 0.38 mmol), AgF (72 mg, 0.57 mmol), and DMF (4 mL). The reaction mixture was stirred at 24 °C for 12 h. TFA (0.06 mL, 0.76 mmol) was added and the reaction mixture stirred for 10 min. The reaction mixture was diluted with Et_2O, washed with H_2O, dried over $MgSO_4$, and concentrated on a rotary evaporator. Column chromatography (SiO_2; 3:17 AcOEt/hexane) yielded **84** as a dark red solid (120 mg; 0.23 mmol, 60%). ^{1}H NMR (500 MHz, CD_2Cl_2, 22 °C): δ = 7.90 (t, J = 8.6 Hz, 4H), 7.41 (d, J = 7.8 Hz, 1H), 7.34-7.29 (m, 5H), 7.22 (t, J = 7.7 Hz, 2H), 7.18 (t, J = 7.8 Hz, 1H), 7.06 (s, 1H), 6.94-6.91 (m, 3H), 3.87 (s, 3H), 3.87 (s, 3H), 3.06 (s, 1H) ppm; MALDI MS m/z calcd for $C_{35}H_{25}O_6$ $[M+OH]^+$ 541.17, found 541.23.

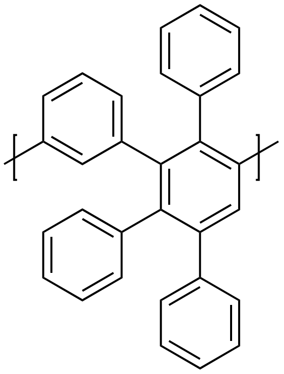

75

poly-compoundcovemono (**75**): A 10 mL Schlenk flask was charged under N_2 with **74** (48.2 mg, 0.12 mmol) in Ph_2O (0.22 mL). The reaction mixture was stirred at 230 °C for 18 h. The reaction mixture was diluted with MeOH and the precipitate was collected via centrifugation. The solid residue was dissolved in THF, triturated with MeOH, and collected via centrifugation to yield **75** (21 mg, 47%) as a colorless solid. ^{1}H NMR (400 MHz, $CDCl_3$, 22 °C): δ = 7.21–6.97 (m, 6H), 6.96–6.78 (m, 5H), 6.76–6.41 (m, 7H), 6.40–6.21 (m, 2H) ppm.

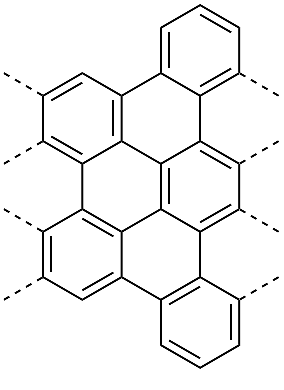

8

Cove-GNR (**8**): A 500 mL Schlenk flask was charged under N_2 with **75** (50 mg) in CH_2Cl_2 (250 mL). A suspension of $FeCl_3$ (1.49 g, 9.20 mmol, 7 equiv for one hydrogen to be removed) in $MeNO_2$ (14 mL) was added. The reaction mixture was stirred at 24 C for 72 h under a continuous stream of N_2. The reaction mixture was quenched with MeOH and filtered.

Washing the precipitate with MeOH (500 mL), 1M HCl (300 mL), H_2O (1000 mL), and THF (500 mL), yielded **8** as a black powder (48 mg, 99%). Raman (powder): 222, 1341, 1608, 2667, 2869, 2935, 3206 cm^{-1}.

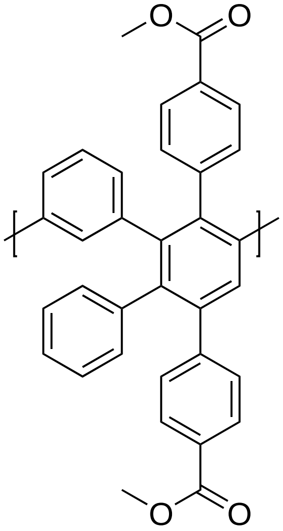

85

*Poly-**84*** (**85**): A 10 mL Schlenk flask was charged under N_2 with **84** (120 mg, 0.23 mmol) in Ph_2O (0.56 mL). The reaction mixture was stirred at 230 °C for 18 h. The reaction mixture was diluted with MeOH and the precipitate was collected via centrifugation. The solid residue was dissolved in THF, triturated with MeOH, and collected via centrifugation to yield **85** (50 mg, 44%) as a colorless solid. ^1H NMR (500 MHz, CD_2Cl_2, 22 °C): $\delta =$ 7.93–7.77 (m, 2H), 7.71–7.45 (m, 2H), 7.17–7.04 (m, 2H), 7.00–6.23 (m, 12H), 3.94–3.77 (m, 6H) ppm.

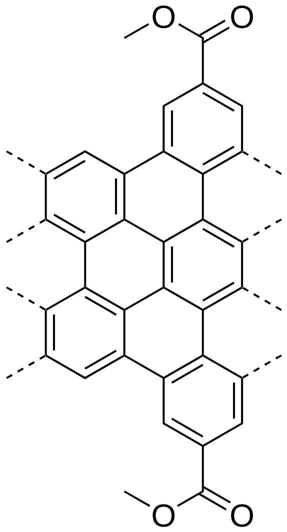

7

Cove$_{ester}$-GNR (**7**): A 500 mL Schlenk flask was charged under N_2 with **84** (50 mg) in CH_2Cl_2 (250 mL). A suspension of $FeCl_3$ (1.3 g, 8.0 mmol, 7 equiv for one hydrogen to be removed) in $MeNO_2$ (14 mL) was added. The reaction mixture was stirred at 24 °C for 72 h under a continuous stream of N_2. The reaction mixture was quenched with MeOH and filtered. Washing the precipitate with MeOH (500 mL), 1M HCl (300 mL), H_2O (1000 mL), and THF (500 mL), yielded **7** as a black powder (48 mg, 99%). Raman (powder): 1303, 1582, 2587, 3180, 2875 cm^{-1}.

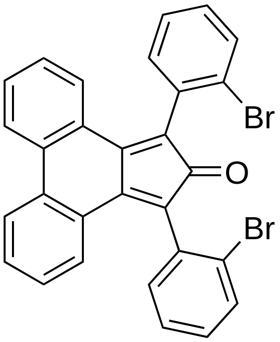

91

1,3-bis(2-bromophenyl)-2H-cyclopenta[l]phenanthren-2-one (**91**): A 25 mL round-bottom flask was charged under air with 1,3-bis(2-bromophenyl)propan-2-one (550 mg, 1.49 mmol), phenanthrenequinone (310 mg, 1.49 mmol), and MeOH (4 mL). To this reaction mixture, a solution of KOH (92 mg, 1.64 mmol) in MeOH (6 mL) was added dropwise. The reaction was heated to 65 °C for 90 min, then cooled to 24 °C and quenched with 1 M HCl, follwed by aqueous/organic workup with DCM. Column chromatography (SiO_2 ; 1:1 hexanes:CH_2Cl_2) yielded **91** as a green solid (588 mg, 1.09 mmol, 73%). ^1H NMR (400 MHz, CD_2Cl_2, 22 °C): δ = 7.87 (d, 2H), 7.75–7.70 (m, 2H), 7.47–7.42 (m, 2H), 7.35–7.27 (m, 6H), 7.12–7.08 (m, 2H), 6.99–6.94 (m, 2H) ppm.

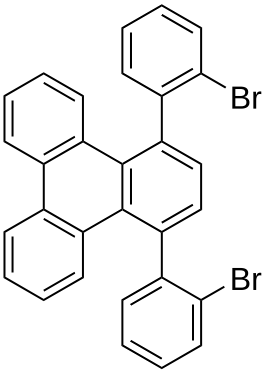

15

1,4-bis(2-bromophenyl)triphenylene (**15**): A narrow 5 mL sealable tube was charged under N_2 with **91** (500 mg, 0.93 mmol), norbornadiene (170 mg, 1.85 mmol, 0.19 mL) and toluene (3 mL). The tube was sealed and heated to 115 °C for 24 h. After cooling to 24 °C, the toluene was removed under vacuum. Column chromatography (SiO_2 ; 3:1 hexanes:CH_2Cl_2) followed by recrystallization from $CHCl_3$ yielded **91** as a colorless solid (155 mg, 0.29 mmol, 30%). ^{1}H NMR (500 MHz, CD_2Cl_2, 22 °C): δ = 8.75 (d, 2H), 8.91 (d, 2H), 7.67 (t, 2 H), 7.64 (t, 2H), 7.56 (t, 2H), 7.40 (t, 2H), 7.25 (t, 2H), 7.16 (d, 2H), 6.43 (s, 2H) ppm.

10.3 Nanoparticle & Composite Synthetic Procedures

Chapter 5

AuNP Synthesis. A 50 mL Schlenk flask was charged under Ar with 1-octadecene (10 mL) and heated to 125 °C for 30 min with stirring. The reaction was cooled to 24 °C, and oleic acid (0.32 mL, 283 mg, 1.0 mmol), oleylamine (0.33 mL, 268 mg, 1.0 mmol), chloroauric acid trihydrate (118 mg, 0.3 mmol), and 1,2-hexadecanediol (517 mg, 2 mmol) were added. The mixture was heated under Ar to 210 °C and stirred for 3 h before cooling to 24 °C. The product was precipitated by addition of a mixture of EtOH (2 mL) and acetone (8 mL) and collected by centrifugation (7500 rpm, 8 min). The collected solid was dried under vacuum to yield AuNPs as a gold-colored solid (32 mg). AuNPs were redispersed in hexane (2 mg mL^{-1}) prior to use.

Preparation of GNR-AuNP Composite Materials. A 3 mL vial was charged with GNRs (0.3 mg) and AuNPs (0.3 mg) in hexane (1 mL). The mixture was sonicated for 1 h. The precipitate was collected by vacuum filtration, washed thoroughly with hexane, and dried under vacuum. The solid was annealed in air for 10 h at 185 °C to yield GNR-AuNP composite as a black powder.

Preparation of GNR-AuNP Composite Samples for TEM. Samples of GNR-AuNP composite for TEM were prepared following the general synthesis above. Prior to annealing the precipitate, it was resuspended in hexane (1 mL) and sonicated for 1 h. The suspension was dropcast on the copper face of a Ted Pella 01824 grid (ultrathin carbon film on lacey carbon, 400 mesh Cu), and promptly wicked away from the opposite side with a laboratory wipe. The grid was annealed in air for 10 h at 185 °C and stored under vacuum prior to imaging.

Preparation of AuNP Composite Working Electrodes. A 3mL vial was charged with the appropriate carbon support material (GNRs or C_{black}, 0.3 mg) and AuNPs (0.3 mg) in hexane (1 mL). The mixture was sonicated for 1 h. The resulting suspension was dropcast onto a 1 cm^2 area of carbon paper (TGP-H-060 Toray). The carbon paper was annealed in air for 10 h at 185 °C prior to contacting with silver wire.

Chapter 6

Tetradecylphosphonic acid-capped CuNPs were prepared by reduction of Cu(OAc) following a reported procedure.[297]

Synthesis of oleylamine-capped CuNPs by reduction of $Cu(acac)_2$. In a N_2 glovebox, a 30 mL sealable tube was charged with $Cu(acac)_2$ (52 mg, 0.2 mmol), 1,2-hexadecanediol (90% technical grade; 172 mg, 0.6 mmol) and n-octyl ether (10 mL), then heated to 105 °C for 20 min. Oleic acid (57 mg, 0.06 mL, 0.2 mmol) and oleylamine (70% technical grade, 77 mg, 0.10 mL, 0.02 mmol) were added, then the tube was quickly sealed and transferred to a pre-heated 190 °C bath outside the glovebox and heated for 1 h. The reaction mixture was cooled to 24 °C and precipitated with EtOH (30 mL). The precipitate was collected by centrifugation (5000 rpm, 5 min), redissolved in a minimum of hexane, then reprecipitated with EtOH and recentrifuged. The resulting black solid was redissolved in hexane to give a blue-green solution.

Synthesis of Cu_2O NPs by reduction of $Cu(acac)_2$. In a N_2 glovebox, a 30 mL sealable tube was charged with $Cu(acac)_2$ (52 mg, 0.2 mmol), 1,2-hexadecanediol (98%; 155 mg, 0.6 mmol) and n-octyl ether (10 mL), then heated to 105 °C for 10 min. Oleic acid (57 mg, 0.06 mL, 0.2 mmol) and oleylamine (70% technical grade, 77 mg, 0.10 mL, 0.02 mmol) were added, then the tube was quickly sealed and transferred to a pre-heated 190 °C bath outside the glovebox and heated for 30 min. The reaction mixture was cooled to 24 °C and precipitated with EtOH (30 mL). The precipitate was collected by centrifugation (5000 rpm, 5 min), redispersed in EtOH and recentrifuged, then dried under vacuum to give an orange-brown powder.

Synthesis of ligand-free CuNPs using electron-transfer catalyst. In an Ar glovebox, a 20 mL vial was charged with lithium metal (7 mg, 1.0 mmol), 4,4'-di-tert-butylbiphenyl (14 mg, 0.05 mmol) and THF (1 mL). To this was added GNR **5**, followed by as suspension of anhydrous $CuCl_2$ (67 mg, 0.5 mmol) in THF (10 mL). The reaction mixture was stirred at 24 °C for 1 h, then filtered with THF to yield a black powder, which was dried under vacuum.

Synthesis of ligand-free CuNPs using lithium naphthelenide. In an Ar glovebox, a 20 mL vial was charged with lithium metal (10 mg, 1.44 mmol), naphthalene (220 mg, 1.73 mmol) and THF (8 mL). A separate vial was charged with anhydrous $CuCl_2$ (110 mg, 0.82 mmol) and THF (7 mL) and set stirring vigorously. The lithium naphthelenide solution was then added dropwise to the suspension of $CuCl_2$ and stirred at 24 °C for 1 h, followed by addition of GNR **5** (30 mg). After stirring another 1h, the dark suspension was filtered and washed with THF to yield a black powder, which was dried under vacuum.

Chapter 7

Synthesis of GNR-SnO_2 composite materials. A 50 mL centrifuge tube was charged with chevron-type graphene nanoribbons (35 mg), sodium dodecyl sulfate (120 mg, 0.42 mmol), and water (15 mL), then sealed, clamped in a bath sonicator, and sonicated for 15 min. Following removal from the sonicator, a magnetic stirbar was added to the reaction mixture together with $SnCl_2$ (113 mg, 0.60 mmol) and HCl (5 ml, 3.8 wt% in H_2O). Then urea (144 mg, 2.4 mmol, 2.4 mL of 1M solution in H_2O) was added dropwise, followed by 2 mL of 1 wt% aqueous H_2O_2. Water was added to bring the total volume to 50 mL, then the tube was capped and the reaction mixture was stirred at 90 °C for 18 h. After cooling to 24 °C, the tube was centrifuged (5000 rpm for 5 min) and the supernatant decanted. To purify, the pellet was resuspended in 50 mL H2O, recentrifuged, and the supernatant decanted again. The pellet was then dried by heating 12 h at 75 °C in air, collected, and annealed for 2 h at 350 °C in air to give the product as a black powder (114 mg).

Preparation of GNR-SnO_2 composite electrodes. To begin, the GNR/SnO_2 composite was dispersed in isopropyl alcohol and ball milled for 12 hr to reduce the size of the aggregates and increase the accessible surface area. The slurry for the GNR/SnO_2 electrode was prepared by mixing the GNR-SnO_2 composite, carbon black (Super C65, IMERYS) and PVDF (Kureha Corp.) in a weight ratio of 82:8:10. N-methyl pyrrolidone (NMP) was used to dissolve PVDF and disperse the slurry. The slurry was mixed overnight on a vortex mixer to homogenize the mixture, printed on a 10 μm thick nickel foil with a doctor blade, and then dried in an oven at 100 °C for 2 h. The electrode sheet was then cut into dimensions of 1.5 1.5 cm^2 to form the working electrode. The loading of the working electrode in each case was approximately 1.5 mg/cm^2.

Chapter 8

Synthesis of GNR-Mg composite materials. In an Ar glove box, a sealable tube was charged with GNRs (5 mg) and THF (10 mL), then removed from the Ar box and sonicated for 1.5 h. Also in an Ar glove box, a 250 mL round-bottom flask was charged with naphthalene (1.92 g, 0.015 mol), lithium metal (0.144 g, 0.021 mol) and THF (96 mL). The sonicated GNR dispersion was returned to the glovebox and a solution of Cp_2Mg (1.848, 0.012 mol) in THF (18 mL) was added. The resulting suspension was stirred for 20 min and then added to the previously prepared lithium naphthalenide solution and stirred for 2 h at 24 °C. The precipitate was collected by centrifugation (10000 rpm, 20 min) and reuspended in THF; this was repeated twice, and the resulting gray powder was dried under reduced pressure.

Chapter 9

Synthesis of GNR-Al composite materials. In a N_2 glovebox, a 20 mL vial was charged with $AlH_3 \cdot N(Me)_2Et$ (168 mg, 1.63 mmol, 3.25 mL of 0.5 M solution in toluene), GNR **5** (20 mg) and Et_2O (5 mL). To this vigorously stirring reaction mixture was added $Ti(OiPr)_4$ (19 mg, 0.068 mmol, 0.02 mL) as a solution in Et_2O. The reaction mixture was stirred at 24 °C for 16 h, then filtered. The resulting gray powder was washed thoroughly with Et_2O and dried under vacuum.

10.4 Electrochemical Procedures

Chapter 3

Electrochemical experiments were performed using a BASi EC Epsilon potentiostat/galvanostat with a 2 dr glass cell vial inside a glove box under N_2 atmosphere. Glassy carbon disk electrode (3.0 mm diameter) was purchased from BASi and polished with alumina prior to use. Ag wire (0.5 mm diameter, >99.99% trace metal basis) reference electrodes, Pt wire (0.5 mm diameter, >99.99% trace metal basis) counter electrodes and Bu_4NPF_6 (>99.0%) were obtained from Sigma-Aldrich. CH_2Cl_2 was obtained from a solvent purifying system and degassed prior to use. CV scans were taken between 1.50 V to -1.50 V vs. Ag wire with scan rates ranging from 25 to 1000 mV/s. The potentials were then calibrated against ferrocene/ferrocenium (Fc/Fc^+) standard, and reported in the main text as values against saturated calomel electrode (SCE, $E_{Fc/Fc^+} = 0.46$ V vs. SCE in CH_2Cl_2).

Chapters 5 & 6

Electrolysis experiments were performed using a BASi EC Epsilon potentiostat/ galvanostat with a glass cell custom made by Adams & Chittenden Scientific Glass. Carbon paper (TGP-H-060 Toray) was purchased from Fisher Scientific. Graphite planchets (2.54 cm diameter, impurity < 2 ppm) were purchased from Ted Pell, Inc. Graphite rods (99.9995% trace metal basis, 6.15 mm diameter x 152 mm length) were purchased from Alfa Aesar. Ag/AgCl reference electrodes were obtained from BASi and stored in saturated KCl solution before use. The anion exchange membrane (Selemion AMV) and Ag wire (99.9% trace metal basis, 0.5 mm diameter) were obtained from Sigma Aldrich. CO_2 (99.995%), CO (99.99%), H_2 (99.999%), Ar (99.998%) and C_2H_4 (99.90%) were purchased from Praxair. Gas production was measured on an SRI gas chromatography instrument (model 8610C) equipped with a Haysep D column (1/8 6) and a 13X Mol Sieve column (1/8 6), with ethylene (C_2H_4) as the internal standard; CO was quantified using flame ionization detector (FID) and H_2 using thermal conductivity detector (TCD).

To prepare the electrolyte solution, a 4000 mL flask was charged with $KHCO_3$ (50.0 g) in H_2O (1000 mL, Milli-Q). The solution was then electrolyzed (graphite cathode and anode) at constant current (0.15 mA) for 16 h under a stream of Ar to remove trace metal impurities.

The solution was filtered (0.22 micron, polyethersulfone membrane) and stored in glass containers prior to use. All electrolysis experiments were performed in a custom three-piece glass electrochemical cell, including a working compartment body, a working compartment lid, and a counter compartment body. An anion exchange membrane (Selemion AMV) separates the working and counter electrode (Pt wire) compartments (200 mL). The body of the working compartment was charged with a 3 cm long Teflon-coated stir bar and 150 mL of electrolyte solution (0.5 M aqueous $KHCO_3$), and the lid was fitted with a composite working electrode and a Ag/AgCl reference electrode. Both electrodes were connected to the outside through a stainless steel rod (1/16 inch diameter 2 inch length, connected to the carbon paper by Ag wire and to the reference electrode through a two-way metal socket). The lid was also equipped with a Teflon sparging line extending into the electrolyte solution and a gas outlet connected to the headspace of the cell. Both of the gas ports were connected to a two-way Swagelok valve, and the valve at the gas outlet was also fitted with a Swagelok female miniature quick-connect. During sample analysis, this quick-connect was adapted to a male miniature quick-connect on the injection line of the GC. The lid and the main body of the working compartment were assembled using an O-ring and a Teflon clamp, and the position of the working electrode was adjusted so that only the bottom area covered with the composite was immersed in the solution. The resulting working compartment has a headspace volume of 100 mL. The counter compartment was filled with 50 mL of electrolyte solution, and equipped with a Teflon cap with a septum, as well as a graphite auxiliary electrode connected to the outside with a stainless steel alligator clip and a Ag wire. The electrolyte solution in the working compartment was sparged for 20 minutes with CO_2. 1 mL C_2H_4 was then injected into the headspace as the internal standard for GC analysis. Electrolysis was performed at a constant potential, and after it had finished, the headspace of the cell was analyzed by GC. All potentials were measured against a Ag/AgCl reference electrode (1 M KCl) and converted to the RHE reference scale using equation 10.1.

$$\text{E (vs. RHE)} = \text{E (vs. Ag/AgCl)} + 0.197V + 0.0591pH. \tag{10.1}$$

Cyclic voltammetry was performed at a scan rate of 50 mV s^{-1} using the same electrochemical setup, following 20 min electrolysis at -1.30 V vs. Ag/AgCl. Multiple working electrodes prepared for each GNR composite sample showed consistent current output. The electrochemically active surface area of working electrodes was determined by by measuring the charge associated with the stripping of an underpotential deposited (UPD) Pb monolayer.[5,185,192,298] The electrodes were immersed in an aqueous KOH (0.1 M) solution containing $Pb(OAc)_2$ (1 mM) purged with Ar in a two-compartment electrochemical cell (Pt gauze counter electrode, Ag/AgCl (3 M KCl) reference electrode). Cyclic voltammograms from 0.0-0.8 V with a scan rate of 50 mV s^-1 were acquired until traces converged. The anodic stripping wave associated with the Au(110) surface was integrated and normalized by comparison to a reference Au foil (0.64 cm^2).

1 h fixed potential CO reduction experiments were performed as described for CO_2 reduction above but using 0.1 M aqueous KOH (pH 13) as electrolyte rather than $KHCO_3$, and

sparging the working compartment with CO for 20 minutes. Additionally, gaseous products were quantified by GC using C_2H_6 (rather than C_2H_4) as internal standard; liquid products were quantified by ^{1}H-NMR using excitation scultping solvent supression (10% D_2O in H_2O) with internal DMSO standard (0.028 μmol mL^{-1}).

Chapter 7

Electrochemical measurements on GNR-SnO_2 electrodes were performed in a pouch cell setup. Prior to encapsulating the battery, the electrodes were heated at 130 °C for 12 h in a vacuum oven connected to an argon-filled glove box, to remove traces of moisture from the electrode. The GNR-SnO_2 working electode was stacked with a 25 μm trilayer polypropylene-polyethylene-polypropylene separator membrane (Celgard) and a pure lithium foil (99.99%, Alfa Aesar) to serve as the counter/reference electrode. The electrode stack (working electrode-separator-counter electrode) was soaked with an electrolyte solution of 1M $LiPF_6$ ethylene carbonate/dimethyl carbonate (EC/DMC, 1:1 v/v). The cell was heat sealed within an aluminum laminated pouch. The cell was allowed to rest for a day before initiating the electrochemical testing. The specific capacity (mAh g^{-1}) was calculated based on the weight of GNR-SnO_2 in the electrode. The cyclic voltammetry test was carried out at 0.1 mV s^{-1} between 0.005 to 3.0 V vs. lithium counter/reference electrode. The galvanostatic cycling was carried out at various charge/discharge rates using a battery analyzer.

10.5 Additional Figures

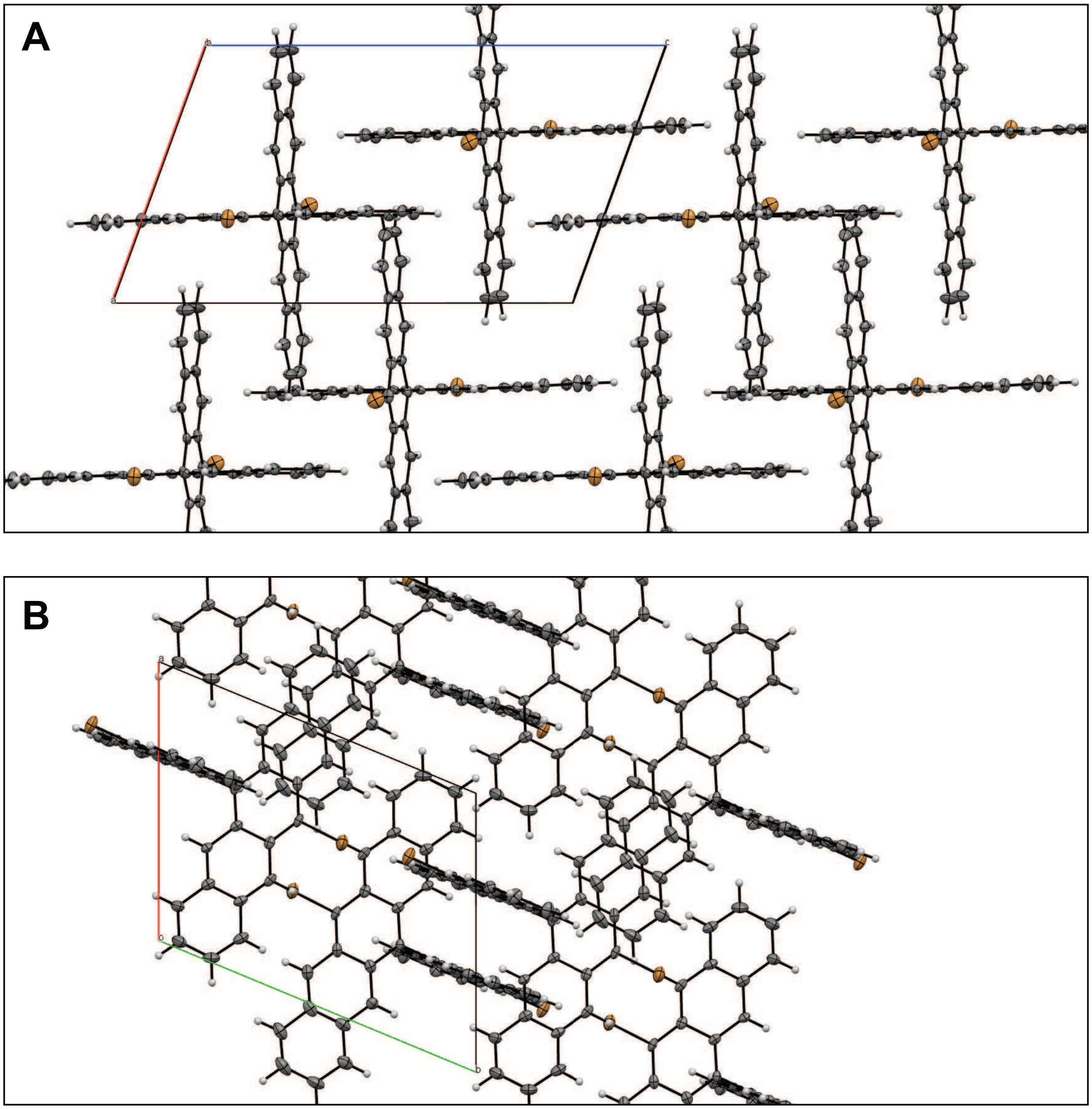

Figure 10.1: X-ray crystal structure of brominated bispentacene derivative **96**, viewed down the b and c axes of the crystal.

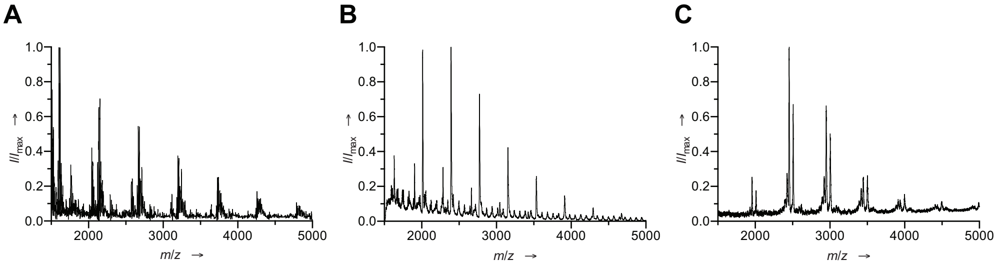

Figure 10.2: MALDI mass spectrometry of (A) chevron GNR precursor **20**, (B) cove GNR precursor **75** (C) ester-functionalized cove GNR precursor **85**.

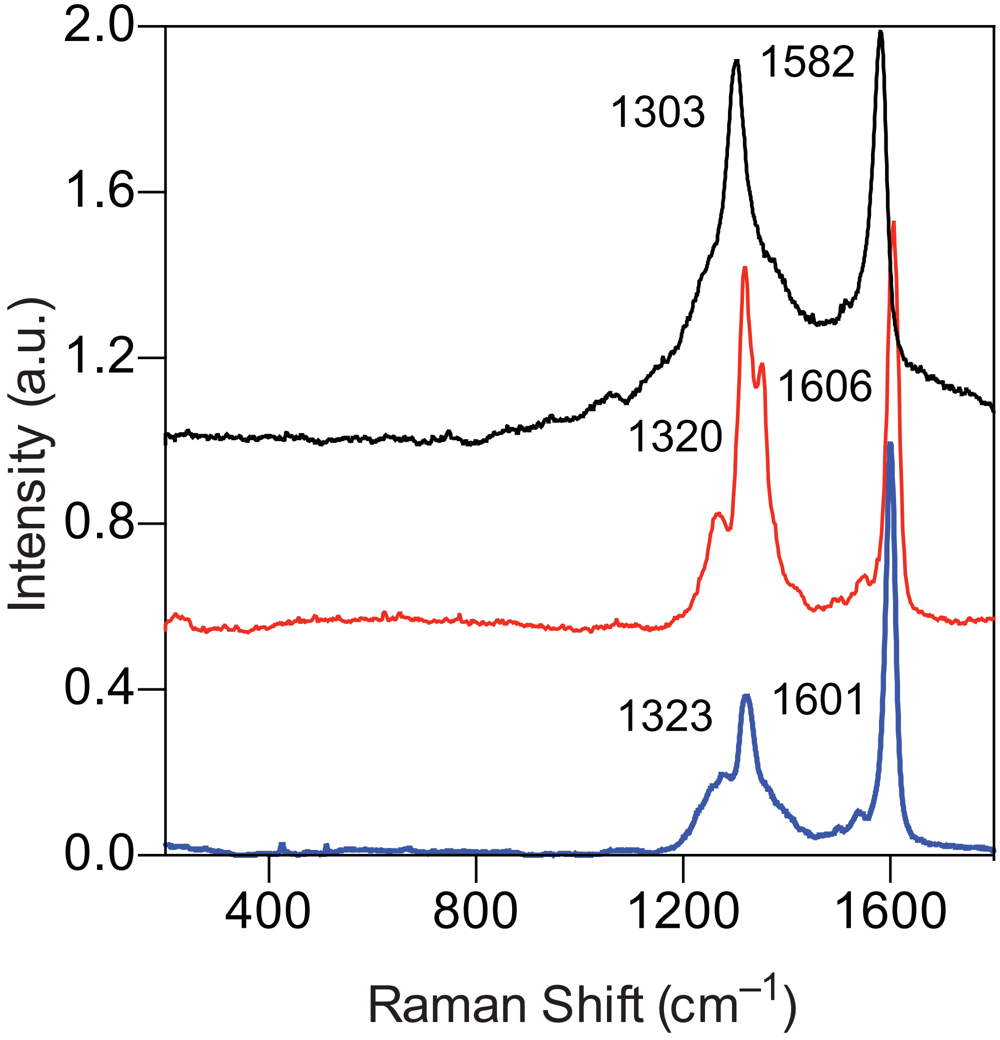

Figure 10.3: Raman spectrometry of chevron GNR **5** (blue), cove GNR **8** (red), and ester-functionalized cove GNR **7**.

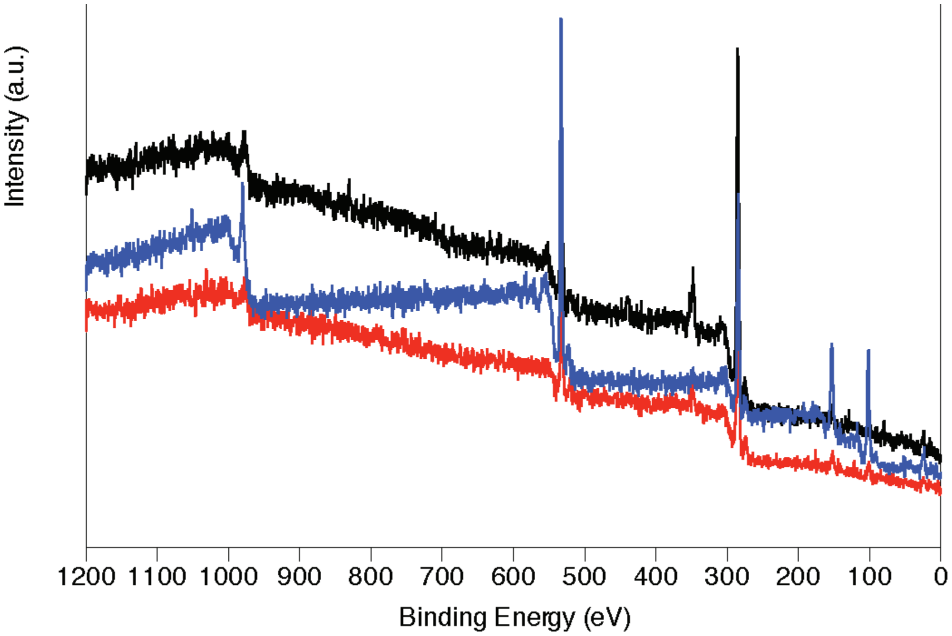

Figure 10.4: X-ray photoelectron spectroscopy (XPS) characterization of chevron GNR **5** (blue), cove GNR **8** (red), and ester-functionalized cove GNR **7** (black). Samples were prepared by sonicating 0.5 mg of the respective GNR in THF (0.5 mL) and dropcasting onto a Si wafer held at 80 °C. All samples show prominent C 1s signals from the deposited GNR, as well as Si and O signals from the underlying substrate. While adventitious Ca was observed in some samples, prominent signals associated with Ni ($2p^{3/2}$, 853 eV; $2p^{1/2}$, 870 eV) and Fe ($2p^{3/2}$, 707 eV; $2p^{1/2}$, 72 eV) used as reagents or catalysts in the GNR synthesis could not be detected in purified GNR.

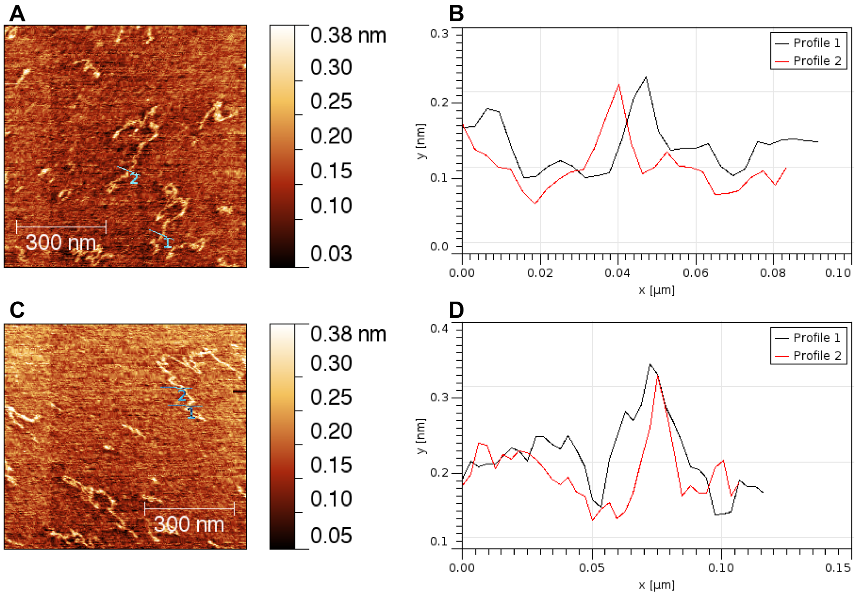

Figure 10.5: AFM characterization of nitrogen-doped chevron-type GNR **6** dropcast from THF onto mica. (A&C) Topography images, with marked paths corresponding to the height profiles shown in (B&D). Measured heights suggest that the observed structures are single isolated GNRs.

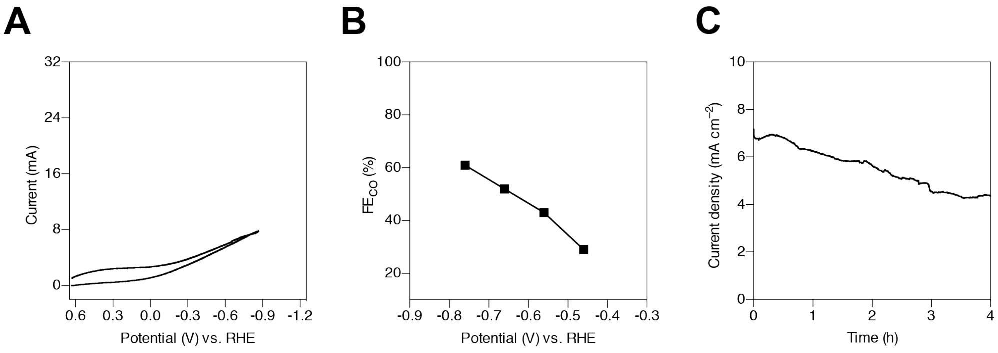

Figure 10.6: Electrocatalytic performance of SWCNT-AuNP composites, which were intended to serve as an additional point of reference for the performance of GNR-AuNP composites. However, the SWCNT-AuNP composite materials exhibit drastically inferior performance, even in comparison to C_{black} composites. In a direct comparison with GNR composites, CO_2 reduction activity was significantly reduced at mildly reducing potentials, and correspondingly FE_{CO} is lower across the entire potential window. SWCNT-AuNP composites were prepared following the same procedure described for GNR and C_{black} composites, but using SWCNTs as support material. All electrochemical experiments were performed in 0.5 M aqueous $KHCO_3$ solution saturated with CO_2 (pH 7.3). (A) Cyclic voltammogram of SWCNT-AuNP composite material. (B) Faradaic efficiencies for CO production (FE_{CO}) by SWCNT-AuNP composite electrodes. Electrolysis performed potentials from -0.47 V to -0.77 V vs. RHE. (C) Total current density for SWCNT-AuNP composite over 4 h at -0.77 V vs. RHE. Note that this potential is more negative than that used for long-term controlled potential electrolysis experiments using GNR or C_{black} support materials (-0.47 V vs. RHE); at -0.47 V the SWCNT composite showed minimal CO_2 reduction activity. Across the 4 h experiment, FE_{CO} for the SWCNT-AuNP composite fell to 27% from its initial value of 61%.

Time (h)	Total Charge (C)	Volume CO (mL)	FE_{CO} (%)	Volume H_2 (mL)	FE_{H2} (%)
0.5	7.8	0.79	80.3	0.24	24.0
1	15.6	1.54	78.2	0.50	25.2
2	31.3	3.10	78.2	0.96	24.3
3	46.8	4.59	77.4	1.45	24.5
4	66.9	6.39	75.5	1.90	22.4
6	103.1	9.54	73.1	3.13	24.0
8	131.2	12.03	72.4	4.13	24.9
10	168.0	15.07	70.8	5.42	25.5

Table 10.1: Controlled potential electrolysis experiments at −0.47 V using GNR **7**-AuNP composite electrodes. Note: The TCD channel of the GC has a high detection limit for H_2 and the internal standard C_2H_4, leading to some uncertainty in the quantification of H_2. As a result, the Faradaic efficiency for H_2 and the overall Faradaic efficiency have an error of up to ± 10%. However, the CO quantification by GC (FID) is accurate, and therefore so are the corresponding Faradaic efficiencies.

Time (h)	Total Charge (C)	Volume CO (mL)	FE_{CO} (%)	Volume H_2 (mL)	FE_{H2} (%)
0.5	6.8	0.59	68.3	0.28	33.1
1	13.4	1.16	68.1	0.58	34.1
2	26.4	2.25	67.3	1.22	36.4
3	40.1	3.40	66.9	1.68	33.1
4	53.0	4.39	65.4	2.38	35.5
6	77.8	6.22	63.1	3.54	35.9
8	103.2	8.03	61.4	4.66	35.7
10	129.6	9.77	59.5	6.08	37.0

Table 10.2: Controlled potential electrolysis experiments at −0.47 V using GNR **8**-AuNP composite electrodes. Note: The TCD channel of the GC has a high detection limit for H_2 and the internal standard C_2H_4, leading to some uncertainty in the quantification of H_2. As a result, the Faradaic efficiency for H_2 and the overall Faradaic efficiency have an error of up to ± 10%. However, the CO quantification by GC (FID) is accurate, and therefore so are the corresponding Faradaic efficiencies.

Time (h)	Total Charge (C)	Volume CO (mL)	FE_{CO} (%)	Volume H_2 (mL)	FE_{H2} (%)
0.5	2.3	0.17	57.3	0.14	49.6
1	4.6	0.33	57.3	0.29	49.2
2	9.2	0.65	55.9	0.59	50.8
3	14.2	0.94	52.1	0.96	53.4
4	19.1	1.19	49.3	1.27	52.6
6	28.5	1.60	44.3	1.90	52.6
8	37.7	1.96	41.2	2.68	56.1
10	47.2	2.41	40.4	3.35	56.1

Table 10.3: Controlled potential electrolysis experiments at -0.47 V using GNR **5**-AuNP composite electrodes. Note: The TCD channel of the GC has a high detection limit for H_2 and the internal standard C_2H_4, leading to some uncertainty in the quantification of H_2. As a result, the Faradaic efficiency for H_2 and the overall Faradaic efficiency have an error of up to ± 10%. However, the CO quantification by GC (FID) is accurate, and therefore so are the corresponding Faradaic efficiencies.

Time (h)	Total Charge (C)	Volume CO (mL)	FE_{CO} (%)	Volume H_2 (mL)	FE_{H2} (%)
0.5	0.30	0.02	45.0	0.02	59.0
1	0.66	0.04	42.9	0.05	60.7
2	1.18	0.06	38.5	0.11	71.1
3	1.95	0.07	27.3	0.19	75.3
4	2.71	0.08	23.0	0.25	73.6
6	3.61	0.09	20.7	0.36	78.8
8	4.63	0.10	16.9	0.49	83.6
10	5.65	0.11	15.0	0.62	87.0

Table 10.4: Controlled potential electrolysis experiments at -0.47 V using C_{black}-AuNP composite electrodes. Note: The TCD channel of the GC has a high detection limit for H_2 and the internal standard C_2H_4, leading to some uncertainty in the quantification of H_2. As a result, the Faradaic efficiency for H_2 and the overall Faradaic efficiency have an error of up to ± 10%. However, the CO quantification by GC (FID) is accurate, and therefore so are the corresponding Faradaic efficiencies.

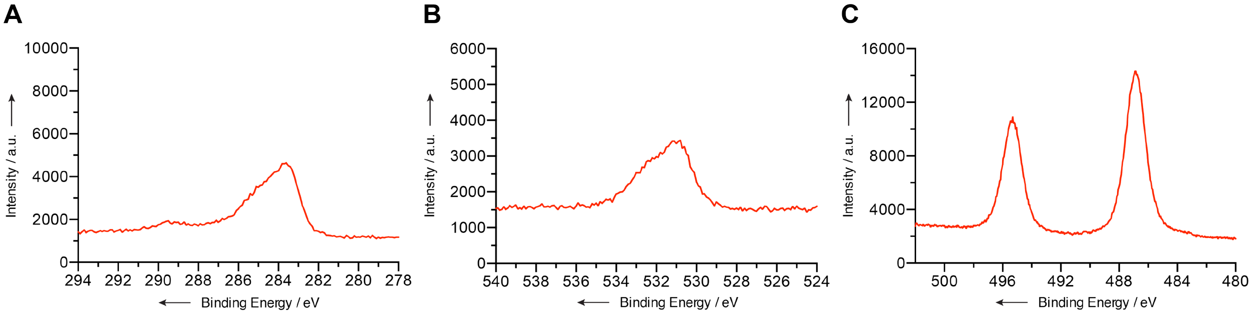

Figure 10.7: XPS multiplexes of printed GNR-SnO_2 composite electrode. (A) C 1s multiplex. (B) O 1s multiplx. (C) Sn 3d multiplex.

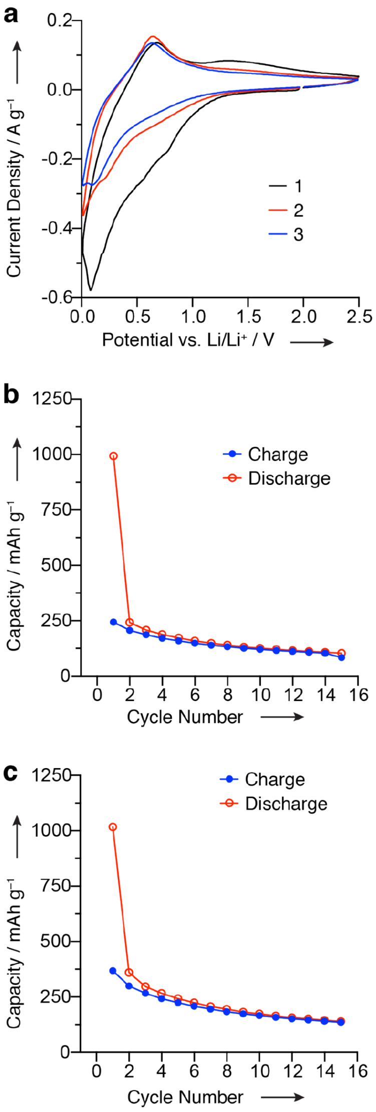

Figure 10.8: Performance of GNR-SnO_2 composite electrodes prepared without ball milling (a) Three cyclic voltammetry curves between 2.5 and 0.005 V vs. Li^+/Li at 0.1 mV s^{-1}. (b) Charge/discharge capacity cycled between 1.2 and 0.005 V vs. Li^+/Li at 100 mA g−1 for 15 cycles. (c) Charge/discharge capacity when cycled between 3.0 and 0.005 V vs. Li^+/Li at 100 mA g^{-1} for 15 cycles.

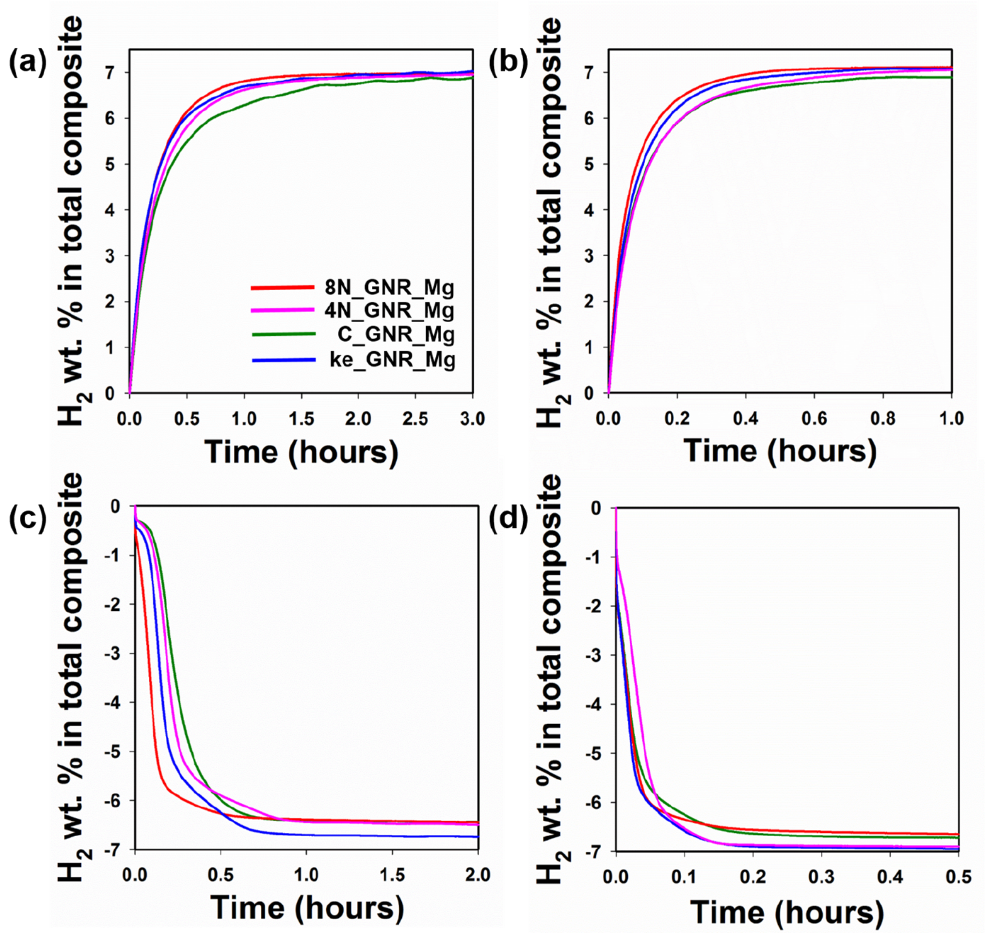

Figure 10.9: Hydrogen absorption at 15 bar H_2 and (a) 225 °C and (b) 250 °C. Hydrogen desorption at 0 bar H_2 and (c) 325 °C and (d) 350 °C.

Bibliography

(1) Raimondi, F.; Scherer, G. G.; Kötz, R.; Wokaun, A. *Angew. Chem. Int. Ed.* **2005**, *44*, 2190–2209.

(2) Guo, Y.-G.; Hu, J.-S.; Wan, L.-J. *Adv. Mater.* **2008**, *20*, 2878–2887.

(3) Coq, B.; Figueras, F. *Coord. Chem. Rev.* **1998**, *178*, 1753–1783.

(4) Reske, R.; Mistry, H.; Behafarid, F.; Roldan Cuenya, B.; Strasser, P. *J. Am. Chem. Soc.* **2014**, *136*, 6978–6986.

(5) Feng, X.; Jiang, K.; Fan, S.; Kanan, M. W. *J. Am. Chem. Soc.* **2015**, *137*, 4606–4609.

(6) Zhou, X.; Qiao, J.; Yang, L.; Zhang, J. *Adv. Energy Mater.* **2014**, *4*.

(7) Manthiram, K.; Surendranath, Y.; Alivisatos, A. P. *J. Am. Chem. Soc.* **2014**, *136*, 7237–7240.

(8) Tauster, S.; Fung, S.; Baker, R.; Horsley, J. *Science* **1981**, *211*, 1121–1125.

(9) Bartholomew, C. H.; Pannell, R. B.; Butler, J. L. *J. Catal.* **1980**, *65*, 335–347.

(10) Coq, B. In *Metal-Ligand Interactions in Chemistry, Physics and Biology*, Russo, N., Salahub, D. R., Eds.; Springer Netherlands: Dordrecht, 2000, pp 49–71.

(11) Tauster, S.; Fung, S.; Garten, R. L. *J. Am. Chem. Soc.* **1978**, *100*, 170–175.

(12) Matsubu, J. C.; Zhang, S.; DeRita, L.; Marinkovic, N. S.; Chen, J. G.; Graham, G. W.; Pan, X.; Christopher, P. *Nat. Chem.* **2017**, *9*, 120–127.

(13) Somorjai, G. A.; Li, Y., *Introduction to surface chemistry and catalysis*; John Wiley & Sons: 2010, pp 390–410, 580–643.

(14) Belton, D.; Sun, Y.; White, J. *J. Phys. Chem.* **1984**, *88*, 5172–5176.

(15) Tauster, S. *Acc. Chem. Res.* **1987**, *20*, 389–394.

(16) Shi, F.; Baker, L. R.; Hervier, A.; Somorjai, G. A.; Komvopoulos, K. *Nano Lett.* **2013**, *13*, 4469–4474.

(17) Yoshitake, H.; Iwasawa, Y. *J. Phys. Chem.* **1992**, *96*, 1329–1334.

(18) Kumar, A.; Ramani, V. *ACS Catal.* **2014**, *4*, 1516–1525.

(19) Iijima, S. *Nature* **1991**, *354*, 56–58.

(20) Geim, A. K.; Novoselov, K. S. *Nat. Mater.* **2007**, *6*, 183–191.

(21) Geim, A. K. *Science* **2009**, *324*, 1530–1534.

(22) Jung, A.; Jess, A.; Schubert, T.; Schütz, W. *Appl. Catal. A* **2009**, *362*, 95–105.

(23) Serp, P.; Corrias, M.; Kalck, P. *Appl. Catal. A* **2003**, *253*, 337–358.

(24) Carneiro, O.; Anderson, P.; Rodriguez, N.; Baker, R. *J. Phys. Chem. B* **2004**, *108*, 13307–13314.

(25) Chambers, A.; Nemes, T.; Rodriguez, N. M.; Baker, R. T. K. *J. Phys. Chem. B* **1998**, *102*, 2251–2258.

(26) Ejigu, A.; Edwards, M.; Walsh, D. A. *ACS Catal.* **2015**, *5*, 7122–7130.

(27) Saito, A.; Tsuji, H.; Shimoyama, I.; Shimizu, K.-i.; Nishina, Y. *Chem. Commun.* **2015**, *51*, 5883–5886.

(28) Shao, Y.; Liu, J.; Wang, Y.; Lin, Y. *J. Mater. Chem.* **2009**, *19*, 46–59.

(29) Klapper, M.; Joe, D.; Nietzel, S.; Krumpfer, J. W.; Müllen, K. *Chem. Mater.* **2013**, *26*, 802–819.

(30) Lee, W. J.; Maiti, U. N.; Lee, J. M.; Lim, J.; Han, T. H.; Kim, S. O. *Chem. Commun.* **2014**, *50*, 6818–6830.

(31) Balgis, R.; Sago, S.; Anilkumar, G. M.; Ogi, T.; Okuyama, K. *ACS Appl. Mater. Interfaces* **2013**, *5*, 11944–11950.

(32) Su, D. S.; Perathoner, S.; Centi, G. *Chem. Rev.* **2013**, *113*, 5782–5816.

(33) Weiß, A.; Munoz, M.; Haas, A.; Rietzler, F.; Steinrück, H.-P.; Haumann, M.; Wasserscheid, P.; Etzold, B. J. *ACS Catal.* **2016**, *6*, 2280–2286.

(34) Qiu, X.; Wu, P.; Xu, L.; Tang, Y.; Lee, J.-M. *Adv. Mater. Interfaces* **2015**, *2*.

(35) Girishkumar, G.; Hall, T. D.; Vinodgopal, K.; Kamat, P. V. *J. Phys. Chem. B* **2006**, *110*, 107–114.

(36) Chan-Thaw, C. E.; Villa, A.; Veith, G. M.; Kailasam, K.; Adamczyk, L. A.; Unocic, R. R.; Prati, L.; Thomas, A. *Chem. Asian J.* **2012**, *7*, 387–393.

(37) Li, Y.; Gao, W.; Ci, L.; Wang, C.; Ajayan, P. M. *Carbon* **2010**, *48*, 1124–1130.

(38) Deng, J.; Deng, D.; Bao, X. *Adv. Mater.* **2017**, *29*, 1606967.

(39) Li, X.; Zhang, X.; Zhao, Y.; Feng, D.; Su, Z.; Zhang, Y. *Electrochim. Acta* **2016**, *191*, 215–222.

(40) Kwak, J. H.; Hu, J.; Mei, D.; Yi, C.-W.; Kim, D. H.; Peden, C. H.; Allard, L. F.; Szanyi, J. *Science* **2009**, *325*, 1670–1673.

(41) Bo, X.; Zhu, L.; Wang, G.; Guo, L. *J. Mater. Chem.* **2012**, *22*, 5758–5763.

(42) Liu, H.; Cao, Y.; Wang, F.; Huang, Y. *ACS Appl. Mater. Interfaces* **2014**, *6*, 819–825.

(43) Truong-Phuoc, L.; Pham-Huu, C.; Da Costa, V.; Janowska, I. *Chem. Commun.* **2014**, *50*, 14433–14435.

(44) Khomyakov, P.; Giovannetti, G.; Rusu, P.; Brocks, G. v.; Van den Brink, J.; Kelly, P. J. *Phys. Rev. B* **2009**, *79*, 195425.

(45) Jeong, G.-H.; Suzuki, S.; Kobayashi, Y. *Nanotechnol.* **2009**, *20*, 285708.

(46) Chan-Thaw, C. E.; Villa, A.; Veith, G. M.; Kailasam, K.; Adamczyk, L. A.; Unocic, R. R.; Prati, L.; Thomas, A. *Chem. Asian J.* **2012**, *7*, 387–393.

(47) Liu, M.; Zhang, R.; Chen, W. *Chem. Rev.* **2014**, *114*, 5117–5160.

(48) Kong, B.-S.; Jung, D.-H.; Oh, S.-K.; Han, C.-S.; Jung, H.-T. *J. Phys. Chem. C* **2007**, *111*, 8377–8382.

(49) Baldé, C. P.; Hereijgers, B. P.; Bitter, J. H.; de Jong, K. P. *Angew. Chem. Int. Ed.* **2006**, *45*, 3501–3503.

(50) Goncalves, G.; Marques, P. A.; Granadeiro, C. M.; Nogueira, H. I.; Singh, M.; Gracio, J. *Chem. Mater.* **2009**, *21*, 4796–4802.

(51) Cho, E. S.; Ruminski, A. M.; Aloni, S.; Liu, Y.-S.; Guo, J.; Urban, J. J. *Nat. Commun.* **2016**, *7*.

(52) Alves, D. C.; Silva, R.; Voiry, D.; Asefa, T.; Chhowalla, M. *Mater. Renew. Sustain. Energy* **2015**, *4*, 2.

(53) Li, X.-H.; Antonietti, M. *Chem. Soc. Rev.* **2013**, *42*, 6593–6604.

(54) Sun, H.; Zhou, G.; Wang, Y.; Suvorova, A.; Wang, S. *ACS Appl. Mater. Interfaces* **2014**, *6*, 16745–16754.

(55) Prabakar, S.; Hwang, Y.-H.; Bae, E.-G.; Shim, S.; Kim, D.; Lah, M. S.; Sohn, K.-S.; Pyo, M. *Adv. Mater.* **2013**, *25*, 3307–3312.

(56) Su, Y.; Li, S.; Wu, D.; Zhang, F.; Liang, H.; Gao, P.; Cheng, C.; Feng, X. *ACS Nano* **2012**, *6*, 8349–8356.

(57) Fan, X.; Shao, J.; Xiao, X.; Wang, X.; Li, S.; Ge, H.; Chen, L.; Wang, C. *J. Mater. Chem. A* **2014**, *2*, 18367–18374.

(58) Wang, G.; Shen, X.; Yao, J.; Park, J. *Carbon* **2009**, *47*, 2049–2053.

(59) Dahn, J. R.; Zheng, T.; Liu, Y.; Xue, J. *Science* **1995**, 590–590.

(60) Liu, Y.; Liu, P.; Wu, D.; Huang, Y.; Tang, Y.; Su, Y.; Zhang, F.; Feng, X. *Chem. Eur. J.* **2015**, *21*, 5617–5622.

(61) Chellasamy, V.; Manoharan, R. In *Materials Science Forum*, 2012; Vol. 710, pp 709–714.

(62) Huang, S.; Zai, J.; Ma, D.; Hu, Z.; He, Q.; Wu, M.; Chen, D.; Chen, Z.; Qian, X. *Electrochim. Acta* **2017**, *241*, 89–97.

(63) Su, H.; Zhang, K.-X.; Zhang, B.; Wang, H.-H.; Yu, Q.-Y.; Li, X.-H.; Antonietti, M.; Chen, J.-S. *J. Am. Chem. Soc.* **2017**, *139*, 811–818.

(64) Xue, Z.-H.; Su, H.; Yu, Q.-Y.; Zhang, B.; Wang, H.-H.; Li, X.-H.; Chen, J.-S. *Adv. Energy Mater.* **2017**.

(65) Wang, Y.; Yao, J.; Li, H.; Su, D.; Antonietti, M. *J. Am. Chem. Soc.* **2011**, *133*, 2362–2365.

(66) Gong, L.-H.; Cai, Y.-Y.; Li, X.-H.; Zhang, Y.-N.; Su, J.; Chen, J.-S. *Green Chem.* **2014**, *16*, 3746–3751.

(67) Guo, L.-T.; Cai, Y.-Y.; Ge, J.-M.; Zhang, Y.-N.; Gong, L.-H.; Li, X.-H.; Wang, K.-X.; Ren, Q.-Z.; Su, J.; Chen, J.-S. *ACS Catal.* **2014**, *5*, 388–392.

(68) Kahri, H.; Sevim, M.; Metin, Ö. *Nano Res.* **2017**, *10*, 1627–1640.

(69) Cai, Y.-Y.; Li, X.-H.; Zhang, Y.-N.; Wei, X.; Wang, K.-X.; Chen, J.-S. *Angew. Chem. Int. Ed.* **2013**, *52*, 11822–11825.

(70) Li, X.-H.; Baar, M.; Blechert, S.; Antonietti, M. *Sci. Rep.* **2013**, *3*.

(71) Jiao, Z.; Zhai, Z.; Guo, X.; Guo, X.-Y. *J. Phys. Chem. C* **2015**, *119*, 3238–3243.

(72) Jiao, Z.-F.; Guo, X.-N.; Zhai, Z.-Y.; Jin, G.-Q.; Wang, X.-M.; Guo, X.-Y. *Catal. Sci. Technol.* **2014**, *4*, 2494–2498.

(73) He, Q.; Huang, S.; Wang, C.; Qiao, Q.; Liang, N.; Xu, M.; Chen, W.; Zai, J.; Qian, X. *ChemSusChem* **2015**, *8*, 817–820.

(74) Huang, S.; Ma, D.; Hu, Z.; He, Q.; Zai, J.; Chen, D.; Sun, H.; Chen, Z.; Qiao, Q.; Wu, M.; Qian, X. *ACS Appl. Mater. Interfaces* **2017**, *9*, 27607–27617.

(75) Stoller, M. D.; Park, S.; Zhu, Y.; An, J.; Ruoff, R. S. *Nano Lett.* **2008**, *8*, 3498–3502.

(76) Lee, C.; Wei, X.; Kysar, J. W.; Hone, J. *Science* **2008**, *321*, 385–388.

(77) Orlita, M.; Faugeras, C.; Plochocka, P.; Neugebauer, P.; Martinez, G.; Maude, D. K.; Barra, A.-L.; Sprinkle, M.; Berger, C.; De Heer, W. A.; Potemski, M. *Phys. Rev. Lett.* **2008**, *101*, 267601.

(78) Balandin, A. A.; Ghosh, S.; Bao, W.; Calizo, I.; Teweldebrhan, D.; Miao, F.; Lau, C. N. *Nano Lett.* **2008**, *8*, 902–907.

(79) Neto, A. C.; Guinea, F.; Peres, N. M.; Novoselov, K. S.; Geim, A. K. *Rev. Mod. Phys.* **2009**, *81*, 109.

(80) Nair, R. R.; Blake, P.; Grigorenko, A. N.; Novoselov, K. S.; Booth, T. J.; Stauber, T.; Peres, N. M.; Geim, A. K. *Science* **2008**, *320*, 1308–1308.

(81) Fan, X.; Peng, W.; Li, Y.; Li, X.; Wang, S.; Zhang, G.; Zhang, F. *Adv. Mater.* **2008**, *20*, 4490–4493.

(82) Xue, Y.; Yu, D.; Dai, L.; Wang, R.; Li, D.; Roy, A.; Lu, F.; Chen, H.; Liu, Y.; Qu, J. *Phys. Chem. Chem. Phys.* **2013**, *15*, 12220–12226.

(83) Chen, L.; Du, R.; Zhu, J.; Mao, Y.; Xue, C.; Zhang, N.; Hou, Y.; Zhang, J.; Yi, T. *Small* **2015**, *11*, 1423–1429.

(84) Fischer, F. R. In *From Polyphenylenes to Nanographenes and Graphene Nanoribbons*, Müllen, K., Feng, X., Eds.; Springer International Publishing: Cham, 2017, pp 33–65.

(85) Osella, S.; Narita, A.; Schwab, M. G.; Hernandez, Y.; Feng, X.; Müllen, K.; Beljonne, D. *ACS Nano* **2012**, *6*, 5539–5548.

(86) Schwierz, F. *Nat. Nanotechnol.* **2010**, *5*, 487–496.

(87) Burghard, M.; Klauk, H.; Kern, K. *Adv. Mater.* **2009**, *21*, 2586–2600.

(88) Yang, L.; Park, C.-H.; Son, Y.-W.; Cohen, M. L.; Louie, S. G. *Phys. Rev. Lett.* **2007**, *99*, 186801.

(89) Son, Y.-W.; Cohen, M. L.; Louie, S. G. *Phys. Rev. Letters* **2006**, *97*, 216803.

(90) Bennett, P. B.; Pedramrazi, Z.; Madani, A.; Chen, Y.-C.; de Oteyza, D. G.; Chen, C.; Fischer, F. R.; Crommie, M. F.; Bokor, J. *Appl. Phys. Lett.* **2013**, *103*, 253114.

(91) Wang, X.; Ouyang, Y.; Li, X.; Wang, H.; Guo, J.; Dai, H. *Phys. Rev. Lett.* **2008**, *100*, 206803.

(92) Gao, J.; Uribe-Romo, F. J.; Saathoff, J. D.; Arslan, H.; Crick, C. R.; Hein, S. J.; Itin, B.; Clancy, P.; Dichtel, W. R.; Loo, Y.-L. *ACS Nano* **2016**, *10*, 4847–4856.

(93) Yoon, W.; Lee, Y.; Jang, H.; Jang, M.; Kim, J. S.; Lee, H. S.; Im, S.; Boo, D. W.; Park, J.; Ju, S.-Y. *Carbon* **2015**, *81*, 629–638.

(94) Kosynkin, D. V.; Higginbotham, A. L.; Sinitskii, A.; Lomeda, J. R.; Dimiev, A.; Price, B. K.; Tour, J. M. *Nature* **2009**, *458*, 872–876.

(95) Lin, J.; Peng, Z.; Xiang, C.; Ruan, G.; Yan, Z.; Natelson, D.; Tour, J. M. *ACS Nano* **2013**, *7*, 6001–6006.

(96) Li, X.; Wang, X.; Zhang, L.; Lee, S.; Dai, H. *Science* **2008**, *319*, 1229–1232.

(97) Shinde, D. B.; Debgupta, J.; Kushwaha, A.; Aslam, M.; Pillai, V. K. *J. Am. Chem. Soc.* **2011**, *133*, 4168–4171.

(98) Bai, J.; Duan, X.; Huang, Y. *Nano Lett.* **2009**, *9*, 2083–2087.

(99) Zhang, X.; Yazyev, O. V.; Feng, J.; Xie, L.; Tao, C.; Chen, Y.-C.; Jiao, L.; Pedramrazi, Z.; Zettl, A.; Louie, S. G.; Dai, H.; Crommie, M. *ACS Nano* **2012**, *7*, 198–202.

(100) Li, Y.-S.; Liao, J.-L.; Wang, S.-Y.; Chiang, W.-H. *Sci. Rep.* **2016**, *6*, 22755.

(101) Dauber, J.; Terrés, B.; Volk, C.; Trellenkamp, S.; Stampfer, C. *Appl. Phys. Lett.* **2014**, *104*, 083105.

(102) Han, M. Y.; Özyilmaz, B.; Zhang, Y.; Kim, P. *Phys. Rev. Lett.* **2007**, *98*, 206805.

(103) Wu, Z.-S.; Ren, W.; Gao, L.; Liu, B.; Zhao, J.; Cheng, H.-M. *Nano Res.* **2010**, *3*, 16–22.

(104) Jacobberger, R. M.; Arnold, M. S. *ACS Nano* **2017**, *11*, 8924–8929.

(105) Yang, X.; Dou, X.; Rouhanipour, A.; Zhi, L.; Räder, H. J.; Müllen, K. *J. Am. Chem. Soc.* **2008**, *130*, 4216–4217.

(106) Cai, J.; Ruffieux, P.; Jaafar, R.; Bieri, M.; Braun, T.; Blankenburg, S.; Muoth, M.; Seitsonen, A. P.; Saleh, M.; Feng, X.; Müllen, K.; Fasel, R. *Nature* **2010**, *466*, 470–473.

(107) Björk, J.; Hanke, F.; Stafström, S. *J. Am. Chem. Soc.* **2013**, *135*, 5768–5775.

(108) Björk, J. *J. Phys. Condens. Matter* **2016**, *28*, 083002.

(109) Huang, H.; Wei, D.; Sun, J.; Wong, S. L.; Feng, Y. P.; Neto, A. C.; Wee, A. T. S. *Sci. Rep.* **2012**, *2*, 983.

(110) Björk, J.; Stafstrofffdfffdm, S.; Hanke, F. *J. Am. Chem. Soc.* **2011**, *133*, 14884–14887.

(111) Cloke, R. R.; Marangoni, T.; Nguyen, G. D.; Joshi, T.; Rizzo, D. J.; Bronner, C.; Cao, T.; Louie, S. G.; Crommie, M. F.; Fischer, F. R. *J. Am. Chem. Soc.* **2015**, *137*, 8872–8875.

(112) Chen, Y.-C.; De Oteyza, D. G.; Pedramrazi, Z.; Chen, C.; Fischer, F. R.; Crommie, M. F. *ACS Nano* **2013**, *7*, 6123–6128.

(113) Ruffieux, P.; Cai, J.; Plumb, N. C.; Patthey, L.; Prezzi, D.; Ferretti, A.; Molinari, E.; Feng, X.; Müllen, K.; Pignedoli, C. A.; Fasel, R. *ACS Nano* **2012**, *6*, 6930–6935.

(114) Van Der Lit, J.; Boneschanscher, M. P.; Vanmaekelbergh, D.; Ijäs, M.; Uppstu, A.; Ervasti, M.; Harju, A.; Liljeroth, P.; Swart, I. *Nat. Commun.* **2013**, *4*, 3023.

(115) Liu, J.; Li, B.-W.; Tan, Y.-Z.; Giannakopoulos, A.; Sanchez-Sanchez, C.; Beljonne, D.; Ruffieux, P.; Fasel, R.; Feng, X.; Müllen, K. *J. Am. Chem. Soc.* **2015**, *137*, 6097–6103.

(116) Ruffieux, P.; Wang, S.; Yang, B.; Sánchez-Sánchez, C.; Liu, J.; Dienel, T.; Talirz, L.; Shinde, P.; Pignedoli, C. A.; Passerone, D.; Dumslaff, T.; Feng, X.; Müllen, K.; Fasel, R. *Nature* **2016**, *531*, 489–492.

(117) Han, P.; Akagi, K.; Federici Canova, F.; Mutoh, H.; Shiraki, S.; Iwaya, K.; Weiss, P. S.; Asao, N.; Hitosugi, T. *ACS Nano* **2014**, *8*, 9181–9187.

(118) Chen, Y.-C.; Cao, T.; Chen, C.; Pedramrazi, Z.; Haberer, D.; De Oteyza, D. G.; Fischer, F. R.; Louie, S. G.; Crommie, M. F. *Nat. Nanotechnol.* **2015**, *10*, 156–160.

(119) Zhang, H.; Lin, H.; Sun, K.; Chen, L.; Zagranyarski, Y.; Aghdassi, N.; Duhm, S.; Li, Q.; Zhong, D.; Li, Y.; Müllen, K.; Fuchs, H.; Chi, L. *J. Am. Chem. Soc.* **2015**, *137*, 4022–4025.

(120) Nguyen, G. D.; Toma, F. M.; Cao, T.; Pedramrazi, Z.; Chen, C.; Rizzo, D. J.; Joshi, T.; Bronner, C.; Chen, Y.-C.; Favaro, M.; Louie, S. G.; Fischer, F. R.; Crommie, M. F. *J. Phys. Chem. C* **2016**, *120*, 2684–2687.

(121) Nguyen, G. D. et al. *Nat. Nanotechnol.* **2017**, *12*, 1077–1083.

(122) Marangoni, T.; Haberer, D.; Rizzo, D. J.; Cloke, R. R.; Fischer, F. R. *Chem. Eur. J.* **2016**, *22*, 13037–13040.

(123) Bronner, C.; Stremlau, S.; Gille, M.; Braußе, F.; Haase, A.; Hecht, S.; Tegeder, P. *Angew. Chem. Int. Ed.* **2013**, *52*, 4422–4425.

(124) Zhang, Y.; Zhang, Y.; Li, G.; Lu, J.; Lin, X.; Du, S.; Berger, R.; Feng, X.; Müllen, K.; Gao, H.-J. *Appl. Phys. Lett.* **2014**, *105*, 023101.

(125) Kawai, S.; Saito, S.; Osumi, S.; Yamaguchi, S.; Foster, A. S.; Spijker, P.; Meyer, E. *Nat. Commun.* **2015**, *6*.

(126) Cai, J.; Pignedoli, C. A.; Talirz, L.; Ruffieux, P.; Söde, H.; Liang, L.; Meunier, V.; Berger, R.; Li, R.; Feng, X.; Müllen, K.; Fasel, R. *Nat. Nanotechnol.* **2014**, *9*, 896–900.

(127) Dössel, L.; Gherghel, L.; Feng, X.; Müllen, K. *Angew. Chem. Int. Ed.* **2011**, *50*, 2540–2543.

(128) Vo, T. H.; Shekhirev, M.; Kunkel, D. A.; Morton, M. D.; Berglund, E.; Kong, L.; Wilson, P. M.; Dowben, P. A.; Enders, A.; Sinitskii, A. *Nat. Commun.* **2014**.

(129) Saleh, M.; Baumgarten, M.; Mavrinskiy, A.; Schäfer, T.; Müllen, K. *Macromolecules* **2010**, *43*, 137–143.

(130) El Gemayel, M.; Narita, A.; Dössel, L. F.; Sundaram, R. S.; Kiersnowski, A.; Pisula, W.; Hansen, M. R.; Ferrari, A. C.; Orgiu, E.; Feng, X.; Múllen, K.; Samorí, P. *Nanoscale* **2014**, *6*, 6301–6314.

(131) Schwab, M. G.; Narita, A.; Hernandez, Y.; Balandina, T.; Mali, K. S.; De Feyter, S.; Feng, X.; Muüllen, K. *J. Am. Chem. Soc.* **2012**, *134*, 18169–18172.

(132) Vo, T. H.; Shekhirev, M.; Lipatov, A.; Korlacki, R. A.; Sinitskii, A. *Faraday Discuss.* **2014**, *173*, 105–113.

(133) Abbas, A. N.; Liu, G.; Narita, A.; Orosco, M.; Feng, X.; Müllen, K.; Zhou, C. *J. Am. Chem. Soc.* **2014**, *136*, 7555–7558.

(134) Narita, A. et al. *Nat. Chem.* **2014**, *6*, 126–132.

(135) Narita, A.; Verzhbitskiy, I. A.; Frederickx, W.; Mali, K. S.; Jensen, S. A.; Hansen, M. R.; Bonn, M.; De Feyter, S.; Casiraghi, C.; Feng, X.; Müllen, K. *ACS Nano* **2014**, *8*, 11622–11630.

(136) Zschieschang, U.; Klauk, H.; Müeller, I. B.; Strudwick, A. J.; Hintermann, T.; Schwab, M. G.; Narita, A.; Feng, X.; Müellen, K.; Weitz, R. T. *Adv. Electron. Mater.* **2015**, *1*.

(137) Konnerth, R.; Cervetti, C.; Narita, A.; Feng, X.; Müllen, K.; Hoyer, A.; Burghard, M.; Kern, K.; Dressel, M.; Bogani, L. *Nanoscale* **2015**, *7*, 12807–12811.

(138) Fantuzzi, P.; Martini, L.; Candini, A.; Corradini, V.; del Pennino, U.; Hu, Y.; Feng, X.; Müllen, K.; Narita, A.; Affronte, M. *Carbon* **2016**, *104*, 112–118.

(139) Jordan, R. S.; Li, Y. L.; Lin, C.-W.; McCurdy, R. D.; Lin, J. B.; Brosmer, J. L.; Marsh, K. L.; Khan, S. I.; Houk, K.; Kaner, R. B.; Rubin, Y. *J. Am. Chem. Soc.* **2017**.

(140) Lehnherr, D.; Chen, C.; Pedramrazi, Z.; DeBlase, C. R.; Alzola, J. M.; Keresztes, I.; Lobkovsky, E. B.; Crommie, M. F.; Dichtel, W. R. *Chem. Sci.* **2016**, *7*, 6357–6364.

(141) Hein, S. J.; Lehnherr, D.; Arslan, H.; J. Uribe-Romo, F.; Dichtel, W. R. *Acc. Chem. Res.* **2017**.

(142) Yang, W.; Lucotti, A.; Tommasini, M.; Chalifoux, W. A. *J. Am. Chem. Soc.* **2016**, *138*, 9137–9144.

(143) Jordan, R. S.; Wang, Y.; McCurdy, R. D.; Yeung, M. T.; Marsh, K. L.; Khan, S. I.; Kaner, R. B.; Rubin, Y. *Chem* **2016**, *1*, 78–90.

(144) Sun, Z.; Zeng, Z.; Wu, J. *Chem. Asian J.* **2013**, *8*, 2894–2904.

(145) Sun, Z.; Ye, Q.; Chi, C.; Wu, J. *Chem. Soc. Rev.* **2012**, *41*, 7857–7889.

(146) Mills, W. H.; Mills, M. *J. Chem. Soc. Trans.* **1912**, *101*, 2194–2208.

(147) Clar, E. *Eur. J. Inorg. Chem.* **1948**, *81*, 52–63.

(148) Ye, Q.; Chi, C. *Chem. Mater.* **2014**, *26*, 4046–4056.

(149) Dorel, R.; Manzano, C.; Grisolia, M.; Soe, W.-H.; Joachim, C.; Echavarren, A. M. *Chem. Commun.* **2015**, *51*, 6932–6935.

(150) Nakada, K.; Fujita, M.; Dresselhaus, G.; Dresselhaus, M. S. *Phys. Rev. B* **1996**, *54*, 17954–17961.

(151) Hod, O.; Barone, V.; Scuseria, G. E. *Phys. Rev. B* **2008**, *77*, 035411.

(152) Jiang, D.-e.; Sumpter, B. G.; Dai, S. *J Chem. Phys.* **2007**, *127*, 124703.

(153) Jiang, D.-e.; Dai, S. *Chem. Phys. Lett.* **2008**, *466*, 72–75.

(154) Moscardó, F.; San-Fabián, E. *Chem. Phys. Lett.* **2009**, *480*, 26–30.

(155) Rivero, P.; Jiménez-Hoyos, C. A.; Scuseria, G. E. *J. Phys. Chem. B* **2013**, *117*, 12750–12758.

(156) Plasser, F.; Pašalić, H.; Gerzabek, M. H.; Libisch, F.; Reiter, R.; Burgdörfer, J.; Müller, T.; Shepard, R.; Lischka, H. *Angew. Chem. Int. Ed.* **2013**, *52*, 2581–2584.

(157) Clar, E., *The Aromatic Sextet*; New York, Wiley: 1972.

(158) Jiang, D.; Dai, S. *J. Phys. Chem. A* **2008**, *112*, 332–335.

(159) Duong, K. S.; Houk, K.; Carter, E. A.; Wudl, F. *J. Am. Chem. Soc.* **2004**, *126*, 7416r7417.

(160) Konishi, A.; Hirao, Y.; Nakano, M.; Shimizu, A.; Botek, E.; Champagne, B.; Shiomi, D.; Sato, K.; Takui, T.; Matsumoto, K.; Kurata, H.; Kubo, T. *J. Am. Chem. Soc.* **2010**, *132*, 11021–11023.

(161) Konishi, A.; Hirao, Y.; Matsumoto, K.; Kurata, H.; Kishi, R.; Shigeta, Y.; Nakano, M.; Tokunaga, K.; Kamada, K.; Kubo, T. *J. Am. Chem. Soc.* **2013**, *135*, 1430–1437.

(162) Li, J.; Zhang, K.; Zhang, X.; Huang, K.-W.; Chi, C.; Wu, J. *J. Org. Chem.* **2010**, *75*, 856–863.

(163) Zöphel, L.; Berger, R.; Gao, P.; Enkelmann, V.; Baumgarten, M.; Wagner, M.; Müllen, K. *Chem. Eur. J.* **2013**, *19*, 17821–17826.

(164) Matsumoto, A.; Suzuki, M.; Kuzuhara, D.; Hayashi, H.; Aratani, N.; Yamada, H. *Angew. Chem. Int. Ed.* **2015**, *54*, 8175–8178.

(165) Tanaka, K.; Aratani, N.; Kuzuhara, D.; Sakamoto, S.; Okujima, T.; Ono, N.; Uno, H.; Yamada, H. *RSC Adv.* **2013**, *3*, 15310–15315.

(166) Li, S.; Jia, Z.; Nakajima, K.; Kanno, K.-i.; Takahashi, T. *J. Org. Chem.* **2011**, *76*, 9983–9987.

(167) Zhang, X.; Jiang, X.; Luo, J.; Chi, C.; Chen, H.; Wu, J. *Chem. Eur. J.* **2010**, *16*, 464–468.

(168) Xiao, S.; Kang, S. J.; Wu, Y.; Ahn, S.; Kim, J. B.; Loo, Y.-L.; Siegrist, T.; Steigerwald, M. L.; Li, H.; Nuckolls, C. *Chem. Sci.* **2013**, *4*, 2018–2023.

(169) Loo, Y.-L.; Hiszpanski, A. M.; Kim, B.; Wei, S.; Chiu, C.-Y.; Steigerwald, M. L.; Nuckolls, C. *Org. Lett* **2010**, *12*, 4840–4843.

(170) Pijper, T. C.; Pijper, D.; Pollard, M. M.; Dumur, F.; Davey, S. G.; Meetsma, A.; Feringa, B. L. *J. Org. Chem.* **2010**, *75*, 825–838.

(171) Clar, E. *Eur. J. Inorg. Chem.* **1949**, *82*, 495–514.

(172) Xiao, S.; Myers, M.; Miao, Q.; Sanaur, S.; Pang, K.; Steigerwald, M. L.; Nuckolls, C. *Angew. Chem. Int. Ed.* **2005**, *44*, 7390–7394.

(173) Liu, J.; Ravat, P.; Wagner, M.; Baumgarten, M.; Feng, X.; Müllen, K. *Angew. Chem. Int. Ed.* **2015**, *54*, 12442–12446.

(174) Bard, A. J.; Faulkner, L. R.; Leddy, J.; Zoski, C. G., *Electrochemical methods: fundamentals and applications*; wiley New York: 1980; Vol. 2.

(175) Lai, Y.; Peck, T. *Aust. J. Chem.* **1992**, *45*, 2067–2071.

(176) Brey, L.; Fertig, H. *Phys. Rev. B* **2006**, *73*, 235411.

(177) Orita, A.; Hasegawa, D.; Nakano, T.; Otera, J. *Chem. Eur. J.* **2002**, *8*, 2000–2004.

(178) Ruffieux, P.; Wang, S.; Yang, B.; Sánchez-Sánchez, C.; Liu, J.; Dienel, T.; Talirz, L.; Shinde, P.; Pignedoli, C. A.; Passerone, D.; Dumslaff, T.; Xinliang, F.; Müllen, K.; Fasel, R. *Nature* **2016**, *531*, 489–492.

(179) Girao, E. C.; Liang, L.; Cruz-Silva, E.; Souza Filho, A. G.; Meunier, V. *Phys. Rev. Lett.* **2011**, *107*, 135501.

(180) Haase, N.; Grigoriadis, C.; Butt, H.-J.; Mufffdfffdllen, K.; Floudas, G. *J. Phys. Chem. B* **2011**, *115*, 5807–5814.

(181) Reisch, H. A.; Bratcher, M. S.; Scott, L. T. *Org. Lett.* **2000**, *2*, 1427–1430.

(182) Hori, Y.; Wakebe, H.; Tsukamoto, T.; Koga, O. *Electrochim. Acta* **1994**, *39*, 1833–1839.

(183) Hori, Y. In *Modern Aspects of Electrochemistry*; Springer: 2008, pp 89–189.

(184) Lu, Q.; Jiao, F. *Nano Energy* **2016**, *29*, 439–456.

(185) Liu, M.; Zhang, R.; Chen, W. *Chem. Rev.* **2014**, *114*, 5117–5160.

(186) Peng, S.; Lee, Y.; Wang, C.; Yin, H.; Dai, S.; Sun, S. *Nano Res.* **2008**, *1*, 229–234.

(187) Zhu, W.; Michalsky, R.; Metin, Ö.; Lv, H.; Guo, S.; Wright, C. J.; Sun, X.; Peterson, A. A.; Sun, S. *J. Am. Chem. Soc.* **2013**, *135*, 16833–16836.

(188) Chen, Y.; Li, C. W.; Kanan, M. W. *J. Am. Chem. Soc.* **2012**, *134*, 19969–19972.

(189) Koh, J. H.; Jeon, H. S.; Jee, M. S.; Nursanto, E. B.; Lee, H.; Hwang, Y. J.; Min, B. K. *J. Phys. Chem. C* **2014**, *119*, 883–889.

(190) Mistry, H.; Reske, R.; Zeng, Z.; Zhao, Z.-J.; Greeley, J.; Strasser, P.; Cuenya, B. R. *J. Am. Chem. Soc.* **2014**, *136*, 16473–16476.

(191) Bard, A. J. *J. Am. Chem. Soc.* **2010**, *132*, 7559–7567.

(192) Kim, D.; Resasco, J.; Yu, Y.; Asiri, A. M.; Yang, P. *Nat. Commun.* **2014**, *5*, 5948.

(193) Choi, H. C.; Shim, M.; Bangsaruntip, S.; Dai, H. *J. Am. Chem. Soc.* **2002**, *124*, 9058–9059.

(194) Pramod, P.; Soumya, C.; Thomas, K. G. *J. Phys. Chem. Lett.* **2011**, *2*, 775–781.

(195) Jiang, K.; Eitan, A.; Schadler, L. S.; Ajayan, P. M.; Siegel, R. W.; Grobert, N.; Mayne, M.; Reyes-Reyes, M.; Terrones, H.; Terrones, M. *Nano Lett.* **2003**, *3*, 275–277.

(196) Cao, Z.; Kim, D.; Hong, D.; Yu, Y.; Xu, J.; Lin, S.; Wen, X.; Nichols, E. M.; Jeong, K.; Reimer, J. A.; Yang, P.; Chang, C. *J. Am. Chem. Soc.* **2016**, *138*, 8120–8125.

(197) Lee, J.; Kim, J.; Hyeon, T. *Adv. Mater.* **2006**, *18*, 2073–2094.

(198) Kim, H.; Robertson, A. W.; Kim, S. O.; Kim, J. M.; Warner, J. H. *ACS Nano* **2015**, *9*, 5947–5957.

(199) Stein, A.; Wang, Z.; Fierke, M. A. *Adv. Mater.* **2009**, *21*, 265–293.

(200) Luo, J.; Jang, H. D.; Huang, J. *ACS Nano* **2013**, *7*, 1464–1471.

(201) McEnaney, B. *Carbon* **1988**, *26*, 267–274.

(202) Rodriguez-Reinoso, F.; Garrido, J.; Martin-Martinez, J.; Molina-Sabio, M.; Torregrosa, R. *Carbon* **1989**, *27*, 23–32.

(203) Sing, K. In Rouqueerol, J.; Rouquerol, F.; Llewellyn, P.; Maurin, G.; Sing, K. *Adsorption by Powders and Porous Solids*; Elsevier: Oxford, 2014, pp 339–360.

(204) Thommes, M.; Cychosz, K.; Neimark, A. In Tascón, J. *Novel Carbon Adsorbents*; Elsevier: Oxford, 2012, pp 111–116.

(205) López, M. B.; Martınez-Alonso, A.; Tascon, J. *Carbon* **2000**, *38*, 1177–1182.

(206) Ehrburger, P.; Pusset, N.; Dziedzinl, P. *Carbon* **1992**, *30*, 1105–1109.

(207) Thommes, M.; Morlay, C.; Ahmad, R.; Joly, J. *Adsorption* **2011**, *17*, 653.

(208) Verdaguer-Casadevall, A.; Li, C. W.; Johansson, T. P.; Scott, S. B.; McKeown, J. T.; Kumar, M.; Stephens, I. E.; Kanan, M. W.; Chorkendorff, I. *J. Am. Chem. Soc.* **2015**, *137*, 9808–9811.

(209) Hamelin, A. *J. Electroanal. Chem.* **1984**, *165*, 167–180.

(210) Hamelin, A.; Lipkowski, J. *J. Electroanal. Chem.* **1984**, *171*, 317–330.

(211) Shao, Y.; Yin, G.; Gao, Y.; Shi, P. *J. Electrochem. Soc.* **2006**, *153*, A1093–A1097.

(212) Wang, X. X.; Tan, Z. H.; Zeng, M.; Wang, J. N. *Sci. Rep.* **2014**, *4*.

(213) Wang, Y.; Nie, Y.; Ding, W.; Chen, S.; Xiong, K.; Qi, X.; Zhang, Y.; Wang, J.; Wei, Z. *Chem. Commun.* **2015**, *51*, 8942–8945.

(214) Subramanian, V.; Wolf, E. E.; Kamat, P. V. *J. Am. Chem. Soc.* **2004**, *126*, 4943–4950.

(215) Su, H.; Zhang, K.-X.; Zhang, B.; Wang, H.-H.; Yu, Q.-Y.; Li, X.-H.; Antonietti, M.; Chen, J.-S. *J. Am. Chem. Soc.* **2017**, *139*, 811–818.

(216) Ding, M.; Tang, Y.; Star, A. *J. Phys. Chem. Lett.* **2012**, *4*, 147–160.

(217) Khoa, N. T.; Kim, S. W.; Yoo, D.-H.; Kim, E. J.; Hahn, S. H. *Appl. Catal. A* **2014**, *469*, 159–164.

(218) Gautier, L.; Le Borgne, V.; Delegan, N.; Pandiyan, R.; El Khakani, M. *Nanotechnol.* **2015**, *26*, 045706.

(219) Giovannetti, G.; Khomyakov, P.; Brocks, G.; Karpan, V. v.; Van den Brink, J.; Kelly, P. J. *Phys. Rev. Lett.* **2008**, *101*, 026803.

(220) Peng, X.; Tang, F.; Copple, A. *J. Phys. Condens. Matter* **2012**, *24*, 075501.

(221) Suzuki, S.; Bower, C.; Watanabe, Y.; Zhou, O. *Appl. Phys. Lett.* **2000**, *76*, 4007–4009.

(222) Fabish, T.; Schleifer, D. *Carbon* **1984**, *22*, 19–38.

(223) Loutfy, R. O. *Carbon* **1986**, *24*, 127–130.

(224) Gileadi, E., *Electrode kinetics for chemists, chemical engineers, and materials scientists*; Capstone: 1993.

(225) Lu, Q.; Rosen, J.; Zhou, Y.; Hutchings, G. S.; Kimmel, Y. C.; Chen, J. G.; Jiao, F. *Nat. Commun.* **2014**, *5*, 3242.

(226) Hori, Y.; Murata, A.; Takahashi, R.; Suzuki, S. *J. Am. Chem. Soc.* **1987**, *109*, 5022–5023.

(227) Hori, Y.; Takahashi, R.; Yoshinami, Y.; Murata, A. *J. Phys. Chem. B* **1997**, *101*, 7075–7081.

(228) Sheng, T.; Wang, D.; Lin, W.-F.; Hu, P.; Sun, S.-G. *Electrochim. Acta* **2016**, *190*, 446–454.

(229) Calle-Vallejo, F.; Koper, M. *Angew. Chem. Int. Ed.* **2013**, *52*, 7282–7285.

(230) Xiao, H.; Cheng, T.; Goddard III, W. A.; Sundararaman, R. *J. Am. Chem. Soc.* **2016**, *138*, 483–486.

(231) Li, C. W.; Ciston, J.; Kanan, M. W. *Nature* **2014**, *508*, 504–507.

(232) Feng, X.; Jiang, K.; Fan, S.; Kanan, M. W. *ACS Cent. Sci.* **2016**, *2*, 169–174.

(233) Bertheussen, E.; Verdaguer-Casadevall, A.; Ravasio, D.; Montoya, J. H.; Trimarco, D. B.; Roy, C.; Meier, S.; Wendland, J.; Nørskov, J. K.; Stephens, I. E.; Chorkendorff, I. *Angew. Chem. Int. Ed.* **2016**, *55*, 1450–1454.

(234) Gong, M.; Cao, Z.; Liu, W.; Nichols, E. M.; Smith, P. T.; Derrick, J. S.; Liu, Y.-S.; Liu, J.; Wen, X.; Chang, C. J. *ACS Cent. Sci.* **2017**, *3*, 1032–1040.

(235) Mott, D.; Galkowski, J.; Wang, L.; Luo, J.; Zhong, C.-J. *Langmuir* **2007**, *23*, 5740–5745.

(236) Yang, H.-J.; Chen, C.-Y.; Yuan, F.-W.; Tuan, H.-Y. *J. Phys. Chem. C* **2013**, *117*, 21955–21964.

(237) Manthiram, K.; Beberwyck, B. J.; Alivisatos, A. P. *J. Am. Chem. Soc.* **2014**, *136*, 13319–13325.

(238) Kim, D.; Kley, C. S.; Li, Y.; Yang, P. *Proc. Natl. Acad. Sci. U.S.A.* **2017**, *114*, 10560–10565.

(239) Fafarman, A. T.; Koh, W.-K.; Diroll, B. T.; Kim, D. K.; Ko, D.-K.; Oh, S. J.; Ye, X.; Doan-Nguyen, V.; Crump, M. R.; Reifsnyder, D. C.; Murray, C. B.; Kagan, C. R. *J. Am. Chem. Soc.* **2011**, *133*, 15753–15761.

(240) Doris, S. E.; Lynch, J. J.; Li, C.; Wills, A. W.; Urban, J. J.; Helms, B. A. *J. Am. Chem. Soc.* **2014**, *136*, 15702–15710.

(241) Rosen, E. L.; Buonsanti, R.; Llordes, A.; Sawvel, A. M.; Milliron, D. J.; Helms, B. A. *Angew. Chem. Int. Ed.* **2012**, *51*, 684–689.

(242) Nag, A.; Kovalenko, M. V.; Lee, J.-S.; Liu, W.; Spokoyny, B.; Talapin, D. V. *J. Am. Chem. Soc.* **2011**, *133*, 10612–10620.

(243) Dong, A.; Ye, X.; Chen, J.; Kang, Y.; Gordon, T.; Kikkawa, J. M.; Murray, C. B. *J. Am. Chem. Soc.* **2010**, *133*, 998–1006.

(244) Alonso, F.; Moglie, Y.; Radivoy, G.; Yus, M. *J. Org. Chem.* **2011**, *76*, 8394–8405.

(245) Nador, F.; Volpe, M. A.; Alonso, F.; Feldhoff, A.; Kirschning, A.; Radivoy, G. *Appl. Catal. A* **2013**, *455*, 39–45.

(246) Chen, J. S.; Lou, X. W. D. *Small* **2013**, *9*, 1877–1893.

(247) Poizot, P.; Laruelle, S.; Grugeon, S.; Dupont, L.; Tarascon, J. *Nature* **2000**, *407*, 496–499.

(248) Bruce, P. G.; Scrosati, B.; Tarascon, J.-M. *Angew. Chem. Int. Ed.* **2008**, *47*, 2930–2946.

(249) Aricò, A. S.; Bruce, P.; Scrosati, B.; Tarascon, J.-M.; Van Schalkwijk, W. *Nat. Mater.* **2005**, *4*, 366–377.

(250) Armand, M.; Tarascon, J.-M. *Nature* **2008**, *451*, 652–657.

(251) Goodenough, J. B.; Kim, Y. *Chem. Mater.* **2009**, *22*, 587–603.

(252) Paek, S.-M.; Yoo, E.; Honma, I. *Nano Lett.* **2008**, *9*, 72–75.

(253) Yao, J.; Shen, X.; Wang, B.; Liu, H.; Wang, G. *Electrochem. Commun.* **2009**, *11*, 1849–1852.

(254) Kil, E.-H.; Ha, H.-J.; Lee, S.-Y. *Macromol. Chem. and Phys.* **2011**, *212*, 2217–2223.

(255) Liang, J.; Wei, W.; Zhong, D.; Yang, Q.; Li, L.; Guo, L. *ACS Appl. Mater. Interfaces* **2012**, *4*, 454–459.

(256) Zhu, X.; Zhu, Y.; Murali, S.; Stoller, M. D.; Ruoff, R. S. *J. Power Sources* **2011**, *196*, 6473–6477.

(257) Wang, D.; Li, X.; Wang, J.; Yang, J.; Geng, D.; Li, R.; Cai, M.; Sham, T.-K.; Sun, X. *J. Phys. Chem. C* **2012**, *116*, 22149–22156.

(258) Zhou, X.; Wan, L.-J.; Guo, Y.-G. *Adv. Mater.* **2013**, *25*, 2152–2157.

(259) Liu, L.; An, M.; Yang, P.; Zhang, J. *Sci. Rep.* **2015**, *5*.

(260) Deng, Y.; Fang, C.; Chen, G. *J. Power Sources* **2016**, *304*, 81–101.

(261) Zhou, W.; Wang, J.; Zhang, F.; Liu, S.; Wang, J.; Yin, D.; Wang, L. *Chem. Commun.* **2015**, *51*, 3660–3662.

(262) Courtney, I. A.; Dahn, J. *J. Electrochem. Soc.* **1997**, *144*, 2943–2948.

(263) Idota, Y.; Kubota, T.; Matsufuji, A.; Maekawa, Y.; Miyasaka, T. *Science* **1997**, *276*, 1395–1397.

(264) Wang, Y.; Lee, J. Y.; Zeng, H. C. *Chem. Mater.* **2005**, *17*, 3899–3903.

(265) Kim, C.; Noh, M.; Choi, M.; Cho, J.; Park, B. *Chem. Mater.* **2005**, *17*, 3297–3301.

(266) Wang, C.; Zhou, Y.; Ge, M.; Xu, X.; Zhang, Z.; Jiang, J. *J. Am. Chem. Soc.* **2009**, *132*, 46–47.

(267) Wang, C.; Du, G.; Ståhl, K.; Huang, H.; Zhong, Y.; Jiang, J. *J. Phys. Chem. C* **2012**, *116*, 4000–4011.

(268) Kim, H.; Park, G. O.; Kim, Y.; Muhammad, S.; Yoo, J.; Balasubramanian, M.; Cho, Y.-H.; Kim, M.-G.; Lee, B.; Kang, K.; Yoon, W.-S. *Chem. Mater.* **2014**, *26*, 6361–6370.

(269) Yoo, E.; Kim, J.; Hosono, E.; Zhou, H.-s.; Kudo, T.; Honma, I. *Nano Lett.* **2008**, *8*, 2277–2282.

(270) Kim, Y.-J.; Lee, H.; Sohn, H.-J. *Electrochem. Commun.* **2009**, *11*, 2125–2128.

(271) Lewis, N. S.; Nocera, D. G. *Proc. Natl. Acad. Sci. U.S.A.* **2006**, *103*, 15729–15735.

(272) Liu, C.-j.; Burghaus, U.; Besenbacher, F.; Wang, Z. L. *ACS Nano* **2010**.

(273) Tollefson, J. *Nature News* **2010**, *464*, 1262–1264.

(274) Schlapbach, L.; Züttel, A. *Nature* **2001**, *414*, 353–358.

(275) Sakintuna, B.; Lamari-Darkrim, F.; Hirscher, M. *Int. J. Hydrog. Energy* **2007**, *32*, 1121–1140.

(276) Orimo, S.-i.; Nakamori, Y.; Eliseo, J. R.; Züttel, A.; Jensen, C. M. *Chem. Rev.* **2007**, *107*, 4111–4132.

(277) Schwarz, R. *MRS Bull.* **1999**, *24*, 40–44.

(278) Cheng, F.; Tao, Z.; Liang, J.; Chen, J. *Chem. Commun.* **2012**, *48*, 7334–7343.

(279) Jeon, K.-J.; Moon, H. R.; Ruminski, A. M.; Jiang, B.; Kisielowski, C.; Bardhan, R.; Urban, J. J. *Nat. Mater.* **2011**, *10*, 286–290.

(280) Rieke, R. D. *Science* **1989**, *246*, 1260.

(281) Liao, T.; Sun, C.; Sun, Z.; Du, A.; Smith, S. *Phys. Chem. Chem. Phys.* **2013**, *15*, 8054–8057.

(282) Navalon, S.; Dhakshinamoorthy, A.; Alvaro, M.; Garcia, H. *Chem. Rev.* **2014**, *114*, 6179–6212.

(283) Graetz, J.; Hauback, B. C. *MRS Bull.* **2013**, *38*, 473–479.

(284) Graetz, J.; Reilly, J.; Yartys, V.; Maehlen, J.; Bulychev, B.; Antonov, V.; Tarasov, B.; Gabis, I. *J. Alloys Comp.* **2011**, *509*, S517–S528.

(285) Hanada, N.; Kamura, A.; Suzuki, H.; Takai, K.; Ichikawa, T.; Kojima, Y. *J. Alloys Comp.* **2011**, *509*, S584–S587.

(286) Manikam, V. R.; Cheong, K. Y.; Razak, K. A. *Mater. Sci. Eng. B* **2011**, *176*, 187–203.

(287) Haber, J. A.; Buhro, W. E. *J. Am. Chem. Soc.* **1998**, *120*, 10847–10855.

(288) Chung, S. W.; Guliants, E. A.; Bunker, C. E.; Hammerstroem, D. W.; Deng, Y.; Burgers, M. A.; Jelliss, P. A.; Buckner, S. W. *Langmuir* **2009**, *25*, 8883–8887.

(289) McClain, M. J.; Schlather, A. E.; Ringe, E.; King, N. S.; Liu, L.; Manjavacas, A.; Knight, M. W.; Kumar, I.; Whitmire, K. H.; Everitt, H. O.; Nordlander, P.; Halas, N. *Nano Lett.* **2015**, *15*, 2751–2755.

(290) Jouet, R.; Carney, J.; Granholm, R.; Sandusky, H.; Warren, A. *Mater. Sci. Technol.* **2006**, *22*, 422–429.

(291) Meziani, M. J.; Bunker, C. E.; Lu, F.; Li, H.; Wang, W.; Guliants, E. A.; Quinn, R. A.; Sun, Y.-P. *ACS Appl. Mater. Interfaces* **2009**, *1*, 703–709.

(292) Jouet, R. J.; Warren, A. D.; Rosenberg, D. M.; Bellitto, V. J.; Park, K.; Zachariah, M. R. *Chem. Mater.* **2005**, *17*, 2987–2996.

(293) Li, H.; Meziani, M. J.; Lu, F.; Bunker, C. E.; Guliants, E. A.; Sun, Y.-P. *J. Phys. Chem. C* **2009**, *113*, 20539–20542.

(294) Graetz, J. *ISRN Materials Science* **2012**, *2012*.

(295) Clasen, H. *H. Clasen, Germany Pat* **1962**, *1141*, 1962–2.

(296) Zidan, R.; Garcia-Diaz, B. L.; Fewox, C. S.; Stowe, A. C.; Gray, J. R.; Harter, A. G. *Chem. Commun.* **2009**, 3717–3719.

(297) Hung, L.-I.; Tsung, C.-K.; Huang, W.; Yang, P. *Adv. Mater.* **2010**, *22*, 1910–1914.

(298) Zhang, S.; Shao, Y.; Liao, H.-G.; Liu, J.; Aksay, I. A.; Yin, G.; Lin, Y. *Chem. Mater.* **2011**, *23*, 1079–1081.